Novel magneto-responsive ultrafiltration membranes for remote controlled switchable molecular sieving

Dissertation

zur Erlangung des akademischen Grades eines Doktors der Naturwissenschaften

- Dr. rer. nat.-

vorgelegt von

Xi Lin

geboren in Sichuan, China

Fakultät für Chemie

der

Universität Duisburg-Essen

Essen 2016

Disputation: Essen, 01.03.2017

Chair: Prof. Dr. Eckhard Spohr

Advisor: Prof. Dr. Mathias Ulbricht

Reviewer: Prof. Dr. Stephan Barcikowski

The work presented here was performed from June 2013 till June 2016 at the Lehrstuhl für Technische Chemie II of the University of Duisburg-Essen and supervised by Prof. Dr. Mathias Ulbricht.

Abstract

Stimuli-responsive separation membranes with tunable molecular scale pore size, which are desirable for on-demand sieving of targeted macromolecules, have attracted increasing attention in recent years. It is well-known that magnetic nanoparticles (MNP) can generate heat when exposed to an alternating magnetic field (AMF), due to hysteresis and relaxation losses. When combined with thermo-responsive polymers, the heat generated by MNP can trigger the phase or conformation change of polymer and therefore by their synergistic effect, magneto-responsive material systems can be designed.

In this study, by using iron oxide MNP as localized heater and thermo-responsive Poly(*N*-isopropylacrylamide) (PNIPAAm) hydrogel as sieving medium and actuator, two kinds of magneto-responsive membranes with excellent responsivity and tunability for molecular sieving have been developed. One type is **magneto-hydrogel pore-filled membrane** constructed by post modification of commercial polyethylene terephthalate (PET) track-etched membrane. Such membranes use the hydrogel mesh as the ultrafiltration sieving medium, and the iron oxide entrapped in the hydrogel network as localized heater. It has been demonstrated that by manipulating AMF and thus controlling the heat generated by the incorporated MNP, the micro-syneresis of PNIPAAm network can be locally triggered and magneto-responsive molecule sieving can be achieved. The other type is **polyethersulfone (PES) mixed matrix membrane blended with prefabricated PNIPAAm nanogel and iron oxide MNP** fabricated by non-solvent induced phase separation (NIPS) process. It has the PNIPAAm nanogels as responsive gates and the co-blended iron oxide nanoparticles as local heaters. By manipulating the swollen/shrunken state of PNIPAAm nanogels triggered by the heat generation of nearby MNP, the molecular sieving performance of the membrane can be adjusted.

Overall, important parameters affecting the construction of both kinds of membranes have been studied, their stimuli-responsive barrier properties including thermo- and magneto-responses have been investigated, and their structure and molecular sieving effect in the ultrafiltration range have been evaluated. Based on the results, correlations between synthesis, structure and separation performance of the novel magneto-responsive membranes and their potential for applications have been discussed in this work.

Acknowledgment

First, I would like to express my sincere gratitude to my supervisor, Prof. Dr. Mathias Ulbricht, for providing me the great opportunity to do research work in his group. It is one of my best luck to make PhD study under his supervision. During my research work, he has not only supported and guided me with his profound knowledge in membrane and material science, but also encouraged me to explore my own ideas. I am grateful for all the inspiring discussions he has offered me, even when he was very busy, and I am always impressed by his patience, kindness, and generosity of time and encouragement to students.

At the same time, I would like give my best thanks to China Scholarship Council (CSC), for providing the doctoral scholarship that enables my study in Germany. I am very grateful for the support from CSC, including my transferring from Berlin to Essen and the extension for my PhD study.

I also want to thank Prof. Dr. Stephan Barcikowski for kindly reviewing my thesis and Prof. Dr. Eckhard Spohr for kindly being the chair of my defense committee.

Special thanks are given to master students Rong Huang and Bao Nguyen Quoc, who have worked together with me for this project. Rong has worked for the magneto-hydrogel pore-filled membranes during her master thesis and Bao has worked for the mixed matrix membrane during his practice work. I have enjoyed working with them and would sincerely thank them for their contribution.

I also owe many thanks to Jürgen Leistikow from Physical Chemistry, who kindly designed and prepared the AMF probe and Helmholtz coils for my project. It was a great pleasure to work with him.

Moreover, I would like to thank Smail Boukercha for SEM visualization, Jasmina Kovacevic for the TGA analysis, Soma Salamon for the magnetization measurements, Prof. Daniel Erni for computer simulation of magnetic field distribution, and Jakub Cichoszewski for size and zeta potential analysis for commercial MNP. I appreciate a lot for their professionalism and kind help.

I am deeply grateful to all the current and former colleagues in Technical Chemistry II, for friendly and supportive working atmosphere. In particular, I would like to thank Inge, Tobias, Jackelyn, and Claudia for the technical support and Mrs.Nordmann for secretarial work. Also, I am very thankful to Martyna and Ibrahim, for help, support and the inspiring discussion on my work. I would also like to thank Anne, Hanna, Clelia, Jania, Inga, Marta, Thorsten (Van Den Berg), Alexander, Ahemd, Dominic, Mathias, Marc, Miao and Nkem, for their help and also for enjoyable time we spent together. At last, special thanks are given to Aleksandra (Gajda) and Dongxu for their help and friendship when I first arrived in Essen.

On the other hand I could not complete my study so smoothly without the support, encouragement and company of many other friends in Germany. I would like to thank my flatmate Xiaoxiao for her company and amusement; she can always cheer me up especially during the stressful moments. Many thanks to Mao, Jingcheng and Hao from Organic chemistry for their friendship, support and the happy times we had together. Moreover, I want to thank Tao who introduced Prof.Ulbricht's group to me in the first place, and fellowmates Quanchao, Jingde, Bin and Mojdeh who encourage me all the time. I wish a good success to them for their doctoral study.

At last, I owe the deepest gratitude to my parents and sister, who are always there for me, for their love, support and understanding during my entire study.

All the best to all of you!

The main parts of this dissertation have been published in the following publications:

1. X. Lin, R. Huang, M. Ulbricht, **Novel magneto-responsive membrane for remote control switchable molecular sieving.** *J. Mater. Chem. B.* **2016**, 4, 867-879.

2. X. Lin, B. Nguyen Quoc, M. Ulbricht, **Magneto-responsive polyethersulfone-based iron oxide cum hydrogel mixed matrix composite membranes for switchable molecular sieving**. *ACS Appl. Mater. Interfaces.* **2016**, 8, 29001−29014.

Content

1. Introduction

1.1 Background and motivation

Since the first commercial synthetic membrane for water purification in 1930s, there has been tremendous development in the membrane field[1]. Nowadays, membrane technology not only provides efficient and sustainable industrial-scale solutions to address water scarcity and pollution[2, 3], produce energy[4], concentrate, fractionate and purify products[5, 6, 7, 8], but also support medical applications like hemodialysis and controlled drug delivery[9, 10], and new arising technology like microfluidics for biosensing, micro-analysis and microreactions, which require small amount membranes but with higher quality and specific functions[5, 11, 12, 13, 14, 15].

However, despite the successful implementation of membranes in various processes, due to their inert barrier and surface properties, traditional membranes have untunable permeability and selectivity and are prone to surface fouling, limited selectivity, which all limit efficiency of their applications[5, 8]. To address those problems, stimuli-responsive functional membranes with tunable barrier or surface properties have been proposed and developed in the last two decades[16, 17, 18, 19, 20, 21, 22]. By coupling traditional porous membrane with various stimuli-responsive polymers, so far, membranes that respond to different signals, including temperature, pH, ions, special molecules or electromagnetic irradiation have been prepared[18, 21, 22].

Biomacromolecules such as nucleic acids, lipids, saccharides, or proteins including enzymes and antibodies, are only few nanometers in size. They are not only very valuable pharmaceutical products but also vital substances for biochemical analysis. For traditional membrane process, it takes several separation steps by coupling several membranes with different pore size to isolate the targeted macromolecule, which is energy and time consuming[5, 8]. Therefore, for applications like drug delivery, biochemical analysis and down-stream processing of bioproducts, it is especially attractive to develop stimuli-responsive separation membranes with tunable molecular scale pore size, to achieve on-demand switchable sieving of targeted macromolecules or nanoparticles[8, 10]. During last two decades many stimuli-responsive gating membranes, with different structures and responsiveness, have been developed. They either rely on the stimuli-responsiveness of linear polymers blended into a membrane substrate or grafted as brushes on the membrane surface[23, 24, 25, 26, 27, 28, 29, 30], on the volume phase transition of blended, coated or

grafted micro- or nanogel particles[31, 32, 33, 34, 35, 36, 37], on expansion/contraction of responsive substrates with pores from sacrificial or volatile components[19, 38], or on responsive mesh-size change of pore-filled hydrogel[39]. However, despite the large number of publications about stimuli-responsive membranes, most reported membranes have only achieved micrometer or sub-micrometer range pore size tuning for changing hydraulic permeability[23, 25, 30, 31, 32] and molecules and ions diffusion[24, 28, 34, 35, 36], and do not have high resolution for the separation of nanoparticular or molecular targets, because pore size of support substrate or the size change of the responsive gating elements is too large.

On the other hand, most reported stimuli-responsive membranes are responsive to direct stimulants in feed like temperature, pH and ions, which could be limited by heat or mass transfer[16, 18]. Very few works explore remote electromagnetic triggers like light[40, 41, 42], electricity[43] and magnetic field[30, 34, 35, 44, 45], which could realize remote controllability with more precise responsivity and higher efficiency. There is a growing interest and effort to expand the breadth of available stimuli to those newly emerging remote stimulants[46, 47, 48]. Magneto-responsive membranes belong to this burgeoning trend and are of special interest, as they can realize spatial, temporal and remote control and have great potential, for instance for microfluidic systems in analytical or therapeutic devices[34, 35, 46, 48].

Based on the discussion above, here we would explore the possibility to develop novel magneto-responsive membranes for switchable molecular sieving, which has been until now absent from literature.

1.2. Aim of the research

Magnetic nanoparticles (MNP) can generate heat when exposed to an alternating magnetic field (AMF), due to hysteresis and relaxation losses. When combined with thermo-responsive polymers, the heat generated by MNP can trigger the phase or conformation change of polymer and therefore could be applied for controlled drug release and shape memory actuators. Poly(*N*-isopropylacrylamide) (PNIPAAm) is one of the most well-known thermo-responsive polymers, due to its pronounced phase change in response of temperature. Here, we would design and prepare novel magneto-responsive separation membranes with remote switchable molecular sieving effect, by using iron oxide MNP as localized heater and PNIPAAm hydrogel as sieving

medium and actuator. Specifically, two different membrane types have been proposed and experimentally achieved.

One type is magneto-hydrogel pore-filled membrane prepared by post modification of commercial polyethylene terephthalate (PET) track-etched membrane, as shown in **Figure 1.1 (a)**. It has MNP composite PNIPAAm hydrogel immobilized inside the pore of PET track-etched membrane. While PNIPAAm hydrogel mesh is expected to work as thermo-responsive sieving medium, MNP inside the hydrogel network are expected to work as localized heaters. At room temperature, when the AMF is turned off, the hydrogel network is in swollen state and the mesh size is relatively small, therefore, only small molecules can pass through the membrane; when the AMF is turned on, MNP will generate heat and cause the microsyneresis of hydrogel network, thus, bigger mesh size will be formed and larger molecules can also pass through the membrane. Therefore, it is expected that by manipulating AMF and thus controlling the heat generated by the incorporated MNP, the micro-syneresis of PNIPAAm network can be locally triggered and magneto-responsive molecule sieving can be achieved.

The other type is polyethersulfone (PES) membrane containing prefabricated PNIPAAm nanogel and iron oxide MNP fabricated by non-solvent induced phase separation (NIPS), as shown in **Figure 1.1 (b)**. Well-established membrane polymer PES is used as substrate material to ensure the easy processing during membrane preparation and good mechanical performance of the membrane, PNIPAAm NG embedded in the skin layer are intended to work as responsive gates for permeate and MNP in the membrane matrix are expected to work as localized heaters. At room temperature, when the AMF is turned off, the NG are in swollen state and will allow no or only very little flux through them; therefore, only small molecules can pass through the barrier layer via the intrinsic nanopores of the PES matrix. When the AMF is turned on, the MNP will generate heat and cause the shrinking of NG, extra gates will be open to allow larger molecules also to pass through the membrane. It is expected that the molecular sieving performance of the membrane can be controlled by the swollen/shrunken state of PNIPAAm nanogel triggered by the heat generation of nearby MNP.

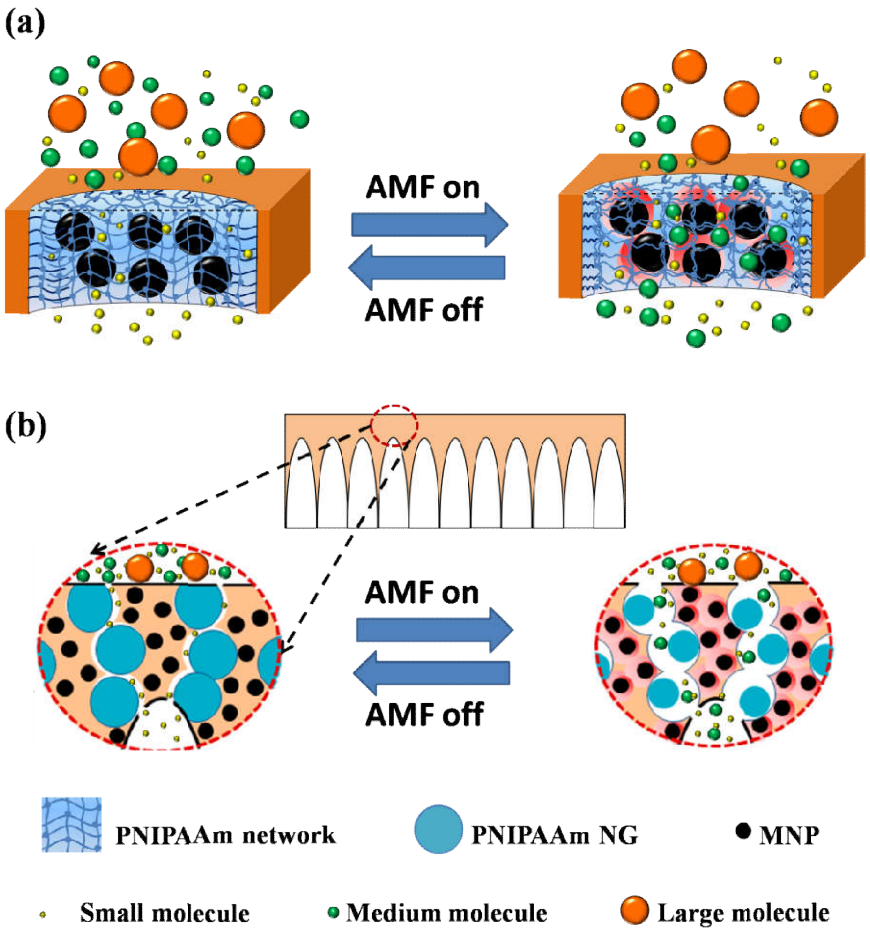

Figure 1.1. Schematic illustration of proposed magneto-responsive separation membranes. (a) Magneto-hydrogel pore-filled membrane, prepared by post modification of commercial PET track-etched membrane; (b) Mixed matrix PES membrane blended with PNIPAAm nanogel and MNP, prepared by non-solvent induced phase separation of solution/dispersion of all components. The scale for the two figures is different.

1.3. Scope of the research

This work focuses on the design of magneto-responsive ultrafiltration membranes for switchable molecular sieving effect. Specifically, the aims are as follows:

1. Investigate and optimize the factors influencing magneto-heating:

    - Synthesize and characterize MNP for effective magneto-heating.

- Investigate and optimize AMF conditions for magneto-heating.

2. Develop magneto-hydrogel pore-filled membranes with switchable molecular sieving effect.

- Synthesize bulk magneto-hydrogel via redox and UV polymerization and investigate their gelation kinetics, microstructure and magneto-heating effect.
- Prepare magneto-hydrogel pore-filled membranes with effective MNP loading procedure and suitable polymerization method.
- Investigate the structure, MNP loading, thermo-responsivity, magneto-responsivity and switchable molecular sieving performance of obtained membrane.

3. Develop MNP and PNIPAAm NG blended mixed matrix membrane with switchable molecule-sieving effect.

- Prepare functional building blocks (MNP and PNIPAAm NG) and study their properties.
- Investigate the influence of dope solution composition and phase separation conditions on membrane structure.
- Investigate the structure, magneto-responsivity, and switchable molecular sieving performance of obtained membrane.

2. Theory and literature review

2.1 Traditional ultrafiltration membranes

2.1.1 General introduction of membranes and ultrafiltration membranes

A membrane works as a selective barrier between two adjacent phases and can regulate the transport either by solution/diffusion selectivity (nonporous membrane) or size exclusion (porous membrane)[5]. As shown in **Figure 2.1**, porous membranes would reject the components larger than their pores and let the components smaller than their pores pass through them. Applications and performance of porous membranes strongly depend on membrane pores, because the pore size distribution would determine their separation targets and separation efficiency, and the porosity, pore length and pore tortuosity would determine their flux. Nowadays, membranes with different pore size are used for various separation processes[20], as shown in **Figure 2.2**. Membrane separation technology has many advantages, such as no additives, no phase change, lower energy consumption and high packing density comparing to classical thermal separation processes(such as, e.g., distillation and extraction), therefore is taken as a promising technology for sustainable development of mankind[20].

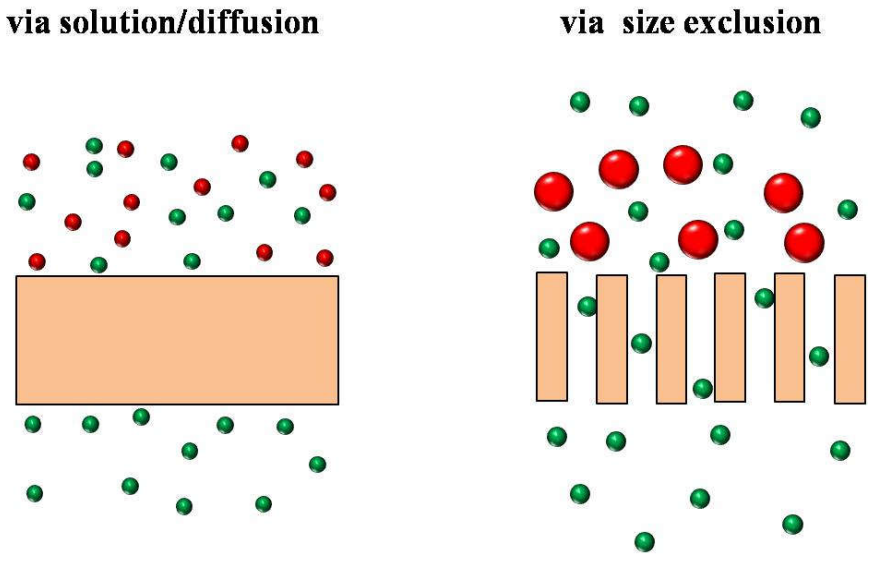

Figure 2.1. Transport mechanisms of solutes through membranes.

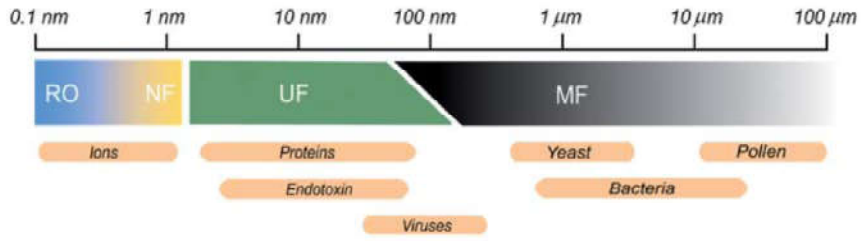

Figure 2.2. Classification of membrane processes according to the pore size range in selective barrier, including reverse osmosis (RO), nanofiltration (NF), ultrafiltration (UF) and microfiltration (MF)[20].

Ultrafiltration membranes with pore size in the range of 2-100 nm separate components (macromolecules and colloids) by size exclusion and are used for concentration, purification and fractionation of macromolecules (e.g. proteins, polysaccharides and plasmid DNA), removal of hazardous components (e.g. endotoxins) or particles (e.g. bacterial and virus removal) from solutions. They are not only extensively employed in separation units for various industries such as food and beverage, pharmaceutical, chemical and biotechnology, but are also used in small-scale and integrated in drug delivery systems or in analytical instruments like microfluidic devices[5, 11, 49].

2.1.2 Preparation of traditional polymeric ultrafiltration membranes

Ultrafiltration membranes can be made of both organic polymeric materials and inorganic materials like ceramics, metals and oxides. Due to the lower cost and easier processing, polymeric ultrafiltration membranes are more prominent in the market. And common polymeric materials for ultrafiltration membrane include cellulose acetate, polysulfone (PSf), polyethersulfone (PES), polyacrylonitrile (PAN), polyamide, or polyvinylidenefluoride (PVDF), which are thermally and chemically stable, and could be processed by phase inversion technique[5]. Ultrafiltration membranes are mostly prepared by phase inversion technique but could also be prepared by track etching.

Track etching is an excellent method to prepare ultrafiltration or microfiltration membranes with uniform pore size[50]. As shown in **Figure 2.3**, this process takes two steps: first bombard the polymer film with charged particles to partially break the polymer chains and leave a sensitized

track; then apply chemical etching by placing the pretreated membrane into strong acidic or basic solution to etch the bombarded sensitized tracks. Therefore, the irradiation intensity and exposure time of bombardment determine the pore density and the etching time determines the pore size. With this method, isotropic membranes with uniform and straight cylinder pores (size can be down to 10 nm) can be prepared. Yet, to avoid the overlapping of pores, the porosity of such membrane is usually kept below 5%, therefore they have innate drawback of low porosity and low permeability, and are limited to only analytical separations.

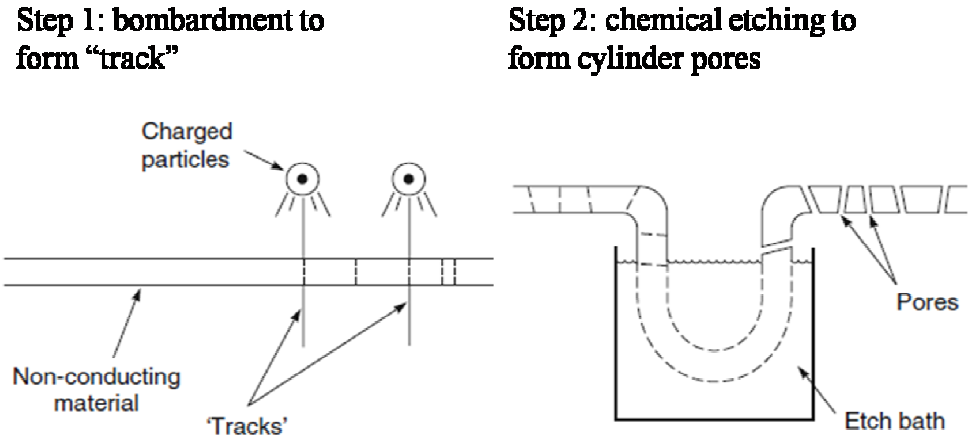

Figure 2.3. Two-step process to prepare track-etched membrane[1].

The most common method to prepare ultrafiltration membranes in industry is nonsolvent induced phase separation (NIPS). Asymmetric membranes consisting of dense skin layer on the top and porous sublayer with large void spaces (macrovoids) can be obtained by this method. It was developed by Loeb and Sourirajan in 1960s and has been one of the major breakthroughs in membrane field[51]. A comprehensive review of this method has been given by Guillen et al.[51].

Membrane preparation by NIPS process is very easy to handle[2], as shown in **Figure 2.4**. First, membrane polymer is dissolved in a good solvent and casted into a thin film with defined thickness. Then the casted thin film is placed into nonsolvent coagulation bath (typically water). Due to the fast exchange between the good solvent and nonsolvent (non-solvent diffuses into the polymer solution while good solvent diffuses into the bath), polymer will quickly precipitate and normally an asymmetric membrane will be obtained. Such asymmetric membrane consists of one

thin skin layer with ultrafiltration range pores on the top as selective barrier and one thick layer with macropores beneath the skin layer as support. Because the skin layer which works as the main barrier is very thin, the membrane permeability is relatively high. NIPS process is one of the most important membrane preparation techniques and it is used to prepare almost all the commercial ultrafiltration membranes[1] .

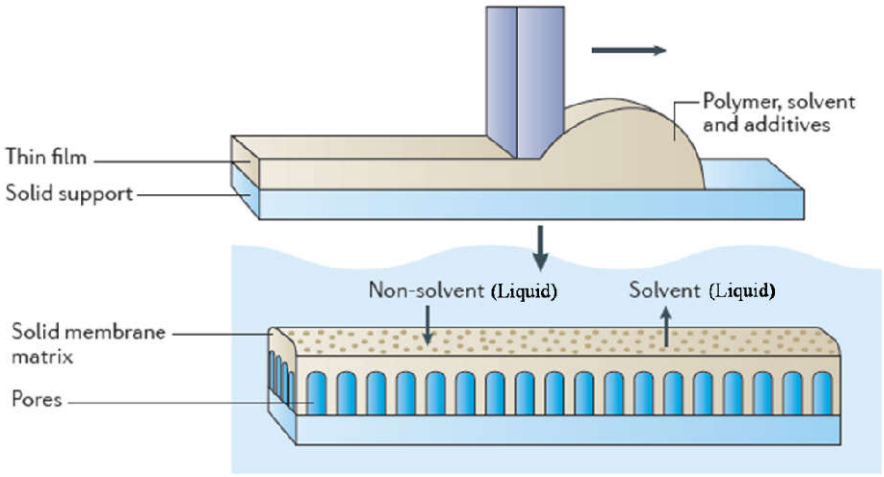

Figure 2.4. Schematic illustration of preparing ultrafiltration membrane by non-solvent induced phase separation[2].

The thermodynamics and kinetics of membrane precipitation process are strongly related to the final morphology of membranes[51]. Ternary phase diagram is often used to discuss thermodynamic aspects of membrane precipitation process[1, 51, 52]. As shown in **Figure 2.5**, the three corners of the triangle represent the pure components including polymer, solvent and nonsolvent, while the points within the triangle represent mixture of the three different components[1]. And there are two regions in the system: the one-phase region within which all components are miscible and the two-phase region where demixing happens and the system is divided into polymer-rich phase and polymer-poor phase[51]. When the casted polymer solution is placed into the coagulation bath consisting of nonsolvent, good solvent will leave the casting solution while non-solvent will get into it. Therefore, casting solution will first get from one-phase region into the metastable region, where the polymer solution compositions are thermodynamically unstable. As solvent exchange further continues, the composition will cross into the unstable two-phase region and polymer precipitation will begin. Because the different locations of polymer solution in casted film have different accessibility to the non-solvent, their

precipitation rate and the path through the phase diagram are also different[1]. The top surface precipitates first and most rapidly. As the composition enters the two phase area very fast and leaves no time for agglomerating, pore size of the top layer would be relatively small. Then the precipitated top layer would work as a barrier slowing the solvent and non-solvent exchange. Therefore, the underlying layer will enter the two phase region slower and form polymer-rich phase and polymer-poor phase first. As polymer-poor phase will eventually form the pores, more macrovoids or finger-like cavity will be formed in the underlying substrate. Phase diagram can be used as a tool to rationalize the interplay of different factors that determine the membrane structure and performance.

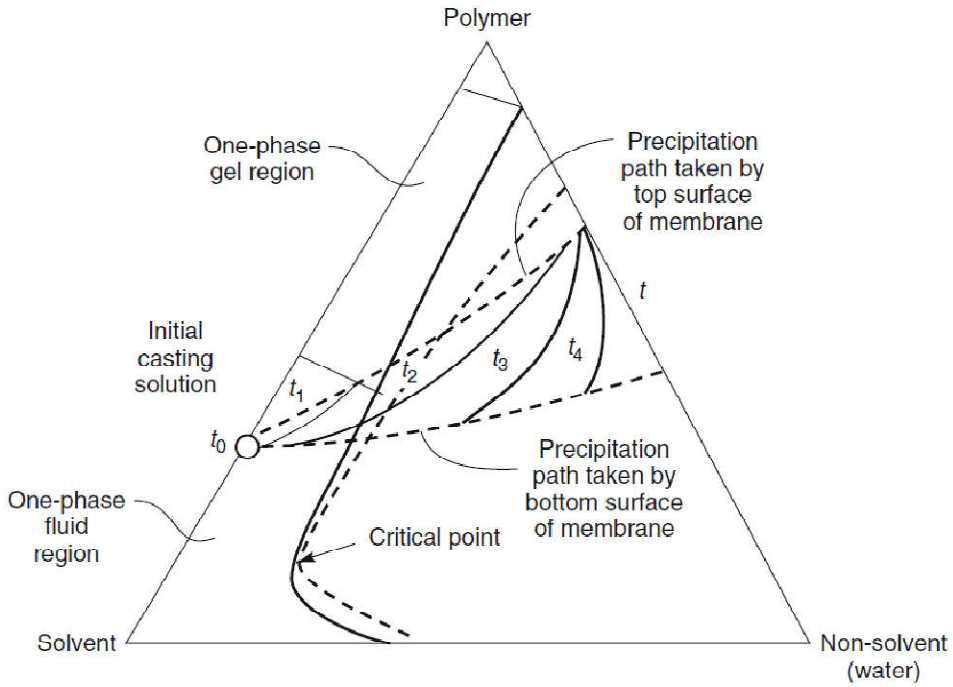

Figure 2.5. Ternary phase diagram for membrane formation by NIPS process: surface layer precipitates faster than the underneath substrate layer[1].

Besides thermodynamics, kinetics during the membrane precipitation process is another factor that significantly influences the membrane morphology. Especially, the exchange rate of solvent-nonsolvent, which determines the precipitation path in the phase diagram during the membrane formation, has drawn most attention[51]. Slow exchange would prolong the existence of metastable solutions and delay the precipitation, resulting in denser structure and suppression of

macrovoids[53]. As viscosity of casting solution would affect the exchange rate, it is an important parameter for the adjustment of membrane formation kinetics and the final membrane morphology. It can be tuned by introducing additives, e.g. PEG and PVP, or by adjusting the preparation temperature (temperature of casting solution and coagulation bath) [51].

Another phase separation method that can be used to prepare ultrafiltration membrane is vapor-induced phase separation (VIPS) process[54]. As shown in **Figure 2.6**, after the thin film is casted, instead of immersing the casted polymer solution film into nonsolvent coagulation bath (cf. **Figure 2.4**), it is placed into a vapor box, which is filled with gaseous state of nonsolvent (very often is water vapor). While membrane solidification happens very fast in NIPS process (almost instantaneous to 30-60 seconds)[1], due to the fast mutual exchange between non-solvent and solvent, membrane solidification via VIPS process is quite slow (depends on composition and VIPS conditions, can be as long as 30 minutes), because of the slow one-way penetration of non-solvent vapor into the casted thin film[54]. Therefore, better control of membrane formation process and more flexibility for tuning the membrane morphology can be obtained with VIPS process, compared to NIPS process[54].

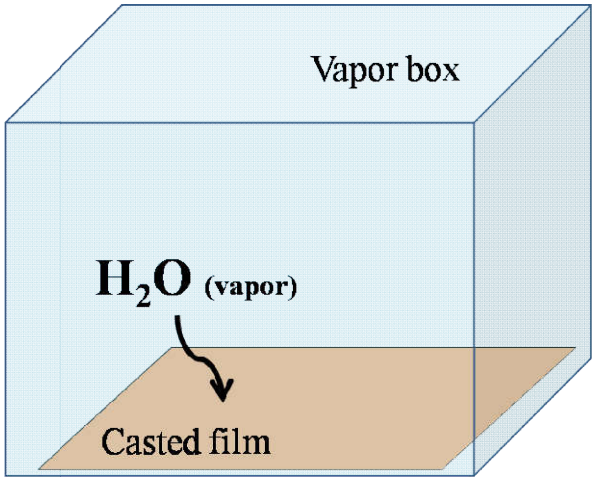

Figure 2.6. Schematic illustration of preparing membrane by vapor-induced phase separation.

The morphology and performance of membrane can be tuned by adjusting processing parameters during VIPS process, including the temperature and relative humidity of water vapor, as well as exposure time to vapor[31, 54]. Especially, exposure time to water vapor is a vital parameter for the

tuning of membrane structure. It is found that, by affecting the droplet size of polymer-lean phase and extent of coarsening, the exposure time can influence the structure of membrane significantly [31, 54, 55]. Moreover, as it would take certain time for the non-solvent vapor to penetrate the polymer solution and cause the phase separation, if the membrane is exposed to vapor in a short time and then placed into water bath, the membrane morphology will be in between the typical morphology obtained by VIPS and NIPS[54].

2.2 Stimuli-responsive ultrafiltration membranes

In the last five decades, commercial ultrafiltration membranes are easily available and ultrafiltration has become a well-established separation technology in large industrial units. However, traditional ultrafiltration membranes have untunable permeation and separation properties, due to the inert property of traditional membrane polymers. Therefore, the efficiency of established membrane-based processes is limited and the applications of membranes in extended areas are also restricted. For instance, when feed consisting of varied sizes of macromolecules needs to be treated, several UF membranes with different MWCO will be employed in sequence to harvest the targeted molecules. And this makes the separation process complicated, time-consuming and space-consuming. Inspired by nature, such as the cell membrane which can dynamically regulate the transportation of substances according to the environment and needs of cell, artificial stimuli-responsive membranes with tunable sieving effect or surface properties were developed and envisioned to address those problems and provide enhanced performance.

In the last two decades, stimuli-responsive membranes responding to different signals (e.g. pH, temperature and ions) have been developed[5, 16, 18, 21, 22]. Yet, among only few have achieved ultrafiltration range of separation[26, 27, 29, 56, 57]. The ion-responsive membrane prepared by Ito et al. is especially interesting[26]. As shown in **Figure 2.7**, the membrane prepared by plasma graft copolymerization can recognize specific ions such as Ba^{+} by its crown ether receptors and make corresponding change of its pore size. It is reported its pore size could change from 5 to 27 nm when Ba^{+} concentration change from 0 to 0.014 mol/l.

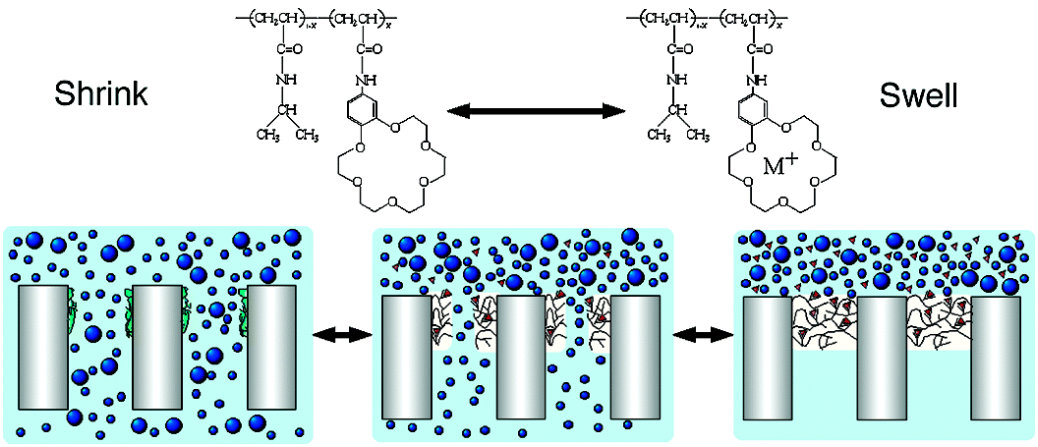

Figure 2.7. Schematic illustration for mechanism of ion-responsive membrane for molecular sieving[26].

2.2.1 Preparation of stimuli-responsive ultrafiltration membranes

By chemically/physically incorporating stimuli-responsive building blocks, such as stimuli-responsive polymer chains or hydrogels into traditional membrane substrate, responsive membranes can be prepared and improved performance can be achieved by the synergistic effect of porous membrane and functional stimuli-responsive polymers. Generally, there are two strategies to achieve this. One is by post-modification after membrane formation; the other is by adding functional components during the membrane formation. Liu et al. have recently written a comprehensive review to introduce stimuli-responsive gating membranes and their preparation[18] , and Yang et al. have given an in-depth review about integrating the functionalities of hydrogels with membranes and enhance membrane performance[20]. The subsection here will focus on preparation of stimuli-responsive ultrafiltration membrane.

2.2.1.1 Functionalization by post-modification

First, extra functionality can be introduced by post modification, such as surface grafting and pore-filling, after membranes have been formed.

The most common surface modification method—surface grafting, including “grafting-to” and “grafting-from” can be used to introduce stimuli-responsive polymers onto surface of porous membrane. For “grafting-to” method, stimuli-responsive components including responsive

polymer chains and micro-/nano-spheres, are coupled onto the surface via chemical bonding/physical adsorption[32, 37, 58, 59]. "Grafting-to" technique has been very often used to bind polymer chains onto membrane surface, and its merit is the structure of polymer can be well defined[5]. Various stimuli-responsive membranes have been constructed by grafting responsive polymer brushes on to membrane surfaces[58, 60, 61]. Recently, there is also a trend to graft stimuli-responsive micro-/nano- gels onto membrane surface as functional gate[32, 37]. For "grafting-from" method, stimuli-responsive polymers grow directly from the active sites on the substrate by surface-initiated polymerization of monomers. Usually this involves two steps: first the immobilization of initiator and then the polymerization of monomers from the immobilized initiators sites. According to the mechanism for the radical generation, "grafting-from" method can be further classified into UV-induced grafting, redox-initiated grafting, plasma-induced grafting, atom transfer radical polymerization (ATRP) and reversible addition-fragmentation chain transfer polymerization (RAFT)[5, 16 26, 62, 63, 64, 65]. An easy and effective UV-assisted heterogeneous graft polymerization method has been established by Ulbricht et al.[5, 66]. As shown in **Figure 2.8**, "type II" photoinitiator such as benzophenone (BP) is first adsorbed onto the membrane surface, then UV is applied to initiate the hydrogen abstraction reaction and produce radicals on the membrane surface, and surface-initiated polymerization of monomers will start. Based on this method, thermo-responsive membranes were obtained by grafting PNIPAAm brush layer onto pore wall of PET track-etched membranes[67], and pH-responsive membranes were obtained by grafting poly(acrylic acid) (PAA) onto base membranes[68].

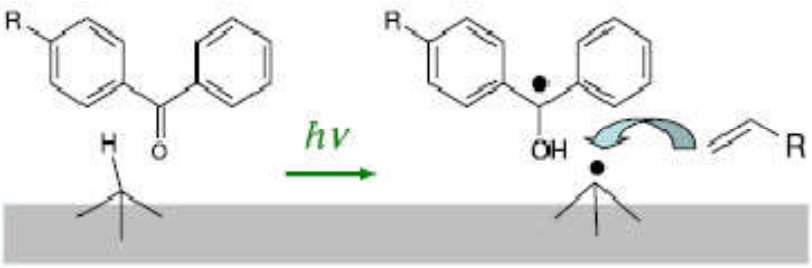

Figure 2.8. UV-initiated surface "grafting-from" by adsorption of type II photoinitiator (e.g. benzophenone derivative)[5].

Pore-filling functionalization was first introduced by Yamaguchi et al.[69]. It was proposed to add extra selectivity to the membrane by filling the membrane pores with functional polymers as shown in **Figure 2.9**. While the filling materials (mostly polymer gels) serve as sieving medium, porous membranes would work as robust support to provide mechanical stability and restriction against excessive swelling of the filling polymers[5, 20]. Both polyelectrolyte gels and neutral hydrogels are used as the filling materials, to achieve the selectivity for ions[70, 71] and macromolecules[39, 72, 73]. Further, to enhance the mechanical stability of the filling materials, Ulbricht et al. introduced an extra prefunctionalization step to generate polymer chains on the membrane substrate as anchors to interpenetrate into the filling material and fix them[39, 74]. It was demonstrated hydrogel pore-filled membrane prepared by this method has stable separation performance up to trans-membrane pressure of 4 bar[39].

Figure 2.9. Concept of pore-filling functionalization of membrane.

2.2.1.2 Functionalization during membrane formation

The other strategy to render the ultrafiltration membranes extra functionalities is to blend active components as additives during membrane formation by phase separation. Both stimuli-responsive copolymers and micro- or nanogels are used as building blocks and introduced into the membrane substrate by this strategy[18]. With such method the production could be easily scaled-up with existing industrial facilities.

Using pre-synthesized stimuli-responsive chain polymers as additives or directly as membrane polymers to construct functional membrane has attracted a lot interest[27, 56, 57, 75, 76, 77, 78]. With such method, membrane with narrow pore size in ultrafiltration range could be obtained, yet so far only some pH-responsive membranes are reported to have molecular sieving effect[27, 56, 57, 78]. And there are concerns about the mechanical properties of such membranes[56, 57].

Membranes blended with sub-micron particles as responsive gates have only been reported by few groups[31, 33, 34, 35, 79]. Chu et al. developed PNIPAAm nanogels composite PES membranes via both NIPS process and VIPS process, and proved their thermo-responsivity and ethanol-responsivity by liquid filtration experiments[31, 33, 79]. Hoare et al. developed a composite membrane with ethyl cellulose as matrix polymer, PNIPAAm nanogels as responsive gates and magnetic nanoparticles as magneto-heaters, and proved its remote-controlled diffusion of small-molecular weight drug mimic fluorescein, triggered by an external magnetic field[34, 35]. However, none of those works has investigated the molecular sieving effect of the membrane by ultrafiltration, which is a very important application for mass separations like concentration or fractionation of (bio)macromolecules.

2.2.2 Thermo-responsive membranes

When thermo-responsive polymeric building blocks are integrated into membrane, thermo-responsive membrane can be obtained. As temperature stimuli can be easily designed and manipulated, thermo-responsive membranes have attracted a lot of interest, especially for drug delivery, sensors and separation process where chemical modification for the feed is not practical or desirable[16]. So far, thermo-responsive elements in micro- or nano-size range, including polymer brushes, hydrogel mesh and micro- or nano- gel, are employed to achieving responsive gating or sieving effect in membrane, as shown in **Figure 2.10**.

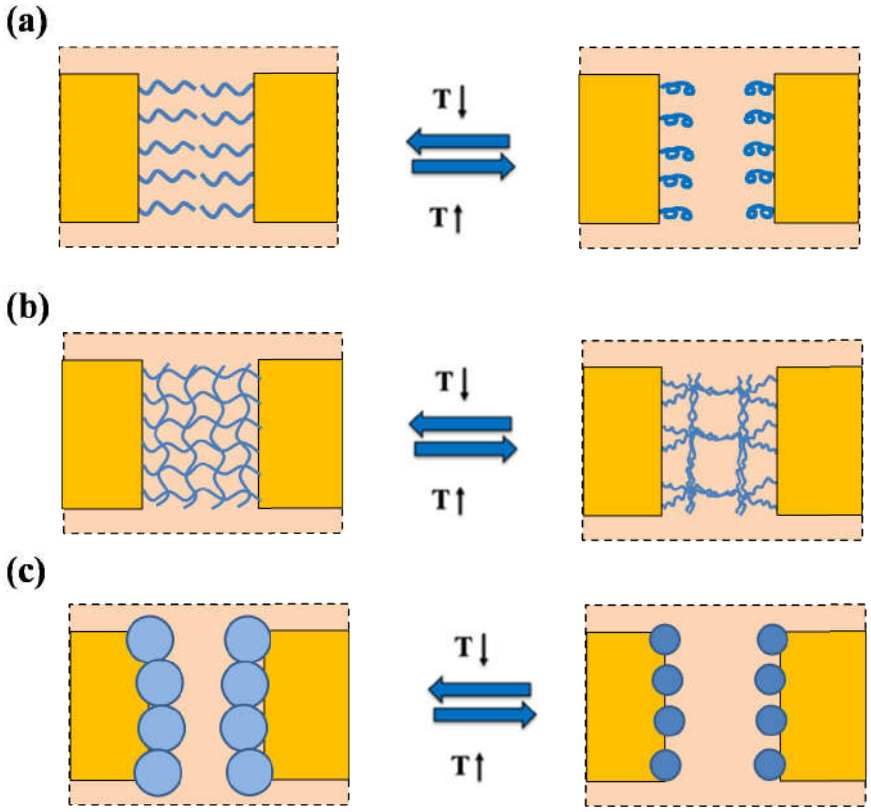

Figure 2.10. Thermo-responsive membrane with different gating elements: (a) linear polymer brush, (b) hydrogel mesh, (c) micro- or nano-gel.

The employment of thermo-responsive chain polymers is the most conventional way to obtain thermo-responsive gating membrane. Such type of membranes can be prepared either during post modification by "grafting to" or "grafting from" techniques, or during membrane formation by blending block polymer with thermo-responsive polymer section (cf. section 2.2.1) [29, 58, 64, 80, 81]. With one end grafted or embedded in the membrane substrate and the other end moving freely, the polymer chain can easily detect the temperature change and make fast response; therefore such membrane can also respond quickly to the environmental change. Yet, the most work only achieved responsive liquid permeability, because of the relatively large pores of the substrate and the weak hindrance of the polymer chains[58]. One exception is the PET track-etched ultrafiltration membrane functionalized with PNIPAAm chains via surface-initiated Atom Transfer Radical Polymerization (SI-ATRP), by Frost et al.[29]. The functionalized membrane demonstrated

switchable selectivity for nanoparticles upon temperature. During the filtration of a mixture of silica nanoparticles with diameter of 21 nm and 35 nm, it was shown, at 23 ^{o}C, only small nanoparticles can pass through the membrane, while at 45 ^{o}C, both sizes of nanoparticles can pass the membrane.

For the utilization of thermo-responsive hydrogel mesh, novel thermo-responsive hydrogel pore-filled membranes with reversible sieving effect has been developed by Adrus et al.[39]. As shown in **Figure 2.11(a)**, such membranes use the thermo-responsive poly(*N*-isopropylacrylamide) (PNIPAAm) hydrogel mesh as the sieving medium, and the hydrogel has been immobilized inside the pore of a robust polyethylene terephthalate (PET) track-etched microfiltration membrane to enhance its mechanical stability. It has been demonstrated that such membranes have excellent thermo-responsive (macro)molecule size selectivity and stable separation performance under relatively high pressure (up to 4 bar) (cf. **Figure 2.11(b))**. Upon increasing the temperature above the lower critical solution temperature of PNIPAAm (33 °C), the flux increased very much and the molecular sieving disappeared, which could be attributed to a micro-syneresis of the pore-immobilized temperature-responsive hydrogel leading to much larger mesh size compared to room temperature[39].

The membranes with thermo-responsive micro- or nano-gel as functional gates are developed in recent years[31, 32, 33, 37, 79]. Menne et al. employed thermo-responsive (*N*-vinylcaprolactam) nanogels with diameter around 500 nm as functional elements to physically adsorb on and modify the surface of PES hollow-fiber membranes. The modified membranes demonstrated not only thermo-responsive water permeability but also thermo-responsive rejection performance[37]. Wu et al. covalently grafted thermo-responsive poly(*N*-isopropylacrylamide-co-glycidyl methacrylate) (PNG) nanogels (900-800 nm) onto the pore wall of flat sheet PET track-etched membrane and achieved thermo-responsive water permeability[32]. On the other hand, there is another trend to blending thermo-responsive micro- or nano-gels during the membrane formation. Wang et al. prepared PES membrane blended with PNIPAAm nanogel via NIPS process[33]. Such membrane also demonstrated excellent reversible thermo-responsive permeability; yet, its separation property was not tested. In parallel, Luo et al. investigated the preparation of PNIPAAm nanogel blended PES membrane by VIPS process[31]. It was found the obtained

thermo-responsive membranes via VIPS process have relatively large water permeability and strong mechanical properties.

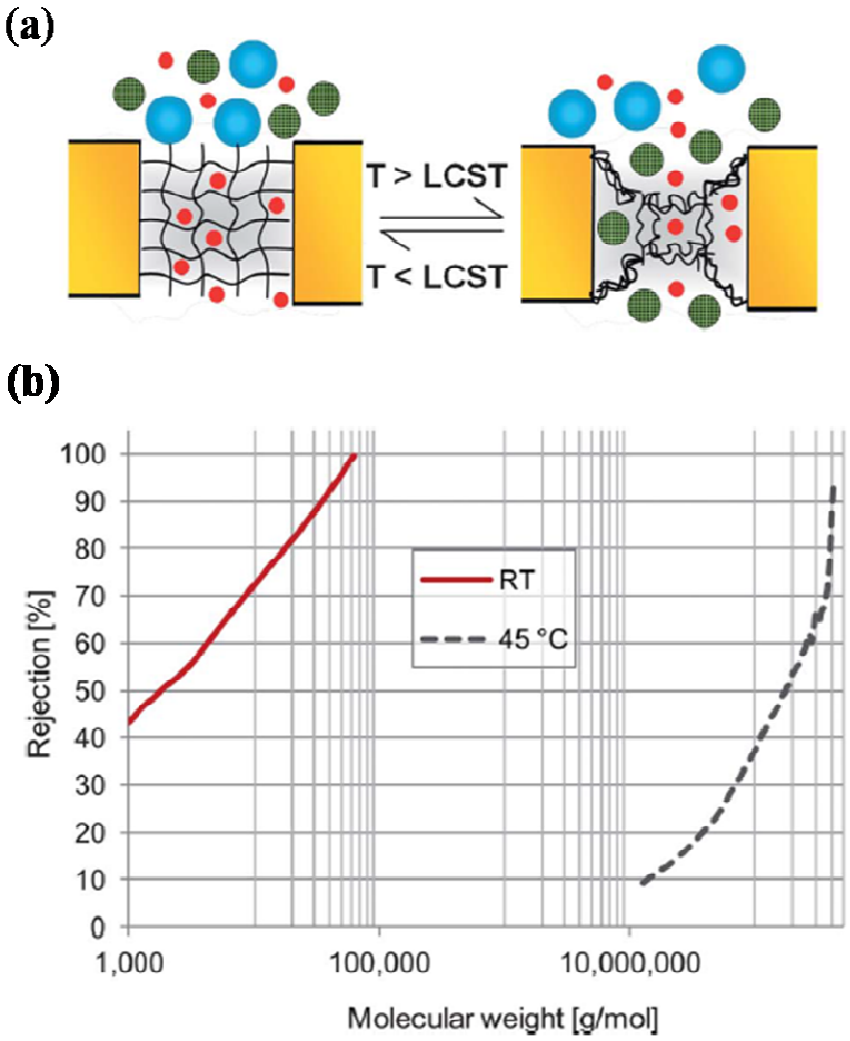

Figure 2.11. (a) Schematic figure of the separation mechanism of proposed thermo-responsive hydrogel pore-filled membrane (b) thermo-responsive ultrafiltration selectivity of PNIPAAm hydrogel pore-filled membrane[39].

Despite the vast study of thermo-responsive membranes, temperature actuation has drawbacks such as relatively slow response and high energy consumption, because the entire feed needs to be heated up. Besides, if the separation targets are biomacromolecules, they could be denatured by the heat.

2.2.3 Magneto-responsive membranes

More recently, there is a growing interest and effort to expand the range of available stimuli from direct stimulants like temperature, pH and ions, which could be limited by heat or mass transfer, to newly emerging remote electromagnetic triggers like light, electricity and magnetic field, to obtain responsive materials with more precise responsivity and higher efficiency[46, 47, 48]. Magneto-responsive membranes belong to this recent trend and are of special interest, as they can realize spatial, temporal and remote control and have great potential, for instance for microfluidic systems in analytical or therapeutic devices[34, 35, 46, 48].

As there are very few intrinsically magneto-responsive polymers, most magneto-responsive materials are composite materials[46], consisting of inorganic MNP with functions of magnetic orientation[30, 44, 82, 83, 84] or magnetic heating[34, 35, 85], and another polymeric component as actuator. There are only few reported examples of magneto-responsive membranes, which could be classified into two types: "nanoactuator" and "nanoheater". Underlying mechanism of magneto-stimulation will be discussed in section 2.4; here the focus is on functionality of material systems.

The "nanoactuator" type utilizes the magnetic motion of MNP under static magnetic field or low frequency AMF, and functions by orientating MNP themselves or the polymer chains coupled with them. One good example for such design is a nanofiltration membrane with micromixers on its surface introduced by Himstedt et al.[44]. Chains of a hydrophilic polymer, poly(2-hydroxyethyl methacrylate) (PHEMA), had on one end been grafted from the polyamide membrane surface and on the other end capped with MNP. As shown in schematic **Figure 2.12**, by the movement of PHEMA-MNP conjugates under low frequency AMF, such membranes could induced turbulences on the micrometer scale and reduce the concentration polarization during nanofiltration and hence improve separation performance[44]. Similar magneto-responsive membrane has been developed by Ng et al..; iron oxide (Fe_3O_4) nanoparticles were deposited onto the surface of a PES membrane by polyelectrolyte modification method and it had then been proven to be effective to suppress fouling during humic acid filtration[83]. The magnetic nanoactuator has also been designed as remote-controlled membrane valve by Himstedt et al.; PHEMA chains were grafted onto the pore walls of PET track-etched polymer membranes and end-capped with MNP and the significant and reversible variation of water permeability by switching on and off a static magnetic field was observed[30].

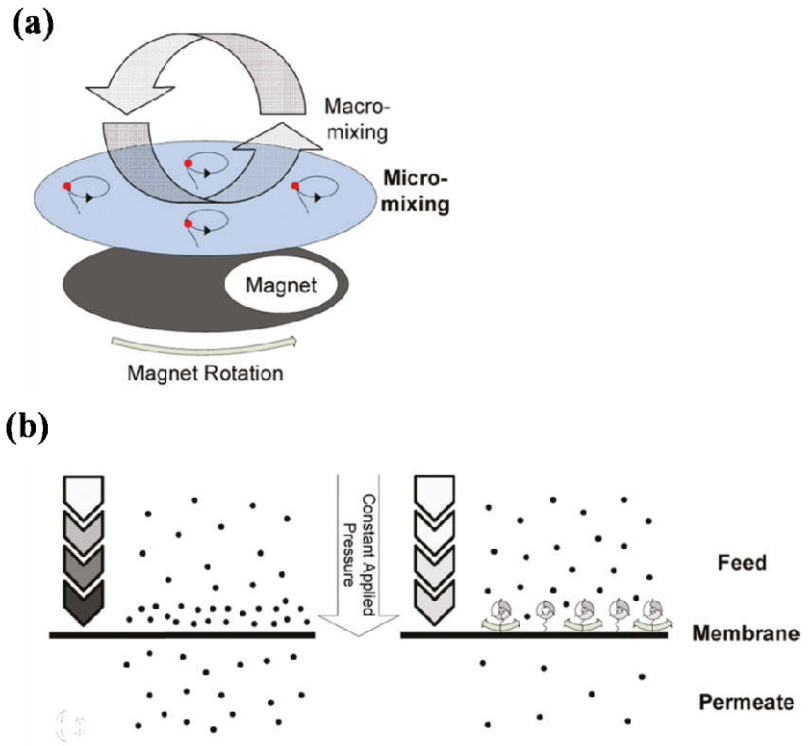

Figure 2.12. Concept of "nanoactuator" type magneto-responsive membrane: (a) activation of micromixer by external magnetic field; (b) reduction of concentration polarization by magnetic micromixer.

The "nanoheater" type utilizes the heating effect of MNP under high frequency of AMF, and usually the systems are combined with thermo-responsive polymers, in order to utilize a synergistic effect of the two components (underlying mechanism of such synergistic effect will be discussed in section 2.3 and section 2.4). Despite that there are many studies about magneto-heating for cancer treatment and for magneto-hydrogel based drug delivery[46, 86, 87], only few work has been done for membrane design with such mechanism[34, 35, 45, 85].

Gajda et al. developed a magneto-responsive gating membrane with linear thermo-responsive PNIPAAm chains as responsive gate and MNP as localized actuator[85]. To construct such membrane, MNP was first immobilized onto the pore walls of PET track-etched membranes and then PNIPAAm chains were also grafted onto the pore wall. As shown in **Figure 2.13**, when there is no magnetic field, the PNIPAAm chains are in swollen state, the gate is closed and the permeability is relatively small; when an external alternating magnetic field is applied, the heat

generated by MNP will cause the shrinking of PNIPAAm chains, gate will be open and water permeability will increase largely. It was proven that by manipulating the external field conditions, the water permeability through the membrane can be controlled[85].

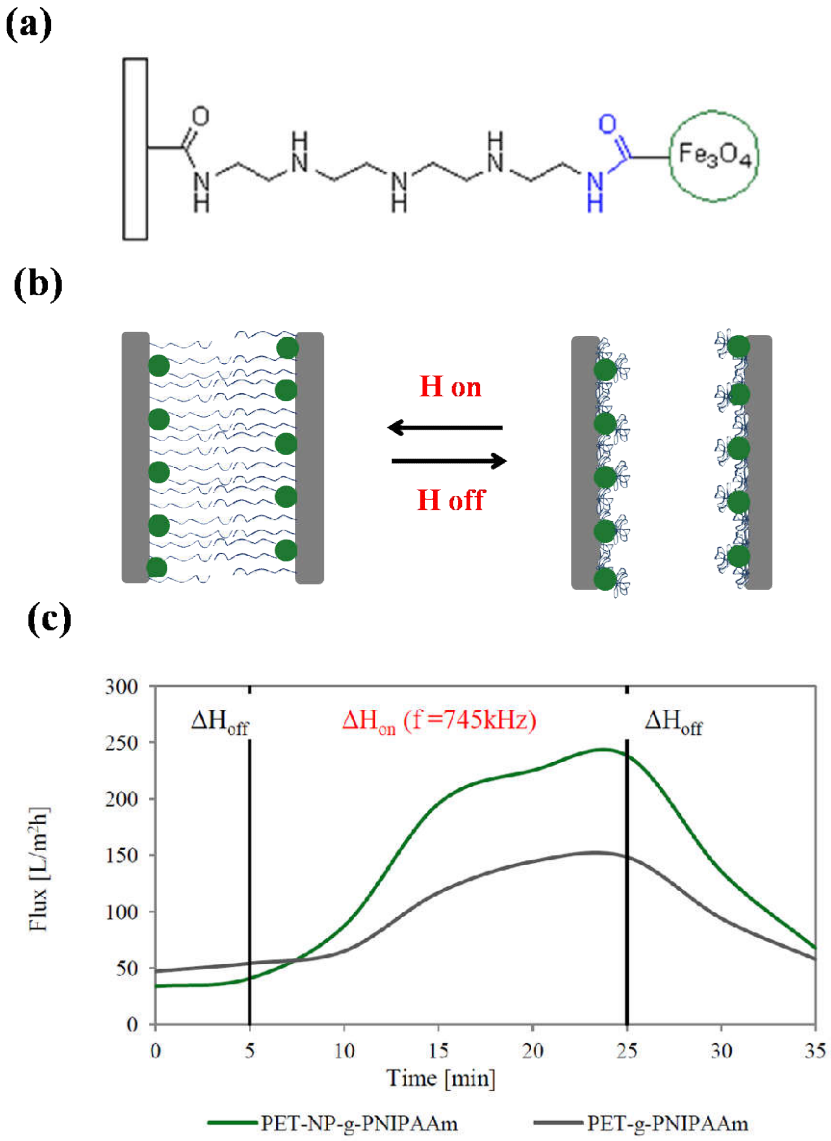

Figure 2.13. Concept and gating effect of "nanoheater" type magneto-responsive membrane: (a) coupling MNP to the end of PNIPAAm chain by peptide bond, (b) schematic illustration of the gating effect, and (c) magneto-responsive water flux of such membrane[85].

Hsu et al. also proposed a magneto-responsive membrane by surface modification with PNIPAAm chains and MNP[45]. As shown in **Figure 2.14**, pH responsive PAA chains, thermo-

responsive PNIPAAm chains and MNP with magnetothermal effect were sequentially grafted onto PVDV membrane. It was proved that such membrane has both pH- and thermo-responsive water permeability. Moreover, the membrane exhibited a magnetic field triggered cleaning property. It was demonstrated, under AMF with frequency of 100 kHz and protein foulants could be easily released from the membrane surface and the membrane would be cleaned.

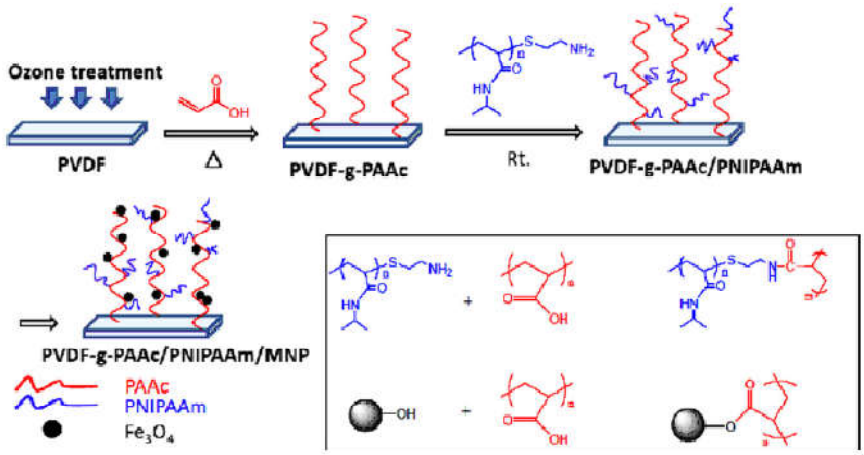

Figure 2.14. Preparation of proposed multiple responsive membrane by surface modification of PVDF membrane[45].

By using PNIPAAm nanogels as the responsive gates, Hoare et al. designed another type of magneto-responsive membrane, as shown in **Figure 2.15(a)**[34, 35]. The monodisperse PNIPAAm nanogels prepared by precipitate polymerization and superparamagnetic MNP (single particle size of around 10 nm) in agglomerate size of 100-300 nm were blended into ethyl cellulose membrane matrix. As shown in **Figure 2.15(b)**, the permeability of such membrane can be controlled by external AMF, as without AMF, the nanogels will be in swollen state and channels are close; when the membrane is exposed to AMF with certain frequency and amplitude, MNP will generate heat and cause the shrinking of nearby nanogel, the channel will be open. Moreover, it was proved the remote-controlled diffusion of small-molecular weight drug sodium fluorescein, can be triggered by an external magnetic field. However, solvent evaporation method was used to prepare such membrane, which takes long time to prepare (around 1 week) and would result in inhomogeneous structure of the membrane. Besides, the molecular sieving effect of the

membrane by ultrafiltration, which is a very important application for mass separations like concentration or fractionation of (bio)macromolecules was missed in this study.

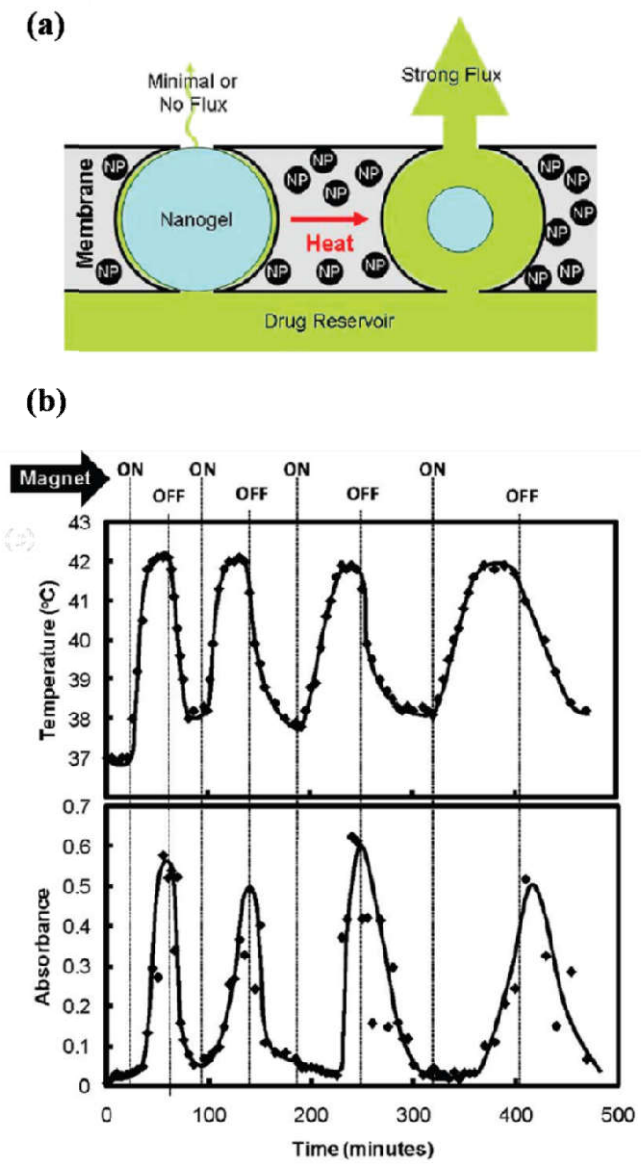

Figure 2.15. (a) Schematic figure of permeation mechanism for proposed magneto-responsive mixed matrix membrane (b) different temperature profiles and fluoresin fluxes of membrane capped sample chamber, by the triggering of external AMF[34].

Moreover, Csetneki et al. designed a mixed matrix membrane that consists of poly(vinyl alcohol) (PVA) as matrix and PNIPAAm hydrogel layer coated magnetic polystyrene beads (MPS-PNIPAAm) as responsive gate. And a perpendicularly placed static uniform magnetic field was used during membrane formation, to get aligned pearl chain structure, as shown in **Figure 2.16**[36]. Such membrane utilizes the thermo-responsive PNIPAAm layer on the magnetic latex beads as responsive gating element. It has relatively small permeability when the temperature is lower than the LCST of PNIPAAm and permeability increase when the temperature is higher than the LCST of PNIPAAm. Because of the magnetic core, such membrane should also have potential magneto-heating effect in AMF and relevant switchable responsive permeability, however, only thermo-responsivity was verified in their work, maybe because the heating effect of the magnetic latex beads is limited, as relatively small magnetic particles are used and fixed in polystyrene matrix. Still, this work provides new design idea for future magneto-responsive membranes.

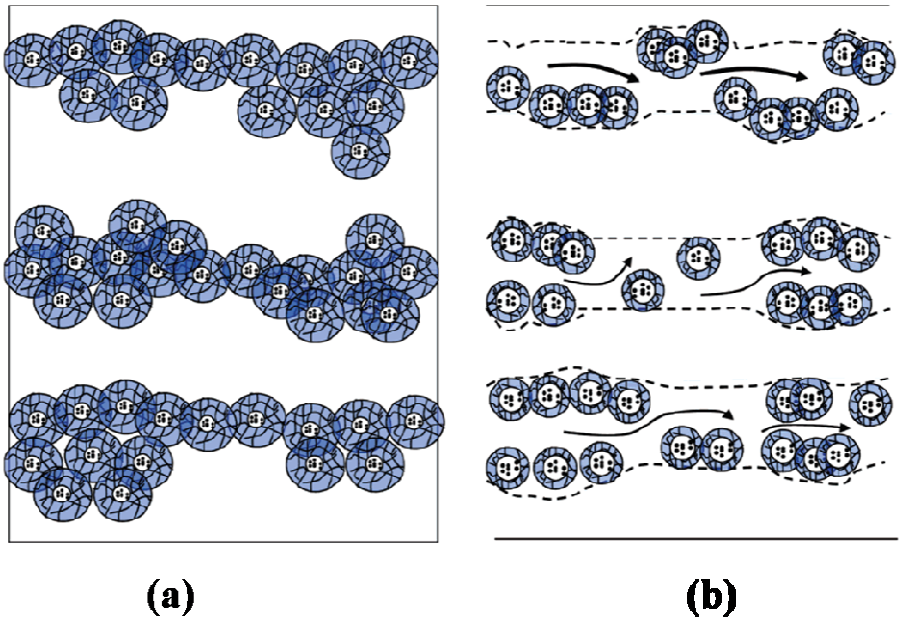

Figure 2.16. Schematic figure of permeation mechanism of through proposed channels, formed by MPS-PNIPAAm latex in the PVA matrix: (a) "off "state of the channel under temperature below collapse transition temperature of PNIPAAm layer; (b) "on" state of the channel above the collapse transition temperature of PNIPAAm layer[36].

As magneto-responsive membranes with switchable molecular sieving have been long absent from literature, in this work we would explore the possibility to develop novel magneto-responsive ultrafiltration membranes by employing different structures, different morphologies of thermo-responsive gate elements and different ratio of magneto-heaters. As thermo-responsive hydrogel and magnetic nanoparticles are used as key elements in such membrane design, in the following two sections, we will discuss them in detail.

2.3 Thermo-responsive hydrogels

2.3.1 Introduction of hydrogels and their application in separation

Hydrogels are 3-D macromolecular networks containing large amount of water between polymer segments. Their hydrophilic moieties e.g. alcohols, carboxylic aides and amides, enable them to hold large amount of water; and the chemical or (and) physical crosslinks, or physical entanglement, endow them integrate structures and make them insoluble in water environment[20].

Broadly defined, hydrogel includes free-standing bulk hydrogel network, grafted linear hydrophilic polymer layers, hydrogel particles (micro and nanosphere) and hydrogel capsules[19]. Due to high water content, potential biocompatibility and various possible morphologies, synthetic hydrogels have wide range of applications, including biomedical applications as synthetic extracellular matrix for tissue engineering[88, 89], delivery matrices for controlled drug release[90, 91], and core components of biosensors for analysis and diagnosis[92] [22], and industrial applications as adsorbents for separation, purification and concentration of products[93, 94], or removal of toxic substances [95, 96], and draw agents for water desalination[97, 98]. Moreover, hydrogel layers are coated or grafted onto substrates to increase surface hydrophilicity and reduce fouling[20] [99, 100, 101, 102].

Because polymeric hydrogels have mesh sizes in the lower nm range and high porosity, they are also used as excellent sieving media to control the transportation of molecules via size exclusion[19, 103, 104, 105]. Their separation effect strongly depends on their mesh size, which would allow solute molecules smaller than the mesh to pass through and reject solute molecules bigger than the mesh. Advantages of using hydrogel as sieving media include their adjustable network structure (by cross-linker monomer fraction and total monomer concentration, i.e. via formation of chemical and physical cross-links) and chemical durability. There are several reviews about

the theoretical transport mechanism of solutes through porous hydrogel[19, 106]. Generally, transport of solutes across the hydrogel network is contribution of both diffusive and convective fluxes. Hindrances for diffusion and convection include the physical obstruction effects (steric exclusion), due to the comparable size between the solute and hydrogel mesh, and hydrodynamic drag, which is the friction drag on solutes caused by the slowing down of fluid in proximity of polymer chains[19, 106, 107]. When no external pressure is applied, and only concentration gradient is present, solute passes through the hydrogel via diffusion; the permeability of solute is proportional to the diffusion coefficient and reversibly proportional to the thickness of the hydrogel. When an external pressure is applied (in case of ultrafiltration), convective transport would dominate; the permeability is proportional to the transmembrane pressure and reversibly proportional to the thickness of the hydrogel[19, 106, 107].

Yet free-standing hydrogel are mechanically weak and could be easily deformed or even damaged by mechanical and osmotic force during the separation process. In order to expand their application to pressure-driven molecule filtration, they need to be stabilized within a porous support, such as membranes[20, 72, 73, 108]. Hydrogel pore-filled membrane is one of such design. The rigid porous membrane provides mechanical support as well as certain confinement to prevent excessive swelling of the hydrogel, while the filled hydrogel would serve as sieving medium to control the transport of solutes within the membrane pores. When the hydrogel filled in the pore is considered as porous medium, Darcy's model can be used to estimate the mesh size of the gel network[39, 73, 109]. As shown in **Figure 2.17**, by combining hydrodynamic permeability with Hagen-Poiseulle and Darcy's model, the mean space between the hydrogel network or the mesh size can be estimated[39].

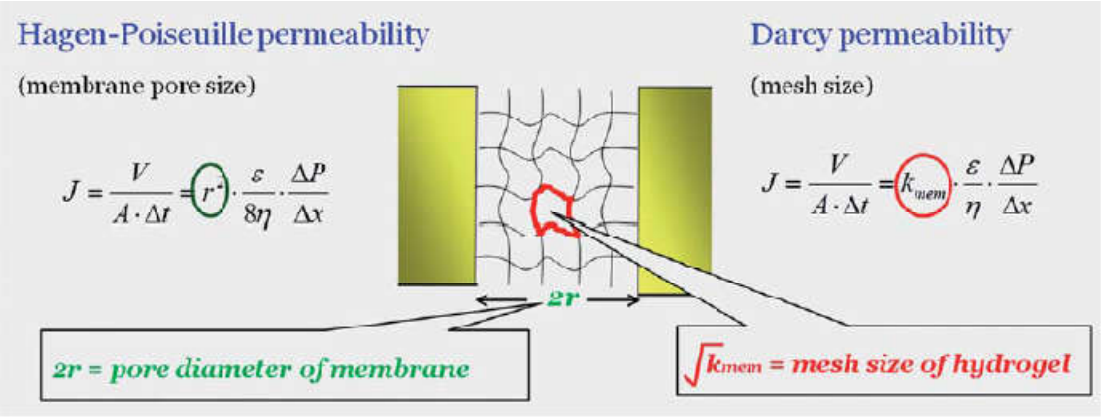

Figure 2.17. Estimation of mesh of hydrogel pore-filled membrane by the combination Hagen-Poiseuille and Darcy model. The Hagen-Poiseuille model in combination of water permeability and average pore size of base membrane, is used to characterize the porosity of the base membrane. And the Darcy model in combination of water permeability of hydrogel pore-filled membrane and membrane porosity, is used to estimate the mesh size. J is water flux through the membrane [l/m^{2}h], V is volume of permeate [l], A is membrane surface area [m^2], Δt is time [s], r is pore radius, ε is membrane porosity, η is water viscosity [Pa.s], ΔP is transmembrane pressure [bar] and Δx is membrane thickness [m][39].

Among all kinds of hydrogels, stimuli-responsive hydrogels are most interesting as they can respond external chemical or physical stimuli with reversible changes in dimension, and surface properties, therefore display tunable swelling behavior, permeability, adsorption capacity, surface polarity and optical properties[20]. Especially, in respect of controlling transport of molecules, their stimuli-responsive properties would provide extra adjustment for the pore size, therefore could regulate the transport of molecules with varied sizes[19]. This is critical for drug delivery system to achieve a desired release profile, for reaction or sensor systems where sequential release of chemicals are needed, and for separation processes which deal with the feed containing a board range sizes of molecules.

In the last two decades, stimuli-responsive hydrogels with responsiveness to specific stimuli have attracted broad interest for both fundamental research and applications, and dramatic progress has been made in designing and synthesizing of those hydrogels. Types of stimuli that have been investigated include temperature[110, 111, 112, 113], pH[29, 114], ionic strength[92, 115, 116], bioactive agents[117, 118], light [119, 120], mechanical stimuli[121, 122, 123] and electromagnetic field[124, 125, 126]. And various morphologies including nanogels, microspheres, microcapsules, grafted

hydrogel layers, bulk hydrogels, or composite hydrogels, targeting different applications have also been studied.

2.3.2 Thermo-responsive hydrogels

Thermo-responsive polymers remained one of the most extensively exploited stimuli-responsive polymers since 1960s [127]. They very often have an abrupt change of aqueous solubility at lower critical solution temperature (LCST), due to the balance of intermolecular forces between the polymers and between the polymer and solvent molecules[128]. When the environmental temperature is lower than the LCST of the polymer, it is soluble in aqueous solution, because of the extensive hydrogen bonding with water molecules and restricted inter- and intra-molecular hydrogen bonding interaction between polymer molecules; when the temperature is about the LCST, while hydrogen bond with water will be disrupted, the inter- and intra- molecular hydrogen bonding and hydrophobic interactions will remain and dominate, resulting in a change in solubility[110, 129].

Table 2.1. Polymers showing LSCT in water[128]

Polymer	LCST [^{o}C]
Poly(*N*-isopropylacrylamide) PNIPAAm	~ 32
Poly(vinyl methyl ether), PVME	~ 40
Poly(ethylene glycol), PEG	~ 50
Poly(propylene glycol), PPG	~75
Poly(vinyl alcohol), PVA	~ 125
Poly(vinyl methyl oxazolidone), PVMO	~ 65
Poly(vinyl pyrrolidone), PVP	~ 160
Poly(silamine)	~ 37
Methylcellulose, MC	~ 80
Hydroxypropylcellulose, HPC	~ 55
Polyphosphazene derivatives	33-100
Poly(*N*-vinylcaprolactam)	~ 30
Poly(siloxyethylene glycol)	10- 60

There are many thermo-responsive polymers, which demonstrate specific transition temperature, as shown in **Table 2.1**[128], and more variety of thermo-responsive polymers could be found in a new review about new research directions of thermo-responsive polymers[129].

2.3.3 Introduction of poly(*N*-isopropylacrylamide) (PNIPAAm)

PNIPAAm is the most extensively investigated thermo-responsive polymer and it has a sharp phase transition at its LCST 32 °C. As shown in **Figure 2.18**, PNIPAAm has hydrophobic isopropyl domains and hydrophilic amide domains. When environmental temperature is lower than its LCST, PNIPAAM chain is swollen and hydrated, as plenty of water molecules bind to its amide groups via hydrogen bonding and also form clusters around its isopropyl groups; when environmental temperature is higher than its LCST, PNIPAAm chain will be in shrunken and dehydrated state because of the cleavage of hydrogen-bonding and release of clustered water[130, 131].

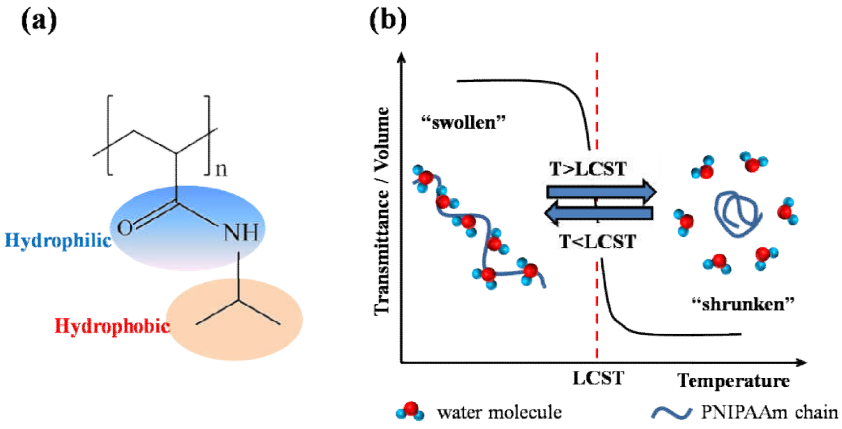

Figure 2.18. (a) Chemical structure of PNIPAAm and (b) mechanism for its thermo-responsivity[130].

When PNIPAAM is made into different morphologies, different scales of size effect to temperature can be achieved. As shown in **Figure 2.19 (a)**, for free standing bulk hydrogel, it has macroscopic size change as a whole, and microscopic size change for its mesh. And for nanogel and grafted brushes, the size change is also microscopic (in the nm range).

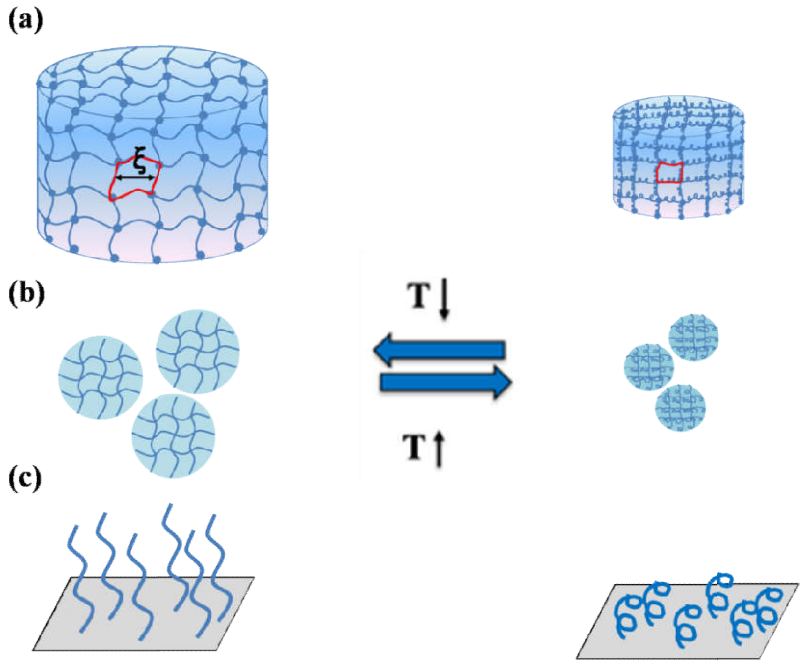

Figure 2.19. Thermo-responsive phase transition of PNIPAAm hydrogel in different morphologies: (a) bulk hydrogel, (b) nanogel and (c) grafted linear polymer brush. The scale for the three figures is different.

PNIPAAm-based thermoresponsive hydrogels possess many merits. First they often have drastic volume change upon temperature which would ensure significant actuation effect; then their LCST can be easily tuned by incorporating hydrophilic components or groups[129]; moreover, by combining with other components or copolymerizing with other responsive monomers, extra responsivities or functionalities can be achieved.

In the following subsection synthesis of both bulk and nano-size thermo-responsive PNIPAAm hydrogels will be discussed.

2.3.3.1 PNIPAAm bulk hydrogel

Macroscopic PNIPAAm hydrogel can be synthesized by using commercially available NIPAAm as functional monomer and *N*,*N*′-methylenebisacrylamide (MBA) as crosslinker monomer. The most used polymerization methods are photo-initiated and redox-initiated free radical polymerization.

For photo-initiated reaction, proper photo initiator and irradiation conditions are required to get homogenous hydrogel. In a typical photo-initiated gelation reaction, first, light with certain wavelength will cause the decomposition of initiator and form radicals; then the free radicals will initiate copolymerization of monomer and crosslinker and form hydrogel. As shown in **Figure 2.20**, there are two types of photoinitiator: while the type I photoinitiators (such as Irgacure 2959) undergo unimolecular bond cleavage to produce radicals, the type II photoinitiators (such as benzophenone) require a co-initiator (usually alcohol or amine) to donate hydrogens and therefore form free radicals. For the formation of PNIPAAm hydrogel by photoinitiation, the most used are water soluble "type I" initiator such as Irgacure 2959[132, 133]. The advantage of using photo-initiation for the synthesis of thermo-responsive hydrogel is that there is no interference of temperature on hydrogel structure and the reaction could be fast. However, for bulk hydrogel, as the penetration of UV light decrease with the depth of reaction solution, there will be a spatial concentration distribution of radicals that eventually leads to inhomogeneous hydrogel.

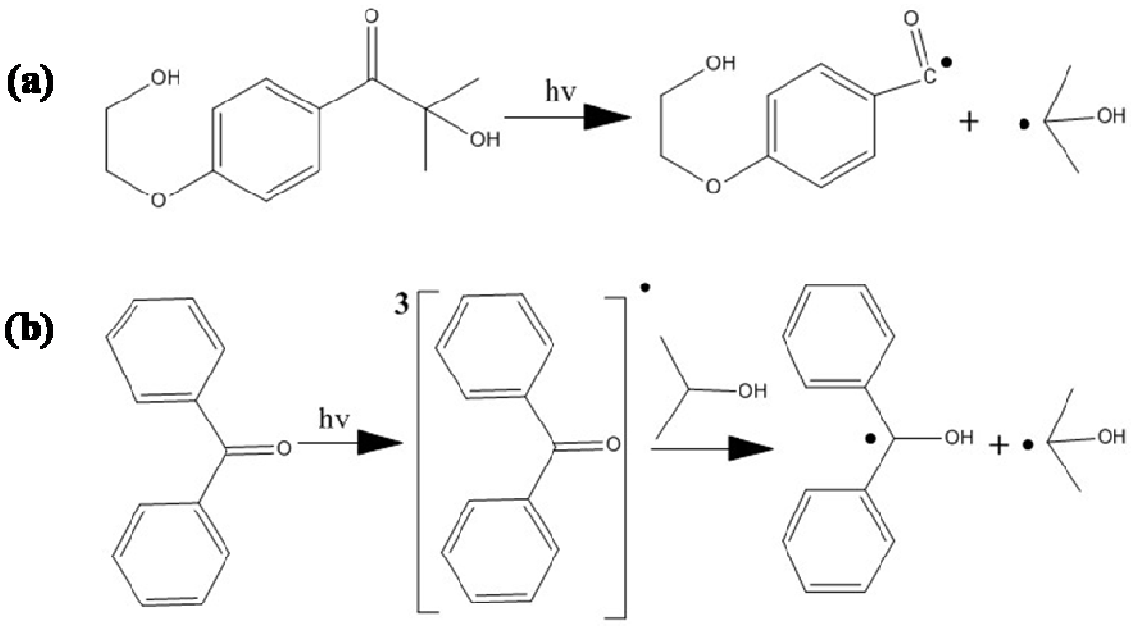

Figure 2.20 UV irradiation induced (a) dissociation of "type I" initiator Irgacure 2959 and (b) bimolecular reaction of "type II" initiator benzophenone.

For redox initiated free radical polymerization, redox initiation system composed of accelerator tetramethylethylenediamine (TEMED) and persulfate initiators such as ammonium persulfate and potassium persulfate are very often used to synthesize PNIPAAm hydrogel[133, 134, 135, 136]. Persulfate initiators can decompose into free radicals themselves, yet their decomposition temperature is relatively high (usually above 70 °C) and takes relatively long time. As shown in **Figure 2.21**, TEMED with a tertiary amine structure can react with persulfate initiators immediately after mixed together and accelerates the formation rate of free radical[137]. Therefore, with TEMED, the polymerization can proceed fast at room temperature. Since the LCST of PNIPAAm hydrogel is around 32 °C, polymerization at room temperature ensures the homogeneity of the hydrogel.

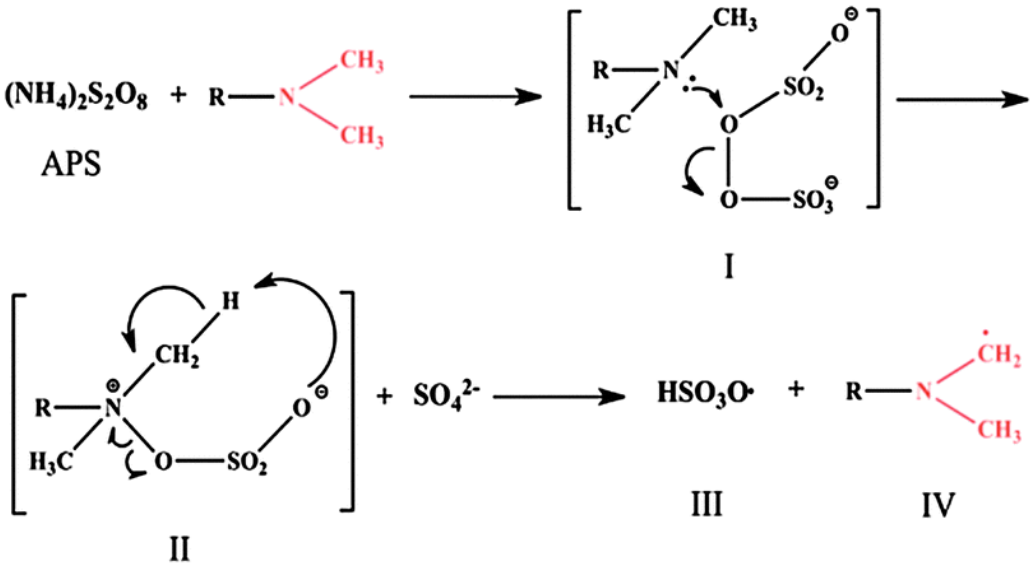

Figure 2.21. Initiation mechanism for persulfate and tertiary amine redox initiator system [137]

When the free radicals are formed, they will attack monomers and start the polymerization. Under the attack of the free radicals, new chemical bond would form between carbon double bond of monomer and the initiator fragment and form oligoradicals. With the incorporation of more monomers and crosslinkers, the oligoradicals will grow into longer chains and get cross-linked. A hydrogel network will be formed until the exhaustion of monomers. The general radical copolymerization process of PNIPAAm is illustrated in schematic **Figure 2.22**.

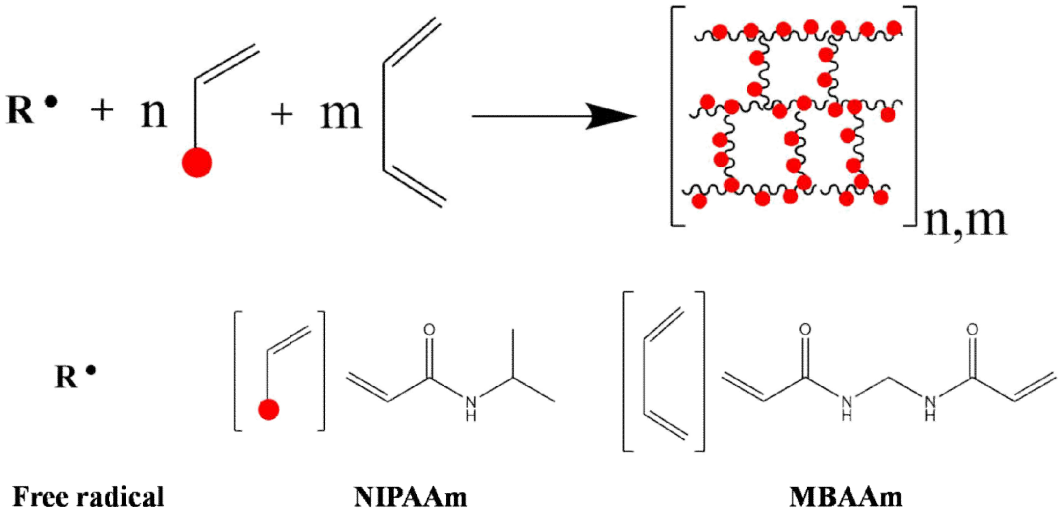

Figure 2.22. PNIPAAm hydrogel formation via radical copolymerization.

2.3.3.2 Thermo-responsive PNIPAAm nanogel

Hydrogel particles with size below 1000 nm are called nanogels or submicrogels. They are well-dispersed colloids and have various potential applications including drug delivery, emulsion stabilization and coating[138, 139, 140]. Basically, the gelation mechanism is the same for nanogels and bulk hydrogels. Yet due to the extra requirements for size control and colloidal stability, nanogel preparation is more challenging. Generally, strategies for nanogels preparation can be categorized into three types: (1) polymerization of monomers and crosslinkers in homogenous phase or nanodroplets; (2) cross-linking or self-assembly of prepolymers; and (3) template-assisted nanofabrication such as photolithographic techniques[141].

Among all of those methods, precipitation polymerization, which belongs to category (1), is an elegant and effective method to prepare thermo-responsive nanogel[111, 142]. The nanogels obtained are monodisperse and easy to purify, as the reaction is water-based and could be surfactant-free. As illustrated in **Figure 2.23**[142], in the homogenous aqueous solution of monomers, crosslinkers and thermal initiators, the initiator will first decompose into radicals and attach the monomers, forming soluble oligomers; with the proceeding of polymerization, the growing chains will reach a critical length and precipitate into a particle nuclei, as the reaction temperature is higher than the LSCT of the polymer; later the nuclei will grow into larger particles by polymerization of

monomers and adsorbing polymer chains or other particles. And when they are redispersed in water at room temperature, they will swell into hydrophilic micro- or nanogel with "hairy" morphology. To introduce electrostatic charges onto particle surface and render them colloidal stability, it is critical to use an ionic water soluble free radial initator[111]. Persulfate initiators like ammonium persulfate and potassium persulfate are most commonly used, as they render the surface of nanogel with negative sulfate groups and keep the nanogels stable during the growth and after redispersion in water.

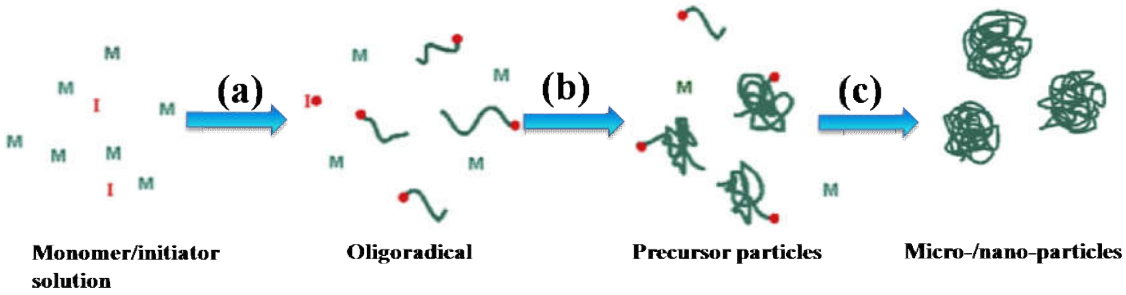

Figure 2.23. Formation of nanogel via precipitation polymerization: (a) initiation and chain growth, (b) precipitation and nucleation, and (c) particle growth [142].

There are many advantages to prepare PNIPAAm nanogel via precipitation polymerization. The procedure is simple and it is a strong tool to produce monodisperse nanogels with tunable size[143, 144, 145], cross-linking density[146, 147], and charge[148]. While the electrostatic charge rendered by the ionic initiator is usually sufficient to keep the nanogel stable, adding extra ionic surfactants can further enhance the electrostatic repulsion during the particle formation. By adsorbing onto the surface of precursor particles to keep them from aggregation, ionic surfactant would result in more nanogel particles with smaller sizes. Therefore, the size of nanogels can be tuned by the concentration of surfactants[145]. So far PNIPAAm based micro- and nanogels from precipitation polymerization are extensively studied, as model system to study rheological behavior of soft colloid particles[143], mimic biological system[149], or drug delivery[111].

2.4 Magnetic nanoparticles

2.4.1 General introduction of magnetic materials

Magnetic materials are materials that can respond to an applied magnetic field and their magnetism arises at atomic level from spin magnetic dipole moments of elementary particles that form the materials.

According to the way that magnetic dipoles of elementary particles interact with each other, magnetic materials can be classified into five types: ferromagnetic, paramagnetic, diamagnetic, ferrimagnetic and antiferromagnetic[150, 151]. For ferromagnetic materials like Fe, Co, or Ni, their atoms have net magnetic moments due to unpaired electrons and those atoms with parallel magnetic moments form domains pointing in certain direction. Because the magnetic moments of domains in ferromagnetic materials are randomly distributed, they demonstrate zero net magnetic moment if there is no external magnetic field. However, when an external magnetic field is applied, all the domains will align their magnetic moments along the direction of external magnetic field, and the ferromagnetic materials will demonstrate a large net magnetic moment. For paramagnetic materials including Mn, Al and Li, their constituent atoms or molecules also have net magnetic moments due to unpaired electrons. However, in absence of external field, all the magnetic dipoles are randomly oriented due to thermal agitation and resulting zero net magnetic moment. When an external field is applied, the magnetic moments of the atoms or molecules will align along the applied field and form a weak net magnetic moment. Most known elements are diamagnetic materials, because the atoms have no unpaired electrons, the overall magnetic moment of the materials is zero. And they only show very weak response against the external field due to realignment of electron orbits. Ferrimagnetic materials are compound materials like Fe_3O_4 and Fe_2O_3 and have different atoms with antiparallel magnetic moments occupying different lattice sites. Because the magnetic moments have different magnitudes and cannot cancel out, such materials demonstrate a net magnetic moment and they have similar behavior with ferromagnetic materials in magnetic field. However, when the antiparallel magnetic moments of different atoms are equal and can cancel out, such compound materials always have zero net magnetic moment and are called antiferromagnetic materials.

2.4.2 Theory and properties of magnetic nanoparticles

When the magnetic materials have at least one dimension in nanoscale, they are referred to as magnetic nanoparticles (MNP) and new properties will appear especially in aspect of magnetism, because the particle sizes are comparable with the sizes of magnetic domains[152]. It has been proven the magnetization (per atom) and the magnetic anisotropy of MNP is much greater than those of bulk materials and therefore they are of great interests for research and applications[152, 153].

Magnetic properties of MNP are governed by various factors, including their chemical composition, crystallinity, particle shape and size, and their interaction with neighboring particles and the surrounding matrix[153]. Especially, it is influenced by the size of the particle counter-effect between the thermal energy and anisotropy energy[154], as shown in **Figure 2.24**. When the size of MNP is sufficiently small, they are single-domain particles and their thermal energy could overcome their anisotropy energy barrier. The particles can flip rapidly and overall demonstrate zero magnetic moment on the timescale of the measurement. Such particles are called superparamagnetic nanoparticles. When the size of MNP increases, they will stay in single-domain range, however, their thermal energy cannot overcome the increased anisotropy energy, therefore, the MNP cannot flip freely and overall they exhibit magnetic moment in certain direction. Such particles are ferromagnetic or ferrimagnetic nanoparticles. And when the particle size of MNP further increase, they will become multi-domain particles and the interaction of different domains will also be involved and situation become more complicated. But overall, such particles also align themselves along certain direction and they are still ferromagnetic or ferrimagnetic.

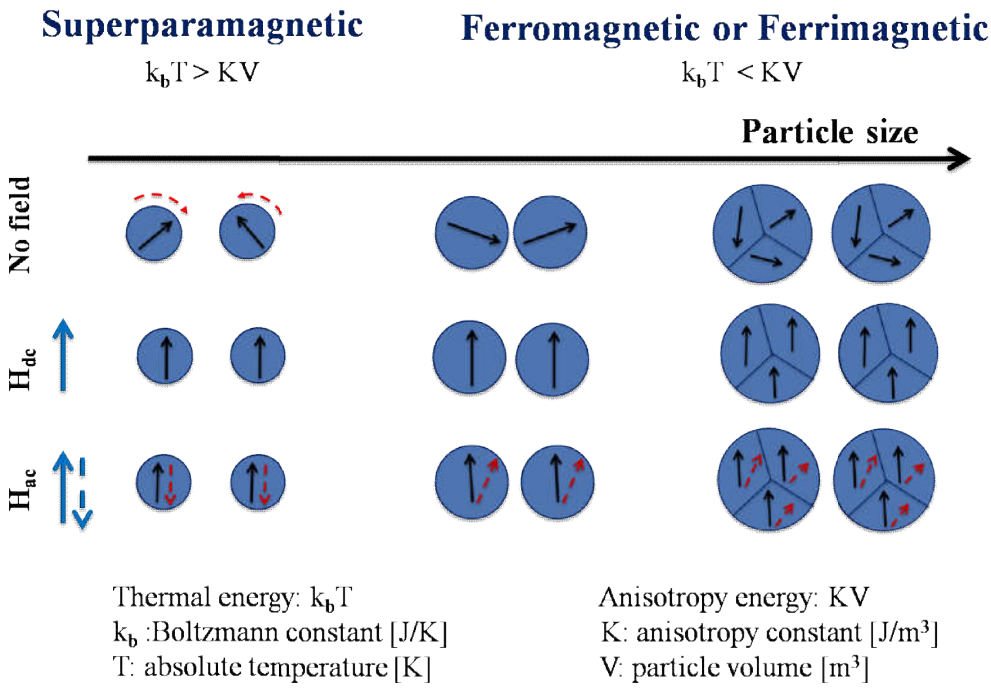

Figure 2.24. Schematic illustration for the behavior of different types of magnetic nanoparticle, in absence of magnetic field and in presence of static (H_{dc}) or alternating magnetic field (H_{ac}).

2.4.3 Synthesis of magnetic nanoparticles

In order obtain highly efficient magneto-responsive materials, it is critical to synthesize MNP with effective magnetic properties; therefore, it would be able to respond to weak stimuli with significant effect. And in recent years, a range of general methods for MNP synthesis, with various compositions and excellent control of particle size, size distribution, shape and stability, have been developed[155].

Among all kinds of magnetic nanoparticles, iron oxide nanoparticles (magnetite, Fe_3O_4) are most commonly used, because their easy preparation, strong magnetic properties and low toxicity[156]. In our research, we also chose it as the magnetic heater; therefore, the following section will focus on synthesis and functionalization of magnetite iron oxide nanoparticles.

2.4.3.1 Coprecipitation

Coprecipitation is one of the most facile and conventional methods to prepare iron oxide nanoparticle, by simply adding base to aqueous Fe(II)/Fe(III) salt solutions under inert atmosphere. By varying the salt nature (sulfates, chlorides and nitrates), the ratio between Fe(II) and Fe(III), pH, reaction temperature, and ionic strength, particles with different size, shape and composition can be obtained[157, 158]. A typical reaction for Fe_3O_4 formation is shown in **Equation (2.1)**. During the coprecipitation process, first the concentration of the species will reach critical supersaturation and nucleation will happen suddenly; then, the nuclei will grow slowly as the solutes diffuse to the surface of the crystal[159, 160].

$$Fe^{2+} + 2Fe^{3+} + 8OH^- \rightarrow Fe_3O_4 + 4H_2O \quad (2.1)$$

By this method, it is possible to obtain particle size in the range of 2-17 nm and they can be stabilized by adding chelating organic anions such as citric and oleic acid, or polymer surface complexing agents like dextran and PVA[157].

The main advantage of this method is that it is easy to be scale up and produce large amount of iron oxide nanoparticles. However, the drawback is that the particles obtained usually have relatively poor crystallinity and wide size distribution, as only kinetic factors control the growth of the crystal[159, 160]. For the hyperthermia purpose, as the optimal AMF frequency depends on particle size, a wide particle size distribution will result in a wide range of optimal frequency, therefore affect the heating efficiency of the particle in specific field condition.

2.4.3.2 Microemulsion

As coprecipitation in bulk solution has relative poor controllability for particle size, nanoreactors like micelles and nanoemulsions were introduced to produce nanoparticles in a confined zone and obtain particles with better size and shape control; such methods are very often referred to as microemulsion synthesis methods[155, 157, 161, 162].

Thermodynamically stable nanodroplets, including micelles (1-10 nm) or water-in-oil nanoemulsions (10-100 nm), can be formed by mixing immiscible oil phase and aqueous phase, with an amphiphilic surfactant at the interface to stabilize the system[163]. By tuning the concentration of the dispersed phase and the surfactant, the size of the droplets could be varied

and controlled within 1-100 nm. The droplets will work as nanoreactors for the precipitation of metal salts, and provide a confinement to kinetically and thermodynamically constrain the particle nucleation and growth[157].

The main advantage of synthesis in confinement is that the particle size can be controlled by modulating the size of the aqueous droplet, tuning the concentrations of metal and base, as well as the reaction temperature[157]. And most magnetite nanoparticles obtained with this method have diameter in the range of 3-12 nm. Despite the relatively better control for the process, comparing with coprecipitation process, this method is not so efficient and difficult to scale up, because the low yield of particles and large consumption of solvent[155].

2.4.3.3 Thermal decomposition

Monodisperse iron oxide magnetic nanoparticle with high crystallinity and excellent size control can be synthesized by thermal decomposition of iron organic precursors in high-boiling hydrocarbon solvents, together with surfactants for stabilizing. The commonly used precursors include iron acetylacetonate ($Fe(acac)_3$), iron cupferronate ($Fe(Cup)_3$), or iron pentacarbonyl ($Fe(CO)_5$). And popular surfactants include oleic acid, other fatty acids and hexadecylamine. In a typical reaction, with the decomposition of organometallic precursor, supersaturation will be reached and a single-burst of nucleation will happen. Then the nuclei grow slowly and finally surfactant will adsorb on the surface of the particles to stabilize the colloid solution. This method can achieve high microstructural control by factors including the nature of precursor and solvent, concentration and ratios of reactants, reaction times and temperature, addition of seeds and complexing strength[164].

Despite all the merits including good controllability and scalable production, thermal decomposition process is relatively complicated and there are also concerns for the high temperature required and the safety of the reactants[157].

2.4.3.4 Hydrothermal/Solvothermal synthesis

Traditional hydrothermal synthesis is defined as method to prepare nanomaterials by crystallization in aqueous solution at raised temperature and pressure[165]. Due to the high temperature and pressure conditions, minerals that are insoluble in aqueous solvents under

ordinary conditions will be dissolved and monodisperse crystals will be formed by heterogeneous chemical reaction. Nowadays, solvent for the reaction has been extended also to nonaqueous solvents, therefore the definition of hydrothermal synthesis has also been broadened as general method to prepare nanostructural materials through a heterogeneous chemical reaction in a closed system in the presence of a aqueous or nonqueous solvent and at a temperature higher than the boiling point of the solvent; so it is also called as solvothermal synthesis[166, 167, 168]. Hydrothermal/solvothermal process has been widely used to prepare nanostructural materials for various applications such as electronics, catalysis, ceramics, biomedical and biophotonics, et cl.[166]. MNP with low dispersity and high crystallinity can also be obtained by this method[155].

Hydrothermal/solvothermal synthesis is usually carried out in a Teflon-lined autoclave, as shown in **Figure 2.25**. As the reaction solution will be heat up above the boiling point of the solvent, there will be pressure developed during the reaction process, so the use of autoclave is necessary to avoid explosion.

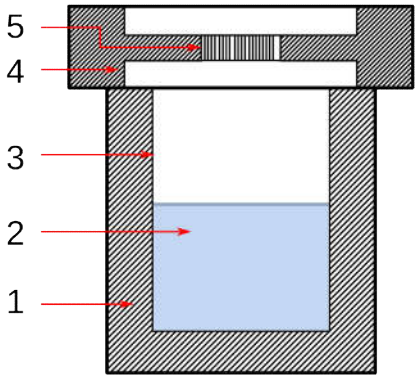

Figure 2.25. Schematic diagram of hydrothermal/solvothermal synthesis setup: (1) stainless steel autoclave, (2) precursor solution, (3) teflon liner, (4) stainless steel lid, (5) bursting disc. Adapted from reference[168].

When the solvent is high-boiling, multivalent alcohols, including low molecular weight ethylene glycol and diethyleneglycol, and high molecular weight polysol like polyethylene glycol, the process is also called polyol synthesis [169]. There are several advantages of polyol as solvent: (i) they have high dielectric constants, therefore have water-comparable solubility for metal-salt precursors; (ii) they have relatively high boiling points (up to 320 ^{o}C) and a wide operating range

for temperature; (iii) they serve as reducing agent and stabilizers to control nanoparticle growth and avoiding particle aggregation[157, 169]. For example, the following equations (**Equation 2.2** and **Equation 2.3)** show how ethylene glycol works as reductant. At temperature 197 ^{o}C, ethylene glycol forms acetaldehyde via dehydration (**Equation 2.2**) Acetaldehyde then will reduce partly ferric (from $FeCl_3$) to ferrous irons (**Equation 2.3**) which leads to the formation of Fe_3O_4[170].

$$2CH_2OH–CH_2OH \xrightarrow{-2H_2O} 2\ CH_3CHO \quad (2.2)$$

$$2\ CH_3CHO + 2\ Fe^{3+} \rightarrow CH_3COCOCH_3 + 2\ Fe^{2+} + 2\ H^{+} \quad (2.3)$$

A highly controllable polyol process to obtain monodisperse magnetite nanopartles with adjustable sizes has been developed by Li et al.[171, 172, 173]. By using iron(III) chloride ($FeCl_3$) salt as ferric source, ethylene glycol as reducing agent and high boiling solvent, and anhydrous sodium acetate (NaAc) as electrostatic stabilizer to prevent particle agglomeration, monodisperse single-crystal magnetite particles with tunable size in the range of 200- 800 nm were obtained[172, 173]. Further, Li's group also demonstrated that, by simply adding 1,6-hexanediamine as functional ligand to reaction solution, amine-functionalized magnetite nanoparticles with high quality could be easily synthesized[171]. Such amine-functionalization would not only ensure better dispersion of the MNP in aqueous and polar solvent, but also enable the bioconjugation of the particle with useful peptide for bioapplications.

When comparing the advantages and disadvantages of the different synthesis methods mentioned above, hydrothermal /solvothermal synthesis is overall more favorable due to the narrow size distribution and the easy implement for surface functionalization[155].

2.4.4 Magneto orientation and magneto heating

2.4.4.1 Magnetic orientation

When MNP are placed in static magnetic field or alternating magnetic field with low frequency, the motion of MNP can be remotely manipulated by external magnetic field. Therefore, when MNP are coupled to the end of functional polymer chain or composited into the polymer matrix,

motile systems with different structures and applications can be obtained. Magnetic orientation's applications include magnetic separation and purification, targeted drug delivery and recoverable catalysts.

One good example of the application of magnetic orientation is magnetic separation technology. It has been successfully used in fields including molecular biology, analytical chemistry, or immunochemistry. For this application, MNP coupled with appropriate affinity ligands are used as magnetic carriers, for easy and sensitive capture of targeted biomolecules like proteins and peptides. And after the capture, the biomolecules can be harvested by eluting from magnetic separation material, with standard elution methods such as the change of pH, ionic strength or use a polarity reducing solvent.

2.4.4.2 Magnetic heating

When ferromagnetic nanoparticles and superparamagnetic nanoparticles are subjected to external AMF, they have different magnetization behaviors, as shown in **Figure 2.26**[174]. For ferromagnetic nanoparticles, due to their high anisotropy energy (single domain nanoparticles) or the movement of domain walls (multi-domain nanoparticles), there is a delay of magnetization, which demonstrates as hysteresis in the M-H curve (cf. **Figure 2.26(a)**). For the superparamagnetic nanoparticles, as their anisotropy energy is very small, they flip fast and change simultaneously with applied AMF, they demonstrate a sigmoidal M-H curve during magnetization (cf. **Figure 2.26(b)**).

Generally, the heat generation of MNP upon AMF is based on three mechanisms: (1) hysteresis (the magnitude represented by the area inside the hysteresis loop, cf. **Figure 2.26(a)),** (2) Néel relaxation (rotation of the magnetic moment within the particle), and (3) Brownian relaxation (physical rotation of the whole particle within the dispersing medium)[174, 175]. Due to the different magnetization behavior, the dominating mechanism of magneto-heating is also different for ferromagnetic and superparamagnetic nanoparticles. While the main source for heat generation of ferromagnetic nanoparticles is hysteresis loss, for superparamagnetic nanoparticles it is relaxation losses[176, 177].

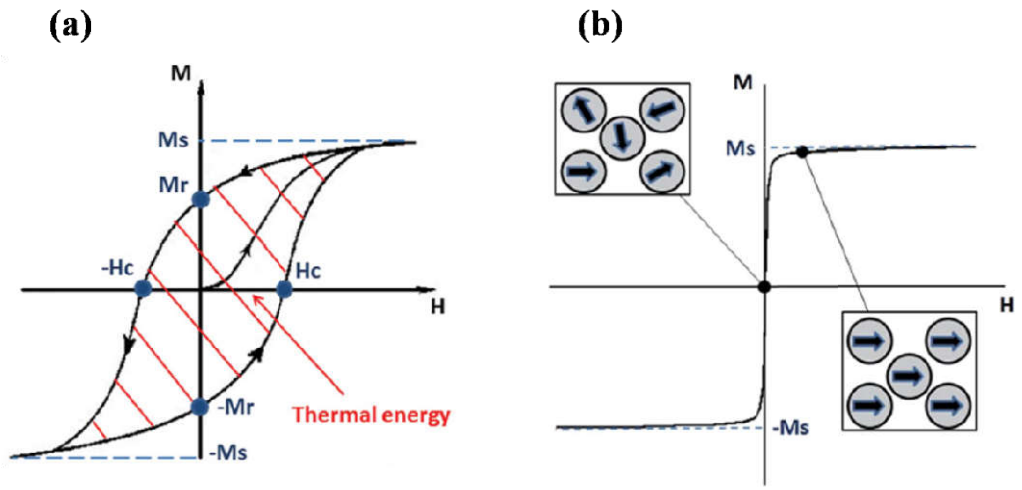

Figure 2.26. Typical M-H curves for (a) ferromagnetic nanoparticles and (b) superparamagnetic nanoparticles during magnetization. The hysteresis loop of ferromagnetic nanoparticles in (a) (the area marked with red stripes), represents the amount of energy dissipation of the material during one magnetization cycle. The superparamagnetic nanoparticles respond to an external field with a sigmoidal curve, but show no hysteresis. Here H is applied external magnetic field, M is magnetization, H_c is coercivity, M_r is remanence magnetization and M_s is saturation magnetization[174].

The heating efficiency of magnetic nanoparticles can be estimated theoretically according to the heating mechanisms and measured experimentally by calorimetry.

Theoretically, the heat dissipation of ferromagnetic nanoparticle (FM) by hysteresis loss can be determined by integrating the area of hysteresis loop (**Figure 2.26(a)**). Loss power density (heat generation per unit volume) of such particle can be calculated by multiplying the frequency with the area of hysteresis loop[178]:

$$P_{FM} = \mu_0 \, f \oint H \, dM \tag{2.4}$$

Where μ_0 is the permeability of free space, f is the frequency of alternating magnetic field, H is the magnetic field amplitude and M is the induced magnetization of MNP.

Experimentally, as there is no dependence between frequency and area of hysteresis loop (integral of Equation 2.4) for ferromagnetic nanoparticle, the power dissipation can be easily

determined from quasi-static measurement of hysteresis by Vibrating Sample Magnetometer (VSM) or Superconducting Quantum Interference Device (SQUID) magnetometer[178].

For superparamagnetic nanoparticles (SPM), as energy barrier for magnetization reversal is very small, the thermal energy is sufficient to cause magnetization reversal and the particles mainly generate heat by relaxation losses. The calculation for relaxation loss of power of superparamagnetic nanoparticles in AMF is relatively complicated and has been well reviewed by Rosensweig and Hergt[177, 179]. According to Hergt et al., the loss power density of superparamagnetic nanoparticles can be calculated according to[177, 179]:

$$P_{SPM} = \mu_0 \pi \Pi''(f) H^2 f \quad (2.5)$$

Where $\Pi''(f)$ is loss component that is related to magnetic loss, μ_0 is the permeability of free space, f is the frequency of alternating magnetic field and H is the magnetic field amplitude.

On the other hand, when the mass density of magnetic particles is known, the loss power density P (W m^{-3}) can be related to the specific loss power (SLP) (W g^{-1}), which describes the power achievable per gram of iron in the material and can also be estimated experimentally by calorimetric method.

Since energy dissipation of all MNP will cause the overall temperature elevation of their dispersion, by measuring the elevated temperature of the particle dispersion (e.g. in water), SLP of MNP can be calculated by following equation[180]:

$$SLP = c \cdot (m_s/m_{Fe}) \cdot (\Delta T_s - \Delta T_w)/\Delta t \quad (2.6)$$

Where c is the heat capacity of water, m_s is the mass of the sample, m_{Fe} is the mass of MNP in the sample, ΔT_s is the temperature increase of the nanoparticle dispersion, ΔT_w is the temperature increase of water, and Δt is time duration with AMF on. Here, $(\Delta T_s - \Delta T_w)/\Delta t$ is the slope of the heating curve with unspecific heat influence eliminated.

A typical setup of calorimetric measurement is shown in schematic **Figure 2.27**. The crucial elements include excitation coils to generate adjustable alternating magnetic field, a temperature probe to detect the temperature change of the sample, and the heat insulation layer to ensure adiabatic control and the accuracy of the measurement.

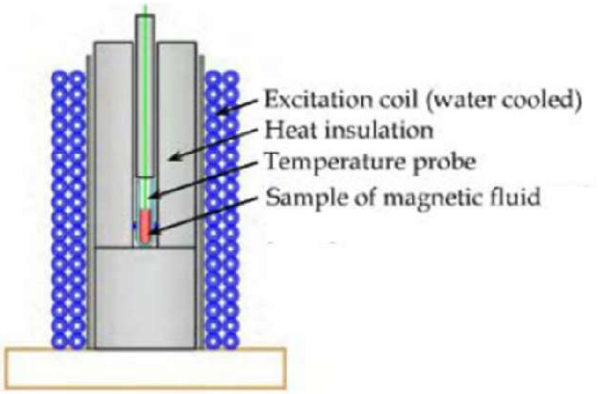

Figure 2.27. Scheme illustrating a typical calorimetry measurement setup for heat generation of MNP[181] .

The heating efficiency of MNP not only relies on the properties of particles, but also the external field conditions. Currently, in most reported studies, the conditions of the tests are not clear or even not mentioned, therefore the heat dissipation of reported MNP is difficult to compare. A standard method or criteria to evaluate the heating efficiency of MNP is needed[182].

To summarize, heating performance of MNP is not only intimately entwined with their materials, structure and mean size, but also on dependence of external magnetic field conditions, including the frequency and field amplitude. A summary of important parameters that affect the magneto-heating efficiency of magnetic particles is made in **Table 2.2**[182]. In general, the heat dissipation increases with the size of the particle, and the frequency and amplitude of applied AMF.

Table 2.2. Summary of important parameters for magneto-heating[182]

Nanoparticle	Medium	Magnetic Field
Saturation magnetization	Particle concentration	Field amplitude
Magnetic anisotropy	Viscosity	Field frequency
Magnetic remanence/cocercivity		Homogeneity
Size		
Polydispersity		
Aggregation		
Coating		

It has been reported that single-domain cubic iron oxide particles can deliver larger heating power, comparing to spherical MNP with similar sizes[183]. This is because that the anisotropy of cubic particles are corroborated at atomic level, therefore, their heating power is also improved.

Moreover, Hergt et al. have done a systematic study of the influence of particle size and distribution on the heating efficiency[177]. They found bigger particles with narrow size distribution are most efficient for heat generation. For example, bacterial magnetosome with mean core size of 38 nm and mean square deviation of 5 nm, which is relatively big and narrow distributed, has superior magneto-heating efficiency. It has specific power of loss of 960 W/g at field condition of 10 kA/m and 410 kHz[184].

There are many applications that utilize the magneto-heating, including hyperthermia therapy to cure cancer, or technical heating processes like hardening of adhesives. Moreover, when MNP are combined with thermo-responsive polymers, the heat generated by MNP can be used to cause thermal effect in thermo-responsive polymeric system by applying a suitable external magnetic field[185]. This synergistic effect can used to design magneto-responsive hydrogels or membranes for controlled release (cf. section 2.2.3)[34, 35, 47, 86, 87, 186] .

3. Experiments

3.1 Materials and chemicals

3.1.1 Membrane

Track-etched polyethylene terephthalate (PET) membranes with a nominal pore diameter of 1000 nm and a thickness of 23 µm from Oxyphen (Germany) were used. They were washed in ethanol for one hour and dried (40 ^{o}C) over night before using for functionalization. **Figure 3.1** shows the chemical structure of the membrane material polyethylene terephthalate and **Table 3.1** shows the information of PET track-etched membrane given by the supplier.

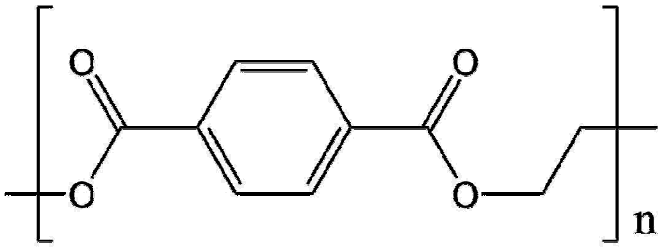

Figure 3.1. Chemical structure of membrane material polyethylene terephthalate (PET).

Table 3.1. Basic information PET track-etched membrane given by supplier

Membrane type	Membrane material	Pore size	Pore density	Permeability
Hydrophilic	polyester	1.08 µm	22 x 10^{6} cm^{-2}	27.8 $l.min^{-1}.cm^{-2}.bar^{-1}$

3.1.2 MNP

For magneto-hydrogel pore-filled membrane, commercial MNP from Ocean Nanotech with size around 40 nm was used, and **Table 3.2** shows its basic information given by the supplier.

Table 3.2. Basic information of commercial MNP provided by supplier

Iron oxide size [nm]	Size distribution	Solvent	Fe concentration [mg/ml]	Chemical composition	Surface functional groups
40	<10%	water	5	Fe_3O_4	Carboxylic acid

3.1.3 Chemicals

Table 3.3 shows all the chemicals used for the preparation of magneto-hydrogel pore-filled membranes and mixed matrix membranes.

Table 3.3. Chemicals used in the experiment

Name	Purity	Company
N-isopropylacrylamide (NIPAAm)	99%	Acros
N,N′-dimethylaminoethyl methacrylamide (DMAEMA)	≥ 99%	Polysciences Inc.
N,N′-methylenebisacrylamide (MBA)	99%	Sigma-Aldrich
benzophenone	99%	Acros
Irgacure 2959	-	Ciba Chemicals
ammonium persulfate (APS)	98%	Acros
potassium persulfate (KPS)	≥ 99%	Fluka
tetramethylethylenediamine (TEMED)	99%	Acros
sodium chloride	≥ 99%	VWR
iron(III) chloride hexahydrate	≥ 99%	Sigma-Aldrich
anhydrous sodium acetate	≥ 98.5%	Fluka
1,6-hexanediamine	98%	Sigma-Aldrich
ethylene glycol	≥ 99.5%	Fluka
polyethersulfone (PES, Ultrason E6020P)	-	BASF
polyvinylpyrrolidone (PVP, K-30)	-	Serva
N-methyl-2-pyrrolidone (NMP)	≥ 99%	Merck
N,N′-dimethylacetamide (DMAc)	≥ 99%	Sigma-Aldrich
ethanol	≥ 99%	Fisher Chemicals
water	Ultrapure (18.1 MΩ cm^{-1})	Milli-Q system (Millipore)

3.1.4 Test solutes for ultrafiltration experiment

1 g/l of aqueous dextran solutions with single or mixed dextran were used for ultrafiltration test. Dextran 4 kDa, 35 kDa and 100 kDa were purchased from Serva; dextrans 70 kDa and 500 kDa were from Pharmacia Fine Chemicals Inc; and dextran 2000 kDa was from Sigma-Aldrich.

The average hydrodynamic sizes of the different dextran fractions were estimated based on a well-established correlation between Stokes diameter and molecular weight[187].

$$d_S = 0.066 \times MW^{0.46} \quad (3.1)$$

Where d_s = Stokes diameter [nm] and MW = molecular weight [g/mol].

Calculated results are shown in **Table 3.4**.

Table 3.4. Stokes diameter of different dextran molecules

Molecular weight [kg/mol]	Stokes diameter [nm]
4	3
35	8
70	11
100	13
500	28
2000	52

3.2 Characterization of alternating magnetic field (AMF) condition

3.2.1 Introduction of AMF generator system

TruHeat HF series 5010 generator from TRUMPF-Hüttinger (Germany) was used to generate electromagnetic field, as shown in **Figure 3.2**. It consists of a generator and an inductor. The current and frequency can adjusted through the interface of the generator, and an alternating electromagnetic field with same frequency and certain amplitude will be generated between the sandwich coils of the inductor, which is made from copper tube. Because of the electrical

resistivity of the coil material (copper), there is inevitable unspecific heat generated when current flows through the coil. Therefore, cooling water with external circuit constantly flows through the lumen of the copper tube during the operation.

Figure 3.2. Inductive heating generator system, consisting of a generator and a sandwich coil as inductor**.**

3.2.2 AMF amplitude distribution

The field amplitude between the coil sandwich was measured by a self-made pickup probe (2 loops made of fine copper wire with a diameter of 7.3 mm) coupled with an oscilloscope, as shown in **Figure 3.3**. Due to electromagnetic induction, there will be electrical current induced in the probe, changing simultaneously with alternating magnetic field.

First, the relation between the input current and field amplitude was investigated by fixing the measuring site in the centre of the sandwich coils. The pickup probe was fixed in the centre of the sandwich coils, and under certain field frequency, including 395 kHz, 614 kHz, 656 kHz and 745 kHz, the input current was varied. The induced peak voltage within the probe was detected by oscilloscope and recorded. And electromagnetic field amplitude (H_0) at the site was calculated according to following equations, derived from Faraday's law of electromagnetic induction.

$$U_{max} = \frac{U_{pp}}{2}$$

$$H_0 = U_{max} \cdot \frac{1}{N} \cdot \frac{1}{f}\left(\frac{2}{\pi^2 \cdot \mu_0 \cdot D^2}\right) \quad (3.2)$$

Where U_{max} is the peak value of induced voltage, U_{pp} is peak-to-peak voltage given by oscilloscope, N is the number of loops of the probe, D is the diameter of the loop, μ_o is permeability constant of copper, f is the frequency of AMF, and H_0 is magnetic field amplitude.

Further, magnetic field amplitude distribution between the coils at certain power input was investigated, by taking coordinate axes along the radius of the coil (r) and height of the coil (h) and placing the probe at different sites between the coils. To ensure high field amplitude, a relatively high power input of the generator was chosen finally and used for all future experiments: the current was I = 15.6 A, and the frequency f = 745 kHz.

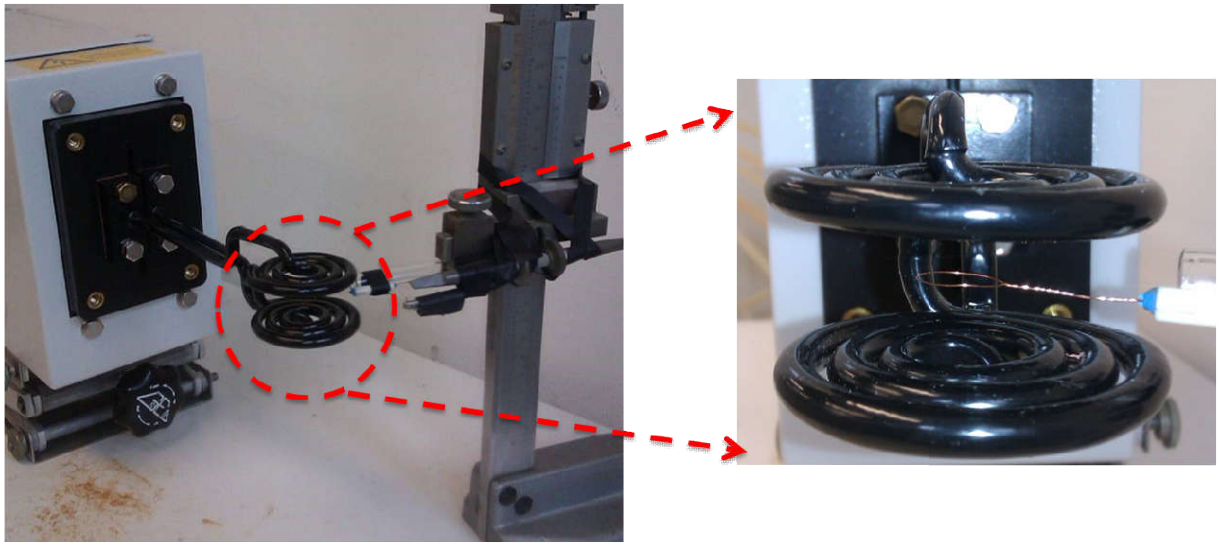

Figure 3.3. Field amplitude inside the sandwich coil inductor was measured by a self-made pickup probe (2 loops made of fine copper wire with a diameter of 7.3 mm).

3.3 Synthesis and characterizations of MNP

3.3.1 Synthesis of MNP

Amine functionalized-MNP were prepared by hydrothermal synthesis according to the literature[171], using $FeCl_3.6H_2O$ as ferric source, 1,6-hexanediamine as functional ligand, anhydrous sodium acetate as alkali source and ethylene glycol as solvent and reducing agent.

First all chemicals were dissolved in ethylene glycol overnight, then the solution was transferred into a Teflon-lined autoclave and reacted at 210 °C for 6 h. By varying the ratio of 1,6-hexanediamine, different sizes of MNP can be obtained. Here four kinds of composition have been tested as shown in **Table 3.5**.

The obtained MNP were washed with water (60 °C) and then with ethanol for several times, assisted by sonication, to get rid of the solvent and unbound 1,6-hexanediamine. Then they were vacuum dried at room temperature for 24 hours and ready for characterization and use.

At last, because the size control by this method is excellent, when the suitable size was chosen, several batches were collected to ensure enough stock for membrane casting.

Table 3.5. Composition of reaction solutions for MNP synthesis

Probe	1,6-hexanediamine [g/ml]	anhydrous sodium acetate [g/ml]	$FeCl_3.6H_2O$ [g/ml]	ethylene glycol [ml]
1	0.23	0.067	0.033	30
2	0.21	0.067	0.033	30
3	0.17	0.067	0.033	30
4	0.15	0.067	0.033	30

3.3.2 General characterization of MNP

3.3.2.1 Morphology of MNP

The morphology of commercial and self-made MNP was investigated by SEM. Diluted sample of MNP dispersion in water was spin-coated onto silicon substrate, dried in vacuum and analyzed without prior sputtering by scanning electron microscopy (SEM) using the instrument ESEM Quanta 400 .

3.3.2.2 Size distribution of MNP

The hydrodynamic particle size and size distribution of both kinds of MNP have been studied with dynamic light scattering (DLS) measurement (Stabisizer, Particle Metrix).

For commercial MNP, its particle size and distribution were further analyzed via analytical disc centrifugation with a CPS Instruments Disc Centrifuge DC 24000 (24000 rpm, 28978 g) and by using traceable standard 0.237 micron PVC as calibration standard.

3.3.2.3 Zeta potential of MNP

Surface charge of both commercial and self-made MNP have been investigated by zeta-potential measurement (ZetaSizer NanoZS , Malvern Instruments GmbH, Germany).

For the commercial MNP, their zeta-potential as the function of pH has been measured by stepwise decreasing the pH from 9 to 1 by automatic titration.

For self-made MNP, first they were dispersed in water by 30 seconds of sonication with an amplitude of 30%, by using the Sonopuls ultrasonic homogenizer HD 3100 instrument (Bandelin, Germany). Then their zeta potential were meaursed at pH 4 , using HCl for manual tritration.

3.3.2.4 Magnetic property of MNP

For self-made MNP, a vibrating sample magnetometer, i.e. the PPMS® DynaCool™ system from Quantum Design Inc. (USA) using the VSM option, was used to study its magnetization. Field amplitude comparable with the later used AMF conditions (20 $\pm$ 10 kA/m) was chosen. The field frequency is 40 Hz and an average time of 1 second per data point was used. During the whole measurement, the temperature was kept at 25 °C.

Due to the high accelerations in VSM measurements, densely mounted samples are required to restrict the mobilization and rotation of the particles, in order to reduce the noise in the moment measurement. Therefore, normally dry state samples with amount around 10 mg are tightly filled into the sample holder for VSM measurement. When the particles are dispersed in a significant fraction of water, they can easily mobilize and rotate during the VSM measurement and lead to noisy data. Thus, liquid dispersed samples are not preferred and can only be measured by using special plastic capsule (e.g. non-soluble polycarbonate capsules). The commercial MNP is dispersed in aqueous solution upon purchase. In order to characterize it with VSM, drying the sample in advance of measurement can be an option. Yet, because the commercial MNP sample is very expensive, this characterization was not performed.

3.3.3 Heating efficiency of MNP

Since power loss of MNP depends not only on the material, morphology and size of the particles, but also on the specific magnetic field conditions[33], the heating efficiency of the used MNP has been studied by calorimetric method. Self-made closed glass vial with vacuum walls, containing 1 ml of MNP aqueous dispersion has been placed between the inductor coils, as shown in **Figure 3.4**, and the temperature of the solution has been measured after certain duration of AMF (I = 15.6 A, f = 745 kHz) exposure by contact thermometer. The same volume of water as background solvent was also tested to evaluate the influence of the unspecific heat emitted by the AFM generator. To describe the power achievable per gram of iron in the material, the specific loss power (SLP) of the MNP has been calculated by **Equation 2.6** (cf. section 2.4.4.2).

Here for commercial MNP, relatively low concentration of 0.05 mg/ml and 5 minutes of AMF exposure was used, since the sample is quite expensive. And for self-made MNP, a higher concentration of 0.5 mg/ml and duration of 1 minute of AMF exposure was used to get a more pronounced heating effect and less influence by environment temperature.

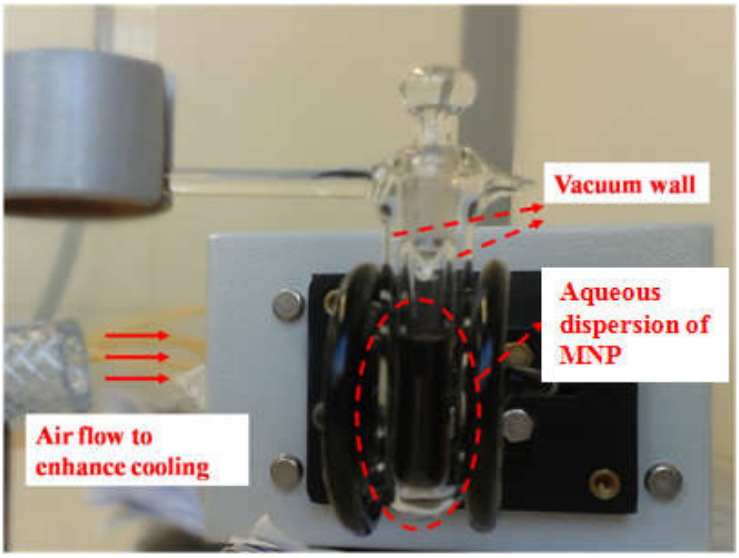

Figure 3.4. Setup for calorimetric measurement of SLP: closed glass vial with vacuum walls, containing 1 ml of MNP aqueous dispersion was placed between the inductor coils and the temperature of the solution was measured before and after certain duration of AMF (current 15.6 A, frequency 745 kHz) exposure by contact thermometer.

3.4 Fabrication and characterization of pore-filled magneto-responsive membranes

3.4.1 Study of bulk magneto-responsive hydrogel

3.4.1.1 Stability of MNP in monomer solutions

Before the hydrogel synthesis, the stability of MNP in monomer solution has been studied with dynamic light scattering (DLS) measurement (Stabisizer, Particle Metrix). Monomer solutions (1 mol/l of NIPAM and 0.02 mol/l MBA) with different MNP concentrations have been prepared and sonicated for 10 minutes before DLS measurements. Samples were measured every 1 hour within a period of 5 hours. For each time point, the sample was measured three times over a period of 60 s for each run to get the number average diameter D_n. And the result is the average of the three measurements.

3.4.1.2 Rheological study of bulk MNP-PNIPAAm hydrogel

To study the influence of MNP on gelation kinetics and microstructure of the MNP-PNIPAAm composite hydrogels and to choose a suitable polymerization method for pore-filling procedure, rheological studies were carried out for *in situ* UV- and redox-initiated cross-linking polymerization of NIPAAm with different MNP concentrations.

Rheometer model MCR-300 (Anton Paar, Austria) equipped with external UV-light source (100 Watt mercury lamp, EXFO Omnicure Series 1000, EXFO, Quebec, Canada) and Peltier device for temperature control was used. Cone-plate geometry with an upper plate of cone angle 0.1° and a diameter 25 mm was chosen and different lower plates were used for different polymerization methods. An optically transparent glass-based lower plate was used for UV polymerization while a Peltier plate was used for redox polymerization. First, *in situ* oscillatory shear measurement with time sweeping mode was carried out, to monitor the gelation process. For each measurement, 200 µL reaction mixture, with 1 mol/l NIPAAm (recrystallized with hexane before use), 0.02 mol/l of MBA, 0.02 mol/l of initator (Irgacure 2959 for UV and APS for redox polymerization), and varied concentrations of MNP (from 0 to 1 wt % relative to NIPAAm), was used. For UV polymerization, UV light with the intensity 21 mW/cm^2 that was directly coupled into the rheometer cell via fiber optics, was used to trigger the polymerization.

For redox polymerization, 0.01 mol/l TEMED was added and mixed for 30 seconds before loading the reaction solution onto the plate, to accelerate the generation of free radicals. The normal force was set at 0 N. An angular frequency of 10 rad/s and small strain amplitude of 0.01% were chosen to ensure linear regime of oscillatory deformation. During all measurements, temperature was controlled at 21 ^{o}C and the evaporation of solvent was minimized by using a solvent trap. After the hydrogel was fully polymerized, frequency sweeping was carried out to characterize mechanical properties and to estimate the microstructure of the hydrogels. While the temperature was kept constant at 21 ^{o}C, the normal force was reset to 0 N, and the strain amplitude was kept at 1%, an angular frequency in the range of 0.1-100 rad/s was applied and the storage modulus of hydrogel was measured. Based on rubber elasticity theory, average mesh size of the hydrogel was estimated from rheological data according to the following equation[38-39].

$$\varepsilon = \left(\frac{RT}{G^{*}N_A}\right)^{\frac{1}{3}} \tag{3.3}$$

Where R is the ideal gas constant, T is the measurement temperature, N_A is Avogadro's constant and G* is the plateau value of storage modulus.

3.4.1.3 Magneto-heating of magneto-responsive hydrogel

Also, to prove the heating effectiveness of magneto-hydrogel in AMF, thermal imaging camera 885-2 from Testo AG (Germany) was used to take thermal images of hydrogels after exposure to the chosen AMF field conditions. Freeze-dried samples of MNP-PNIPAAm composite hydrogel with 1% of MNP and pure PNIPAAm hydrogel were prepared by redox polymerization. After placing both samples at the middle plane between the inductor coils (I = 15.6 A, f = 745 kHz) for 1 minute, infrared photos were taken.

3.4.2 Characterization of base membrane

3.4.2.1 Morphology of base membrane

Top surface and cross-section images of commercial PET track-etched membranes were obtained by scanning electron microscopy (ESEM Quanta 400 FEG, FEI, USA), after sputtering thin layer of gold/palladium.

3.4.2.2 Pore size distribution of base membrane

Gas flow/pore dewetting permporometry was carried out to analyze the pore size distribution of the commercial PET track-etched membranes, by using a capillary flow porometer (Porous Materials, Inc.,Ithaca, NY, USA). Here membrane samples with diameter of 25 mm were tested via the "Dry up/ Wet up" method. The gas flow through the dry sample was tested first as "Dry up" test. Then for "Wet up" test, membranes were wetted by 1,1,2,3,3,3-hexafluoropropene ("Galwick", with surface tension of 16 $dyn.cm^{-1}$) before gas flow test. Pore size distribution of the membrane was deduced by the comparison of the dry and wet membrane data by the PMI software. The maximum transmembrane pressure used for air flow measurement was 5 bar.

3.4.3 Pre-modification of base membrane

In order to facilitate MNP loading and provide robust anchors for the stable immobilization of hydrogel during pore-filling step, polymer chains with specific charges and moderate chain length were grafted onto PET membrane. Surface initiated "grafting-from" was used, with conditions adopted and optimized according to previous work[67, 68]. To render surface charges, different monomer solutions were used. Specifically, for "method 1", 0.2 mol/l of aqueous NIPAAm solution was used to graft neutral PNIPAAm chain, and for "method 2", 0.01 mol/l DMAEMA was added on the basis of 0.2 mol/l NIPAM (recrystallized with hexane before use), to graft positively charged P(DMAEMA-co-NIPAM) chains. The general procedures were as follows: Pre-washed PET membrane samples (44 mm diameter disks) were first coated with photo-initiator; the samples were soaked in 0.1 mol/l benzophenone solution in ethanol/water (10:1) for about 60 min before immersing them in degassed aqueous monomer solutions in Petri dish. Then the Petri dish was placed inside a UV system (UVA Cube 2000, Hönle AG, Germany; equipped with a 20 cm long mercury lamp, allowing a homogeneous irradiation of 0.1 m^2 area via reflecting walls) with a UVA filter on top (to prevent membrane degradation). UV irradiation was carried out with UV intensity of 40 mW/cm^2 for 15 minutes. At last, functionalized membranes were washed with water for 24 hours, dried at 40 ^oC and cut into 25 mm samples, ready for characterization and further pore-filling functionalization.

3.4.4 Pore-filling functionalization

Pore-filling functionalization has been conducted with pre-modified membranes with diameter of 25 mm. To ensure high loading of MNP, loading procedure with step-wise increase of MNP concentration and prolonged loading (soaking) time was applied. First, pre-modified membrane samples were placed in a vial with 1170 µl reaction solution with following composition: 1.5 mol/l NIPAAm, 0.03 mol/l MBA, and 0.03 mol/l APS, and containing 0.85 mg MNP (170 µl of 5 g/l MNP, 0.5 wt% relative to final monomer amount), and 1.5 mg NaCl. The vial was placed on a shaker with speed of 300 rpm and mixing was done for 1 hour. Then 0.85 mg MNP (170 µl of 5 g/l MNP) and 1.5 mg NaCl (dissolved in 20 µl water) were added to the monomer solution and mixing continued for 1 hour, and this addition was repeated once more to reach overall volume of 1550 µl and concentrations of NIPAM 1 mol/l, MBA 0.02 mol/l, MNP 1.5 wt% (relative to monomer), APS 0.02 mol/l, and NaCl 50 mmol/l. After loading procedure, 0.01 mol/l TEMED was added and mixed for 30 seconds. Then, the fully soaked membranes were taken out and placed between two glass plates. The glass plates were clamped and the gap between them was sealed with vaccum grease to prevent water evaporation. After 24 hours of polymerization at room temperature, the membranes were taken out and washed with water for at least three times for 24 hours before characterization.

At last, in order to obtain a denser hydrogel network for more effective molecular sieving, the concentrations of all chemicals were increased for preparation of the pore-filled membrane used in dextran filtration experiments: 1.1 mol/l NIPAAm, 0.022 mol/l MBA, 1.5 wt% MNP (relative to monomer), 0.022 mol/l APS, 50 mmol/l NaCl, and 0.011 mol/l TEMED were used.

3.4.5 General characterization of membranes

3.4.5.1 Zeta potential of pre-modified membrane

Zeta potential of base and pre-modified membranes from both methods were measured by SurPass electrokinetic analyzer (Anton Paar, Austria). During the all measurements, 1 mmol/l of KCl was used as electrolyte and 0.1 mol/l of NaOH solution or 0.1 mol/l of HCl solution were used to adjust the pH between 3 and 10. All measurements started around pH 3 and then the pH was increased by step-wise addition of NaOH solution. The zeta potential data at different pH

values were calculated by the software of the instrument according to the Helmholtz-Smoluchowski equation:

$$\zeta = \frac{\Delta E_{SP}}{\Delta P} \times \frac{\eta \times \kappa}{\varepsilon_r \times \varepsilon_o} \tag{3.4}$$

Where $\Delta E_{SP}/\Delta P$ is the change in streaming potential with pressure, η is the electrolyte solution viscosity, κ is the conductivity of the electrolyte solution; ε_0 is the permittivity of free space and ε_r is the permittivity of the electrolyte solution.

3.4.5.2 Morphology and MNP loading of pore-filled membrane

To investigate the MNP loading of pore-filled membranes, scanning electron microscopy coupled with energy dispersive X-ray spectroscopy (SEM/EDX) was used to visualize and quantify the loading, both inside the pore and on the outer membrane surface. While images of surface and cross-section topography were obtained from secondary electron emission, characteristic X-rays emitted from the sample gives qualitative and quantitative elemental information, like here the iron content on the sample surface. Membrane samples for both surface and cross-section imaging were sputtered with thin layer of gold-palladium (80:20) using a K550 sputter coater from Emitech Ltd. (Ashford, UK). Then SEM/EDX was performed with instrument ESEM Quanta 400 FEG from FEI Co. (Hillsboro, USA).

Further, to quantify MNP loading of magneto-hydrogel pore-filled membrane, thermogravimetric analysis was carried out for PET base membrane, PNIPAAm hydrogel pore-filled membrane and magneto-hydrogel porefilled membrane (prepared via “method 1”), with instrument STA 449 F1 Jupiter (Netzsch, Germany). To maximize the decomposition of organic substances, air atmosphere was used. Heating rate was kept at 10 ^{o}C/min and the temperature was kept in the range of 30-1000 ^{o}C.

3.4.6 Filtration performance of membranes

3.4.6.1 Thermo- and magneto-responsive water permeability

To examine the incorporation of thermo-responsive PNIPAAm chains for pre-modified membranes and PNIPAAm hydrogel network for pore-filled membranes, water filtration at both

25 °C and 45 °C was carried out after each functionalization step. Self-constructed dead-end filtration cell with 3.14 cm^2 effective membrane area was used. The trans-membrane pressure was adjusted by hydrostatic pressure or gas pressure, and the temperature of feed was controlled by thermostat (Julabo, Germany). Mass of permeate was measured gravimetrically and flux through of the membrane J and membrane permeability P were calculated accordingly.

$$J = \frac{m}{\rho_T \cdot A \cdot \Delta t}$$

$$P = \frac{J}{\Delta p} \tag{3.5}$$

Where m is the mass of permeate during filtration duration Δt, ρ_T is the water density at temperature T, A is effective filtration surface area of membrane, Δp is the trans-membrane pressure.

For the pre-modified membranes, to evaluate the length of the grafted polymer chains, hydrodynamic layer thickness was calculated according to Hagen-Poiseuille equation[67, 68].

$$J = d^2 \cdot \frac{\varepsilon}{32\,\eta} \cdot \frac{\Delta p}{\Delta x}$$

$$L_h = \frac{d_{BM} - d_{PM}}{2} \tag{3.6}$$

Where J is the water flux through the membrane, d is the pore diameter, ε is the membrane porosity, η is viscosity of water, Δp is the trans-membrane pressure, Δx is the membrane thickness, d_{BM} is the average pore diameter of base membrane, d_{PM} is the average pore diameter of pre-modified membrane and L_h is the hydrodynamic layer thickness of the grafted layer on the pore wall. This estimation is valid for isoporous membranes as it is the case for this type of track-etched membranes and assuming an even functionalization of all pores as has been proven in previous studies[67, 68, 188]. Specifically, for the calculation, the average pore diameter d_{BM} measured via gas flow/pore dewetting permporometry was taken (cf. section 3.4.2.2). Then, with Hagen-Poiseuille equation and water filtration data of base membrane, membrane porosity ε was calculated which can then be used to estimate, by using d_{BM}, pore density. Assuming that the pore density would not change during pore surface functionalization, and with water filtration

data of modified membrane, the average pore diameter of pre-modified membrane (d_{PM}) was calculated. At last the hydrodynamic layer thickness (L_h) was estimated by comparing the average diameter of membrane before and after pre-modification.

Moreover, gating factor $R_{45/25}$, which represents the ratio of effective average pore diameter, i.e. permeability, at 45 °C and 25 °C, was also introduced and calculated, to quantify the thermo-responsivity of pre-modified membranes[64]. Specifically, first, the effective average pore diameter of pre-modified membrane at different temperature (45 °C and 25 °C) was calculated according to the evolved version of Hagen-Poiseuille equation. Then, by assuming that the number of pores per unit membrane area (n) stays constant at different temperature, gating factor is calculated by comparing the effective average pore diameter of pre-modified membrane at at 45 °C and 25 °C.

$$d_T = \left(\frac{128 \cdot \eta_T \cdot J_T \cdot \Delta x}{\pi \cdot n \cdot \Delta P}\right)^{\frac{1}{4}}$$

$$R_{45/25} = \frac{d_{45}}{d_{25}} = \left(\frac{J_{45} \cdot \eta_{45}}{J_{25} \cdot \eta_{25}}\right)^{\frac{1}{4}} \quad (3.7)$$

Where d_T, d_{45} and d_{25} are the effective average pore sizes of membrane at T °C, 45 °C and 25 °C, respectively; J_T, J_{45} and J_{25} are the water flux at T °C, 45 °C and 25 °C, respectively; η_T, η_{45} and η_{25} are the values of water viscosity at T °C, 45 °C and 25 °C, respectively; n is the number of pores per membrane area; Δp is the trans-membrane pressure; Δx is the membrane thickness.

For pore-filled membrane, a thermo-responsivity factor, $N_{45/25}$, which represents the permeability ratio at different temperatures, without the water viscosity influence, was also introduced:

$$N_{45/25} = \frac{J_{45} \cdot \eta_{45}}{J_{25} \cdot \eta_{25}} \quad (3.8)$$

At last, to test the magneto-responsivity of the pore-filled membranes, a programmed AMF condition was applied during water filtration. Self-made filtration cell was placed in the middle plane of the coils to obtain a relatively homogenous magnetic field distribution (I = 15.6 A, f = 745 kHz). During the filtration, while the feed temperature was kept at 25 °C and the trans-membrane pressure was kept constant at 0.15 bar, the AMF was switched off for 15 minutes, then it was switched on for 60 minutes and thereafter again off for 25 minutes. Water permeate

samples were taken every 5 minutes and weighted. Water permeability was calculated according to **Equation 3.5**.

3.4.6.2 Magneto-responsive molecular sieving performance of pore-filled membranes

Specific pore-filled membranes functionalized by "method 1" with good responsivity and relatively low water permeability because of tighter network structure (cf. section 3.4.4) were chosen for further filtration tests, including tests with and without AMF. Aqueous solutions with 1 g/l of single molecular weight dextran (4 kDa, 500 kDa, or 2000 kDa) were used as feed. During filtration, while the pressure was set at 800 mbar and feed temperature was set at 25 ^{o}C, permeate samples were first taken with AMF off and then with AMF on (I = 15.6 A, f = 745 kHz). Dextran concentration in permeate and feed was determined by total organic carbon analyzer (TOC-Vcpn system, Shimadzu, Japan; calibrated from 0 to 200 mg/l) and dextran rejection was calculated.

$$R = (1 - C_P/C_F) \times 100(\%) \quad (3.9)$$

Where R is the rejection for dextran, C_p is concentration of dextran in the permeate and C_F is the concentration of dextran in the feed.

To eliminate fouling effects, the filtration tests were done in the sequence of 4 kDa, 500 kDa and 2000 kDa. Furthermore, in between the dextran filtrations, the membrane was washed with water for 2 hours with 3 times of water change and to monitor possible fouling, water flux tests were carried out to see the effectiveness of washing. In all cases, permeability of membrane was monitored by weighting the permeate.

3.5 Preparation and characterization of magneto-responsive mixed matrix membrane

3.5.1 Synthesis and characterization of PNIPAAm NG

3.5.1.1 Synthesis of PNIPAAm NG

PNIPAAm NG with 5% or 2.5% MBA was synthesized by precipitation polymerization[111], using 0.1 mol/l NIPAAm (recrystallized with hexane before use), 0.005 mol/l or 0.025 mol/l MBA and

0.001mol/l KPS, all dissolved in 200 ml of water. After purging with nitrogen for 15 minutes to remove dissolved oxygen, the reaction solution was stirred with a speed of 400 rpm and kept at 70 ^{o}C for 5 hours, to complete the reaction. Then the solid product was purified by three cycles of centrifuging and redispersing in water. At last, it was freeze-dried, and thus ready for characterization and use for membrane casting.

3.5.1.2 Morphology and size distribution of PNIPAAm NG

Diluted NG in water dispersion was spin-coated onto silicone substrate, dried in vacuum, and sputtered with thin layer of platinum before scanning electron microscopy (SEM) observation using the instrument ESEM Quanta 400 FEG (FEI Co., Hillsboro, USA).

3.4.1.3 Thermo-responsive swelling property of PNIPAAm NG

To evaluate the hydrodynamic diameter of the NG in water and NMP, dynamic light scattering (DLS) of the NG dispersion in both solvents was performed with a Zetasizer Nano ZS (Malvern Instruments, Germany) with 633 nm laser and using the Smoluchowski method. To evaluate the thermo-responsivity of the dispersed NG, measurements were carried out at 25 ^{o}C and 40 ^{o}C. Before each measurement, the sample was incubated at fixed temperature for 15 minutes.

3.5.2 Dispersion optimization of MNP by sonication

For mixed matrix membrane, self-made MNP with diameter around 40 nm was used, to reduce the cost and optimize the heating performance. Before preparing the dope solution for membrane preparation, optimization of MNP dispersion in NMP was carried out, by sonicating with the Sonopuls ultrasonic homogenizer HD 3100 instrument (Bandelin, Germany). The same concentration of MNP as for composite membrane (10% mass ratio relative to the PES in NMP; i.e. or 0.17 g per 10 g of NMP) was evaluated. An ice bath was used to prevent overheating, and as shown in **Table 3.6**, different sonication procedures with different amplitudes, energy inputs and sonication time programs have been tried to optimize the dispersion. At last, an optimized sonication procedure with continuous sonication for 30 s with amplitude 30% and energy 30 W (cf. **Table 3.6**, probe 3) was used to prepare dope solution for membrane casting, as it gave the smallest average particle size and sufficient dispersion stability. After sonication, the agglomerate size in MNP dispersion was evaluated by DLS using StabiSizer® PMX 200S

instrument (Particle Metrix, Germany) at a laser wavelength of 780 nm and a laser power of 5 mW. Each sample was measured 3 times over a period of 30 s, and the data was presented as distribution by number.

Table 3.6. Dispersion optimization of MNP via different sonication procedures

Probe	Energy input	Amplitude	Time program
1	50 W	30%	continuous, 30 seconds
2	50 W	50%	continuous, 30 seconds
3	30 W	30%	continuous, 30 seconds
4	30 W	40%	continuous, 30 seconds
5	30 W	50%	continuous, 30 seconds
6	30 W	30%	5 seconds on, 5 seconds off, 60 seconds
7	30 W	30%	5 seconds on, 5 seconds off, 90 seconds

3.5.3 Preparation of mixed matrix membranes by NIPS

Based on a base dope solution with 14.5 wt% of PES (dried at 110 °C overnight before use) in NMP, membranes with different compositions have been prepared by blending with different mass ratios of NG or MNP to PES: pure PES membrane, NG-PES membrane with 10 % of PNIPAAm NG, MNP-PES membrane with 10 % of MNP, and MNP-NG-PES membrane with both 10% MNP and 10 % of PNIPAAm NG. To ensure the homogenous mixing of the different components in the dope solution the following protocols were used. For NG-PES membranes, 10% of freeze dried NG was first dispersed in NMP by magnetic stirring for 3 hours and then PES was added. For MNP-PES membranes, 10% MNP was first dispersed in NMP by optimized process of sonication (cf. section 3.5.2), and then PES was added and mixed by mechanical stirring. For MNP-NG-PES membrane, 10% MNP were first dispersed in NMP by sonication, then 10% NG was added to the solution and mixed by mechanical mixer for 3 hours, and finally PES was added in three steps during 24 hours, until homogenous dope solution was obtained.

Then composite membranes were prepared by NIPS with water as the non-solvent. For membranes containing PNIPAAm NG, to obtain a denser barrier layer of the membrane with better thermo-responsivity and also more effectively fixed NG particles, it is critical to reduce

the viscosity of the dope solution in NMP and obtain a partially shrunken state of PNIPAAm NG during the phase separation process of the membrane polymer (upon cooling of the aqueous coagulation bath, the PNIPAAm NG would then re-swell to fill the surrounding macropores). Therefore, the whole casting and coagulation process was performed at 45 ^{o}C, by preheating of the dope solution, the casting knife, the casting plate and the water bath. Specifically, the dope solution was casted on a clean glass plate with a stainless steel casting knife using a COATMASTER 510 (Erichsen, Germany). The gap between the glass plate and the knife blade was kept 200 μm and casting speed was kept at 5 mm/s. When the casting was finished, the plate with polymer film was immediately immersed into the coagulation bath with containing water at 45 ^{o}C. After keeping in water for 24 hours for complete precipitation (during that period water cooled down to ambient temperature), the membranes were washed 3 times with water and then ready for characterization. At last, membranes with varied composition: PES membrane, NG-PES membrane, MNP-PES membrane, and MNP-NG-PES membrane, were also prepared at room temperature as references (cf. **Appendix A**).

3.5.4 General characterization of mixed matrix membranes

3.5.4.1 Morphology

SEM imaging with the ESEM Quanta 400 FEG was used to observe the morphology and the distribution of nanomaterials (MNP and NG) in the porous membranes. Membranes were vacuum dried at room temperature for 24 hours. Then samples for both, outer surface and cross-section imaging, were sputtered with thin layer of gold-palladium (80:20) using a K550 sputter coater from Emitech Ltd. (Ashford, UK).

3.5.4.2 MNP loading

To investigate the MNP loading, thermogravimetric analysis was carried out for different membrane samples under air atmosphere, within a temperature range of 30-1000 ^{o}C and heating rate of 10 ^{o}C/min, by using the instrument STA 449 F1 Jupiter (Netzsch, Germany).

3.5.4.3 PNIPAAm NG loading

To investigate the PNIPAAm NG loading, elemental analysis was carried out for dry membrane samples using the CHNS analyzer EURO EA (EuroVector Instruments, Italy).

3.5.4.4 Membrane heating efficiency

The heating efficiency of MNP-NG-PES composite was evaluated by calorimetric method, analogously to the analysis of MNP in section 3.3.3. MNP-NG-PES composite membrane containing 0.5 mg MNP was cut into small pieces, dispersed in 1 ml of water and tested.

3.5.4.5 Surface chemistry of membranes

To study the surface chemistry of the membranes and verify the presence of NG in the top layer, attenuated total reflection infrared (ATR-IR) spectroscopy was applied for both surfaces of different membranes, by using the instrument 3100 FT-IR Excalibur (Varian Inc., USA) equipped with a horizontal ATR unit. A total of 64 scans were performed at a resolution of 4 cm^{-1} using a diamond crystal plate for the vacuum-dried samples. As the angle of incidence of IR beam was 45 degree, it can penetrate the sample with a depth of about 2 µm.

3.5.4.6 Thermo-responsive contact angle of membrane surfaces

Contact angle measurements of both sides of the membrane at 25 ^{o}C and 40 ^{o}C were carried out, to verify the distribution of PNIPAAm NG and MNP on the surfaces, with an optical measurement system (OCA 15 Plus, Dataphysics, Germany) and the captive bubble method. After the membrane samples were fully wetted and equilibrated by immersing into water at fixed temperature for 5 minutes, an air bubble of 5 µl was injected onto the sample surface under water. Ellipse fitting was used for data analysis, and at least 3 measurements were taken for each surface and the results were averaged.

3.5.5 Filtration performance of membranes

3.5.5.1 Thermo- and magneto-responsive Hydraulic permeability

To verify effective thermo-responsive gating function of PNIPAAm NG in membranes, water filtration at 25 ^{o}C and 40 ^{o}C was carried out for NG-PES and MNP-NG-PES membranes, analogous to the protocol described in section 3.4.6.1. Self-constructed dead-end filtration cell with 3.14 cm^2 effective membrane area was used. The trans-membrane pressure was adjusted by gas pressure, and the temperature of feed was controlled by thermostat (Julabo, Germany). Mass

of permeate was measured gravimetrically and flux through of the membrane, J, and membrane permeability, P, were calculated according to **Equation (3.5)** (cf. section 3.4.6.1).

Further, the magneto-responsivity of MNP-NG-PES membrane was tested using the same filtration system as describe above. The filtration cell was placed in the middle plane of the coils to obtain a relatively homogenous magnetic field distribution (H = 20 $\pm$ 10 kA/m, f = 745 kHz). During the filtration, the feed temperature was kept at 25 ^{o}C and the trans-membrane pressure was kept constant at 0.25 bar. A programmed AMF condition, with the magnetic field switched off for 20 minutes and switched on for 30 minutes, was used. To prove the performance reproducibility, three cycles of such program were applied. Water permeate samples were taken every 5 minutes and weighted. Water permeability was calculated according to **Equation (3.5).**

3.5.5.2 Thermo- and magneto-responsive molecular sieving during ultrafiltration

The thermo-responsive molecular sieving performance of NG-PES membrane was analyzed by dextran ultrafiltration at feed temperatures of 25 ^{o}C and 40 ^{o}C in the set-up described in section 3.4.6.1. 1 g/l of aqueous dextran solution, with 50% of dextran 35 kDa and 50% of dextran 2000 kDa, was used as the feed. During the filtration, the pressure was kept constant at 0.5 bar. To minimize fouling effects as result of subsequent experiments, in between each dextran filtration (AMF off and AMF on), the membrane was rinsed three times by water and backwashed at 1.5 bar for 10 minutes. The water and dextran filtrate flux and respective permeability at each stage were monitored by weighting permeate samples and calculating according to **Equation (3.5)**. Overall dextran concentrations in permeate and feed samples were determined by total organic carbon (TOC) analyses, performed with the TOC-Vcpn system (Shimadzu, Japan). Dextran rejection, R, was calculated by **Equation (3.9)** in section 3.4.6.2. Moreover, to further identify the magneto-responsive change of rejection for solutes of specific size, magneto-responsive change of rejection factor is introduced as the ratio of rejection for dextran molecules at off state relative to on state of AMF.

The magneto-responsive molecular sieving performance of MNP-NG-PES membrane was evaluated first by ultrafiltration of a series of 1 g/l solutions of single molecular weight dextrans (4 kDa, 35 kDa, 70 kDa, 100 kDa, 500 kDa, 2000 kDa) as well as a mixture of 50% dextran 35 kDa and 50% dextran 2000 kDa. Because MNP-NG-PES membrane was found to be quite

homogenous, for each dextran ultrafiltration, a new membrane sample was used to avoid the effect of fouling on observed rejection. During the filtration, trans-membrane pressure was fixed at 0.5 bar and temperature of feed was kept at 25 ^{o}C. A frequency of 745 kHz and field amplitude of 20 $\pm$ 10 kA/m was applied when AMF was on. Flux, permeability and overall dextran rejection during filtration were determined as described above. To monitor the fouling on membrane surface, water permeability of membranes before and after each step was also recorded.

Furthermore, compositions and concentrations of feed and permeate samples from ultrafiltration of mixed dextran (35 kDa and 2000 kDa) solutions were also analyzed by high performance gel permeation chromatography (HP-GPC) to verify the shift of MWCO by AMF. Two SUPREMA columns (linear, 10 µm, 8 x 300 mm, calibrated from 100 to 100,000,000 g/mol), the RI-101 differential refractive index detector (Shodex Showa Denko K.K., Tokyo, Japan) and the software Win GPC Unity from PSS (Polymer Standards Service GmbH, Germany) were used to acquire and analyze data. Water with 0.01 M $NaNO_3$ was used as the mobile phase at flow rate of 1 ml/min at 45 ^{o}C. The molecular weight distribution of the dextran mixture (used for this ultrafiltration test as feed) was determined by GPC, as shown in **Figure 3.5**. Rejection for each dextran molecular weight was calculated using **Equation (3.9)** (cf. section 3.4.6.2) by using the data obtained from GPC.

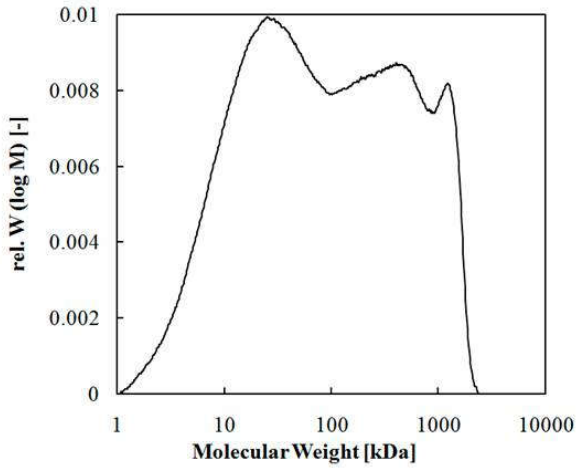

Figure 3.5. Molecular weight distribution of mixed dextran feed used for MWCO determination by ultrafiltration.

3.6 Preparation and characterization of MNP-PVP-PES mixed matrix membrane

To explore the effect of porogen polyvinylprrolidone (PVP) on the performance of mixed matrix membrane, MNP-PVP-PES membrane with 10% of MNP and 1% PVP (mass ratio relative to PES) was prepared. Based on 14.5 wt% of PES in NMP, 10 % of MNP and 1% PVP (mass ratio relative to PES) were also added for the dope solution. The membrane was prepared by NIPS process described in section 3.5.3.

Further, the hydraulic permeability of such membrane was tested by pure water filtration at 25 ^{o}C, analogous to the protocol described in section 3.4.6.1. The membrane permeability was calculated according to **Equation (3.5)** (cf. section 3.4.6.1) and compared with the MNP-PES membrane.

The molecular sieving performance of the membrane at 25 ^{o}C was also evaluated by the filtration of single dextran solutions (4 kDa, 35 kDa, 100 kDa and 2000 kDa) according to the protocol described in section 3.4.6.2. The dextran concentrations in permeate and feed samples were determined by TOC analyses and the rejection was calculated according to **Equation (3.9)** (cf. section 3.4.6.2)

3.7 Preparation and characterization of NG-PES mixed matrix membrane via VIPS process

Comparing with NIPS process, VIPS is a more convenient method to tune the membrane structure, as the membrane solidification in VIPS is slower. Here VIPS was applied to explore alternative structure for mixed matrix membranes.

First, based on different contents of PES (14.5% or 17%) in *N,N*-dimethylacetamide (DMAc), dope solutions blended with different fraction of PNIPAAm NG (10%, 15%, 20%, mass ratio relative to PES in DMAc) were prepared. Then dope solution was casted on a clean glass plate with a stainless steel casting knife using a COATMASTER 510 (Erichsen, Germany). The gap between the glass plate and the knife blade was kept 200 μm and casting speed was kept at 5 mm/s. When the casting was finished, the plate with polymer film was first keeping in the humidity box (cf. **Figure 2.6** in section 2.1.2) with 80% humidity for different durations (2

minutes, 4 minutes or 10 minutes) and then immersed into water (room temperature) to complete the phase separation.

After keeping in water for 24 hours for complete precipitation, the membranes were washed 3 times with water, dried with vacuum oven and ready for characterization. SEM imaging with the ESEM Quanta 400 FEG was used to observe the morphology and the distribution of NG in the membrane matrix analogous to the protocol in section 3.5.4.1.

4. Results and discussion

4.1 Characterization of magnetic field conditions

4.1.1 Influence of input current and frequency

In this work, ferromagnetic MNP (commercial or self-made) with size around 40 nm were chosen as magneto-heater. As they generate heat via relaxation losses and hysteresis loss, which are strongly related to the frequency and field amplitude of AMF, it is very important to explore the AMF field conditions at the beginning.

First, the relation between the input current and field amplitude was investigated by fixing the measuring site in the centre of the sandwich coil and applying different frequency and input current. As shown in **Figure 4.1(a)**, field amplitude is in good linear relationship with input current, while no effect of the field frequency is observed. And high input current will result in high field amplitude. Further, as shown in **Figure 4.1(b)**, when all the data of input current and resulted amplitude were collected and correlated, according to the trend line, a relationship of H = 1.861 * I could be derived, from which, the field amplitude (in A/m) can be estimated by input current (in A).

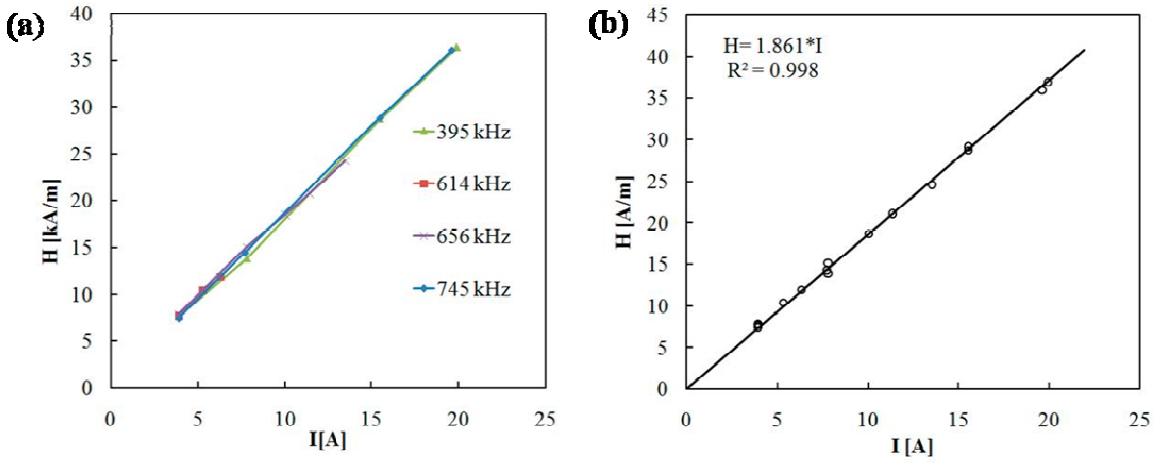

Figure 4.1. (a) Field amplitude in the centre of sandwich coils with different current and frequency input; (b) linear relation between field amplitude and input current.

4.1.2 AMF amplitude distribution at optimized condition

Generally, it has been known that magnetic heating is an increasing function of frequency and field amplitude[175]. In consideration of optimal heating efficiency and the limitation of our generator, an input current of 15.6 A (relatively high input current of the instrument), and a frequency of 745 kHz (the highest frequency of the instrument) were chosen, to maximize input power and enhance magneto-heating effect. Therefore, the amplitude distribution between the coils was measured under this input condition.

When placing the coordinate axes along the radius (r) and height of the coils (h) as shown in **Figure 4.2(a)**, the electromagnetic field distribution between the inductor coils, calculated from the induced peak voltage (**Equation (3.1)**), was as shown in **Figure 4.2(b)**. The field amplitude distribution was not even; it was quite high near to surface (h = $\pm$ 40 mm) and in the centre (r = 0 mm) of the coils and relatively low along the outer circle of the coils (r = $\pm$ 10 mm). Moreover, results of computer simulation were used to describe the amplitude distribution based on the inductor coil geometry (**Figure 4.2(c)**) and it matches well with the experimental results. As is shown, the magnetic field is well confined between the coils and field amplitude is relatively even around the centre of the coils. Therefore, in order to ensure constant field conditions throughout all experiments, the same current and frequency inputs (I = 15.6 A, f = 745 kHz) were always used and the samples (MNP dispersion, hydrogels and membranes) were always placed in the centre of the middle plane (h = 0 mm), where the AMF amplitude was 20 $\pm$ 10 kA/m.

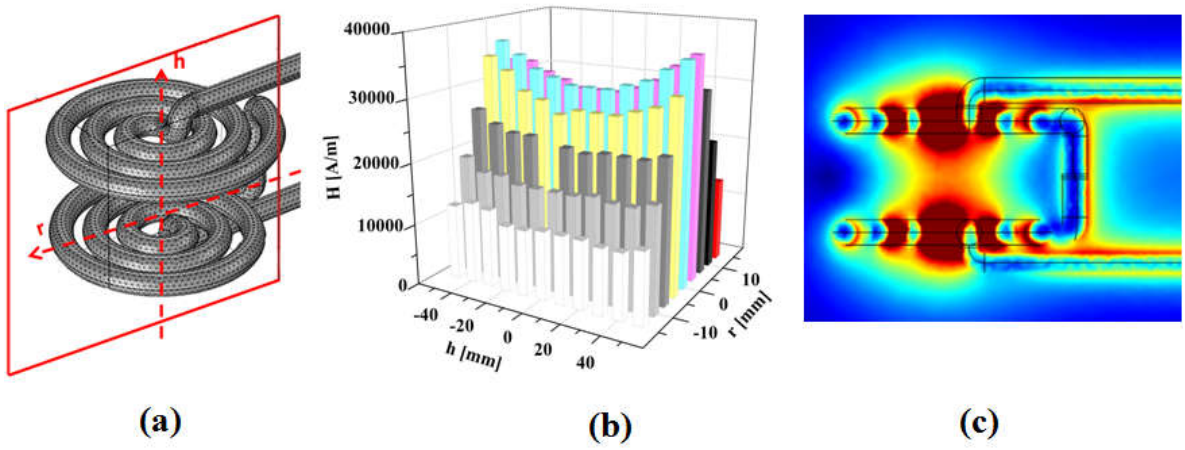

Figure 4.2. Electro-magnetic field amplitude distribution between the two inductor coils; (a) geometry of the inductor coils and placing of coordinates; (b) measured field amplitude distribution with current input of 15.6 A and frequency of 745 kHz; (c)[i] computer simulation of field amplitude distribution (highest intensities red, lowest blue; no scale used because simulation were done with other current and frequency input parameters than in experiments).

4.2 Magneto-hydrogel pore-filled membrane

4.2.1 Characterization of commercial MNP

Here MNP are employed as localized heater in hydrogel network. The heat dissipation of MNP comes from the magnetic losses during different processes of magnetization reversal, therefore, it not only depends on the amplitude and frequency of AMF, but also in strong relation with particle properties, like materials, shape, crystallinity, average size and size distribution[177]. Many research papers report on magneto-responsive composite hydrogels with small superparamagnetic MNP[46, 86, 87], because it is facile to use hydrophilic MNP obtained by co-precipitation or to prepare the nanoparticles *in situ* in the hydrogel network by precursor reduction[46]. However, it has been proved that, in principle bigger MNP have better heating efficiency[184]. Here, commercially available MNP with size of 40 nm and good water dispersibility were chosen. Besides better heat generation, the relatively big size was also

[i] The computer simulation has been kindly provided by Prof. Daniel Erni's group at Department of Electrical Engineering, UDE.

expected to prevent the leaching out from the hydrogel network during filtration, because mesh size of such gel is typically less than 20 nm[46, 133, 189, 190].

4.2.1.1 Morphology and size distribution of MNP

The commercial MNP from Ocean NanoTech had been functionalized with amphiphilic polymer. With the surface covered with carboxylic acid groups, they are quite stable in aqueous solution.

First, their morphology was investigated by SEM. As shown in **Figure 4.3(a)**, the MNP have very good spherical morphology and an average diameter around 38 nm. Moreover, its weigh-average diameter is around 35 nm according to analytical disc centrifugation (ADC) (**Figure 4.3(b)**), and hydrodynamic diameter is around 40 nm according to dynamic light scattering (DLS) (**Figure 4.3(c)**).

ADC measures the sedimentation time of the particles in the fluid medium with known density and viscosity, and estimates the diameter (the equivalent spherical diameter) according to stokes law[191, 192]. For the calculation, the density of the nanoscopic material is needed. For a polymer coated nanoparticle (such as the commercial MNP), which has mixed density difficult to estimate, by taking density of the inorganic material of the hard sphere, the calculated diameter will be smaller than its actual geometric diameter[192]. This should explain why the diameter of MNP estimated by ADC is smaller than the diameter observed by SEM.

DLS technique is based on the Rayleigh scattering of the suspended nanoparticles, which undergo Brownian motion. First, diffusion speed of particles is estimated by illuminating the sample with a laser source, and then according to Stokes–Einstein equation, hydrodynamic radius, which includes the polymer coating and hydration layer outside the particle, is calculated. Therefore, the particle estimated by DLS is normally larger than by other methods[191, 192].

The narrow distribution of particle size was also proved by both methods. All those data correlates well with the supplier's data (cf. **Table 3.2**).

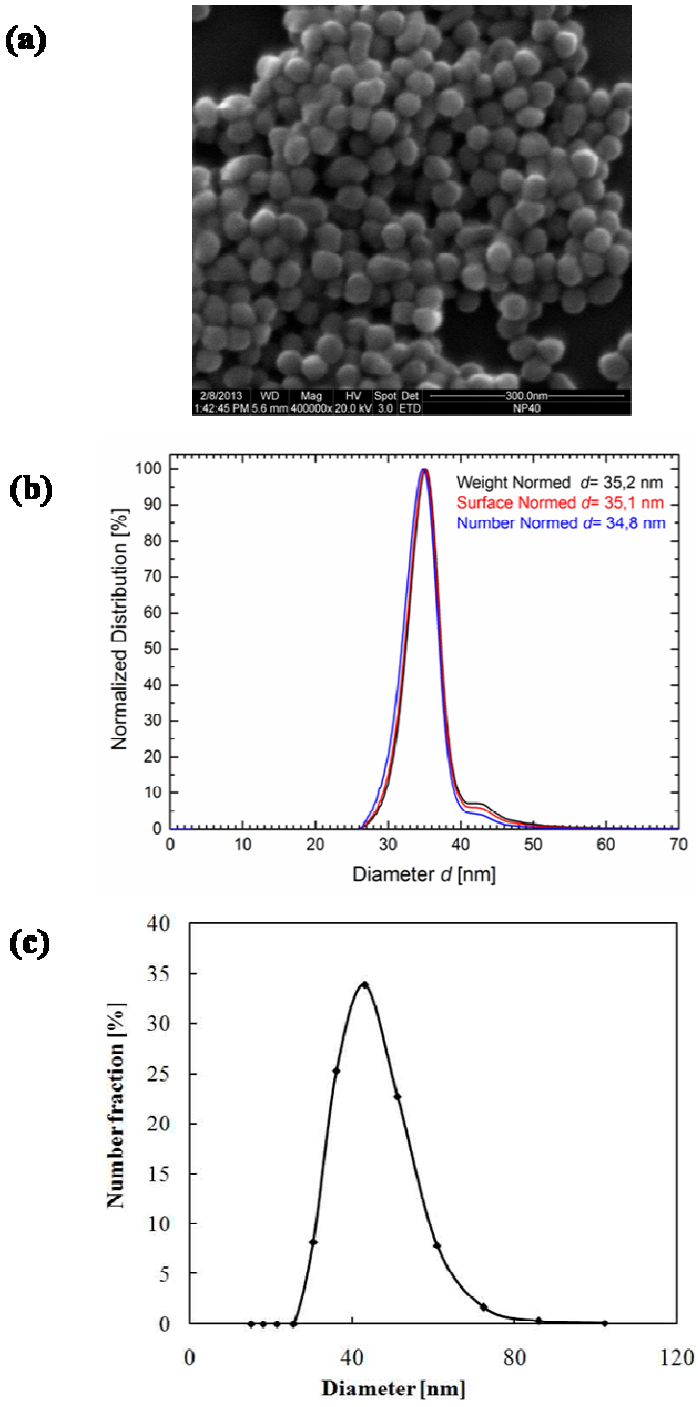

Figure 4.3. (a) SEM image, (b)[ii] size distribution by analytical disc centrifugation, and (c) size distribution by DLS for commercial MNP.

[ii] The Analytical Disc Centrifugation measurement was kindly conducted and data provided by Dr. Jakub Cichoszewski from Prof. Stephan Barcikowski's group at Department of Technical Chemistry I, UDE.

4.2.1.2 Zeta potential

The surface charge of the commercial iron oxide nanoparticle has been investigated by zeta-potential measurement. As shown in **Figure 4.4**, because the surface of the MNP has been functionalized with carboxylic acid groups, it has an isoelectric point (IEP) around pH 2.2 and its zeta potential is below -25 mV when the pH is above 4. The sufficient surface charge of such MNP ensures its dispersion stability within a wide range of pH values in aqueous solution.

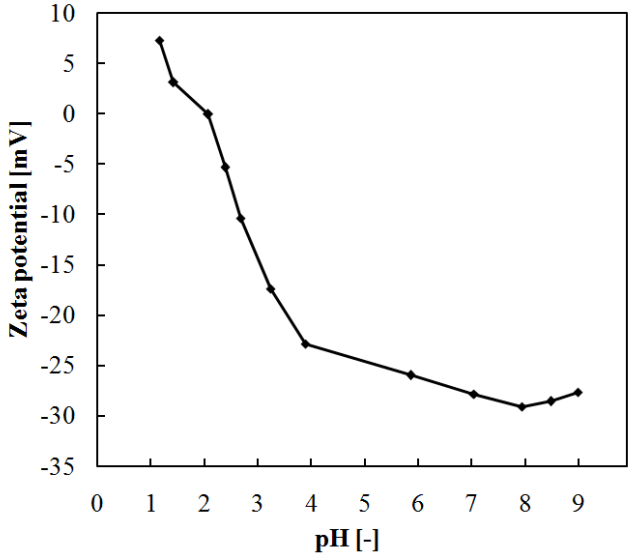

Figure 4.4. Zeta potential of commercial MNP as function of pH value[iii].

4.2.1.3 Heating efficiency

When MNP are exposed to AMF, heat will be dissipated during to the magnetic losses during the reversal magnetization process of the particles[175]. Here the heating efficiency of commercial MNP was investigated by calorimetric method. The temperature changes for 1 ml of water and 0.05 mg/ml MNP dispersion after 5 minutes of AMF exposure are shown in **Table 4.1**. The SLP calculated using **Equation (2.6)** is 672 W/g and it correlates well with the reported SLP of iron oxide nanoparticles with similar size and under similar field conditions (magnetosome: diameter

[iii] The zeta potential measurement was kindly conducted and data provided by Dr. Jakub Cichoszewski from Prof. Stephan Barcikowski's group at Department of Technical Chemistry I, UDE.

30-40 nm, f = 410 kHz, H = 10 kA/m, SLP = 960 W/g)[184], indicating the relatively good heating efficiency of the particles and AMF conditions used in this study.

Table 4.1. Temperature changes of the commercial MNP sample upon AMF excitation (I = 15.6 A, f = 745 kHz, H ~ 20 kAm^{-1})

Sample	Time [minutes]	Temperature change [^{o}C]
Water	5	2 ± 0.4
MNP dispersion	5	4.4 ± 0.7

4.2.2 Bulk magneto-hydrogel

4.2.2.1 Dispersibility of MNP in monomer solution

Before the preparation of magneto-hydrogel, stability of MNP in monomer solution has been studied with DLS measurement. As shown in **Figure 4.5**, for aqueous solution with different concentration of MNP, the diameter of MNP stayed around 40 nm and there is no apparent aggregation within 5 hours, indicating the excellent stability of MNP in monomer solution.

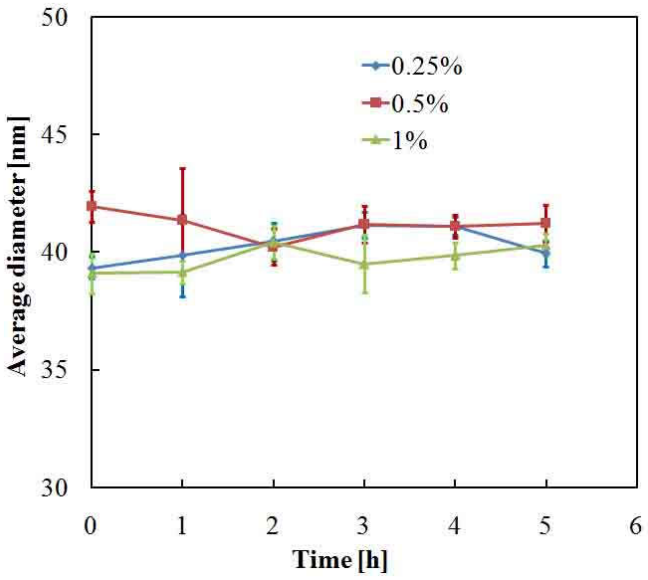

Figure 4.5. Dispersibility and dispersion stability of MNP in monomer solution analyzed by DLS.

4.2.2.2 Influence of MNP on gelation kinetics

As introduction of nanofillers influences gelation, structure and mechanical properties of the resulting hydrogel network[186, 193, 194], rheological studies were first carried out to investigate the influence of MNP on gelation kinetics of the hydrogel and to choose a suitable initiation method for pore-filling procedure. Then, mechanical property of resulted hydrogel was also investigated.

UV-initiated gelation was investigated first, as previous study had shown that UV polymerization is a better option for *in situ* preparation of tailored functional hydrogels and fabrication of hydrogel pore-filled membranes[39, 133]. However, the results for MNP composite hydrogels were not as ideal as expected. As shown in **Figure 4.6(a)**, similar to the results of previous investigations, gelation during UV polymerization of monomer mixture without particles started soon (within 50 seconds) and was complete early (within 400 seconds). However, with the increase of MNP concentration, the gelation was systematically delayed and the storage modulus of the resulting hydrogel systematically decreased (by 20% when comparing 0% and 1% MNP fraction). This may be because the MNP can block the penetration of UV light, which is responsible for the generation of radicals; this results in reduced extent of polymerization. When comparing the hydrogel thickness in rheological study (the gap distance, 101 μm) and in pore-filled membrane (membrane thickness, 23 μm), the blocking effect for UV should be small. However, to avoid any influence from this and obtain a well-defined magneto-hydrogel, UV initiation was ruled out for pore-filling functionalization and was not further studied here.

Redox polymerization was evaluated as another option. As shown in **Figure 4.6(b)**, redox polymerization took longer than UV-initiated polymerization to lead to gelation (300-500 seconds) and to reach full conversion (more than 2000 seconds). However, there was no apparent influence of the MNP concentration on the course of polymerization and the mechanical properties of the resulting hydrogels. MNP-PNIPAAm composite hydrogels had similar storage modulus as the pure PNIPAAm hydrogel and variations of storage modulus after full conversion were less than 5% around the average value for all data. This indicates that redox polymerization is applicable to synthesize magneto-hydrogels at full conversion for the entire range of MNP loading. In addition, because it takes 300-500 seconds for gelation to start, pore-filling modification via redox polymerization should be applicable, as there would be enough time for

all the chemicals, including the accelerator TEMED, to reach equilibrium in the membrane pores. Therefore, further investigations of the microstructure were carried out with hydrogels obtained after redox-initiation.

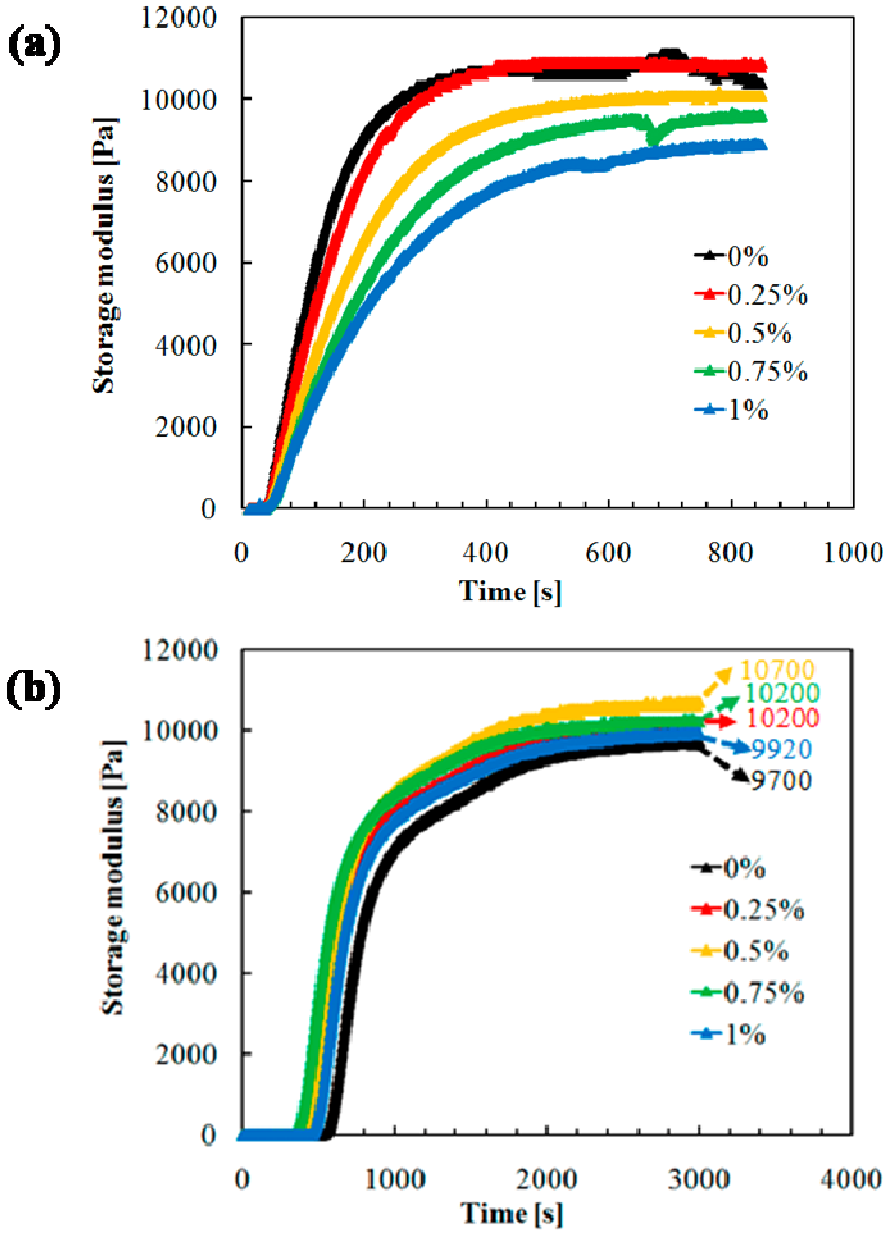

Figure 4.6. Gelation kinetics study by *in situ* rheology. (a) UV-initiated polymerization; (b) redox polymerization; both with different MNP concentrations in the reaction mixture comprising NIPAAm and MBA in water.

4.2.2.3 Mesh size estimation

The rheological properties of representative hydrogels with MNP concentrations of 0 %, 0.25 % and 1 %, obtained after *in situ* redox polymerization were further studied by frequency sweeping and the result is shown in **Figure 4.7**. The storage modulus of the hydrogels was independent of the angular frequency, indicating almost perfect gelation of the hydrogel. The mesh size which represents the microstructure of such "perfect gel" can be estimated by using theory of rubber elasticity (**Equation (3.3)**)[133, 195], and the result is shown in **Table 4.2.** Despite different concentrations of the MNP, the mesh size of all hydrogels was around 7 nm, which is well within the ultrafiltration range. It should be noted that the data have been measured for the hydrogels in state after synthesis, i.e. not in equilibrium swelling state (with excess of water). When magneto-hydrogels with the same composition and structure are *in situ* formed and immobilized in the pores of the PET track-etched membrane, they are also expected be restricted in their swelling and thus to have similar mesh size; hence they should be able to serve as ultrafiltration medium.

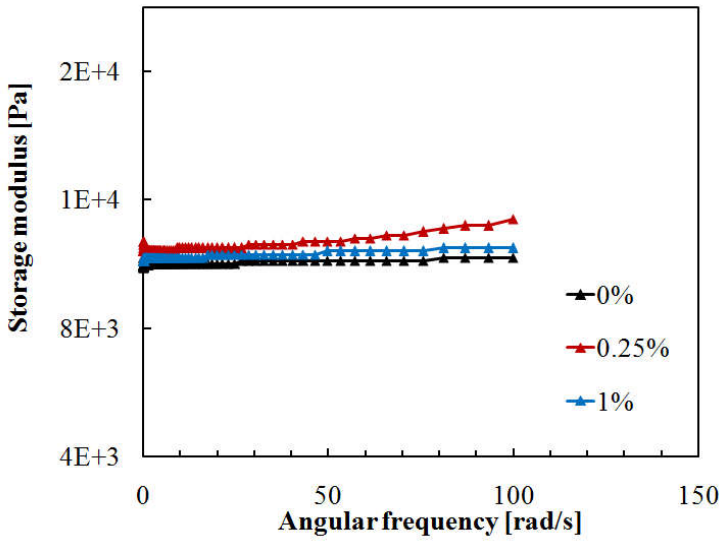

Figure 4.7. Storage modulus at 21 °C as a function of shear frequency for hydrogels prepared with different MNP concentration.

Table 4.2. Storage modulus and calculated mesh size of MNP-PNIPAAm composite hydrogels with different MMP concentration

MNP concentration [%]	Storage Modulus [Pa]	Mesh size [nm]
0	10000 ± 500	7.3
0.25	10200 ± 500	7.2
1.0	10500 ± 500	7.2

Moreover, there is possibility to tune the mesh size by adjusting the composition of the monomer solution, as shown from the investigation for the microstructure of pure PNIPAAm hydrogels, conducted by Adrus et al.[196]. In their research, rheological study for PNIPAAm hydrogels with varied compositions was carried out, and relevant mesh sizes were estimated according to theory of rubber elasticity (**Equation (3.3)**). As shown in **Figure 4.8**, by varying the monomer content or crosslinker fraction, the storage modulus of PNIPAAm hydrogel can be adjusted. Increase of storage modulus was observed either by the increase of monomer (NIPAAm) content (7.5 to 15 wt%) or by the increase of crosslinker (MBA) fraction (2 to 10 wt% relative to NIPAAm). For the mesh size, as shown in **Table 4.3**, values in the range of 4 to 10 nm were obtained by varying the composition. When comparing the MNP-PNIPAAm composite hydrogels prepared in this work (NIPAAm: 1 mol/l, MBA: 0.02 mol/l, MNP: varied) (cf. **Table 4.2**), with those PNIPAAm hydrogels (cf. **Table 4.3**), they have most similar monomer and crosslinker content with M10DC05 ((NIPAAm: 0.88 mol/l, MBA: 0.032 mol/l). The data shows their mesh size is also similar, in the range of 7-8 nm. Therefore, the blending of MNP perhaps won't affect the network of hydrogel so much. At last, in the future, maybe the mesh of composite hydrogel can also be further tuned by adjusting monomer content and crosslinker fraction.

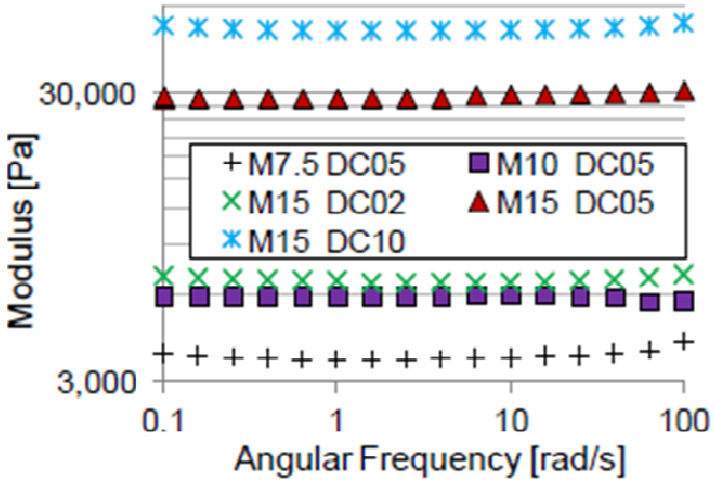

Figure 4.8. Storage modulus at 20 °C as a function of shear frequency for hydrogels prepared with different compositions (NIPAAm: 10 and 15 wt% → M10, M15; MBA: 2, 5 and 10 wt% relative to NIPAAm → DC02, DC05 and DC10)[196]

Table 4.3. Calculated mesh size of PNIPAAm hydrogels with various compositions (via UV-initiated polymerization, with 15 minutes of irradiation)[196]

Hydrogels	Mesh size [nm]
M7.5DC05	10.3
M10DC05	8.8
M15DC02	8.5
M15DC05	5.2
M15DC10	4.3

4.2.2.4 Heating effect for magneto-hydrogel

The heating effect of magneto-hydrogel under the used electromagnetic field conditions was evaluated by placing the samples (PNIPAAm hydrogel with 1 wt% MNP and without

nanoparticles) in the middle plane of the inductor coil arrangement for 1 minute. As shown in the thermal image in **Figure 4.9**, compared with the environment temperature of 24 °C, the magneto-hydrogel had a temperature increase of 7 °C, while the temperature of blank hydrogel increased only by 2 °C, because of unspecific heat of the instrument. Therefore, the field condition is suitable for effective heating for the magneto-hydrogel.

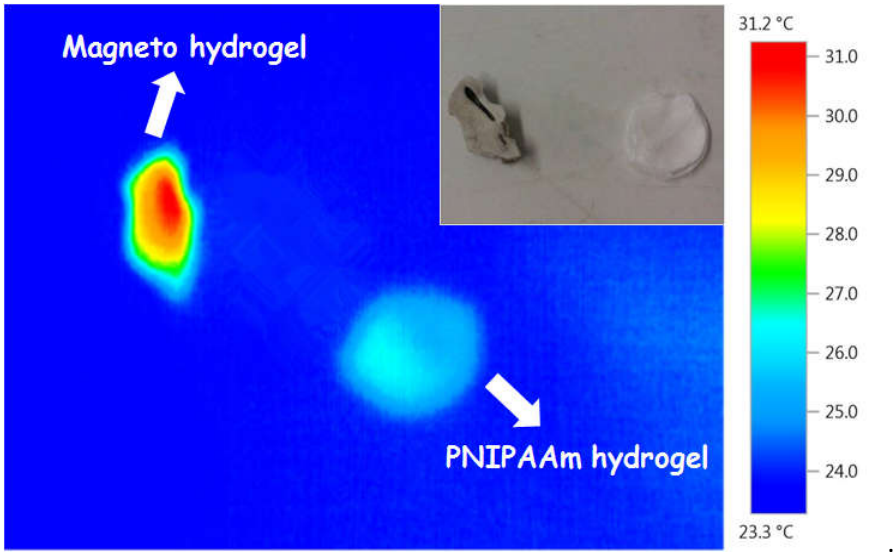

Figure 4.9. Thermal images of magneto-hydrogel and reference material without MNP after 1 minute of AMF exposure (I = 15.6 A, f = 745 kHz, H ~ 20 kAm^{-1}).

4.2.3 PET base membrane

Here PET track-etched membranes with nominal pore diameters 1000 nm was employed as support materials. According to the previous study of PNIPAAm hydrogel pore-filled membrane, base membrane with such size range are most suitable to provide good fixation and confinement for hydrogel[39]. To ensure the accuracy of basic information of the membrane, it was fully characterized before use.

4.2.3.1 Morphology of base membrane

As shown in **Figure 4.10**, the PET track-etched membrane has straight circular pores with narrow size distribution. Despite the relatively low porosity, overlapping of pores still happens sometimes. Overall, such membrane is a good basis for pore-filling functionalization.

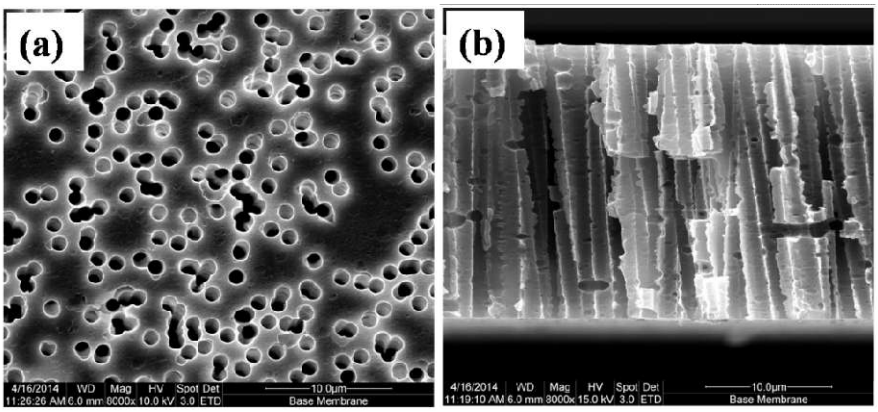

Figure 4.10. SEM images of base membrane: (a) top surface and (b) cross-section

4.2.3.2 Water permeability

The water permeability of base membrane at 25 ^{o}C and 45 ^{o}C was determined under hydrostatic pressure of 0.015 bar, as shown in **Table 4.4**. This permeability data would be used to estimate membrane porosity, as well as compare with the permeability of pre-functionalized and pore-filled membranes at different temperatures.

Table 4.4 Mean barrier pore size and water permeability of PET base membrane at 25 ^{o}C and 45 ^{o}C

Pore size [nm]	Permeability at 25 ^{o}C [$l.h^{-1}.m^{-2}.bar^{-1}$]	Permeability at 45 ^{o}C [$l.h^{-1}.m^{-2}.bar^{-1}$]
1582 $\pm$ 50	183000 $\pm$ 11000	234000 $\pm$ 12000

4.2.3.3 Pore size distribution and pore density

The pore size and pore size distribution of PET track-etched membrane was evaluated by gas flow/pore dewetting permporometry. As shown in **Figure 4.11**, the unmodified PET membrane demonstrated a narrow size distribution with a peak around 1600 nm. According to calculation of the software, the average pore size of the base membrane is 1582 nm (cf. **Table 4.4**), which is significantly higher than the nominal pore size from the manufacturer. This might be caused by

the manufacturing process, as over-etching may happen and lead to larger pores than intended, which has also been observed in other studies[29, 67].

Moreover, by water permeability data of base membrane at 25 °C and its average pore diameter obtained by gas flow/pore dewetting permporometry, the porosity of such membrane can be calculated via Hagen-Poiseuille equation (**Equation (3.6)**) and is 13.4%. Further, the pore density of the membrane can be calculated and is 6.8 x 10^6 cm^{-2}, which is around 3 times lower than the nominal pore density (22 x 10^6 cm^{-2}) provided by the company (cf. **Table 3.1**).

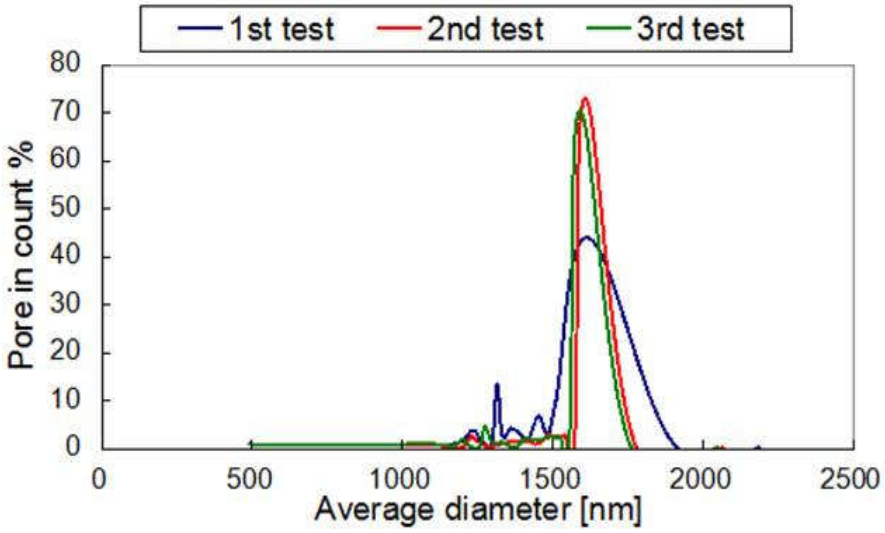

Figure 4.11 Pore size distribution of base membrane by gas flow/pore dewetting permporometry

4.2.4 Membrane pre-modification

For pre-modification, the polymer chains "grafted from" the surface of pore wall are expected to provide sufficient anchoring effect for the pore-filled hydrogel, while not influencing the membrane structure too much and keep the pore geometry preserved for better pore-filling effect[39]. Moreover, as MNP loading is integrated in pore-filling procedure in this work, the prefunctionalized membrane should also have suitable geometry (minimal geometric hindrance) and surface charge (minimal electrostatic repulsion) for MNP loading. Therefore, polymer chains with optimal length and charge are required. To achieve this goal, as shown **Figure 4.12**, two

methods which provide membrane surface with suitable polymer chain with different charges are employed (cf. section 3.4.3).

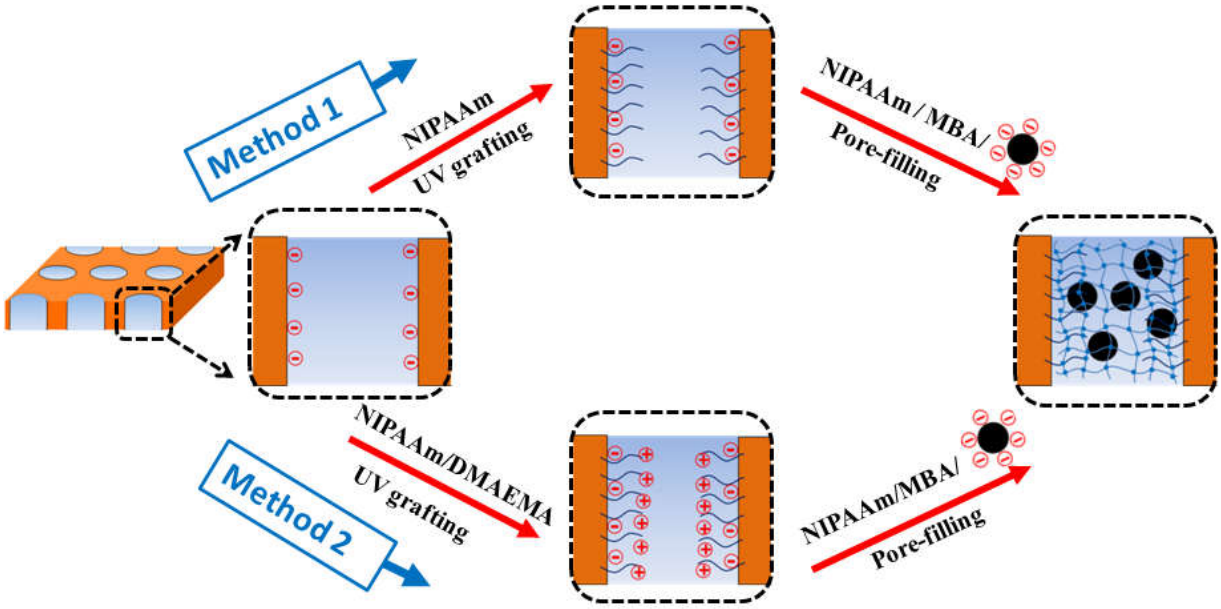

Figure 4.12. Schematic illustration for fabrication of magneto-responsive hydrogel pore-filled membranes. At first step, two kinds of pre-modification methods was carried out for the grafting linear polymer chains: "method1" was to graft charge-neutral PNIPAAm chains, and "method 2" was to graft positively charged P(NIPAAm-co-DMAEMA) chains (cf. section 3.4.3). After grafting linear polymer chains as anchors for hydrogel fixation, hydrogel network was prepared in second step via *in situ* cross-linking polymerization (cf. section 3.4.4).

For "method 1", 0.2 mol/l of monomer NIPAAm was chosen to obtain charge-neutral polymer chains with moderate length, according to previous study[67]. For "method 2", to render the surface optimal positive charge while keep the polymer chain length comparable with "method 1"; on the basis of 0.2 mol/l of NIPAM, different concentrations of comonomer DMAEMA (0.01, 0.025 and 0.05 mol/l) were added and the water permeability of pre-modified membranes measured and compared. As shown in **Figure 4.13**, with increase of DMAEMA fraction, the water permeability of membranes decreased significantly. This could be related to a higher degree of grafting because of higher total monomer concentration used, better incorporation of DMAEMA compared to NIPAAm on the carboxyl-functional PET surface, and also because the increasing fraction of tertiary amino groups in the chains which will be protonated in pure water

(pH ~ 6) will cause reduction in effective pore diameter due to expansion of grafted polymer chains. Therefore, 0.01 mol/l of DMEAMA was chosen as the optimal concentration to reach similar water permeability as for membranes obtained from "method 1" and to provide moderate surface charge.

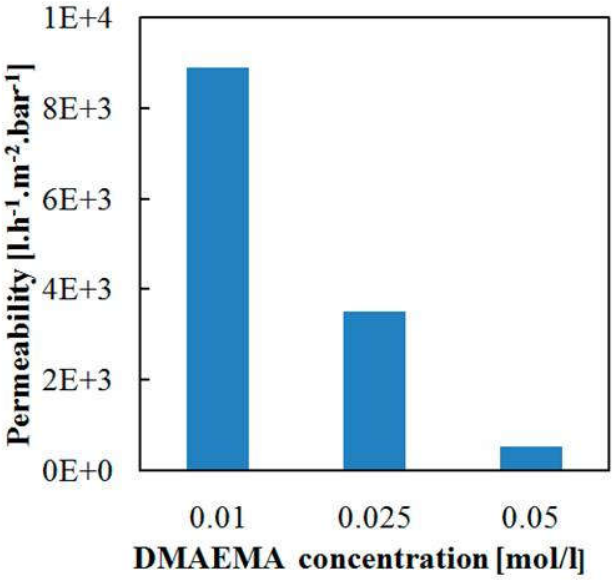

Figure 4.13. Influence of DMEAEMA concentration in the reaction mixture with 0.2 mol/l NIPAAm on water permeability of pre-modified membrane obtained by "method 2".

Further, thermo-responsive water permeability and zeta-potential of membrane modified by two methods (0.01 mol/l DMAEMA for "method 2") were tested and compared. As shown in **Figure 4.14**, the much lower water permeability of both modified membranes proved the successful grafting of polymer chains onto the track-etched pore walls was achieved by both methods. Further, the much higher water permeability at 45 ^{o}C than at 25 ^{o}C and the corresponding high gating factors of pre-modified membranes indicated excellent thermo-responsive permeability which was attributed to the grafted PNIPAAm. Very similar permeabilities have been obtained for "method 1" and "method 2", indicating similar degree of grafting for the homo- and the copolymer. According to Hagen-Poiseuille law (**Equation (3.6)**), effective hydrodynamic layer thickness of grafted polymers was calculated from the water flux data and found to be within the range of 400 to 600 nm. This is smaller than the pore radius of ~790 nm. Because photo-initiated

free radical polymerization was used, a gradient in polymer segment density from the pore wall to the interior can be expected, but the relatively large thickness should provide robust anchoring of the cross-linked hydrogel from the same polymer, *in situ* formed during the pore-filling step.

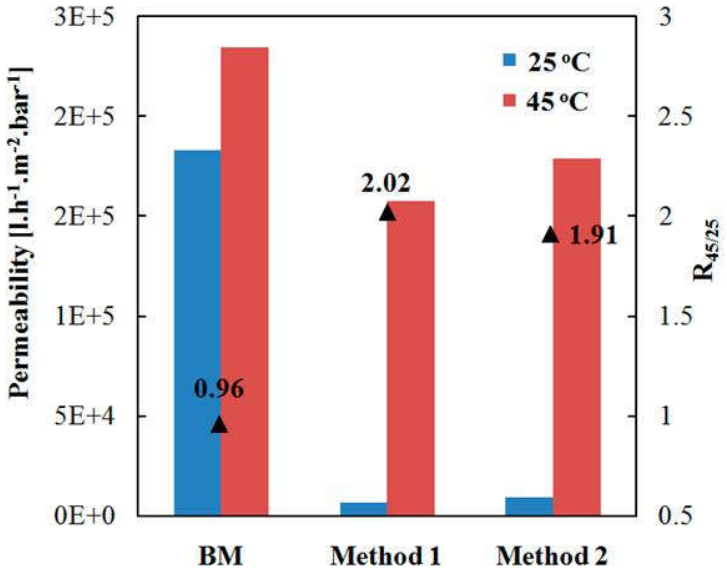

Figure 4.14. Thermo-responsivity of water permeability of pre-modified PET track-etched membranes obtained by "methods 1" and "method 2".

The zeta potential of base membrane and two kinds of pre-modified membranes is shown in **Figure 4.15**. First, the PET base membrane was negatively charged as expected because of the carboxylic acid groups generated by the alkaline hydrolysis step during the track-etching process in the PET. Surface of pre-modified membrane from "method 1" was less negative compared with the base membrane, which can be attributed to screening of PET surface charge by the neutral PNIPAAm hydrogel layer. The membrane functionalized by "method 2" showed much more positive zeta potential in the analyzed pH range, indicating the successful incorporation of PDMAEMA segments into the grafted PNIPAAm chains. Hence, the result proves that 0.01 mol/l of DMAEMA is sufficient to render moderate positive charge density while obtaining comparable layer thickness as the "method 1".

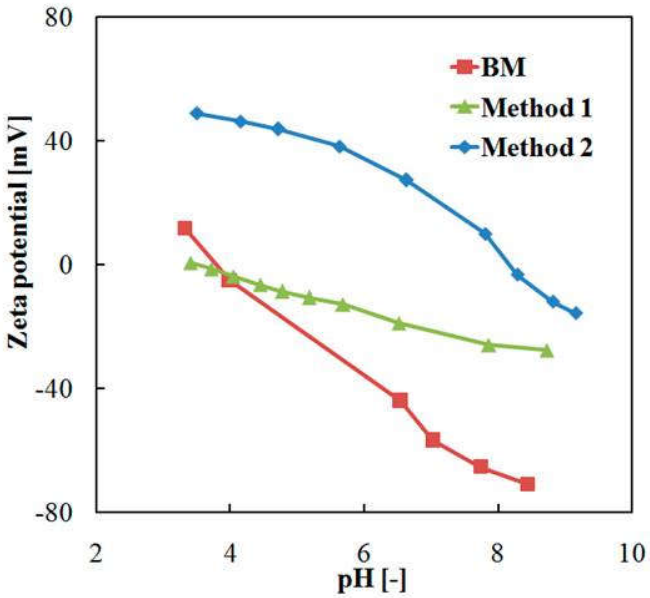

(b)

Figure 4.15. Zeta potential of pre-modified PET track-etched membranes obtained by "method 1" and "method 2".

4.2.5 Pore-filling functionalization

The pore-filling functionalization not only involves the formation of semi-interpenetrating hydrogel network within the membrane pores, but also the loading of MNP into the pore-filled hydrogel. To obtain a membrane with excellent magneto-responsivity and sieving effect, several factors should be taken care for: (1) the hydrogel should be well cross-linked and homogenously filled in most of the pores; (2) the pore-filled hydrogel should have good swelling/deswelling effect in response to temperature; (3) the loading of MNP should be sufficient to cause enough magneto-heating effect for actuation. Therefore, the MNP loading, as well as thermo- and magneto- responsive water permeability were characterized for hydrogel pore-filled membranes.

4.2.5.1 Morphology and MNP loading

Several factors would influence the MNP loading: the pore size of the functionalized membranes, the electrostatic interactions between membrane surface and the MNP, and the mutual electrostatic repulsion between the negatively charged MNP. To enhance the loading of the MNP,

pre-modifications with moderate chain lengths and with either neutral ("method 1") or positive charges ("method 2") were adopted (cf. section 4.2.4), a step-wise loading procedure for MNP with long loading times was used, and small amounts of NaCl were also added to reduce the mutual repulsion between the MNP.

The effect of NaCl concentration on the MNP loading was investigated. As shown in **Figure 4.16**, when different concentrations (final concentration were 0, 35 and 50 mmol/l, added on three steps, cf. section 3.4.4) were applied, for membranes pre-modified by both methods, the MNP loading with 50 mmol/l of NaCl was the highest, indicated by the darkest colours in optical pictures.

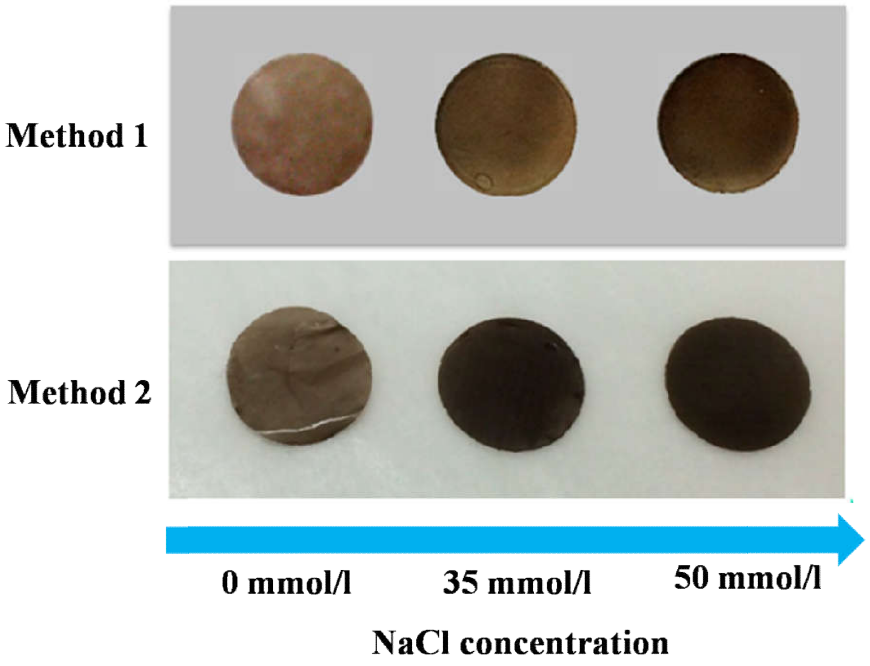

Figure 4.16. Influence of NaCl concentration on MNP loading. The MNP adding and NaCl addition was performed on three steps with final content of MNP 1.5 wt% (ratio relative to monomer) and different NaCl concentrations (0, 35 and 50 mmol/l).

As shown in **Figure 4.17**, this optimized loading procedure, greatly enhanced MNP loading for membranes modified via both routes, comparing with first experiments where the loading was done in one step and without addition of NaCl.

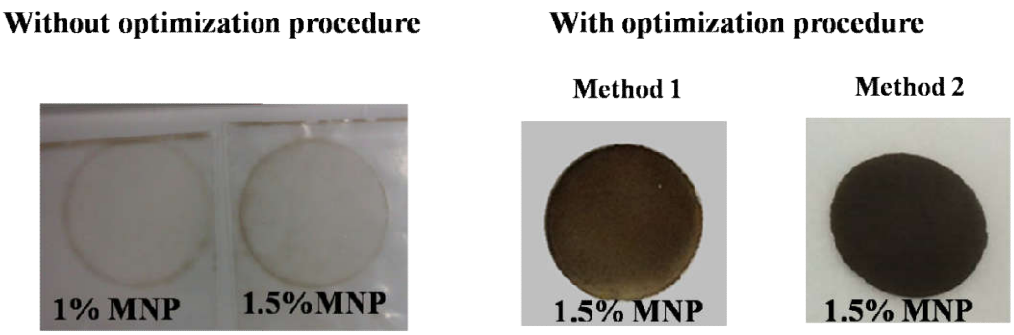

Figure 4.17. Influence of the procedure on obtained MNP loading; left: membranes pre-functionalized according to "method 1", loading in one step and without addition of NaCl; right: membranes pre-functionalized according to "method 1" or "method 2", loading on three steps and with addition of NaCl.

Further, the pore-filled membranes obtained from optimized procedure were characterized by SEM and EDX, and the result is shown in **Figure 4.18**. The images reveal that the outer and inner surface of the membrane is tightly covered with particles and that the hydrogel is rather hard to distinguish from the other features. It must be noted that the samples were analyzed in dry state where the hydrogel was collapsed; consequently, the visualization of PNIPAAm in SEM was also complicated as in previous work[39]. To semi-quantify the MNP loading for the two methods, EDX was also carried out for the obtained membranes. Result reveals there is high loading of MNP inside the pores and on the surface for membranes made from both methods. For "method 1", the MNP loading on the surface estimated is 6 times higher than inside the pores, and for "method 2", loading of MNP inside the pore is significantly higher than for "method 1" which can be attributed to the positively charged groups provided by grafted poly(NIPAAm-*co*-DMAEMA). That the loading with MNP inside the pores was smaller than on the outer membrane surface could be due to sterical hindrance between particles and pores which are partially filled with grafted PNIPAAm (cf. **Figure 4.14**). However, as shown in **Figure 4.19**, it is also possible that a µm-thin hydrogel layer formed on the two outer surfaces of the membrane is contributing to that effect. This has been observed before[39], and it can be explained by the preparation procedure where the membrane which is filled with reaction mixture is then tightly sandwiched between two glass plates; the laminar film between membrane surface and glass will also be cross-linked to form a (composite) hydrogel.

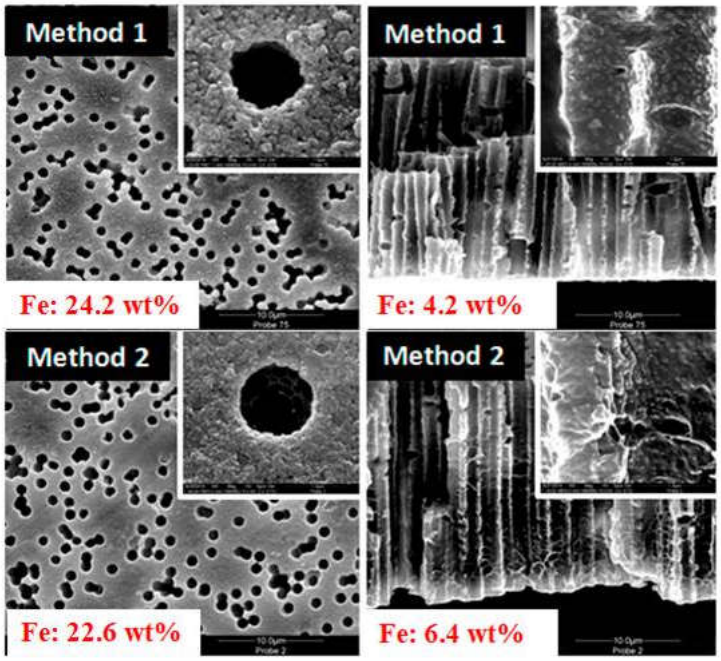

Figure 4.18. Visualization by SEM and quantification by EDX of MNP loading for hydrogel pore-filled membranes obtained by the two different methods.

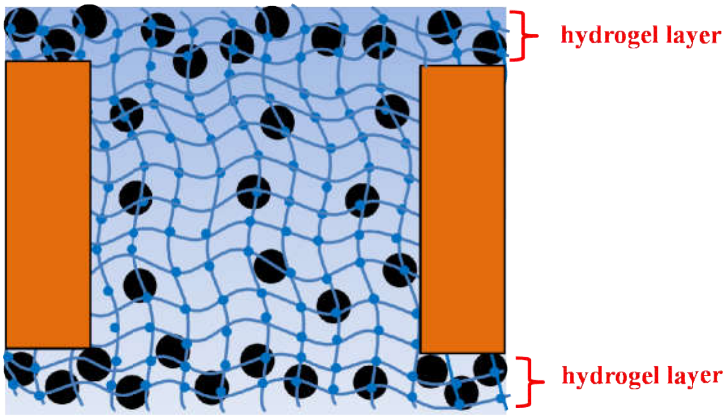

Figure 4.19. Schematic illustration of the µm-thin composite hydrogel layers that could be formed on the outer surfaces of the membrane during pore-filling functionalization.

Moreover, to further quantify the loading of MNP, TGA measurement was carried out for base PET membrane, PNIPAAm hydrogel pore-filled membrane and magneto-hydrogel pore-filled membrane (prepared via "method 1). As shown in **Figure 4.20**, after the decomposition at 900 ^{o}C, there is around 1 % residue for PET base membrane and pure PNIPAAm membrane, and 5.77% residue for the magneto-hydrogel pore-filled membrane which loaded with MNP. Therefore, by eliminating the residue from the base membrane and hydrogel, there was 4.77 % iron oxide nanoparticle left in magneto-hydrogel pore-filled membrane. When oxidation of Fe_3O_4 nanoparticles at high temperature in air atmosphere is considered, the residue should be Fe_2O_3 nanoparticles. By taking the content of iron constant, the mass of Fe_3O_4 can be calculated from the mass of Fe_2O_3, as shown in **Equation 4.1**:

$$2Fe_3O_4 + \frac{1}{2}O_2 \rightarrow 3Fe_2O_3$$

$$m_{Fe_3O_4} = 0.97 m_{Fe_2O_3} \quad (4.1)$$

Where $m_{Fe_3O_4}$ is the mass of Fe_3O_4 and $m_{Fe_2O_3}$ is the mass of Fe_2O_3.

Therefore, the estimated loading of MNP (Fe_3O_4 nanoparticles) in membrane should be around 4.63%.

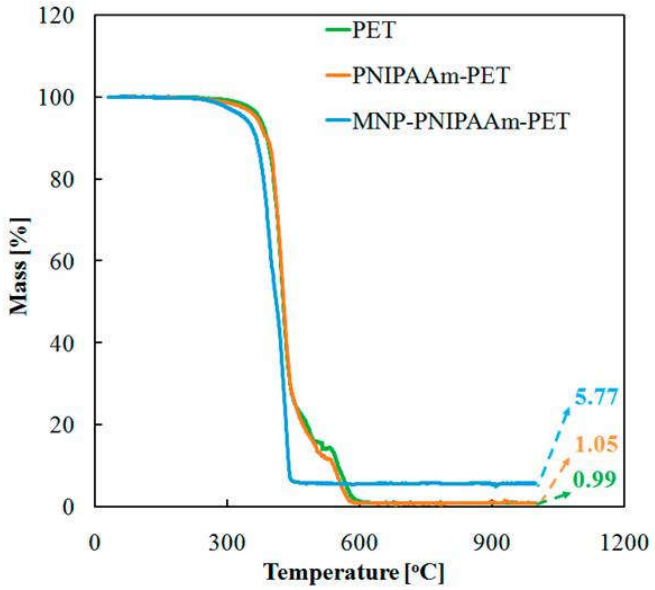

Figure 4.20. TGA curves for membranes with different composition.

4.2.5.2 Thermo- and magneto-responsive water permeability

Thermo-responsive water permeability of pore-filled membranes was evaluated by water filtration at different temperatures (25 ^{o}C and 45 ^{o}C). In the previous work by Adrus and Ulbricht[39], for PET track-etched membrane with pore size of about 1600 nm and using 1.3 mol/l of NIPAM and 0.05 mol/l of MBA in reaction solution, water permeability of pore-filled membranes was around 100 $l.h^{-1}.m^{-2}.bar^{-1}$. Here relatively lower concentration of monomer NIPAAm (1 mol/l) and cross-linker MBA (0.02 mol/l) were used, and the water permeabilities of various individual membranes were ranging from 50 to 1000 $l.h^{-1}.m^{-2}.bar^{-1}$. The broad range of water permeability and the partially higher absolute values indicated relatively poor homogeneity of the hydrogel network (or the pore-filling) and/or a rather loose network structure. This perhaps was caused by the relatively low concentration of monomer and cross-linker, but an effect of the relatively large MNP (diameter 40 nm) on the network structure also cannot be excluded.

Despite the relatively poor reproducibility of water permeability, all membranes showed clearly significant temperature responsivity (thermo-responsivity factor $N_{45/25}$ in the range 3 to 25; for unmodified membrane R or N factors are ~1). It was also noticed that the thermo-responsivity factor was in a broad range, but correlated well with water permeability: membranes with high water permeability had low thermo-responsivity factor and membranes with low permeability had high thermo-responsivity. This indicates clearly that pore-filled membranes with high permeability had looser hydrogel network or uneven pore-filling leading to poor barrier properties even at 25 ^{o}C, so that the change upon increase of temperature was relatively small. Overall, no difference with respect to achievable membrane quality could be seen when comparing preparations according to “method 1” and “method 2”.

The water permeability and thermo-responsivity factor of two specific membranes from both preparation methods is shown in **Figure 4.21**. Both membranes demonstrated relatively high thermo-responsivity, indicating good function of PNIPAAm network. The membrane from “method 2” had a lower water permeability and higher thermo-responsivity factor than the one from “method 1” only because a representative membrane with *excellent* thermo-responsivity was chosen here while the membrane from “method 1” represents a membrane with *good* thermo-responsivity.

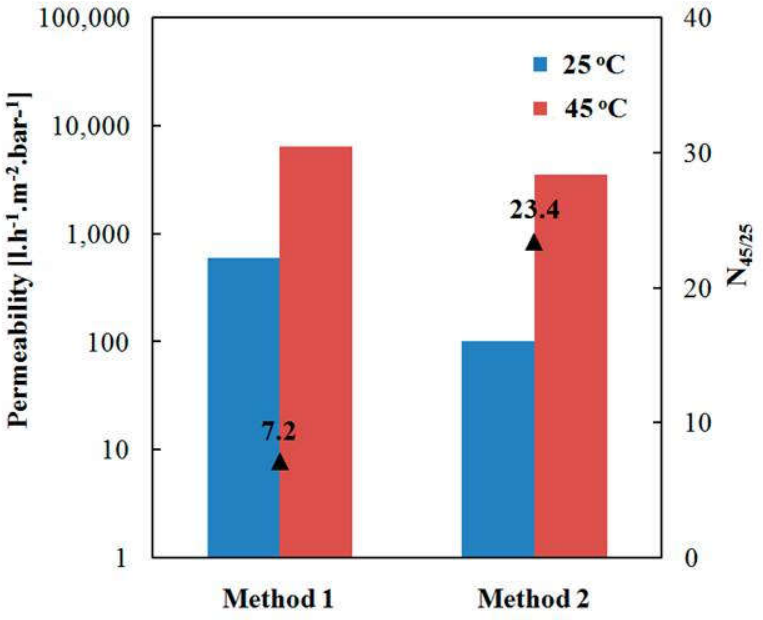

Figure 4.21. Thermo-responsive water permeability of two representative pore-filled membranes.

4.2.5.3 Magneto-responsive water permeability

Further, magneto-responsivity of the two specific membranes from both preparation methods was verified. As shown in **Figure 4.22**, both membranes demonstrated certain magneto-responsive water permeability. When the AMF was turned off in the first 15 minutes, both membranes showed relatively low permeability. After the AMF was switched on, the permeability of both membranes increased significantly within 20 minutes and reached a plateau value. As part of the heat generated by MNP inside the pore could be carried away by the convective flow through the pores, during the filtration, the magneto heating and convective cooling would interplay with each other. When the AMF was just switched on, the water flux was small and convective cooling effect is also relatively weak, therefore, upon magneto-heating, the local temperature would increase, cause microsyneresis of hydrogel network and create bigger meshes for more water flux to pass through the membrane. As the water flux further increases, eventually an equilibrium state will be reached. This has been proved by the plateau permeability in **Figure 4.22**, which indicated the stationary state between heat generation by the MNP and cooling by convective flow of the feed (kept at 25 °C) through the pores. The absolute

increase in water flux due to AMF was significantly larger for the membrane from "method 2", which can be explained by its lower permeability allowing only smaller flux and, hence, leading to less convective cooling compared to membrane from "method 1". Thus, the membranes behaved analogous to the magneto-responsive valve membranes reported earlier[85].

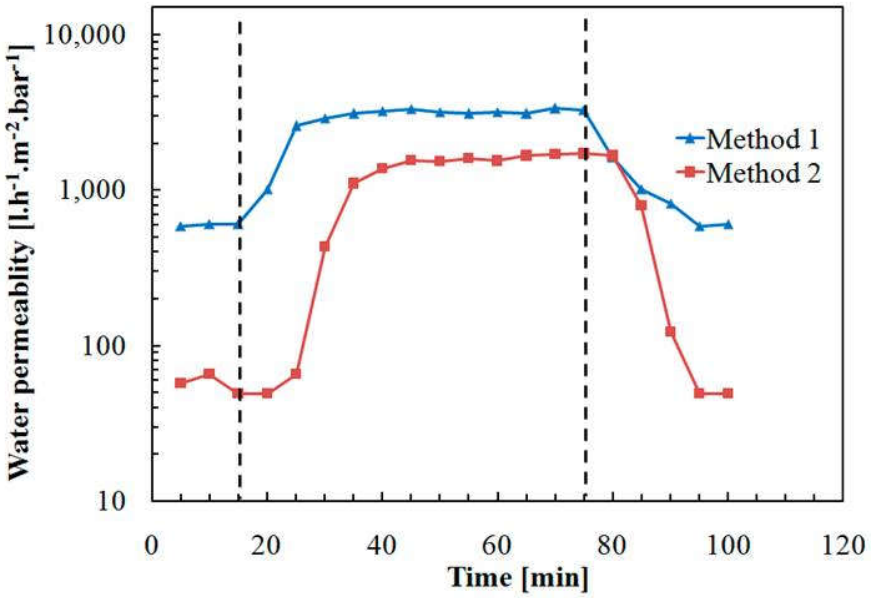

Figure 4.22. Magneto-responsive water permeability of two representative pore-filled membranes.

For both membranes, the plateau water permeability was much higher than the initial permeability, but lower than their permeability at 45 °C (cf. **Figure 4.21**), therefore the temperature in the membrane pores under AMF condition was in the range of the lower critical solution temperature of PNIPAAm, but lower than 45 °C. It must be noted that the estimation of the actual temperature in the pores from the measured permeability is not straight forward because of the largely sigmoidal shape of the viscosity-normalized flux vs. temperature curve, as shown in **Figure 4.23**[85]. While this indicates that the heat generation under the used conditions is limited, it also suggests that it would provide favorable conditions for the separation of biomacromolecules as the temperature is still within a mild range.

Finally, when AMF was switched off again, the permeability returned to the value at the beginning of the experiment (cf. **Figure 4.22**). This proved the heat generated by the MNP can

largely change the conformation of PNIPAAm network under the used AMF condition and that the permeability of the membranes can be fully reversibly manipulated by external AMF.

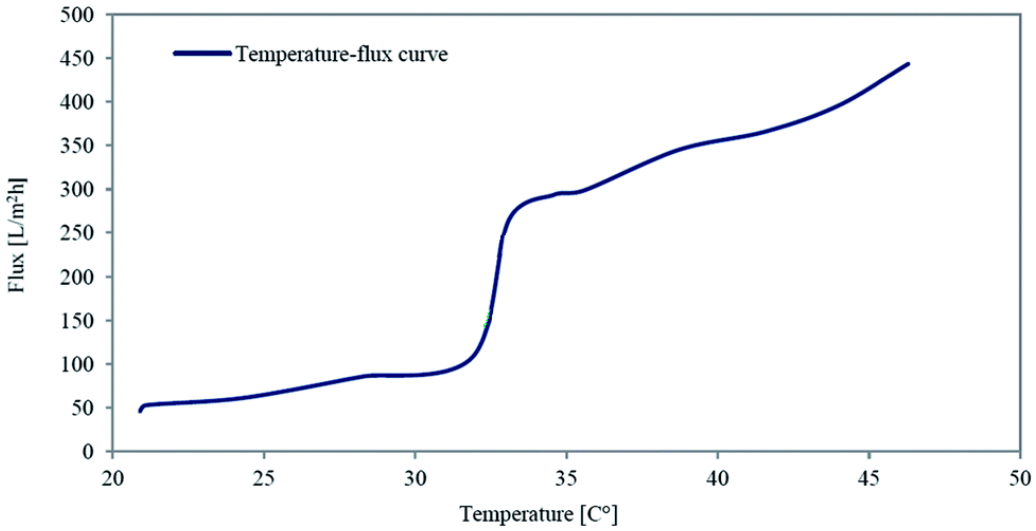

Figure 4.23. Typical water flux vs. temperature curve for PNIPAAm functionalized membrane in literature[85].

Assuming the heat capacity of the membrane is constant and there is no convective flow when the AMF is just switched on, the time for the hydrogel network to reach 32 °C (LCST of PNIPAAm) and can start to respond can be estimated as below[85]:

$$\Delta t = (\Delta T_w \cdot m_w \cdot c)/Q_m \quad (4.2)$$

Where ΔT_w is temperature difference of water, m_w is the mass of water in contact with membrane, c is the heat capacity of water, Q_m is the heat dissipated by the membrane, Δt is time duration with AMF on (or the response time).

By taking the SLP of commercial MNP is 672 W/g, the typical loading of MNP in one 25 mm diameter magneto-hydrogel pore-filled membrane is 0.6 mg (estimated from typical membrane weight of 13 g and MNP loading of 4.63%, cf. section 4.2.5.1), Q_m for membrane sample with diameter of 25 mm is 0.403 W. On the other hand, membrane volume was around 0.022 ml (estimated from the effective filtration area of 3.14 cm, membrane thickness of 100 µm and typical porosity of PES ultrafiltration membrane of 70%), and here a self-made filtration cell

with a water reservoir (volume of 0.942 ml) in direct contact with the membrane was used (cf. **Appendix B**), therefore m_w is assumed as 0.964 g. At last, by assuming that the temperature difference is 7 ^oC (temperature increase from 25 ^oC to 32 ^oC), the response time should be 70 seconds. The relatively slow response can be attributed to a large extent to the relatively larger external systems volume relative to the very small membrane volume[85]. On the other hand, permeate was taken every 5 minutes in experiment, therefore, the time resolution for the responsive water permeability curve in the **Figure 4.24** is quite rough, due to long interval between sampling. The first response for both membranes in **Figure 4.24** was recorded after around 5 minutes, after measuring the first permeate sample with AMF on, and the water permeability reached a plateau after 10-20 minutes with AMF on.

4.2.6 Optimized magneto-hydrogel pore-filled membrane for effective molecular sieving

4.2.6.1 Enhanced hydrogel network for effective molecular sieving

Finally, magneto-responsive molecule sieving performance of the magneto-hydrogel pore-filled membranes was investigated. Because the membranes functionalized with 1 mol/l NIPAAm had relatively high and poorly reproducible water permeability, also dextran rejection had typically been low. As shown in **Figure 4.24**, the magneto-responsive switching of rejection of the two specific membranes from section 4.2.5 (pre-modified with different methods and both pore-filling functionalized with 1mol/l NIPAAm) (cf. **Figure 4.21** and **Figure 4.22**), was semi-quantitatively demonstrated by the filtration of dextran 2000 kDa. For the specific membrane prepared via "method 1" with relative high water permeability (590 $l.h^{-1}.m^{-2}.bar^{-1}$ at AMF off state and 3200 $l.h^{-1}.m^{-2}.bar^{-1}$ at AMF on state) (cf. **Figure 4.22**), there was no rejection for dextran 2000 kDa, no matter the AMF was turned off or on. For the specific membrane prepared via "method 2" with relative low water permeability (60 $l.h^{-1}.m^{-2}.bar^{-1}$ at AMF off state and 1600 $l.h^{-1}.m^{-2}.bar^{-1}$ at AMF on state) (cf. **Figure 4.22**), it had rejection for dextran 2000 kDa around 84% at AMF off state, and no rejection at AMF on state. This indicated that denser hydrogel network was required to achieve effective molecular sieving.

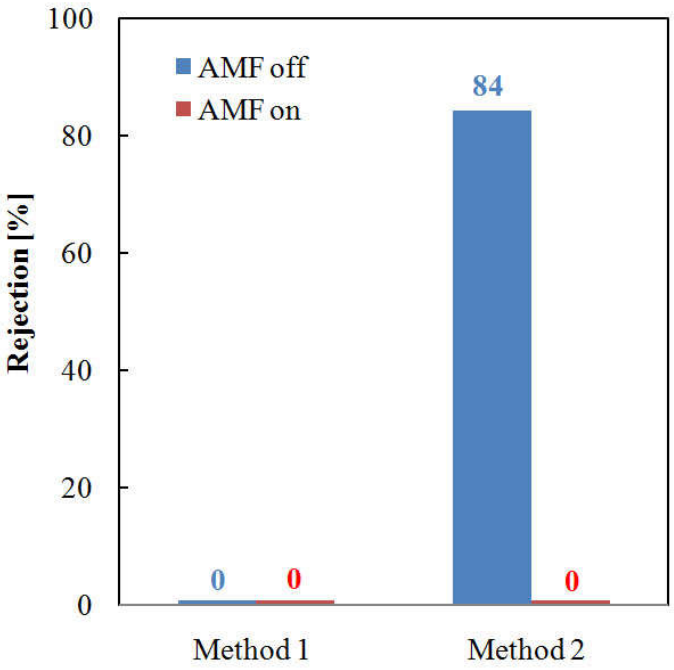

Figure 4.24. Molecular sieving behaviour of specific magneto-hydrogel pore-filled composite membranes prepared with 1 mol/l NIPAAm.

Therefore, the NIPAAm concentration during preparation according to "method 1" was increased to 1.1 mol/l (and concentrations of all other components were also increased accordingly), aiming to obtain a denser network for more effective molecular sieving. It turned out that the water permeability of obtained membranes decreased significantly, and the values at 25°C narrowed down to the range 2 to 10 $l.h^{-1}.m^{-2}.bar^{-1}$ and thermo-responsive factor $N_{40/25}$ was in the range of 16 to 20. Compared with the previously reported thermo-responsive PNIPAAM hydrogel pore-filled membrane[39], such hydrogel pore-filled composite membranes have clearly lower water permeability. This is probably because the embedded MNP reduced the free space in the hydrogel network. As shown in **Figure 4.25**, two pore-filled membranes prepared under those conditions demonstrated also very good thermo- and magneto-responsivity of water flux.

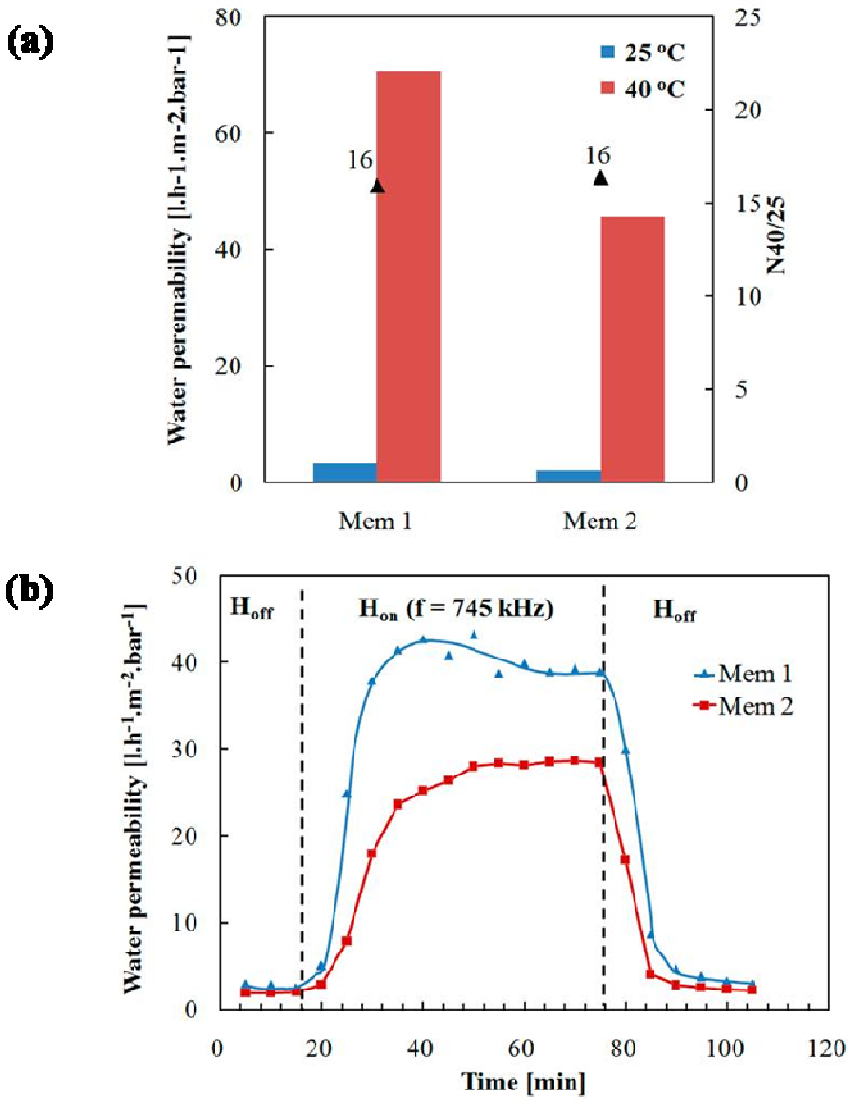

Figure 4.25. Thermo-responsive (a) and magneto-responsive (b) water permeability of two membranes prepared according to "method 1" at higher NIPAAm concentration (1.1 vs. 1.0 mol/l).

4.2.6.2 Thermo-responsive molecular sieving

To investigate the thermo-responsive molecular sieving property of the membrane, the membrane 1 in **Figure 4.25** was used for single dextran solution filtration at 25 °C and 40 °C. As shown in **Figure 4.26**, this membrane has demonstrated a temperature-switchable molecular sieving behavior. It showed relatively high rejection for all sizes of dextran at 25 °C, while

demonstrated a lower rejection in all cases at 40 °C. Moreover, its rejection for dextran 4 and 500 changed significantly upon temperature change. When the temperature raised from 25 °C to 40 °C, the rejection for dextran 4 dropped from 60% to 9% and for dextran 500 it dropped from 92% to 41%, indicated average mesh size the hydrogel changed from less than 4 nm (stokes diameter of dextran with MW 4 kDa, cf. section 3.1.4) to bigger than 28 nm (stokes diameter of dextran with MW 500 kDa, cf. section 3.1.4). On the other hand, the reject of membrane for relatively large dextran molecule, dextran 2000 (with stokes diameter of 52 nm, cf. section 3.1.4), only dropped from 97% to 72% percent upon temperature change (25 °C to 40 °C), indicating the mesh size of the hydrogel at 40 °C is still under 52 nm. Overall, this specific membrane has relatively good thermo-responsive molecular sieving effect for those two small dextran molecules. For dextran 2000, the temperature effect was smaller because its average mesh at 40 °C is still quite small compare with dextran 2000.

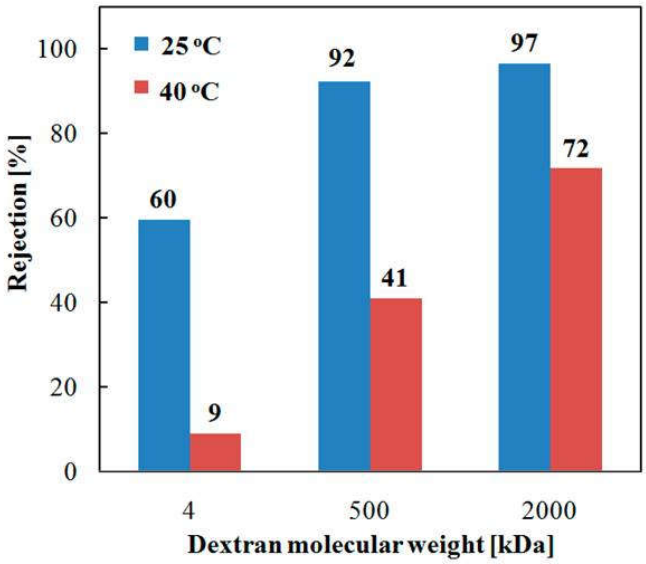

Figure 4.26. Thermo-responsive sieving behaviour of a specific magneto-hydrogel pore-filling composite membrane (prepared with 1.1 mol/l NIPAAm)

4.2.6.3 Magneto-responsive molecular sieving

Further, membrane 2 from **Figure 4.25** was taken for magneto-responsive molecular sieving test. Its thermo- and magneto-responsive water permeability and dextran sieving behaviour are shown in **Figure 4.27**. As can be seen in **Figure 4.27(a)**, the chosen membrane had a rather dense and even pore-filling hydrogel network, therefore its permeability at 25 ^{o}C was quite low and responsivity was quite high (thermo-responsive factor, $N_{40/25}$ = 13). As shown in **Figure 4.27(b)**, during dextran filtration tests, it demonstrated largely different rejection for different sizes of dextran molecules at 25 ^{o}C. For small dextran with average molecular weight of 4 kDa and average Stokes diameters of 3 nm, only 26% was rejected; for medium dextran with molecular weight of 500 kDa and Stokes diameter of 28 nm, a higher percentage, 58%, was rejected; for dextran with molecular weight of 2000 kDa and Stokes diameter of 54 nm, 94% was rejected. Hence the molecular weight cut-off, defined at 90% rejection, was clearly below 2000 kDa / 50 nm. Average mesh size estimated for bulk gels, prepared at slightly lower monomer concentration and directly after synthesis was much smaller, i.e. ~7 nm (cf. **Table 4.2**), and cut-off values for only hydrogel pore-filled membranes had also been lower ($\leq$ 100 kDa)[39]. This implies that the relatively large MNP may introduce heterogeneities into the network structure which reduce its size-selective fractionation performance. However, when the AMF was switched on, the membrane permeability increased more than 10 times, and molecular sieving properties changed accordingly. The rejection for dextrans 4 kDa and 500 kDa decreased to 0 %, and for dextran 2000 kDa, the rejection was also largely reduced, from 94% to 30%. This indicates that the average mesh size was very much enlarged and that the molecular weight cut-off was largely shifted to values beyond 50 nm, because of the magneto-actuation. Therefore, such MNP-PNIPAAm hydrogel pore-filled composite membrane has demonstrated magneto-switchable molecular sieving behaviour.

Also the permeability of membrane 2 during the dextran filtration and for pure water after the washing were tested and recorded to evaluate the reversibility of the membrane performance. As demonstrated in **Figue 4.27(c)**, the membrane permeability for same conditions slightly fluctuated during the filtration steps. However, the effect of AMF was much larger, dextran filtrate fluxes increased by more than an order of magnitude. The permeability decreased somewhat after the filtration of dextran 500 kDa. Also flux during ultrafiltration of dextran 2000

kDa was much smaller than during ultrafiltration of the smaller dextrans. This suggests that the mesh size of the membrane is relatively small for these solutes and the membrane could be fouled by the large dextran molecules. However, it had also been shown that permeability can be recovered by washing with water at the end of the cycle ("water 4"). Overall, the decrease of permeability during the filtration was not high and fouling was reversibly. As demonstrated, one membrane could be used for three cycles of ultrafiltration experiments, always including switching AMF on and off, and the initial membrane permeability was fully recovered, therefore, such stimuli-responsive change of molecular sieving effect is fully reversible.

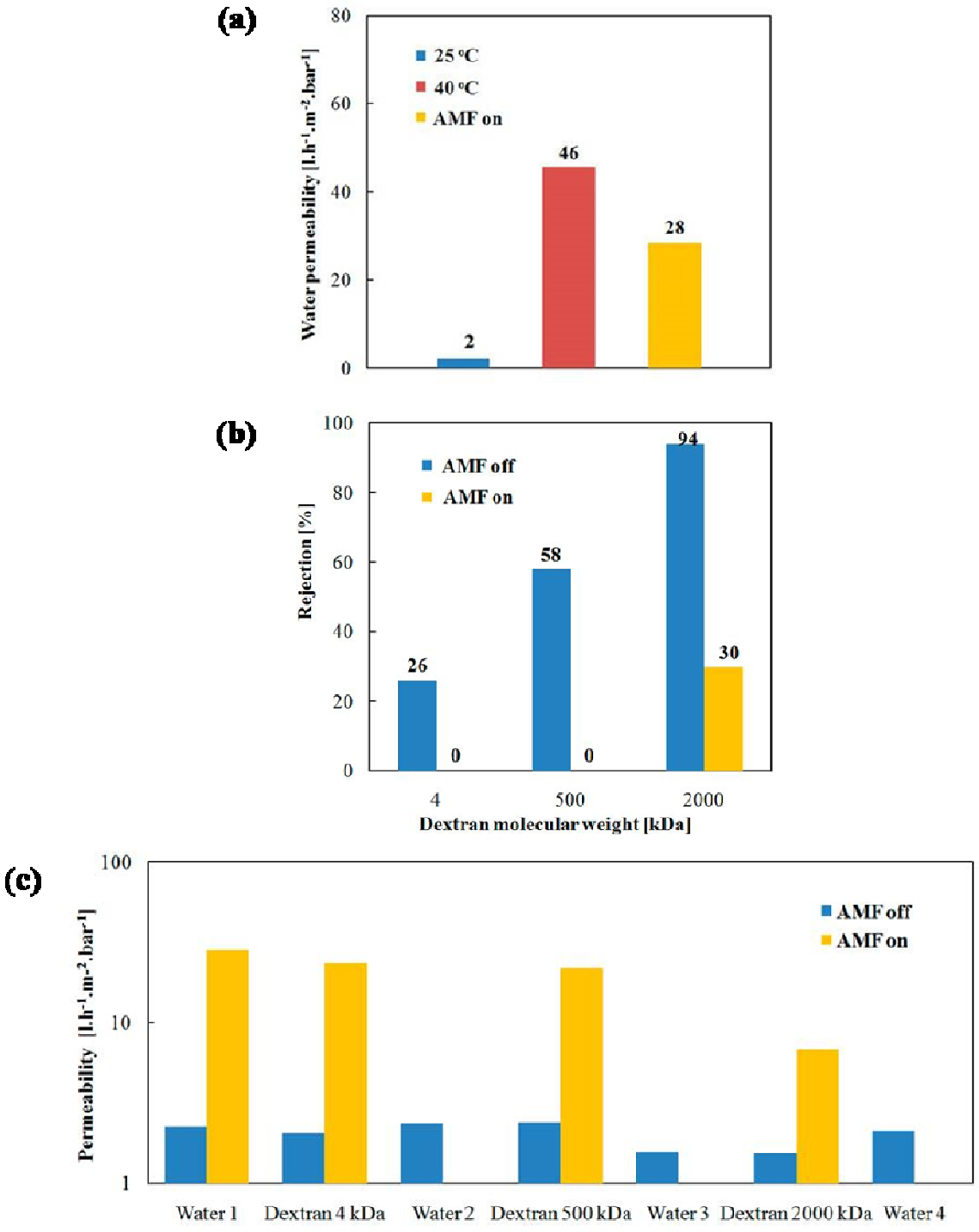

Figure 4.27. Responsive water permeability (a), molecular sieving behaviour (b), and water and dextran filtrate permeabilities (c) of a specific magneto-hydrogel pore-filling composite membporane (prepared with 1.1 mol/l NIPAAm).

4.3 MNP and PNIPAAm mixed matrix composite membrane

4.3.1 Self-made MNP

Here polyol synthesis method was chosen to produce MNP as building block for the mixed matrix composite membrane. This preparation method is relatively simple and inexpensive. Moreover, it has excellent controllability for particle size and good reproducibility. In addition, the amine functional groups on the surface of the MNP introduced by the specific version of the method would later allow good dispersion of the particles in casting solvent NMP[171].

4.3.1.1 Morphology and size distribution

By adjusting the ratio of 1,6-hexanediamine and anhydrous sodium acetate, different sizes of MNP can be obtained (cf. **Table 3.3**) and it has been proved that MNP made by this method is well crystallized Fe_3O_4 nanosphere surface-functionalized with amine groups[171]. As shown in SEM pictures in **Figure 4.28**, by decreasing 1,6-hexanediamine usage from 0.23 g/ml to 0.15 g/ml, the average diameter of the particles increased from 15 $\pm$ 5 nm to 70 $\pm$ 10 nm. Here we choose the MNP with size 40 $\pm$ 10 nm (synthesized with 0.17 g/ml of 1,6-hexanediamine, cf. section 3.3.1) for further characterization and experiment because the size is comparable with the commercial MNP we have used for magneto-hydrogel pore-filled membrane. Moreover, it is expected, while such relatively large size particles can generate more heat in AMF than other smaller particles like particles with diameter of 15 $\pm$ 5 nm and 25 $\pm$ 5 nm, it can also be better dispersed than even larger particles, like the one with diameter of 70 $\pm$ 10 nm.

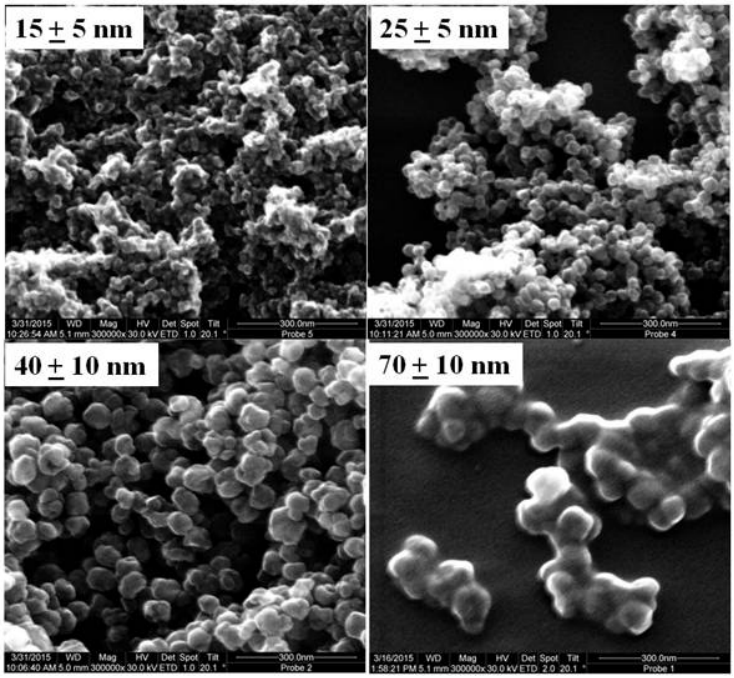

Figure 4.28. MNP with different sizes were synthesized by adjusting the amount of 1,6-hexanediamine in reaction solution. The MNP with diameter of 15 ± 5, 25 ± 5, 40 ± 10, 70 ± 10 nm were synthesized respectively with 0.23, 0.21, 0.17, 0.15 g/ml of 1,6-hexanediamine (concentrations of $FeCl_3.6H_2O$ and anhydrous sodium acetate were constant, 0.033 g/ml and 0.067 g/ml, respectively)

4.3.1.2 Zeta potential

Successful amine functionalization for MNP with size of 40 nm has been proven by the positive zeta potential (55 mV) of the MNP dispersion at pH 4.

4.3.1.3 Magnetization

The MNP with diameter 40 ± 10 nm is in the ferromagnetic range for iron-based magnetic nanoparticles[175]. This has been further proven by analysis of the H-M curve of the MNP, as there is a hysteresis loop with respect to magnetization when external magnetic field is varied (**Figure 4.29**). The hysteresis loss per one magnetization cycle is in dependence of field amplitude and could be determined by integrating the hysteresis loop[178]. Here, we performed tests under an external field comparable with AMF field amplitude of 20 ± 10 kA/m, which was later used for evaluation of magneto-responsive properties (cf. sections 3.5.4.4 and 3.5.5). And as shown in

Figure 4.29, higher maximum external magnetic field amplitude results in higher hysteresis loss. When MNP are subjected to AMF, they can generate heat based on three mechanisms: (1) hysteresis (the magnitude represented by the area inside the hysteresis loop), (2) Néel relaxation (rotation of the magnetic moment within the particle), and (3) Brownian relaxation (physical rotation of the whole particle within the dispersing medium)[184] (cf. section 2.4.4.2). In this research, Brownian relaxation will not contribute to the heat release because the AFM frequency is much too high to allow the MNP to follow the external field and since the MNP are embedded in the membrane matrix[44]. Therefore, hysteresis loss and Neel relaxation are the main source for the heating. Moreover, as ferromagnetic nanoparticles are used, hysteresis loss is the dominant loss mechanism, and AMF with high amplitude and high frequency is a rational choice[176, 177].

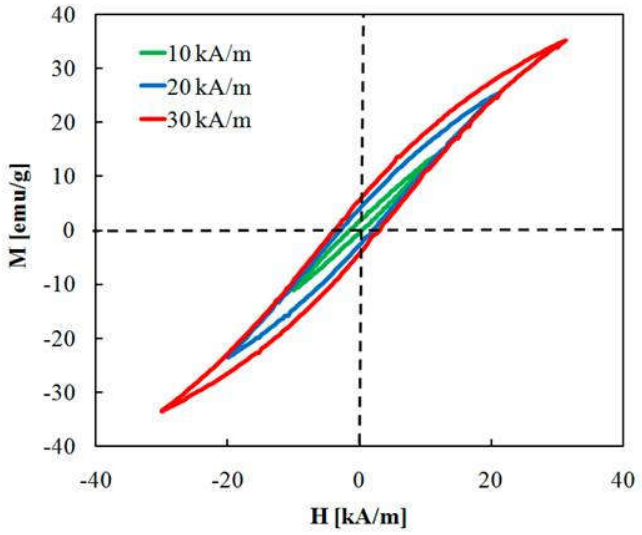

Figure 4.29. Magnetization of MNP under different field amplitude (10 kA/m, 20 kA/m and 30 kA/m)[iv].

4.3.1.4 Dispersion in NMP

As a homogenous dispersion of MNP in the membrane would ensure an efficient and homogenous heating, amine functionalization of the surface was introduced during the synthesis

[iv] The magnetization measurements have been kindly conducted by M.Sc. Soma Salamon from Prof. Dr. Heiko Wende's group, Faculty of Physics, UDE.

of MNP to promote a more stable dispersion of MNP in the casting solvent NMP and the coagulation bath water. Moreover, sonication was employed and optimized to obtain a good dispersion of MNP in NMP eventually in the dope solution and ultimately in the composite membrane (cf. section 3.5.2). During intensive sonication, while the ultrasonic cavitation is expected to generate high shear and break the particle agglomerates into individual dispersed particles, the high energy input and strong mechanical force would on the other hand result in high temperature, high flow speed and high pressure, and this cause agglomeration again[197]. Therefore, it is vital to identify an optimal sonication procedure, with suitable energy input, amplitude and time program, that matches the particle material and its interactions. Varied sonication procedures were tested (cf. **Table 3.6**), and the resulted particle size distributions are shown in **Figure 4.30**. First, energy input of 30 W was confirmed to be better than 50 W, as with the same sonication amplitude and time program (continuous sonication with amplitude of 30%), it ensured a narrower size distribution (cf. **Figure 4.30(a)**). Then, under continuous sonication with 30 W, effect of various of amplitudes (30%, 40% and 50%) were evaluated and the results indicated that narrowest size distribution could be obtained with amplitude 30% (cf. **Figure 4.30(b)**). Further, different time programs were compared; based on sonication power of 30 W, amplitude of 30%, and effective sonication time of 30 seconds, different durations of pause interval were applied. Despite certain duration of pause interval between sonication was expected to avoid overheating of the dispersion[198], as shown in **Figure 4.30(c)**, here long pause interval turned out to cause more agglomerates and wider size distribution.

Therefore, an optimal procedure, continuous sonication with input power of 30 W, amplitude of 30%, for 30 seconds, was chosen. As shown in **Figure 4.30(d)**, with the final optimized dispersing procedure, average particle diameter of 250 nm with relatively narrow size distribution was obtained. Despite the amine functionalization, the dispersion of such MNP is still quite tricky to handle, because the only electrostatic repulsion (weak in the organic solvent) without additional sterical stabilization (due to use of small molecule for surface functionalization) is not strong enough to counteract with magnetic attraction of such ferromagnetic nanoparticles. However, the particle size distribution for the liquid dispersions is comparable with particle size (100 – 300 nm) in the magneto-responsive membranes reported by Hoare et al.[34, 35]. Therefore, it was decided to use such dispersions to further cast membranes.

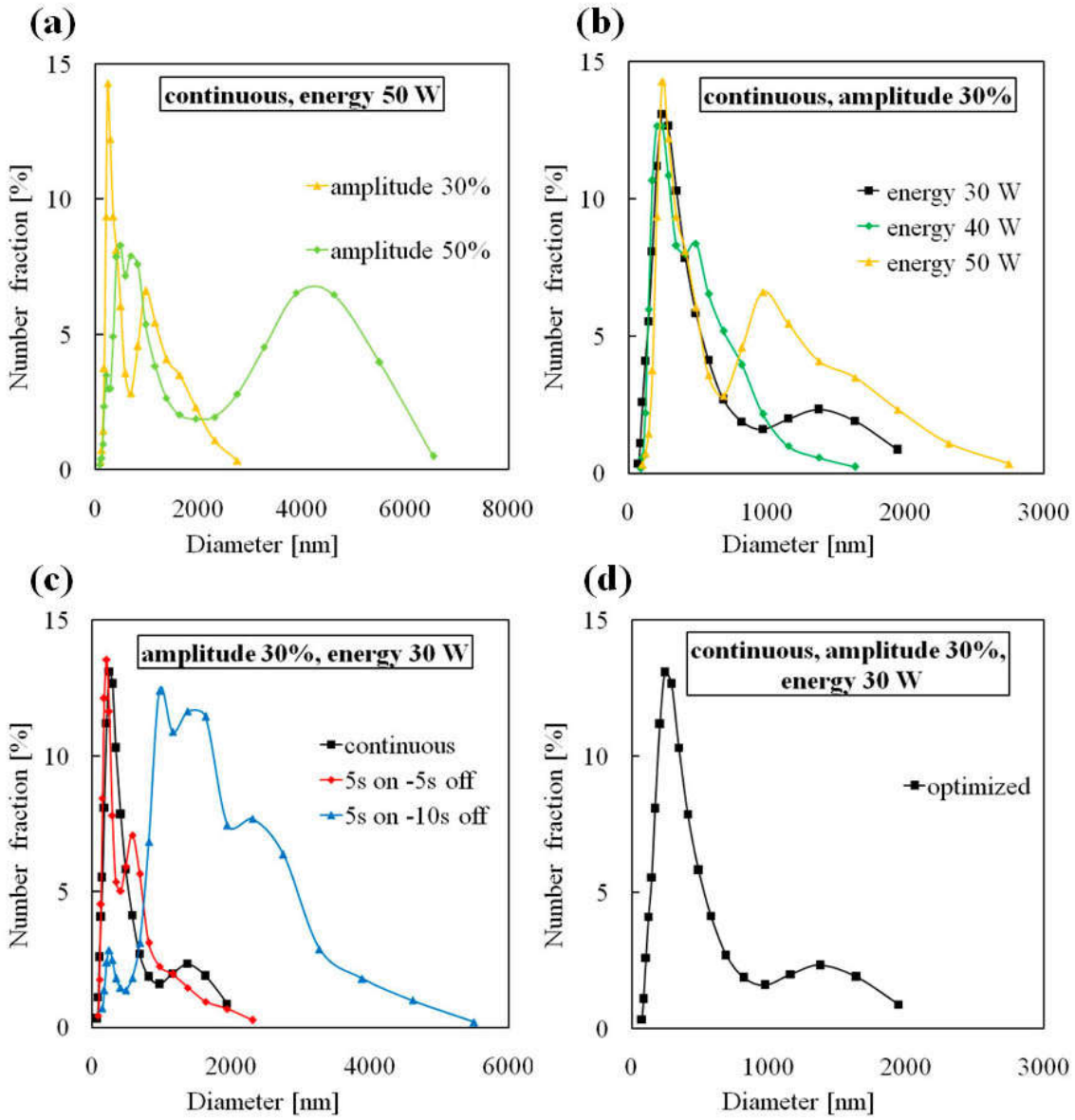

Figure 4.30. Optimization for MNP dispersion in NMP via varied sonication programs (cf. **Table 3.6**): (a) variation of amplitude, (b) variation of energy input, (c) variation of time program, and (d) the final optimized size distribution.

4.3.1.5 Heating efficiency of MNP

The heat generation by the MNP upon excitation with AMF was investigated by a calorimetric method; data can be seen in **Table 4.5**. After 1 minute exposure to the AMF, MNP aqueous dispersion showed a temperature increase of 2.5 $\pm$ 0.7 ^{o}C, while water only had a temperature increase of 0.6 $\pm$ 0.3 ^{o}C. The specific loss of power calculated from that data is 265 Wg^{-1}. This is somewhat smaller than the SLP of similar commercial MNP (672 Wg^{-1}), which is 40 nm iron oxide nanoparticle coated with amphiphilic polymer (used in magneto-hydrogel pore-filling membrane) (cf. section 4.2.1.3). This may be caused by relatively wider size distribution of the self-made MNP, as the optimal AMF frequency for magnetic heating of MNP also depends on the absolute size and size distribution of the particles[184]. The distribution of particle sizes would lead to a distribution of optimal frequencies for heating; and as only one specific frequency can be applied, the overall heating efficiency in this case is compromised. However, more important, the materials seem to be suited very well for their intended function.

Table 4.5. Temperature changes of the self-made MNP sample upon AMF excitation (I = 15.6 A, f = 745 kHz, H ~ 20 kAm^{-1})

Sample	Time [minutes]	Temperature change [^{o}C]
Water	1	0.6 $\pm$ 0.3
MNP dispersion	1	2.5 $\pm$ 0.7

4.3.2 PNIPAAm NG

4.3.2.1 Morphology

The morphology of the thermo-responsive PNIPAAm NG was characterized first. As shown in **Figure 4.31**, both kinds of PNIPAAm NG were highly monodisperse and both of them had average diameter around 400 nm in dry state. The contrast of the two SEM images was different,

only because the particle concentration and the sputter coating for the two NG samples were not identical as they were not characterized at same time.

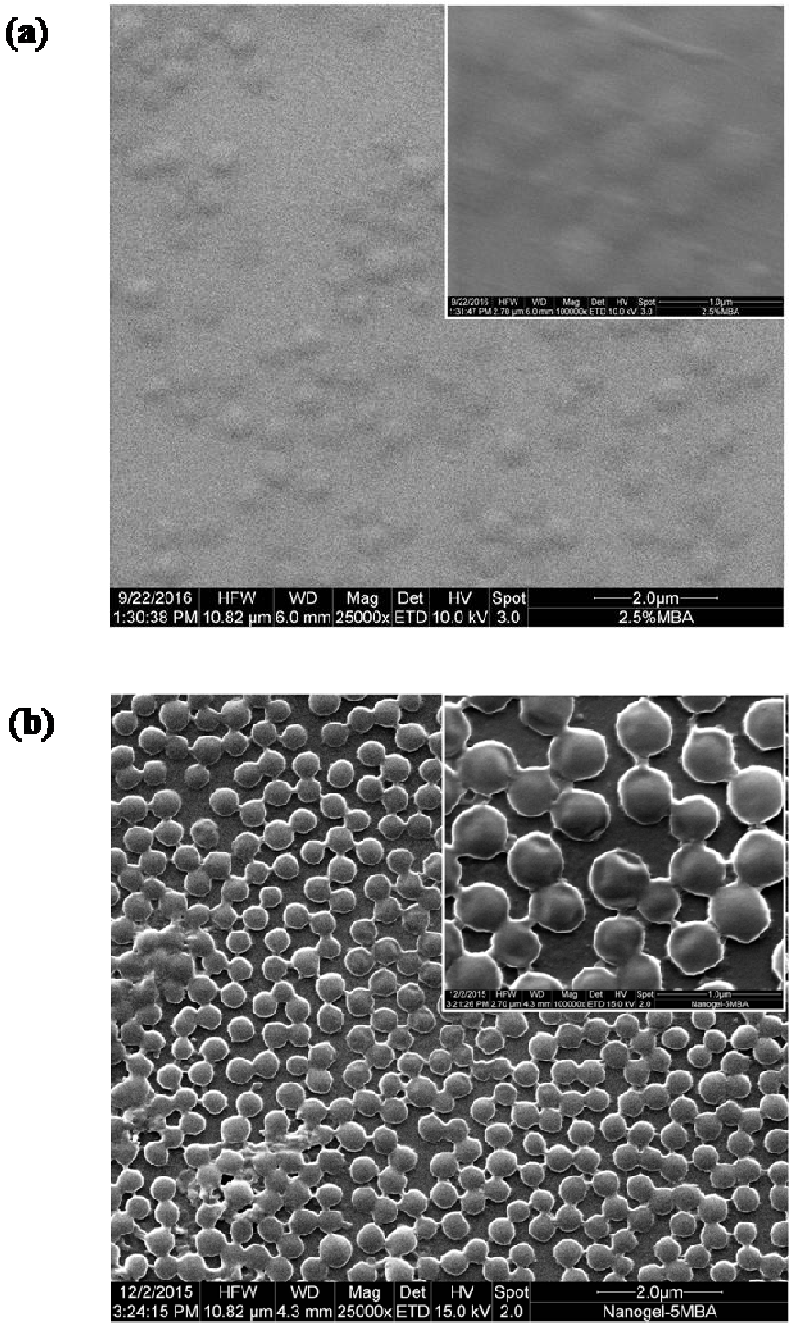

Figure 4.31. SEM image of PNIPAAm NG in dry state: (a) synthesized with 2.5% MBA and (b) synthesized with 5% MBA.

4.3.2.2 Size distribution and swelling property in different solvents

Further, NG swelling property was studied with dynamic light scattering. As the PNIPAAm nanogel will be dispersed in NMP, the good solvent for membrane materials when preparing the membrane, and will be in water environment in application, the hydrodynamic diameters of two kinds of NG in water and NMP were measured at 25 ^{o}C (below LCST) and 40 ^{o}C (above LCST) to evaluate the influence of temperature and solvent on phase transition. As shown in **Table 4.6**, NG with 2.5% MBA, in water it was swollen at 25 ^{o}C with an average diameter of 649 nm and shrunken at 40 ^{o}C with an average diameter of 298 nm. The volume reduction along the temperature was around 55%. However, in NMP, the average hydrodynamic diameter at 25 ^{o}C was 743 nm and at 40 ^{o}C it was 787 nm. As shown in **Table 4.7**, for NG with 5% MBA, in water the average hydrodynamic diameter at 25 ^{o}C was 710 nm and 410 nm at 40 ^{o}C. The volume reduction upon temperature rising was around 42% and was comparable with other reports[31, 33]. Similar as the lower cross-linked NG, in NMP, its average hydrodynamic diameter seemed to be almost constant, with 1020 nm at 25 ^{o}C and 960 nm at 40 ^{o}C. Temperature induced (de)swelling of PNIPAAm is linked to its solvation. As it is well-known, in water, when the temperature is lower than its LCST, due to the formation of hydrogen bonds between amide groups and water and water clusters around the hydrophobic isopropyl groups, PNIPAAm is in swollen state; and when temperature is raised above LCST, because in this temperature range hydrogen bonds are broken and clustered water is released, PNIPAAm will be in shrunken state. In contrast, in the organic solvent NMP, this amphiphilic character of PNIPAAm does not play a role. Because NMP and PNIPAAm have similar structure, NMP is an even better solvent than water, as seen by the larger particle diameter, and the only weak deswelling response to temperature can also tentatively be explained by breaking a fraction of hydrogen bonds between polymer and solvent.

Table 4.6. Average hydrodynamic diameter of PNIPAAm NG with 2.5% MBA in two different solvents at 25 and 40 °C

	Water		NMP	
Temperature [°C]	25	40	25	40
Hydrodynamic diameter [nm]	649 ± 9	298 ± 3	743 ± 19	787 ± 14
Polydispersity index [-]	0.09 ± 0.03	0.08 ± 0.02	0.2 ± 0.08	0.21 ± 0.06

Table 4.7. Average hydrodynamic diameter of PNIPAAm NG with 5% MBA in two different solvents at 25 and 40 °C

	Water		NMP	
Temperature [°C]	25	40	25	40
Hydrodynamic diameter [nm]	709 ± 14	410 ± 2	1022 ± 36	963 ± 14
Polydispersity index [-]	0.15 ± 0.02	0.1 ± 0.02	0.29 ± 0.03	0.26 ± 0.03

Moreover, the data imply that the nanogel is more swollen in the casting solution than in water which is the environment during application of the membrane. If the membranes were formed with the nanogel in fully swollen state, the shrinking under application conditions would cause the nanogel to be smaller than the voids in the PES matrix to hold it, resulting in unstable performance of the membrane. Therefore, this was one argument to perform the entire membrane preparation process (casting of the dope solution and coagulation in the water bath) at a higher temperature (and also above LCST of PNIPAAm), to better fix the NG in the forming membrane matrix. It is anticipated that NG will deswell upon solvent exchange from NMP to water at 45 °C,

and upon later reduction of temperature to 25 °C the NG will re-swell into the void in the PES matrix (cf. **Figure 1.1(b)**). And here we decided to choose the NG with 5% of MBA as responsive element and prepare composite membranes at 45 °C, to get a less significant volume change and ensure the new created gate at high temperature to be within macromolecular range (cf. **Figure 1.1(b)**). In the meantime, composite membranes were also prepared at room temperature as reference (cf. **Appendix A**).

4.3.3 Rheological study of dope solution

After the investigation of building blocks including MNP and NG, a detailed rheological study on the dope solution, for its viscosity as function of shear rate was performed at temperatures 25 ^{o}C and 45 ^{o}C, in order to explore the effects of composition, temperature and external force (also with view on shear stress during casting) on their behavior. And self-made MNP with 40 nm diameter and PNIPAAm NG with 5% of MBA were used.

Rheological properties of particulate suspensions are sensitive to volume fraction and specific properties of the particles (modulus, size, shape, and surface chemistry)[199, 200, 201]. Very complicated systems were considered here as dope solutions, with the chain polymer PES, the amino-functionalized hard oxidic nanoparticles (MNP), and the soft submicron PNIPAAm hydrogels (NG), all well-dispersed in the polar aprotic solvent NMP. The components have different chemical composition, size, morphology and intrinsic modulus, and they could interact with each other. Specifically, the long chain polymer PES could work as bridge to enhance the interaction of the particles, causing shear thickening or shear thinning effect under critical shear stress[202, 203, 204]. However, most related studies used hard particles as model; rheological studies of suspensions of soft particles, especially in multiple components systems, are still rare[202, 205, 206].

It is known that addition of nanomaterial (MNP or NG) would generally cause an increase of viscosity, due to the increase of effective phase volume[200, 201]. As shown in **Figure 4.32(a)**, at 25 ^{o}C, for the dope solutions blended with NG (NG-PES system and MNP-NG-PES system), the zero-shear viscosity is significantly higher (around four times of magnitude compared to the pure PES dope solution, and more than three times higher than for the MNP-PES system), perhaps because the strong swelling of the NG in NMP (cf. **Table 4.7**) greatly increased the effective phase volume of this additive. More interestingly, when shear was applied, a small thickening

happened, probably because at this stage shear forced the PES chains to transform from coil form into stretched conformation (this is hardly seen for the pure PES system due to different scale; cf. **Figure 4.32(a)**) and thus to function as a bridge between the PNIPAAm NG particles, resulting in an increase of viscosity. However, as the shear rate was further increased, severe shear thinning happened. Presumably when PES chains and PNIPAAm NG became more aligned in the shear direction at high shear rate, their mutual interaction was broken; but the easy deformability of the soft nanogel under higher shear stress had by far the largest contribution to the pronounced shear thinning[143]. Consequently, the rheology of the MNP-NG-PES dope solution is dominated by the effects of the PNIPAAm nanogels (as indicated by the very similar curve compared to NG-PES); only at high shear rates, it can be seen that the effects of the two different particulate additives are similar, i.e. related to their mass fraction in the system.

With respect to temperature influence, as shown in **Figure 4.32(b)**, the viscosity of all dope solutions dropped upon the increase of temperature from 25 ^{o}C to 45 ^{o}C, because the interactions of the dissolved or dispersed components with the solvent decreased. However, while the drop of initial viscosity is around 2 times for dope solution with pure PES and for PES blended with MNP, it is 4.5 times for the one blended with PNIPAAm NG and 3 times for the one blended with both NG and MNP. This may be caused by the drastically weakened bridging effect of PES between the nanogel particles at high temperature. Also, in case of temperature 45 ^{o}C, a higher shear stress is required to counteract with the thermal motion of PES chains; therefore, the range of shear thickening is shifted to higher shear rate.

It is well-known that the viscosity of the dope solution would significantly influence the structure and morphology of the membranes prepared by phase separation process. A dope solution with lower viscosity is easier to process and could speed up the phase separation during NIPS (cf. section 2.1.2). Therefore, later the higher temperature and a casting speed of 5 mm/s (corresponding to a shear rate of 15.9 s^{-1}) were selected, which ensure a stable and relatively low viscosity.

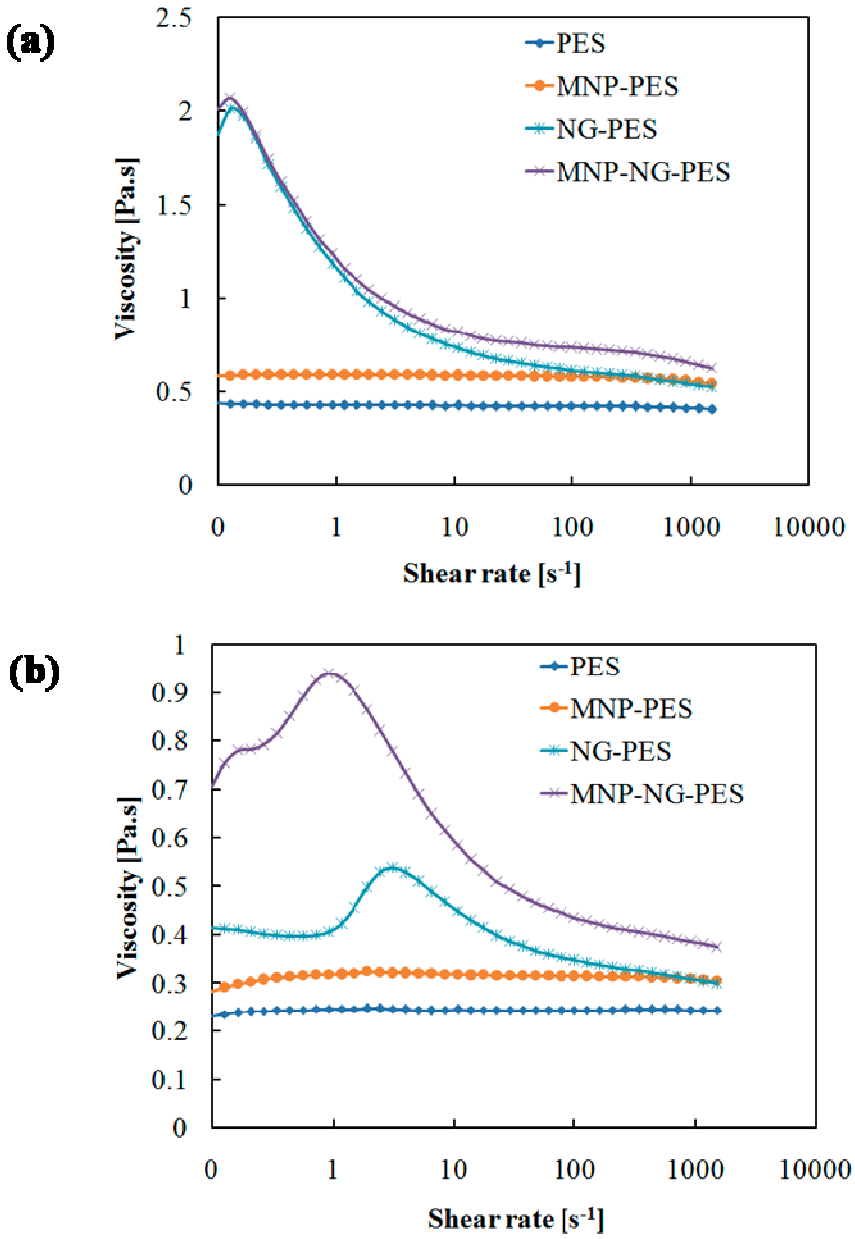

Figure 4.32. Viscosity of dope solutions in NMP (14.5 wt% PES; 10 wt% additive relative to PES) as function of shear rate, at (a) 25 °C and (b) 45 °C.

4.3.4 General characterization of mixed matrix membranes

4.3.4.1 PNIPAAm NG loading

To investigate the PNIPAAm NG loading, elemental analysis was carried out for dry membrane samples including PES, NG-PES and MNP-NG-PES membranes. The loading of NG was estimated by assuming that all nitrogen comes from PNIPAAm NG. As shown in **Table 4.8**, the elemental analysis results fit well with the theoretical loading of 10 wt% PNIPAAm NG in the NG-PES and the NG-MNP-PES membranes. This proved that under the used casting conditions, the nanogel can be quantitatively embedded and well kept in the porous membranes.

Table 4.8. Elemental analysis results

	C	H	S	N	Theoretical content of N
PES	62.5%	3.48%	14%	0%	0% (0% of NG)
NG-PES	62.3%	3.86%	12.4%	1.27%	1.13% (10% of NG)
MNP-NG-PES	57.5%	3.77%	11.5%	1.08%	1.03% (10% of NG)

4.3.4.2 MNP loading

To quantify the fraction of MNP in composite membranes, TGA analysis was conducted. Results for the different membranes are shown in **Figure 4.33**. While PES and NG-PES membranes were almost totally decomposed around 700 ^{o}C, MNP-PES and MNP-NG-PES had a residue of 8.3% and 11.8% respectively at this temperature. The residue must be Fe_2O_3 nanoparticles, because oxidation of Fe_3O_4 nanoparticles at high temperature in air atmosphere is expected (cf. section 4.2.5.1). When it is considered that the estimated mass of Fe_2O_3 was formed from Fe_3O_4, the loading of MNP was 8% in MNP-PES membrane and 11.4% in MNP-NG-PES membrane (cf. **Equation 4.1** in section 4.2.5.1). Considering the error of this estimation, the values are similar to the theoretical loading of 10% MNP, and this indicates that a quantitative embedding of the magnetic particles in the membrane matrix can be achieved during the NIPS process.

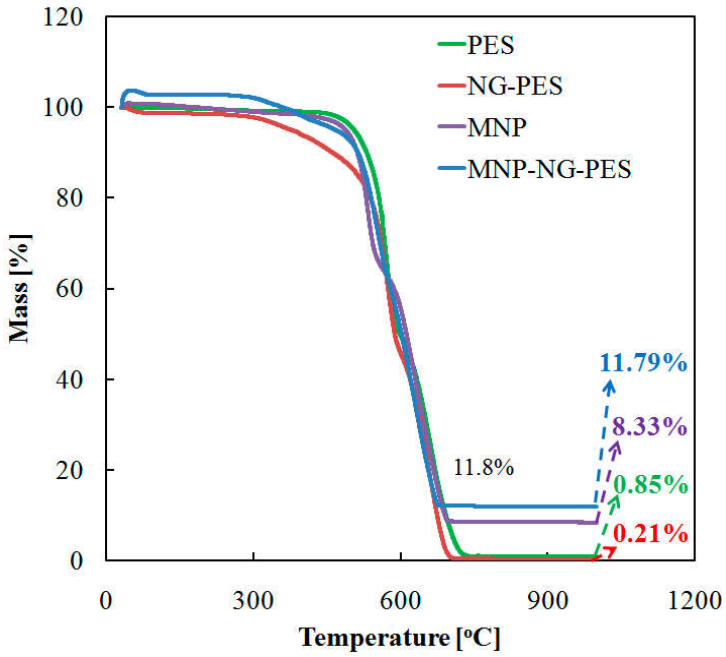

Figure 4.33. TGA curves for membranes with different composition.

4.3.4.3 Surface properties of the mixed matrix membranes

Both surfaces of the membranes were analyzed by ATR-FTIR spectroscopy. Because a diamond crystal was used and the angle of incidence of IR beam was 45 degree, the penetration depth was about 2 µm. As shown in **Figure 4.34(a)**, all membranes blended with PNIPAAm NG showed an extra peak at 1650 cm^{-1}, which can be attributed to amide groups of PNIPAAm. Therefore, there should be PNIPAAm NG on both top surface and bottom side of NG-PES and MNP-NG-PES membranes.

Further, this was verified by the thermo-responsivity of water contact angle. As it is well-known, PNIPAAm will transform from hydrophilic into less hydrophilic upon the increase of temperature[131, 207]. **Figure 4.34(b)** provides an overview on CA data as function of membrane composition, for their top and bottom sides and at two temperatures. Compared to pure PES, CA was significantly decreased by addition of MNP, what can be attributed to their hydrophilic oxidic structure. Except for the PES-NG membrane, CA data were significantly different for top and bottom surfaces. For pure PES membrane, the largest CA difference and highest CA value

for the bottom surfaces among all membranes were observed; this is explained by the higher porosity and roughness of the top compared to the bottom surface. Because CA had been measured in captive bubble mode with the pores filled by water, wettability with water is increasing with the fraction of pores in the otherwise relatively hydrophobic surface. The very low porosity on the bottom surface can be related to the fact that these membranes had been prepared without a "porogen" (e.g. polyvinylpyrrolidone) which is usually used to prepare porous PES membrane). The presence of additive (MNP or NG) increased also the wetting of the bottom surface with water. Most important with view on membrane functionality is that the PES and MNP-PES membranes showed only small change of CA between 25 ^{o}C and 40 ^{o}C while both sides of NG-PES and MNP-NG-PES membranes showed a pronounced increase of CA upon temperature rise. This can be attributed to thermo-responsive PNIPAAm NG particles exposed on the surface of the mixed matrix membranes.

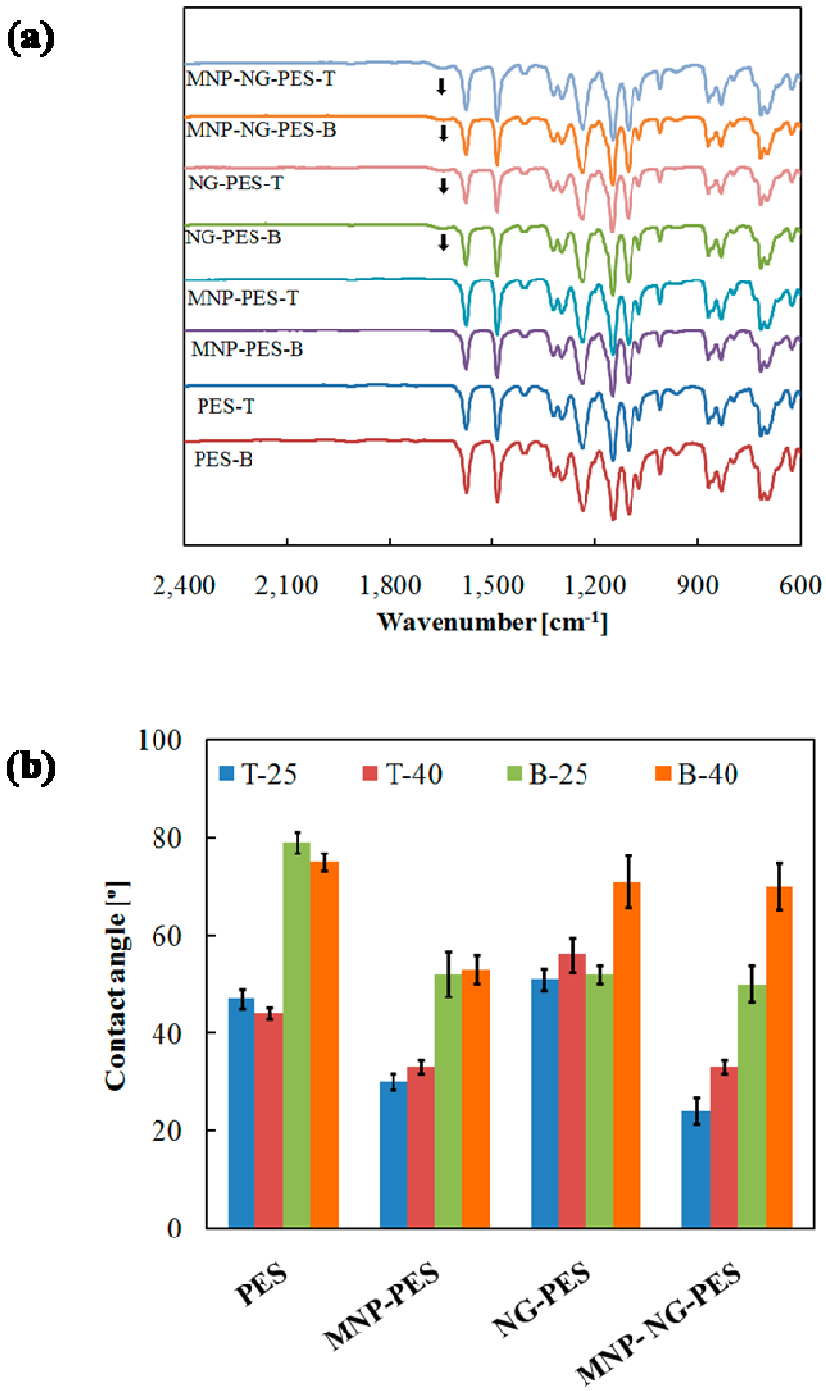

Figure 4.34. Surface properties of top (T) and bottom (B) sides of mixed matrix composite membranes; (a) ATR-IR spectra, (b) contact angles at 25 °C and 40 °C.

4.3.4.4 Morphology of mixed matrix membranes

To further clarify the structure of the different membranes, SEM images of the barrier layer surface and the cross-section were taken and are shown in **Figure 4.35**. The first column of images (**a1**, **b1**, **c1** and **d1**) shows the cross-section of the membranes. First of all it is important that all membranes have anisotropic cross-section morphology with a µm-thin dense layer on top and a macroporous support layer; this is a precondition for a high permeability. For the membranes containing PNIPAAm NG (**c1**, **d1**), the "finger pore" structure is less pronounced compared to the other two membranes (**a1**, **b1**), what is most presumably caused by the delay of demixing due to the higher viscosity of the dope solutions containing NG (cf. **Figure 4.32**). The second column (**a2**, **b2**, **c2**, and **d2**) provides detail images of the cross-section to visualize the nanomaterials. Except for some small agglomerates (size 1-2 µm), it is not easy to find MNP in MNP-PES (**b2**) and MNP-NG-PES (**d2**) membranes, despite the high loading deduced from the TGA results (cf. section 4.3.4.2). This may be because the majority of well-dispersed MNP were well incorporated into the PES matrix of the porous membrane. Concerning the NG, many particles are found inlaid in the inner pore walls in the NG-PES membrane (**c2**), while much less could be seen in the MNP-NG-PES membrane (**d2**), despite the high NG loading of both membranes suggested by elemental analysis (cf. section 4.3.4.1). Therefore, in the latter case most NG should be hidden in PES matrix. This may be due to viscosity difference between MNP-NG-PES dope solution and NG-PES dope solution. As the viscosity of NG-PES dope solution is lower than that of MNP-NG-PES dope solution, NG has more mobility in the former; therefore, more of the gel particles have been driven to the water-NMP interface during the solvent-nonsolvent exchange process, resulting in more NG accumulation on the pore walls and bottom surface. In comparison, for MNP-NG-PES membrane with more viscous dope solution, the NG could be more evenly immobilized in the PES matrix. Moreover, as shown in rheological study (cf. section 4.3.3), significant thickening happens for MNP-NG-PES dope solution at 45 ^{o}C at very low shear rate. During the NIPS process, after the film was cast, the shear rate reduced from 15.9 s^{-1} to zero, so that the stronger thickening effect of MNP-NG-PES dope solution would lead to a more homogenous distribution of NG in the membrane than in case of the membrane with only NG. The third column (**a3**, **b3**, **c3** and **d3**) contains images of the top surface, i.e. the barrier layer of the membrane. It is easy to see MNP just beneath the surface of MNP-PES membrane (**b3**) and NG embedded in the surface of NG-PES membrane (**c3**). For MNP-NG-PES

membrane (**d3**), the NG seem to be buried deeper into the membrane, probably again due to higher viscosity of dope solution. And when looking closely at this mixed matrix structure (see the magnified image in **d3**), there are some magnetic nanoparticles around the nanogel particles. The last column (**a4**, **b4**, **c4** and **d4**) shows the porosity of the barrier layer surface at a magnification of 400,000 fold, and it can be seen that all membranes prepared by this NIPS-based method have intrinsic nanopores in the PES matrix, with a diameter around 10 nm in dry state. Such a barrier pore size could make the membranes suitable for ultrafiltration separations based on differences in (macro)molecule size.

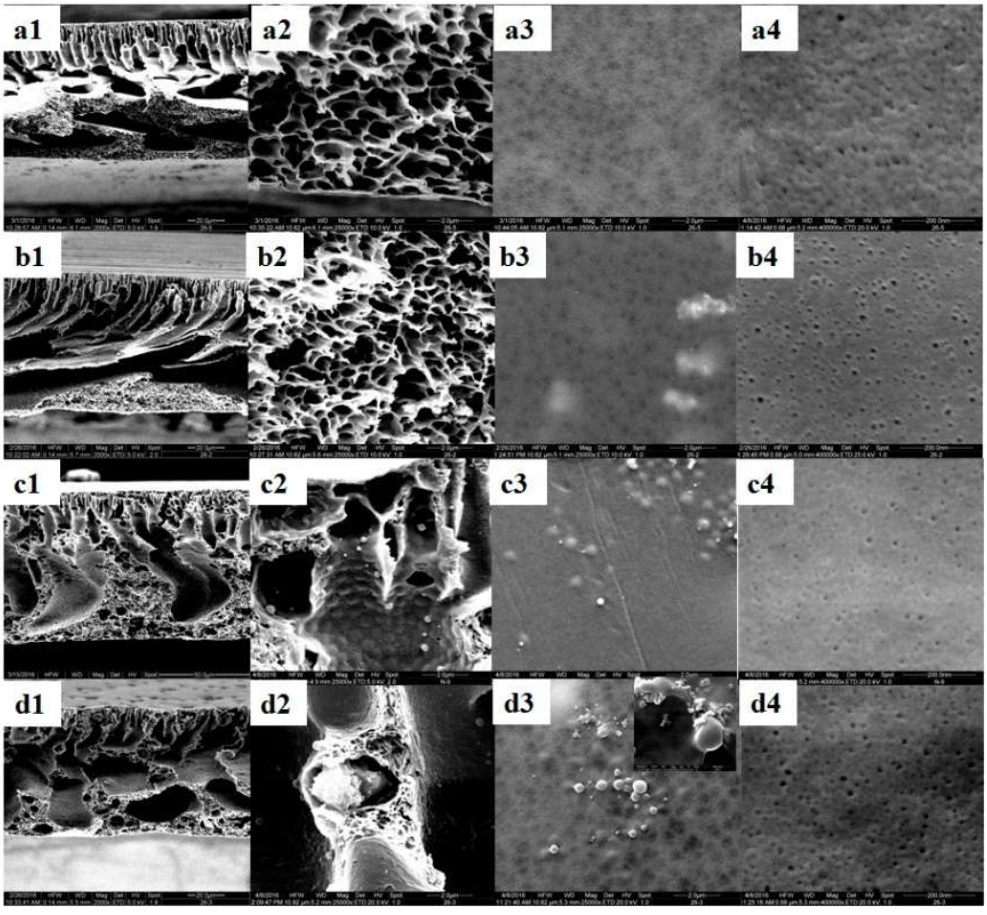

Figure 4.35. SEM images of the different membranes: a1-a4 PES membrane; b1-b4 MNP-PES membrane; c1-c4 NG-PES membrane, and d1-d4 MNP-NG-PES membrane; column 1: cross-section overview; column 2: details in cross-section; column 3: overview on top layer surface; column 4: top layer surface at very high magnification.

4.3.4.5 Water permeability of mixed matrix membranes

Figure 4.36 shows the pure water permeability of different membranes at 25 °C. While the reference PES membrane had a relatively high permeability at 145 ± 95 $l.h^{-1}.m^{-2}.bar^{-1}$, the membranes containing nanomaterials (NG or MNP) had a significantly lower permeability in the range of 30-60 $l.h^{-1}.m^{-2}.bar^{-1}$. Water permeability of ultrafiltration membranes is determined by the thickness, porosity and pore size of the "skin" (barrier) layer and it may also be influenced by the porosity of the whole membrane. Here, the reduction of water permeability by the addition of MNP or NG, can be related to the higher viscosity of the respective dope solutions (cf. section 4.3.3), causing slow-down of phase separation and resulting in a thicker skin layer and a more compact overall membrane structure[208]. Such trend has been seen for the cross-sections, but it is much more complicated to verify for the thin barrier layer (cf. section 4.3.4.4). Moreover, NG-PES membranes had smaller permeability distribution (see the error bars) than MNP-PES membranes, indicating more homogenous distribution within the membrane of the NG compared to the MNP. However, the mixed matrix composite MNP-NG-PES membrane had a permeability of 45 ± 8 l $h^{-1}.m^{-2}.bar^{-1}$, indicating a quite homogenous membrane structure. And this value is still in the range which is typical for ultrafiltration membranes.

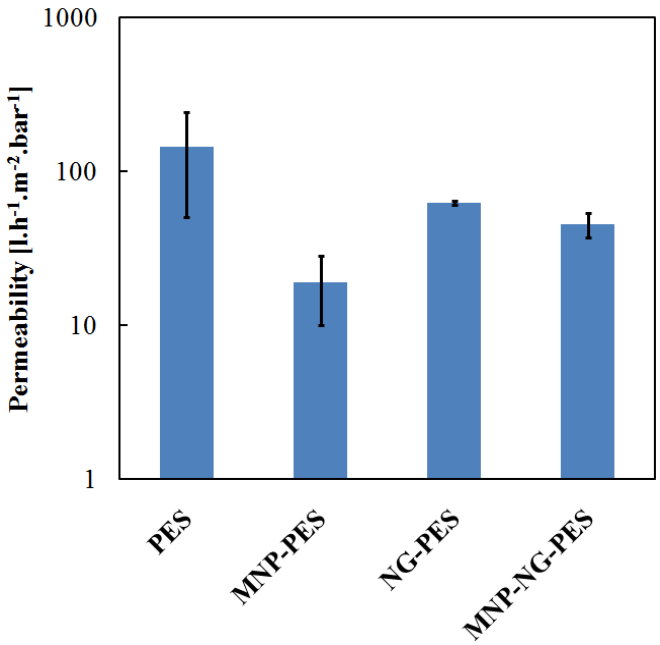

Figure 4.36. Pure water permeability of different membranes at 25 °C; for each type of membrane, data from at least 3 independent samples were taken and averaged.

4.3.4.6 Heating efficiency of MNP- NG-PES membrane

Analogous to the study of the MNP dispersion in water, the heating by exposing the MNP-NG-PES membrane to AMF was also studied; data are provided in **Table 4.9**. Considering the MNP content of the mixed matrix membranes (cf. section 4.3.4.2), their SLP was estimated to be 242 Wg^{-1}, while for MNP alone the value was 265 Wg^{-1} (cf. section 4.3.1.5). Also considering that the calorimetric method provided only a rather rough estimation, it can be concluded that the heating effect of MNP in both forms, dispersed and embedded in the membrane, is identical. These results also indicated that embedding the MNP into the polymer PES which has low heat conductivity had apparently no major effect onto the overall heat transfer rate toward bulk water (cf. section 4.3.1.5).

Table 4.9. Temperature changes of the membrane sample upon AMF excitation (I = 15.6 A, f = 745 kHz, H ~ 20 kAm^{-1})

Sample	Time [minutes]	Temperature change [^{o}C]
Water	1	0.3 ± 0.3
MNP-NG-PES membrane	1	2.0 ± 0.3

4.3.5 Thermo- and magneto-responsive ultrafiltration performance of membrane

4.3.5.1 Thermo-and magneto-responsive water permeability of membranes

Thermo-responsivity of the PNIPAAm NG in the composite membranes was verified by water permeability tests of NG-PES and MNP-NG-PES membranes at 25 ^{o}C and 40 ^{o}C. As shown in **Figure 4.37(a)**, both membranes demonstrated very good thermo-responsivity, with 4 times permeability change for NG-PES membrane and 9 times for MNP-NG-PES membrane upon temperature change, after eliminating the viscosity influence from the measured data presented in the figure. The lower responsivity of NG-PES compared to MNP-NG-PES membrane may be caused by a less even NG distribution in the "skin" (barrier) layer as discussed based on the SEM

data (cf. section 4.3.4.4). Overall, the thermo-responsive water permeability of both membranes indicates the vertical distribution of PNIPAAm NG particles in the skin layer of the membranes; at 40 ^{o}C these particles shrink and create new channels for extra water to pass through the membrane. Considering the thickness of the membrane's barrier (skin) layer of approximately 1 µm (cf. section 4.3.4.4) and the diameter of the NG particles (between ~400 nm in shrunken and ~700 nm in swollen state; cf. section 4.3.2.2), at least some of these "gates" might only contain one PNIPAAm NG particle. Furthermore, despite the microscopically heterogeneous distribution of NG particles in horizontal orientation, which is suggested by the clusters of NG on the membrane top surface in SEM images (cf. **Figures 4.35(c3)** and **Figures 4.35(d3)**), the small error bars in **Figure 4.37(a)** indicate that the variation of water permeability of different samples and hence over larger membrane area is very small. Therefore, macroscopically, the horizontal distribution of NG particles is rather homogenous; at least on the scale of several cm^2 (size of individual membrane sample was 3.1 cm^2). This achievement can be related to the good compatibility of all components in the dope solution, irrespective their complex interactions as indicated by the rheology studies (cf. section 4.3.3).

To evaluate the magneto-responsivity, one MNP-NG-PES membrane with a water permeability of 41 l.h^{-1}.m^{-2}.bar^{-1} at 25 ^{o}C, and 553 l.h^{-1}.m^{-2}.bar^{-1} at 40 ^{o}C was chosen. With AMF amplitude fixed at 20 $\pm$ 10 kA/m and frequency kept at 745 kHz, three cycles of AMF on-off were applied, with each cycle 20 minutes off and 30 minutes on, to test the responsivity and its reproducibility. As shown in **Figure 4.37(b)**, the membrane demonstrated very good magneto-responsivity (with average permeability of 390 l.h^{-1}.m^{-2}.bar^{-1} when AMF is on) and the performance was reproducible over repeated AMF on-off cycles, indicating that the effect of the phase transition of the NG blended in the membrane was totally reversible.

The response time will be influenced by various factors, including content of NG and MNP, the frequency and amplitude of the AMF, the temperature of the feed water and the initial water flux (determining the magnitude of convective cooling)[85]. The content of MNP and the AMF condition would determine the magneto-heating effect: high content of MNP, and high frequency and amplitude of the AMF would ensure more effective heating and therefore shorten the response time. The temperature of the feed water and the initial water flux would influence the convective cooling: short response time is expected with high temperature of feed water and low

initial water flux, as the heat loss by convective cooling is reduced. For the content of NG, high content of NG in PES substrate is also expected to shorten response time, as it would ensure more NG in vicinity with magneto heaters (MNP) and therefore reduce the distance for heat transfer. Here, the steady-state flux achieved about 10 min after switching on the AFM has been somewhat lower than the value observed by heating the feed to 40 °C and it is determined by the interplay between the efficiencies of local heating within the membrane and convective cooling by the feed water kept at 25 °C. The data indicate that the steady state local temperature in the membranes would be below 40 °C, but clearly above the LCST of PNIPAAm, as indicated by the large increase of water flux. However, making a more precise statement is complicated because of the non-linear dependency of PNIPAAm NG swelling on temperature (cf. **Figure 4.23**)[111]. As PNIPAAm NG and MNP were randomly distributed in the PES matrix of the MNP-NG-PES membrane, it can be expected that they would be either directly in contact with each other, or that there could be a PES layer between the magneto-heater MNP and the actuator NG. Upon turning AMF on, the heat generated by MNP can be transferred to PNIPAAm NG via three routes; i) for MNP and NG in direct contact, heat transfer can be direct and very fast; ii) with a PES layer between MNP and NG, heat conduction through PES will add a resistance; iii) heat from MNP or MNP/PES can also be transferred to PNIPAAm NG via conduction through water in the pores. Heat transfer rate by conduction is directly proportional to thermal conductivity of the material and inversely proportional to the thickness of the material. Thermal conductivities of PES (0.13-0.18 $Wm^{-1}K^{-1}$) and water (0.58 $Wm^{-1}K^{-1}$) are relatively low, and much smaller than for iron oxide (4 $Wm^{-1}K^{-1}$; all data for 25 °C). However, in the skin layer of the membrane which is determining the water flux, the average distance between MNP and PNIPAAm NG is very small (estimated to be not more than 1 µm, i.e. the approximate thickness of the skin layer). Therefore, local heat transfer should be fast and the effect of the thermal insulating layer of PES or water should not have an effect on the macroscopic response. This estimation is supported by the results for heating efficiency (cf. section 4.3.1.5 and section 4.3.4.6), as AMF stimulation of the same mass of MNP either embedded in the mixed matrix composite membrane or just dispersed in water lead, within the range of error, to the same rate of temperature increase in the surrounding bulk water (about 2 ^{o}C of temperature increase in 1 minute).

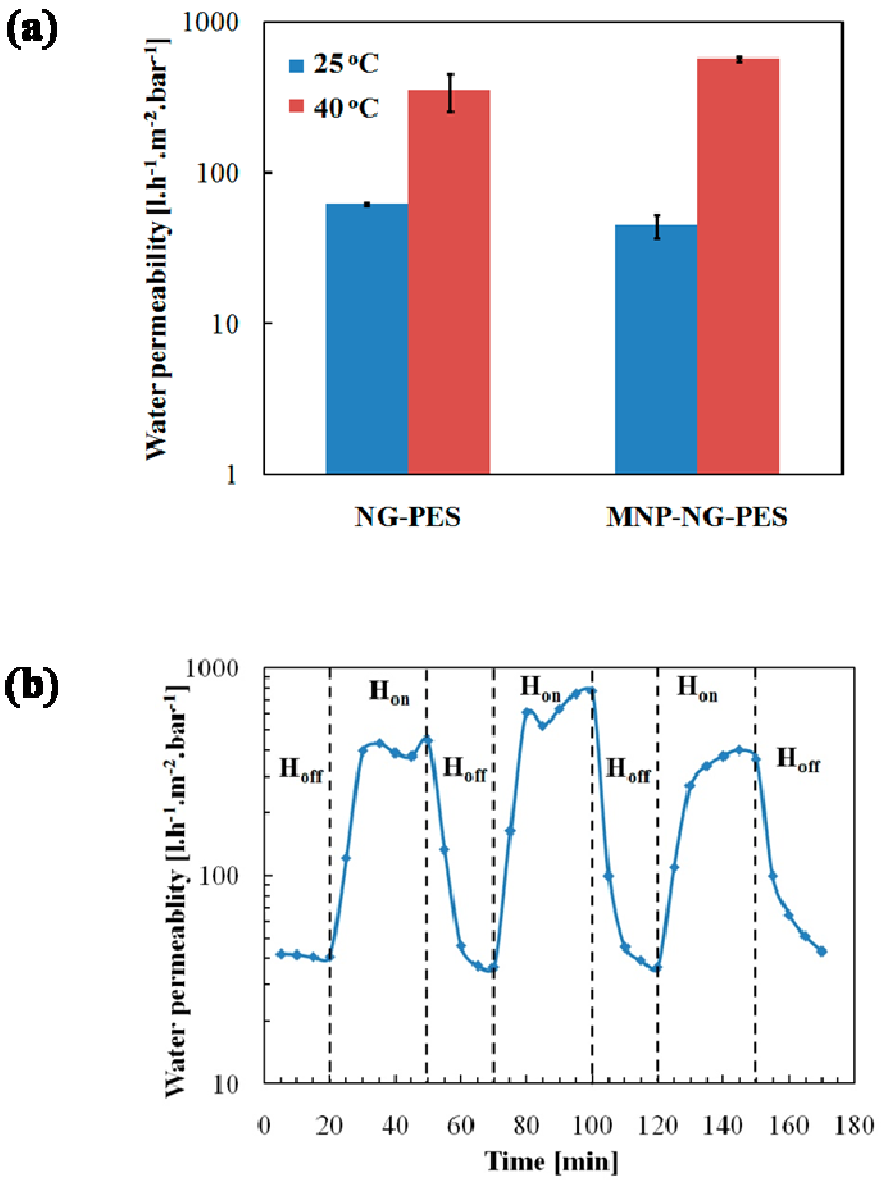

Figure 4.37. (a) Thermo-responsive water permeability of NG-PES and MNP-NG-PES membranes; for each kind of membrane, data from 4 samples were taken and averaged; (b) magneto-responsive water permeability of a representative MNP-NG-PES membrane.

Moreover, fluxes are stable under constant conditions and the observed response is reproducible over a few cycles, indicating sufficient stability of the composite membrane with respect to leaching of the active particles. For the separation and responsive function, only the fraction of particles in the relatively dense barrier layer of the membrane (cf. **Figure 4.35**) is important, and it seems plausible that the relatively large particles will be very well entrapped in that porous layer. For the macroporous support layer and the bottom surface with pores having diameters in the µm range, there is a risk that some MNP could be washed out and leach from the membrane. Still, leaching of the nanomaterials during application can be avoided by extensively washing the membrane before use. Overall, the data suggest that the NG work as effective gate for the water flux which can be triggered by the MNP.

4.3.5.2 Thermo-responsive molecular sieving

To evaluate thermo-responsive molecular sieving performance of the nanogel gates, dextran ultrafiltration for NG-PES membrane was carried out at both 25 ^{o}C and 40 ^{o}C. A membrane with initial water permeability of 60 $l.h^{-1}.m^{-2}.bar^{-1}$ at 25 ^{o}C was chosen and 1 g/l of dextran mixture consisting half of dextran with 35 kDa and half of dextran with 2000 kDa was used as feed. As shown in **Figure 4.38(a)**, while dextran rejection was around 76% at 25 ^{o}C, it dropped to only 14% at 40 ^{o}C. Dextran ultrafiltration flux at 25 ^{o}C was much lower than water flux due to concentration polarization; a large increase of ultrafiltration flux was observed. The pure water permeability at 25 ^{o}C before, in between and after dextran ultrafiltration was similar, with a slight decreasing tendency, suggesting low extent of fouling effects (**Figure 4.38(b)**).

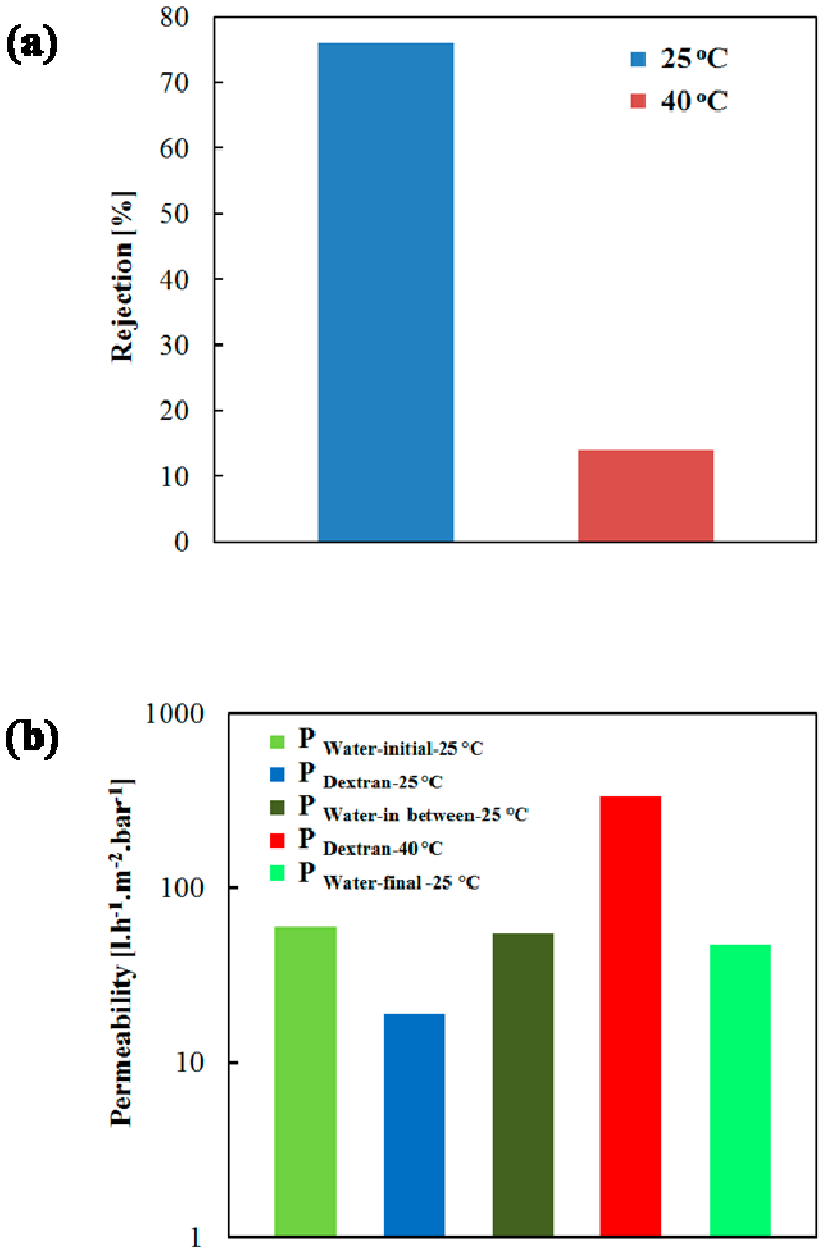

Figure 4.38. Molecular sieving performance of NG-PES membrane at 25 °C and 45 °C: (a) overall rejection for a mixture of dextran 35 kDa and 2000 kDa analyzed by TOC, (b) water and dextran filtrate solution permeabilities monitored during filtration tests.

4.3.5.3 Magneto-responsive molecular sieving

Ultimately, magneto-responsive molecular sieving performance of MNP-NG-PES membranes was studied by ultrafiltration of solutions of dextran with different sizes, with and without excitation by AMF. Because this mixed matrix composite membrane was quite homogenous as indicated by very small deviation of water permeability and stimuli-responsivity between different samples (cf. **Figure 4.37(a)**), four membrane samples with similar water permeability and stimuli-responsivity were used for ultrafiltration of different dextran solutions, in order to eliminate the possible influence of dextran fouling during the ultrafiltration[209].

As shown in **Figure 4.39(a)**, when AMF was off, the membrane had over 90% of rejection for dextran with molecular weight of 70 kDa (hydrodynamic diameter 11 nm, cf. **Table 3.4**). When the AMF was on, it lost its rejection for dextran molecular weight less than 100 kDa (13 nm, cf. **Table 3.4**), and had only 50% rejection for dextran 500 kDa (28 nm, cf. **Table 3.4**), but the rejection for dextran 2000 kDa (52 nm, cf. **Table 3.4**) remained around 83%. Therefore, there was an obvious shift of the molecular weight cut-off (MWCO, defined as molecular weight for what rejection is >90%) from less than 70 kDa without to more than 500 kDa when the AMF was on. To further evaluate the magneto-responsive change of rejection for dextran with specific size, the magneto-responsive change of rejection factor is introduced as the ratio of rejection for dextran molecules at off state relative to on state of AMF. As shown in **Figure 4.39(b)**, a change of rejection by switching on or off the AMF by a factor of 170 can be obtained for dextran with molecular weight of 35 kDa, i.e. somewhat below the MWCO. This factor is very high ($\geq$ 90) in the solute size range of ~8 to ~13 nm (measured for dextran 35 kDa to 100 kDa) and rather low for solute sizes below and above this range, indicating such membrane would have a good switchable sieving effect for solute in the size of ~8 to ~13 nm.

Furthermore, the ultrafiltration of a dextran mixture has been carried out, composed of dextran 35 kDa and dextran 2000 kDa, to find out the exact MWCO of the membrane. It should be noted that both dextrans have a rather broad molecular weight distribution so that the entire molecular weight range is well covered (cf. **Figure 3.5**). As shown by the results in **Figure 4.39(c)**, the MWCO of the membrane shifted from 68 kDa at room temperature without AMF to 1750 kDa with AMF on. The slope of the sieving curve is steep which indicates a good quality of the ultrafiltration barrier. Considering the trade-off between flux and selectivity, the membrane

cannot compete with the commercial conventional polymeric UF membranes which have higher pure water permeabilities (100-1000 $l.h^{-1}.m^{-2}.bar^{-1}$) at the same $MWCO^{210}$, but its overall performance is good.

The permeability of the membranes was also monitored during the ultrafiltration tests and is shown in **Figure 4.40**. The permeability of all membranes was quite stable at 25 ^{o}C without AMF and largely increased when AMF is on, indicating the high effectiveness of magneto-heating. Moreover, the permeability of all membrane had fully recovered after each round of dextran filtrations, suggesting that the stimuli-responsive molecular sieving behavior of such membranes is reversible.

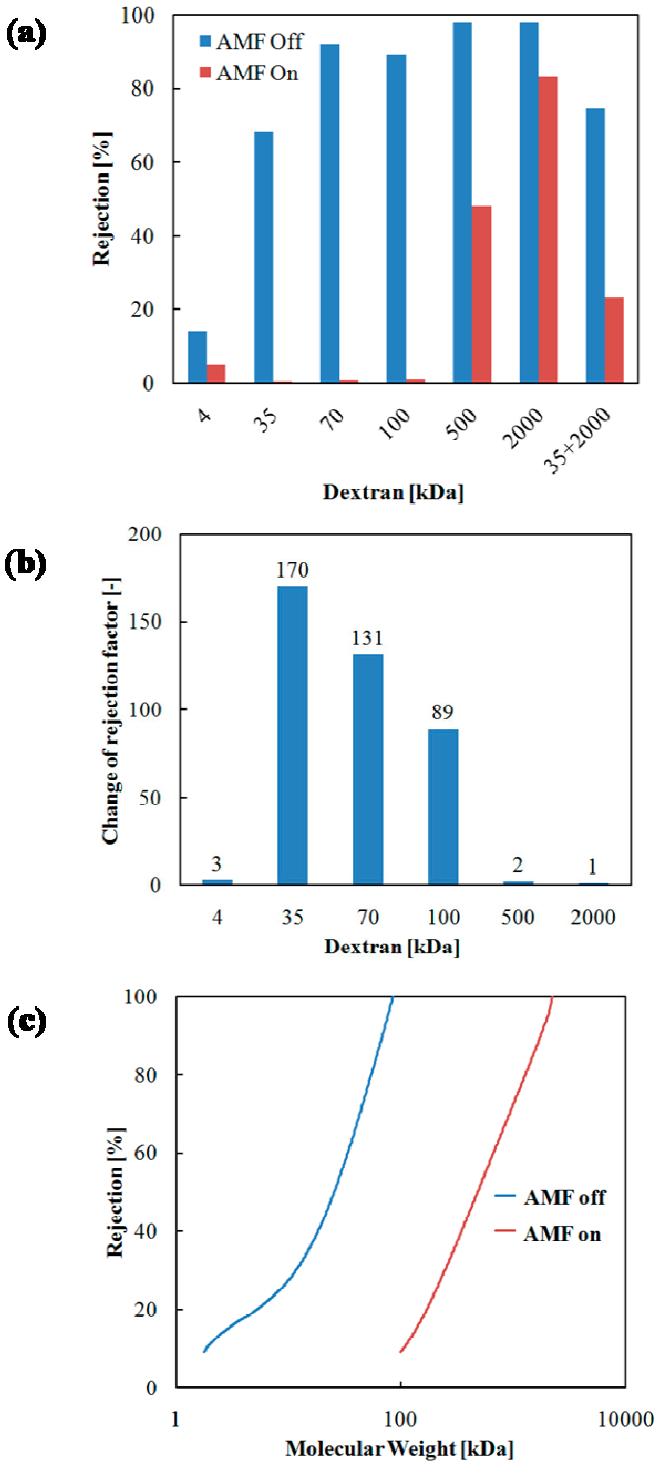

Figure 4.39. Molecular sieving performance of MNP-NG-PES membranes with and without AMF: (a) rejection of different sizes of dextran analyzed by TOC, (b) magneto-responsive change of rejection factor for different sizes of dextran (c) dextran rejection curve analyzed by GPC.

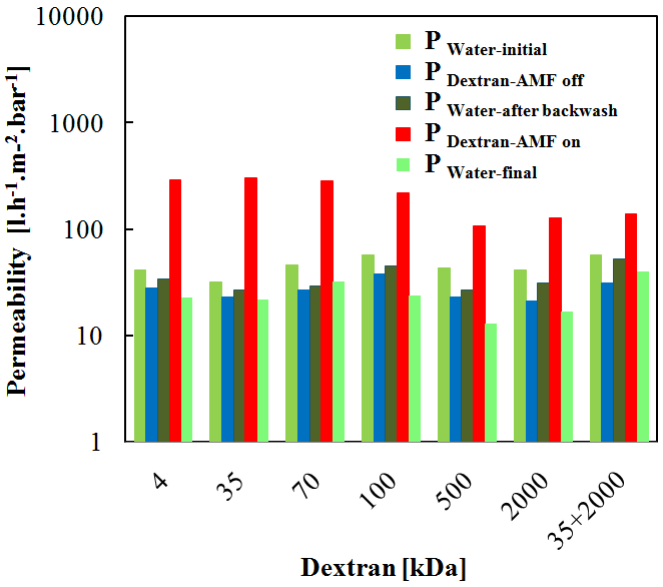

Figure 4.40. Water and dextran solution filtrate permeabilities of membranes monitored during ultrafiltration tests.

The drastic shift of MWCO along with the other UF data proves the hypothesis of two types of channels in the membrane's barrier layer (as shown in **Figure 4.41**), which had simultaneously been formed in the NIPS process after casting the dispersion of NG and MNP in the PES solution (cf. sections 4.3.3 and 4.3.4). It is hypothesized that at 25 °C and without AMF, the PNIPAAm NG is swollen and essentially impermeable at the applied trans-membrane pressure (less than 1.5 bar) so that only a relatively small flux and relatively small molecules (diameter less than ~11 nm) can pass through the intrinsic nanopores of the PES-based membrane (note that this nanoporosity was detected in the high resolution images of the top layer surface of all four membranes; cf. **Figure 4.35** in section 4.3.4.4). When the AMF is on, the heat generated by MNP can cause the shrinking of NG particles which are immobilized in the porous PES matrix, thus opening extra channels, which are much larger than the intrinsic nanopores in the PES; therefore much higher flux is observed and much bigger molecular (up to a diameter of ~50 nm) can pass.

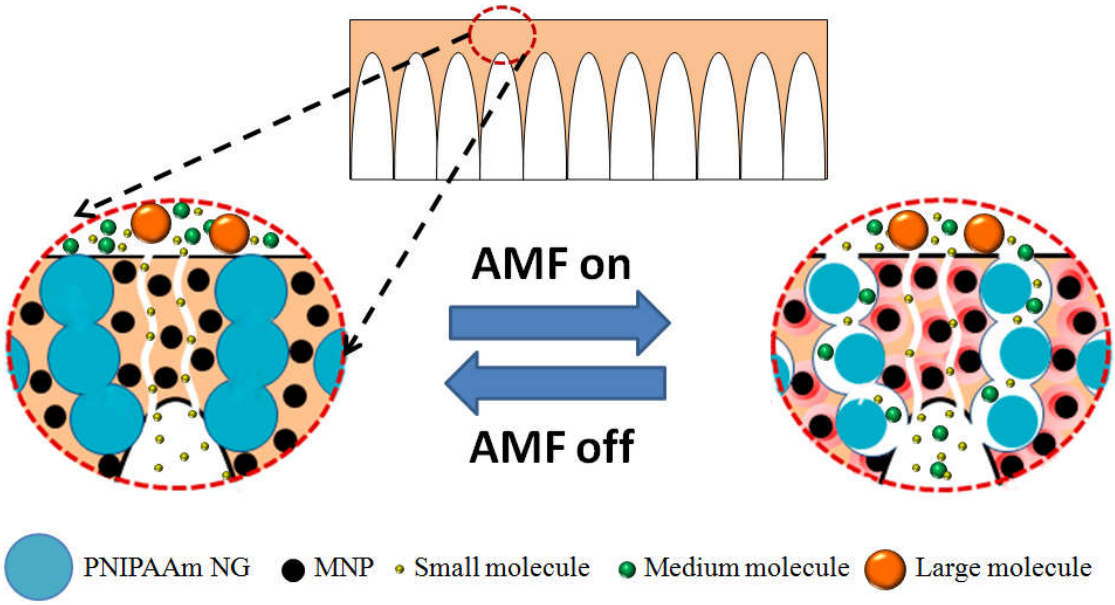

Figure 4.41. Schematic illustration of anisotropic magneto-responsive PES-based iron oxide and hydrogel mixed matrix composite ultrafiltration membrane with two types of channels: the inert channel formed by intrinsic nanopores of anisotropic PES substrate; only allows small molecules to pass through the membrane; the tunable channel formed by the PNIPAAm NG; can reversibly adjust molecule sieving through the thin porous barrier layer of the membrane, by remote control triggering of nearby "nanoheaters" with AMF.

4.4 Comparison of magneto-hydrogel pore-filled membrane and mixed matrix membrane

4.4.1 Comparison of two membrane types (preparation, structure and performance)

While magneto-hydrogel pore-filled membranes and mixed matrix membranes demonstrate analogous magneto-responsive molecular sieving effect, they are different in many aspects. A comparative overview for the two different kinds of magneto-responsive ultrafiltration membranes is given in **Table 4.10**, with respect to structure, separation performance and preparation.

With respect to structure, first, the morphology of thermo-responsive elements in two types of membranes is different. The magneto-hydrogel pore-filled membranes use PNIPAAm hydrogel

mesh as the responsive sieving medium while the mixed matrix membranes use PNIPAAm nanogel as thermo-responsive gates. The mesh size of acrylamide-based hydrogel is typically less than 20 nm at room temperature [133, 190], therefore it is very good ultrafitration sieving medium. For PNIPAAm nanogel with 5% MBA, despite its size change could be as large as 300 nm in response to temperature change from 25 °C to 40 °C when it is placed in free space; the size change of created channel can be also controlled within ultrafiltration range; by confining the nanogel within a limited space. Therefore, both mesh size of PNIPAAm hydrogel and the entire PNIPAAm NG particle could be designed as responsive gating elements for ultrafiltration. Second, the MNP size distribution and loading are different for the two types of membrane. For magneto-hydrogel pore-filled membrane, 40 nm commercial MNP with narrow size distribution and high heating capacity (SLP = 672 W/g) was used. However, due to low porosity of the PET track-etched membrane and complexity for MNP loading inside the micrometer-range pores, the overall loading of MNP in this case is only around 5% (cf. section 4.2.5.1). Still, as MNP are directly located in the actuator and sieving medium, the PNIPAAm hydrogel network, the magneto-heating was effective enough to cause switchable molecular sieving effect (cf. section 4.2.6.3). For mixed matrix membrane, 40 $\pm$ 10 nm self-made MNP with broader size distribution and medium heating capacity (SLP = 265 W/g) was used. Yet the loading of MNP in such membrane can be easily adjusted by tuning the composition of dope solution, and here a high loading (10 %, mass ratio relative to PES) was used to achieve comparable heating effect. At last, while the magneto-hydrogel pore-filled membranes, prepared by post-modification of commercial track-etched PET membrane, are symmetric membranes with large barrier thickness (23 μm) and limited porosity (13.4%), the mixed matrix membranes prepared by NIPS process, are asymmetric membranes with thin skin layer as barrier (less than 1 μm) and relatively high porosity (typical porosity for PES ultrafiltration membrane is around 70%).

With respect to the performance, magneto-hydrogel pore-filled membrane has relatively low permeability in the range 2-10 $l.h^{-1}.m^{-2}.bar^{-1}$ at 25 °C, due to low porosity of PET track-etched membrane and the large barrier thickness (see above). Mixed matrix membrane has higher permeability at around 40-60 $l.h^{-1}.m^{-2}.bar^{-1}$ at 25 °C, which is more near to permeability of commercial conventional polymeric UF membranes (100-1000 $l.h^{-1}.m^{-2}.bar^{-1}$) at the same MWCO. And this is due to the asymmetric structure (see above). For the molecular sieving effect, magneto-hydrogel pore-filling membrane has a rather rough tuning for MWCO, with

MWCO smaller than 2000 kDa at "off state" of AMF (at 25 ^{o}C) and much bigger than 2000 kDa at "on state" of AMF, perhaps due to the heterogeneity of composite hydrogel network. In comparison, mixed matrix membrane can achieve a shaper separation effect with finer tunability within the ultrafiltration range. This is because of the two channel mechanism: at AMF off state, the NG channels are closed as the PNIPAAm NG are in swollen state, therefore, only small molecules can pass through the membrane via nanopore channels and a sharp MWCO can be obtained due to the narrow size distribution of the nanopores (cf. **Figure 4.35** and **Figure 4.39(c)**); at AMF on state, the NG channels are open as the PNIPAAm NG is in shrunken state, therefore, big molecules can also pass through the membrane via newly created NG channels and MWCO of the membrane is shifted to higher value (cf. **Table 4.7**, **Figure 4.39(a)** and **Figure 4.39(c)**). For the magneto-heating effect, due to the higher loading of MNP for mixed matrix membrane, its response time is shorter than the response time of magneto-hydrogel pore-filled membrane. At last, overall the mixed matrix membranes demonstrated low propensity to fouling (cf. **Figure 4.40** and **Figure 4.27**), due to their asymmetric structure. In comparison, the magneto-hydrogel pore-filled membranes are easier to foul; this is caused by the more crosslinked 3-D network of hydrogel, which can easily trap the foulants within it.

With respect to preparation, magneto-hydrogel pore-filled membranes were prepared by *in situ* reactive pore-filling functionalization of commercial PET membrane, which is complicated and time-consuming; while mixed matrix membranes were obtained by industrialized NIPS process, which promises the mass production of such membrane in a simple way.

So overall, the mixed matrix membranes have better performance and easier fabrication route than the magneto-hydrogel pore-filled membrane.

Table 4.10. Overview on two types of magneto-responsive molecular sieving membranes

		Magneto-hydrogel pore-filled membrane	**Mixed matrix composite membrane**
Structure	Responsive gating element	PNIPAAm hydrogel mesh	PNIPAAm nanogel
	Size distribution of MNP	40 nm	40 $\pm$ 10 nm
	Loading of MNP	~5%	~10%
Filtration Performance	Water permeability at 25 °C	2-10 $l.h^{-1}.m^{-2}.bar^{-1}$	40-60 $l.h^{-1}.m^{-2}.bar^{-1}$
	MWCO at 25 °C	< 2000 kDa	~ 70 kDa
	Water permeability at AMF on state	25-50 $l.h^{-1}.m^{-2}.bar^{-1}$	350-550 $l.h^{-1}.m^{-2}.bar^{-1}$
	MWCO at AMF on state	>> 2000 kDa	1750 kDa
	Response time	15-20 minutes	~10 minutes
	Fouling by dextran	moderate	low
Preparation	Preparation method	Post modification via novel pore-filling technique	Industrially established NIPS process
	Scalability	Difficult	Easy and scalable

4.4.2 Further attempts to improve mixed matrix membrane

Despite the advantages mentioned above for mixed matrix membrane, there is still space for improvement:

1. The permeability is lower than that of commercial traditional ultrafitration membrane with same MWCO[210], therefore, it should be further improved.
2. While the major responsive sieving effect comes from PNIPAAm NG and MNP in the skin layer, PNIPAAm NG and MNP are distributed all through the matrix. It would be more favorable to design a more ordered structure with PNIPAAm NG and MNP only present in the skin layer, therefore to save those functional components.

Based on those considerations, two preliminary investigations were performed separately:

1. Use porogen polyvinylpyrrolidone (PVP) to increase the porosity of the membrane, therefore improve water permeability.

2. Use VIPS to prepare an alternative membrane structure with more ordered and controlled pore morphology.

4.4.2.1 Increase of water permeability for mixed matrix membrane (by adding PVP)

PVP is a commonly used porogen in membrane industry to increase the porosity and permeability of polymeric membranes. It is found that, by adding PVP in dope solution, the porosity of the membrane will increase while the pore size will decrease[211, 212]. And it is suggested that, the hydrophilic PVP would not only work as porogen, which is eluted out and forms pores during NIPS process, but also work as polymer surfactant to increase the surface of contact between polymer agglomerates and nonsolvent (water) and therefore reduce size of void spaces during phase separation process[211, 212]. Here, based on the MNP-PES membrane discussed before, 1% PVP (mass ratio relative to PES) was added. As shown in **Figure 4.42**, the membrane with 1% of PVP has permeability of 479 $\pm$ 52 $l.h^{-1}.m^{-2}.bar^{-1}$, while membrane without PVP has only permeability of 19 $\pm$ 9 $l.h^{-1}.m^{-2}.bar^{-1}$. Therefore adding PVP can significantly increase the porosity of the membrane.

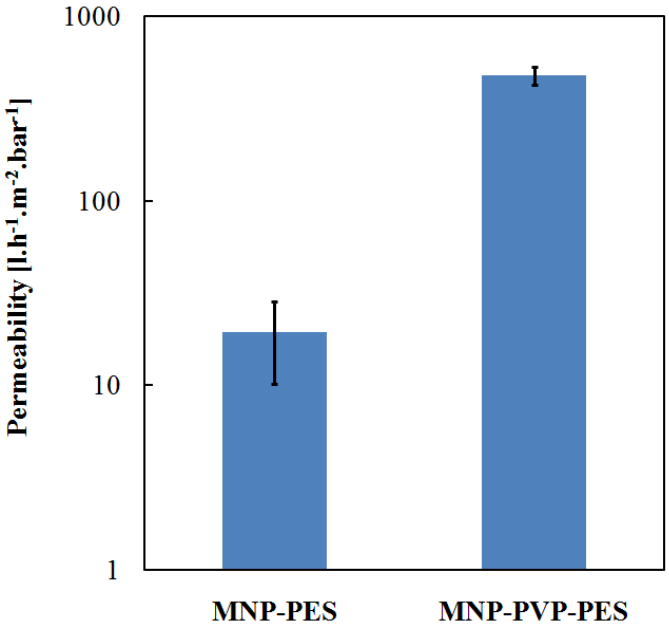

Figure 4.42. Water permeability of membranes with and without PVP: MNP-PES membrane contains 10% of MNP, MNP-PVP-PES membrane contains 10% MNP and 1% PVP.

Further, dextran filtration tests for dextran molecules with different molecular weight were carried out, to determine the MWCO of membrane with 1% PVP (MNP-PVP-PES membrane). As shown in **Figure 4.43**, such membrane has 62% rejection for dextran 35 kDa, 95% rejection for dextran 100 kDa, and 99% rejection for dextran 2000 kDa. Therefore its MWCO should be around 100 kDa, which is still within ultrafiltration range and similar with the MNP-NG-PES membrane (cf. **Figure 4.39(c)**).

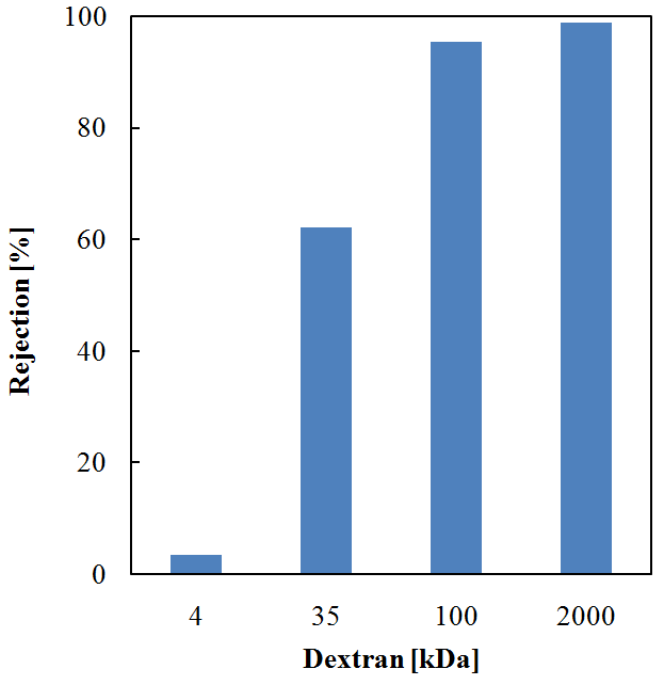

Figure 4.43. Molecular sieving performance of MNP-PVP-PES membranes at 25 °C: rejection of different dextrans analyzed by TOC.

So overall, adding PVP will increase the barrier layer porosity while not affecting ultrafiltration property of the membrane. This could be employed in the future to improve the performance of such magneto-responsive mixed matrix membranes.

4.4.2.2 Alternative membrane structure prepared by VIPS process

To improve the performance of mixed matrix membrane, alternative membrane structure, like an asymmetric membrane with thermo-responsive PNIPAAm NG inlaid in nonporous substrate as

gates for permeate, as shown in **Figure 4.44**, was also envisioned. It is believed that, unlike the mixed matrix membranes prepared before, which have two kinds of channels: inert nanopore of PES substrate, and thermo-responsive PNIPAAm NG, membrane with such structure will only have the responsive channel of PNIPAAm NG. Therefore, there would be more flexible for the tuning of molecular sieving.

As more flexibility for tuning the membrane morphology can be obtained with VIPS process[54] (cf. section 2.1.2), VIPS in combination with NIPS, was introduced to obtain proposed structure in **Figure 4.44**. It is expected that by adjusting dope solution composition and VIPS condition, a microporous top surface and a dense nonporous bottom surface inlaid with a lot of PNIPAAm NG as responsive gate will be obtained. And the dense nonporous bottom surface was planned to be used as effective ultrafiltration layer in application.

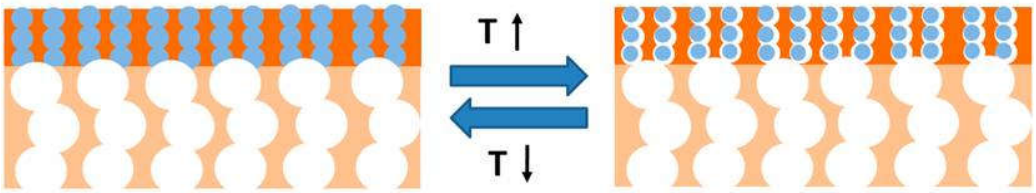

Figure 4.44. schematic illustration of asymmetric membrane with only thermo-responsive PNIPAAm as gates for permeate.

A prototype membrane was prepared based on 14.5% PES and 1.45% of PNIPAAm NG, with DMAc as solvent. The membrane was prepared by first 4 minutes of exposure to humid air (relative humidity, RH: 80%, 25 ^{o}C), and then immersion into water bath (25 ^{o}C). As shown in **Figure 4.45**, there are many PNIPAAm NG isolated from each other and well inlaid on the top and bottom surfaces (**Figure 4.45(a) and (b)**). Moreover, while for the top surface, there are some micron-range pores, the bottom surface is smooth and without pore. Perhaps, this is because during the short exposure time (4 minutes), water vapor didn't penetrate to the bottom surface, therefore a smooth surface is formed due to the fast solvent exchange between DMAc and water when the casted film is placed into water bath. Moreover, at high magnification (**Figure 4.45(c)**), it can be seen, that the PES substrate of such membrane is quite dense and almost has no pore (in comparison, the PES membrane prepared with NMP has nanopores, cf.

Figure 4.35). The cross-section structure is demonstrated in **Figure 4.45(d)**, and it shows a typical symmetric cellular-like structure obtained by VIPS process. Yet, the water permeability of such membrane was extremely low. At 25 ^{o}C, there was no water flux at 2 bar. At 40 ^{o}C, maybe because the shrinking of PNIPAAm NG created new channels for water pass through, the permeability was about 1 $l.h^{-1}.m^{-2}.bar^{-1}$.

Based on this prototype, VIPS process parameters (eg. exposure time) and formulation (PES and PNIPAAm NG content) were varied to obtain ideal structure and performance. It is expected that a membrane with more porous top surface and dense nonporous bottom surface covered with NG should be obtained on the basis of the prototype membrane. Moreover, the membrane should have relatively higher water permeability and certain thermo-responsivity.

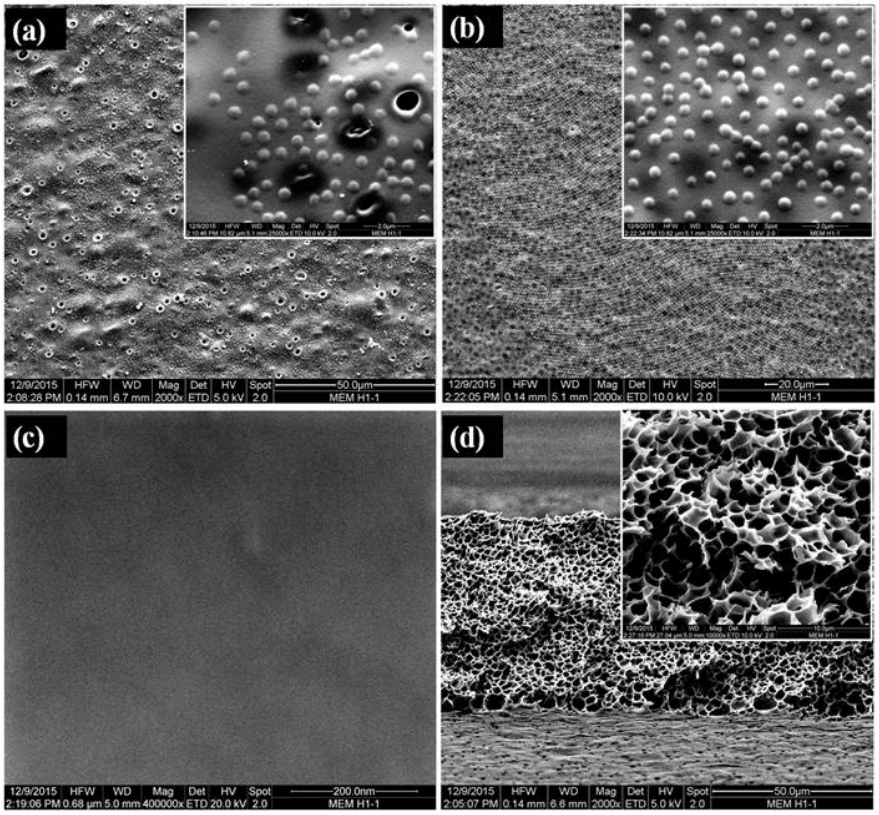

Figure 4.45. Prototype NG-PES membrane obtained by introducing VIPS process, based on 14.5 % PES: (a) top surface, (b) bottom surface, (c) high magnification of PES substrate (of bottom surface) and (d) cross-section.

Based on 14.5% PES dissolved in DMAc, mass ratio of PNIPAAm NG to PES and exposure time to humid air (RH: 80%, 25 °C) were varied, to explore influence of formulation and processing parameters on membrane structure. It is expected the ratio of hydrophilic additive PNIPAAm NG in dope solution would not only affect the content of NG in resulted membrane, but also influence the structure of membrane by affecting the hydrophilicity and viscosity of dope solution. With higher content of NG, while the hydrophilicity of dope solution would increase and accelerate the transfer of water from atmosphere to the dope solution, viscosity of dope solution would also increase, decelerating the (de)mixing of the system and hindering the phase-separation kinetics[54]. For the exposure time, as it would influence the penetration depth of vapor into the casted film and porous structure (cf. section 2.1.2), it is expected, with certain exposure time, the vapor will only reach certain depth but not to the bottom of the casted film, and an ideal structure with micrporous structure on the top surface and dense nonporous bottom surface can be obtained (cf. **Figure 4.44**).

The cross-sections of different membranes are shown in **Figure 4.46(a)**. While the membrane without NG (**Figure 4.46(a)**, first line) has typical symmetric cellular structure with relatively small cell size, membranes blended with NG generally have bigger cell sizes. Moreover, for membranes blended with NG, a lot of NG particles were found self-assembled on the wall of the cells. Similar finding was made by Luo et al., for the PNIPAAm NG-PES membrane prepared with NMP as solvent via VIPS process[31]. Yet, not much difference can be seen on cross-section for membranes prepared with different exposure time. For the top surface (**Figure 4.46(b)**), more difference can be seen for the membrane with different formulation and exposure time. First, generally, membranes with NG are more porous on top surface and it seems higher fractioin of NG would result in more pores. This is related to the hydrophilicity of PNIPAAm NG: more hydrophilic NG enhances the penetration of water vapor into the membrane. Further, it was found that the longer exposure time would lead more porous and smoother top surface, indicating that certain time is needed for pore formation due to the slow demixing during VIPS process. Yet, despite the high fraction of NG in dope solutions, for all cases, very few NG were found on the top surface. For the bottom surface of membranes with 10% and 15% NG, some NG were aggregated and not integrated into the PES substrate. As PES dope solution prepared with DMAc has much lower viscosity than the dope solution with same content of PES prepared with NMP [213]. It was suspected that, during solvent and nonsolvent exchange, there is less

diffusive hindrance for NG to reach surface. Therefore, they could easily project too much out of PES substrate, and eventually lead to more loss of NG during the washing step.

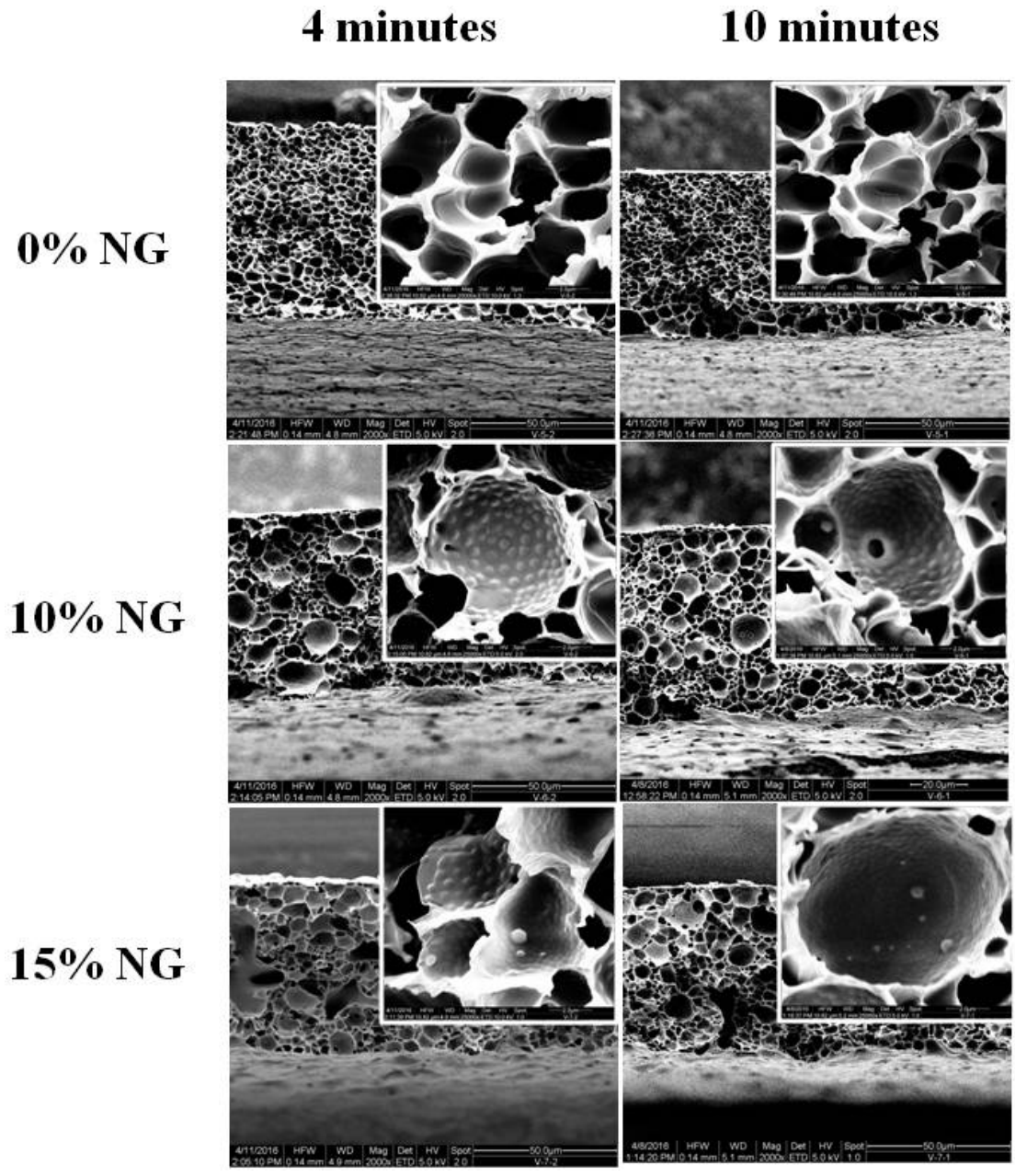

(a)

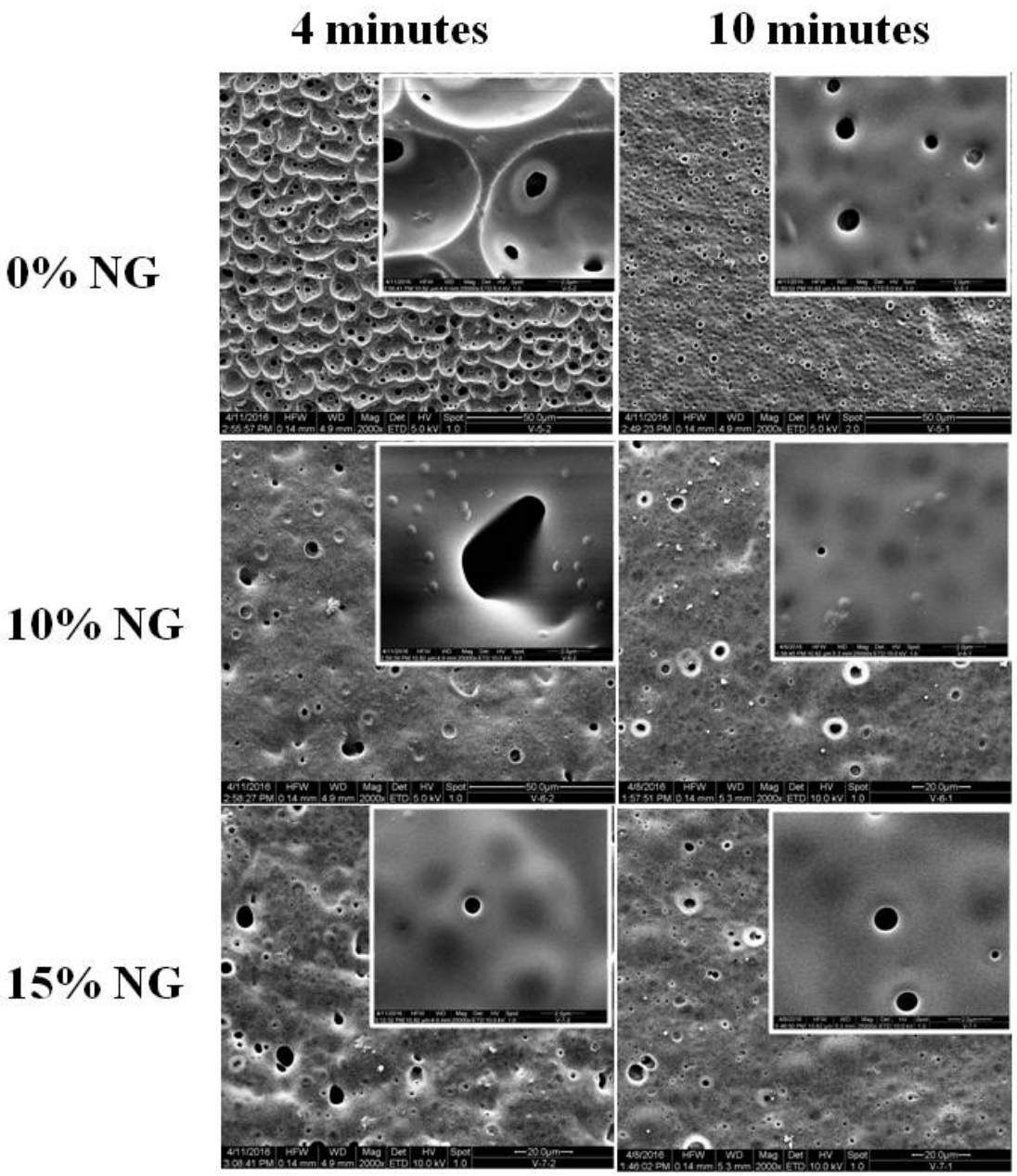

(b)

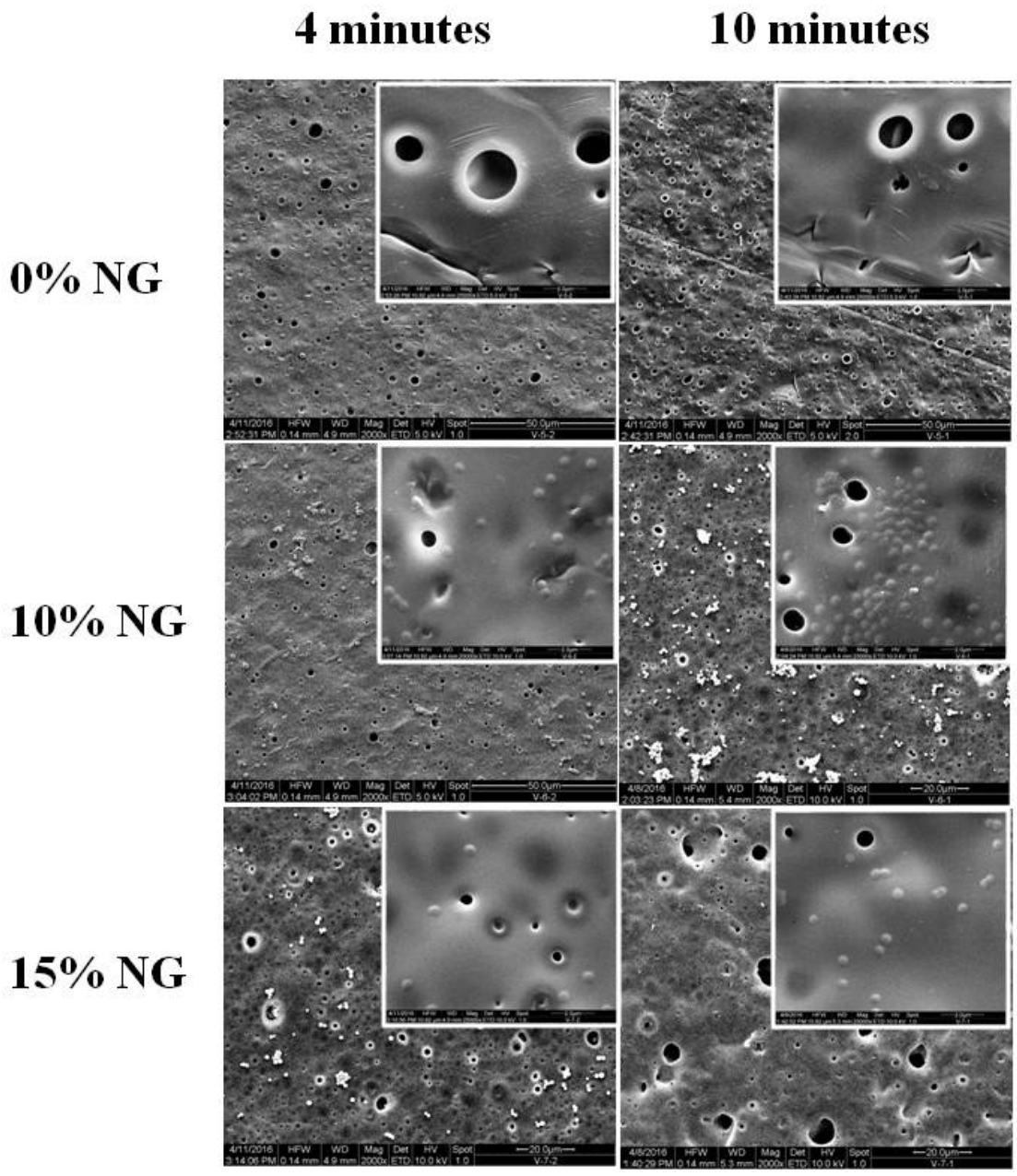

Figure 4.46. SEM pictures of PES membranes based on 14.5% PES and prepared with different PNIPAAm NG fractions and VIPS durations: (a) cross-section, (b) top surface and (c) bottom surface.

Further, the PES content was increased to 17% in order to increase the viscosity of dope solution. Various NG fractions (mass ratio relative to PES, 0%, 10%, 15%, 20%) and exposure times (2 minutes, 4 minutes and 10 minutes) during VIPS were investigated. As shown in **Figure 4.47 (a)**, all membranes blended with NG, demonstrated structure with big pores with nanogel laid in cross-section. While the membrane blended with 10% and 15% NG still has the cellular-like structure, with a lot of NG inlaid on the wall of cells, the cross-section of membrane blended with 20% NG is more amorphous and the cells are interconnected. Maybe because membrane with 20% NG has too much hydrogel component, which is quite fragile, when it was dried under vacuum at room temperature, the hydrogel shrunk and affected the structure. When looking at the top surface (**Figure 4.47 (b)**), with the increase of NG fraction and exposure time, the surface is more porous, due to the enhanced water vapor transfer across the polymer solution. With respect to NG, overall, NG presence on top surface also increases with the increase of exposure time. Maybe this is because longer exposure time allows more NG to transfer to the interface of the membrane. At last, for the bottom surface, which we would like to use as effective ultrafiltration layer, the NG presence also increases with increase of exposure time. Membranes exposed to water vapor for 10 minutes have most NG present on the bottom surface. Moreover, it seems 10% of NG in dope solution is enough to get bottom surface covered with NG. However, for all membranes, micron range pores are also found on the bottom surface, therefore, we failed to obtain a structure presented in **Figure 4.44**, with NG inlaid in nonporous PES substrate. Maybe we can only achieve such structure when the water taken up from vapor doesn't penetrate the casted dope solution, and this is difficult to control. As the proposed ideal structure (cf. **Figure 4.44**) was not obtained, the water permeability test was not carried out for those membranes.

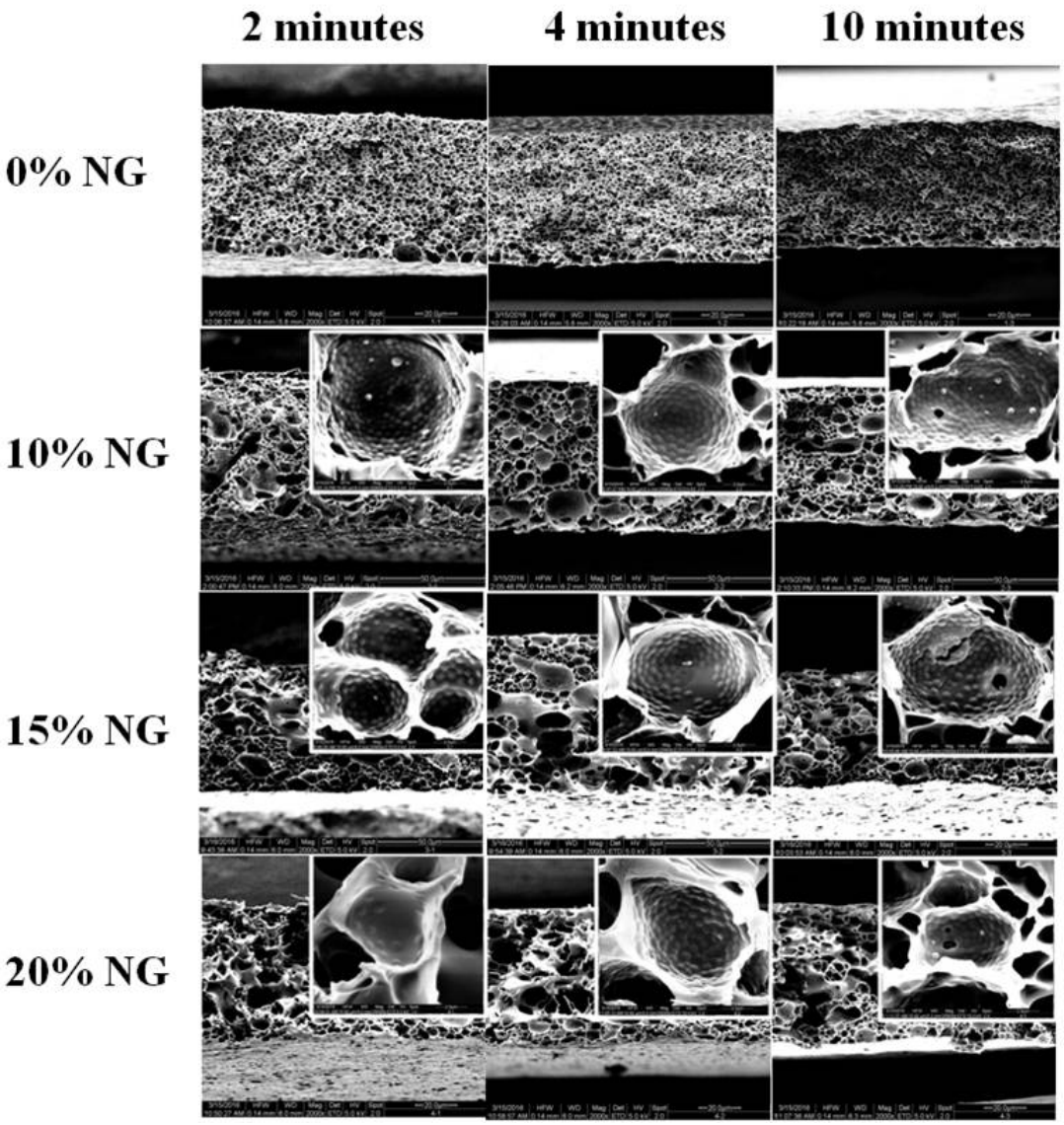

(a)

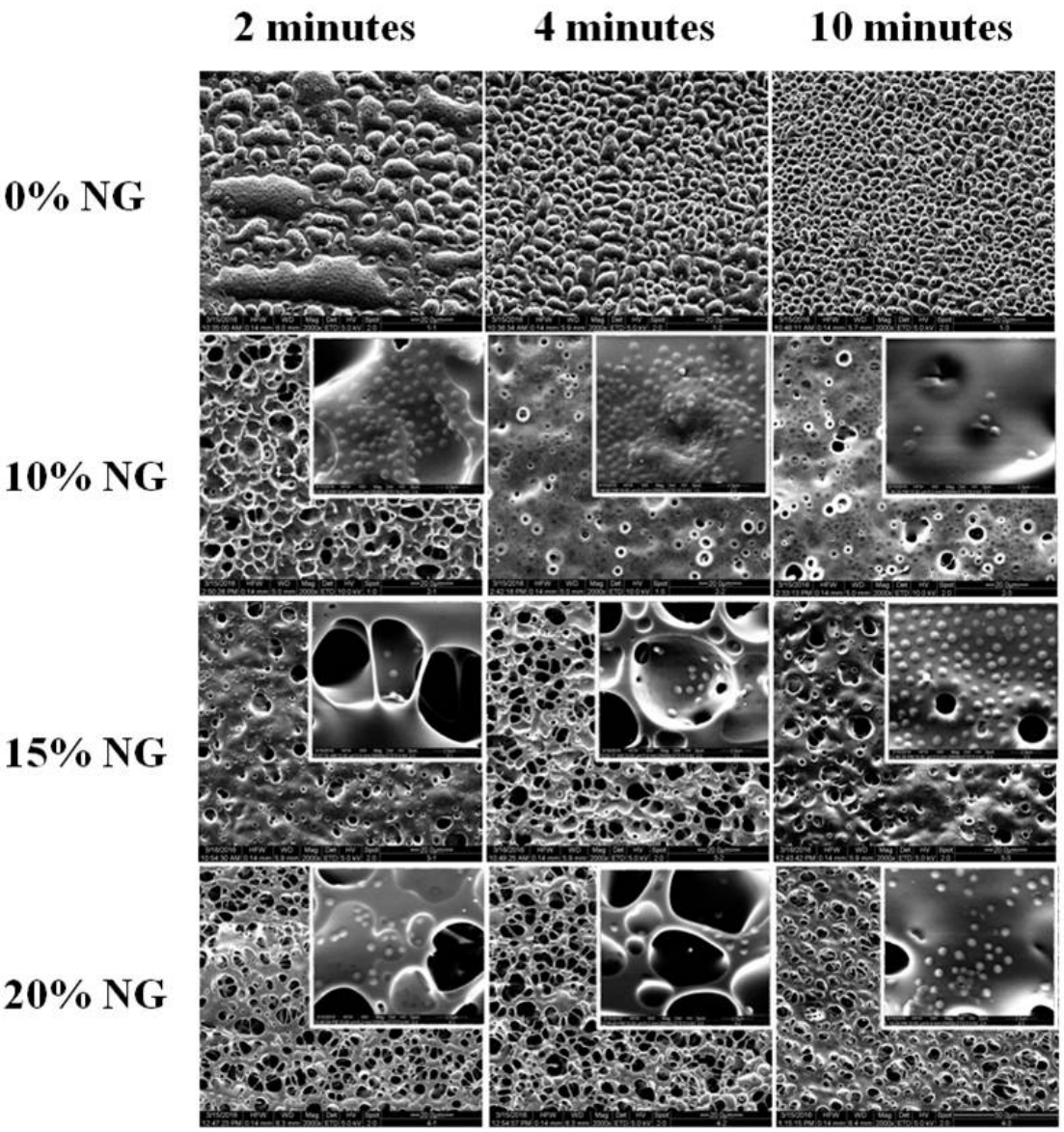

(b)

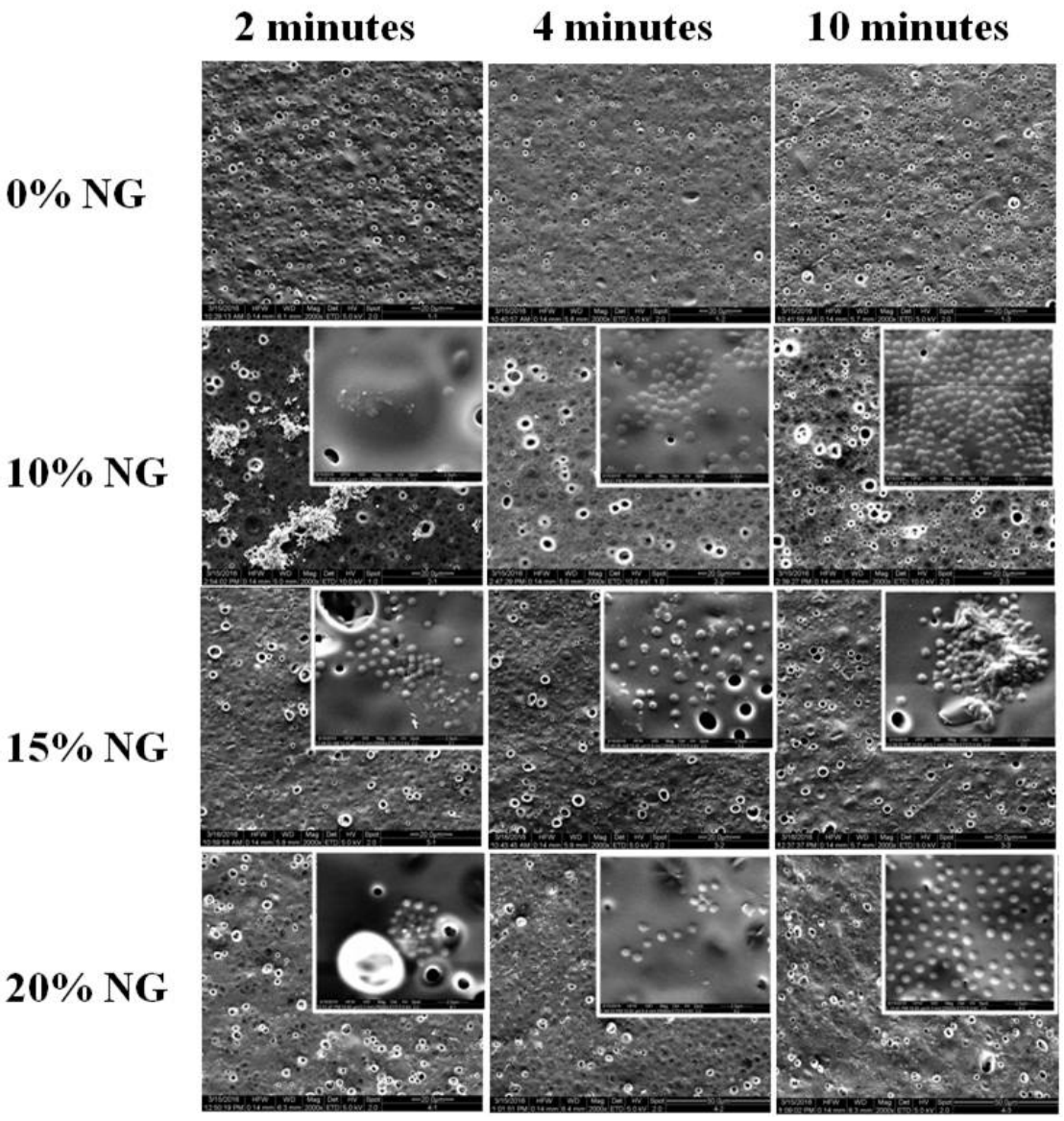

Figure 4.47. SEM picture of PES membranes based on 17.5% of PES and prepared with different PNIPAAm NG fractions and VIPS durations: (a) cross-section, (b) top surface and (c) bottom surface.

5. Conclusion

In this work, by using iron oxide nanoparticles as magneto-heaters and PNIPAAm hydrogel (either hydrogel mesh or nanogel) as thermo-responsive actuator, two types of magneto-responsive membrane with different structures have been designed and prepared. Both of them have demonstrated good magneto-responsivity and switchable molecular sieving effect.

The first type is **magneto-hydrogel pore-filled membrane**, prepared by post modification of commercial PET track-etched membrane via reactive pore-filling functionalization. Such membrane has iron oxide nanoparticles composite PNIPAAm hydrogel immobilized inside the pores of PET membrane. The commercial iron oxide nanoparticles with diameter around 40 nm work as localized heaters, while the PNIPAAm hydrogel mesh works as responsive sieving medium. At room temperature, when the AMF is turned off, the hydrogel network is in swollen state and the mesh size is relatively small; therefore, only small molecules can pass through the membrane. When the AMF is turned on, MNP will generate heat and cause the microsyneresis of hydrogel network, thus, bigger mesh size will be formed and larger molecules can also pass through the membrane. Therefore switchable molecular sieving effect is obtained.

Critical points to achieve good performance of the membrane include ensuring macromolecule sieving effect and temperature-responsivity of the PNIPAAm hydrogel network and efficient heating of MNP under chosen AMF field condition.

With respect to hydrogel network, redox-initiated polymerization is a proper method to prepare MNP composite PNIPAAm hydrogel as the polymerization will not be affected by the presence of MNP and resulted hydrogels will have mesh size in ultrafiltration range. When such composite hydrogel is immobilized into pore of PET base membrane, it also retains good thermo-responsivity as the water permeability of functionalized membrane at 45 ^{o}C is significantly higher than that at 25 ^{o}C (with viscosity influence eliminated). Yet, due the incorporation of the nanoparticles, such composite hydrogels possess heterogeneous structure and result in poor reproducibility for water permeability of such magneto-hydrogel pore-filled membranes.

With respect to magneto-heating, optimal field condition with high magnetic field frequency (745 kHz) and correspondingly high field amplitude (20 $\pm$ 10 kA/m), proper MNP with relatively big size (40 nm) and narrow size distribution, and moderate nanoparticle loading (4.6 % relative to the weight of membrane) ensure effective heating effect. High loading of MNP inside the membrane pore is not easy due to the sterical hindrance between the particle and premodified membrane pore, and electrostatic repulsion between particles and between particle and membrane surface. It can be optimized by tuning the effective pore size and surface charge of premodified membrane via suitable premodification method, reducing electrostatic repulsion between nanoparticles and prolonging the loading time.

The resulted membranes demonstrate significant reversible water permeability in response to switching on and off the AMF. At 25 ^{o}C when the AMF is turned off, their water permeability in the range of 2-10 $l.h^{-1}.m^{-2}.bar^{-1}$; when an AMF (f = 745 kHz, H = 20 $\pm$ 10 kA/m) is applied, their water permeability will increase largely, and reach a plateau in the range of 40-60 $l.h^{-1}.m^{-2}.bar^{-1}$ in 15-20 minutes. The initial water permeability is relatively low due to low porosity of PET track-etched membrane and large barrier thickness of isotropic cross-section structure of such pore-filling functionalized membrane. This could be improved by using a base membrane with higher porosity and introduce an anisotropic structure in the future.

Most importantly, such magneto-hydrogel pore-filled membranes demonstrate good magneto-responsive molecular sieving effect, with certain rejection for various sizes of dextran molecule (4 kDa, 500 kDa and 2000 kDa) when AMF is in “off state”, and significantly reduced rejection for all dextrans when AMF is in “on state”. For the first time, smart membrane with magneto-responsive molecular sieving effect has been developed. Its molecular sieving behaviour can be remotely controlled by manipulating external alternating magnetic field, so that heating the feed solution for stimulating the membrane can be avoided. Yet, due to the heterogeneity of magneto-hydrogel network, the tuning for MWCO is quite rough, with MWCO in the range of 500-2000 kDa at “off state” of AMF and bigger than 2000 kDa at “on state” of AMF.

The second type is **mixed matrix PES membrane blended with MNP and PNIPAAm NG**, prepared by simple one-step phase separation procedure. Such membrane consists of the well-established membrane polymer PES as substrate material, PNIPAAm NG embedded in the skin layer as responsive gate, and MNP in the membrane matrix as localized heaters. At room

temperature and without AMF, the NG is in swollen state and will allow no or only very little flux through it; the only pathway through the barrier layer is via the intrinsic nanopores of the PES-based ultrafiltration membrane, thus restricting larger molecules from passing through. When the temperature is above the LCST of PNIPAAm NG, either by conventional heating of the entire system or by local magnetic heating of the composite membrane in the external AMF, the NG will shrink and the extra gates will be open to allow also larger molecules to pass through the membrane.

The mixed matrix membrane is prepared with tailor-made building blocks (MNP and PNIPAAm NG), via industrially established NIPS process. Therefore, by rational tuning the property of the building blocks, the composition of dope solution, and the condition of NIPS process, it is very easy to get customerized membrane in large scale. The monodisperse PNIPAAm NG, prepared by precipitation polymerization are used as thermo-responsive acuators, therefore sharp MWCO can be ensured. Moreover, the size[143, 144, 145] and the cross-linking degree[146, 147] of the NG can be easily tuned by composition of reaction solution and reaction conditions for precipitation polymerization. Iron oxide nanoparticles, prepared via simple polyol synthesis and with relatively narrow size distribution, are used as magneto-heaters. The amine functionalization ensured their good compatiblity with membrane solvent NMP, the size of particle can be easily tuned by adjusting the content of 1,6-hexanediamine in reaction solution, and relatively big particles which are favored for magneto-heating can be obtained by this method (15-70 nm). For the dope solution composition, the percentage of different building blocks can be easily adjusted to tailor the composition of resulted membrane. Yet, the effect of phase volume on viscosity and eventually the casting process and resulted membrane structure should not be neglected. Here it is found, that with 10% NG and 10% MNP in PES dope solution, the viscosity increases largely. And higher temperature (45 ^{o}C) and relatively fast casting speed (5 mm/s) were required to ensure a stable and relatively low viscosity during membrane preparation. Moreover, the high preparation temperature at NIPS process is also intended to fix the PNIPAAm NG in the voids of PES matrix via the synergistic effect of shrinking of PNIPAAm NG and fast solification of PES at high temperature in NIPS process.

In terms of magneto-responsive water permeability, the obtained membrane shows around 9 times difference in pure water permeability between AMF off and on states, which is comparable

with its permeability change between 25 ^{o}C and 40 ^{o}C in conventional thermo-responsive water permeability tests, indicating the high effectiveness of localized magnetic heating. Its water permeability is in the range of 25-50 $l.h^{-1}.m^{-2}.bar^{-1}$ at 25 ^{o}C or AMF "off state", and in the range of 350-550 $l.h^{-1}.m^{-2}.bar^{-1}$ at 40 ^{o}C or AMF "on state". This is significantly higher than the permeability of magneto-hydrogel pore-filled membrane, due to anisotropic cross-section pore morphology obtained by NIPS process. Overall, such membrane demonstrate a basis for a good overall ultrafiltration membrane performance in terms of permeability.

Furthermore, a remarkable magneto-responsive molecular sieving performance has been demonstrated by shifting of the MWCO for dextran from ~70 kDa to ~1750 kDa, or a change of rejection for dextran with average size of 8 nm by a factor of 170, between AMF off and on states. Compared with magneto-hydrogel pore-filled membrane, a finer tunability for a much lower MWCO within the ultrafiltration range has been achieved.

As such magneto-responsive performance is reproducible over multiple AMF on-off cycles, indicating that the NG network and its functionality will not be disturbed upon integration into the porous PES matrix, and that the effects of NG volume phase transition in the membrane are fully reversible. Therefore, this gives a good example for the design of magneto-responsive separation membranes via efficient and synergistic co-assembly of three different materials.

Overall, this study provided two good examples for the designing of magneto-responsive separation membranes with tunable and responsive size-selective barrier properties, via rational design. Two kinds of novel magneto-responsive membranes with different structures have been prepared and they are expected to be used in microfluidic and other systems for analytical, mass separation or biomedical applications.

6. Outlook

Magneto-responsive membrane is still a new topic in membrane area, and there are many further improvements needed to be made and new trends can be explored:

1. For **magneto hydrogel pore-filled membrane**, in future work, it is expected that the original size of hydrogel mesh and its stimuli-responsive effect could be tuned by varying monomer concentration and cross-linker proportion during the preparation. Moreover, as the real structure of the network is quite complex, due the incorporation of the nanoparticles, which have a larger diameter than the average mesh size of the bulk hydrogel, attempts to further characterize the network of such composite hydrogel in detail and optimize it, are also relevant. This is of particular importance because the magnitude and rate of magneto-responsivity can be increased by nanoparticle loading or size. Also, absolute permeabilities of the obtained membranes are low compared to established (anisotropic) ultrafiltration membranes with similar molecular weight cut-off; this is mainly because of the much larger barrier thickness and lower barrier porosity of the used macroporous substrates which had been pore-filled completely. Therefore, adapting the method to porous membranes with smaller barrier thickness and higher porosity is another target of further development.
2. For the **mixed matrix membrane blended MNP and PNIPAAm NG**, its water permeability can be further increased by adding porogen PVP (cf. section 4.4.2.1), the magneto-responsivity can be enhanced by increase the content of MNP, and the switchable range of MWCO can be tuned by the size and cross-linking degree of PNIPAAm NG. Moreover, maybe new structure of such membrane can be obtained by introducing VIPS process (cf. section 4.4.2.2).
3. Also new **mixed matrix membrane blended with MNP composite PNIPAAm NG** can be envisioned, as shown in **Figure 6.1**. MNP composite PNIPAAm NG with iron oxide nanoparticle as core and PNIPAAM hydrogel as shell, is expected to be swollen at temperature higher than LCST of PNIPAAm and with AMF turned off, and be shrunken at temperature above LCST and with AMF turned on. And the size change of PNIPAAm shell to magneto-stimuli is expected to be within 100 nm and be in ultrafiltration range. Therefore, when such composite NG is incorporated into selective layer of conventional membrane substrate like PES, a magneto-responsive molecular sieving effect resemble the mixed matrix membrane blended with MNP

and PNIPAAm NG is expected. As MNP are directly embedded in the PNIPAAm network, the direct thermal conduction would ensure faster and larger response. So far, there are many investigations for such iron oxide core–PNIPAAm shell NG, yet either the yield is low or the size distribution of obtained NG is not ideal[214, 215, 216]. However, if available, such particles could in addition to the use in the "classical" NIPS or VIPS process, also be utilized in attempts to achieve an alignment toward selective channels with a magnetic field during the membrane preparation, in analogy to the example shown in **Figure 2.16**.

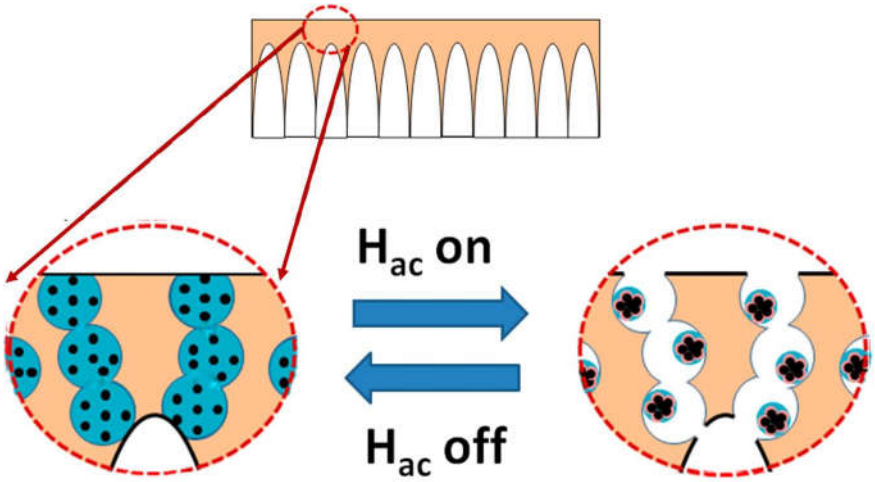

Figure 6.1. Schematic illustration of matrix membrane blended with MNP composite PNIPAAm NG: MNP work as magneto-heater while PNIPAAm shell work as responsive actuator.

4. It is well-known that temperature differences in fluid would introduce density gradient and eventually cause flow motion, which is called thermal ("free") convection. Mixed matrix membrane blended with MNP can be heat up in AMF with certain frequency and magnitude. Its surface should have higher temperature than the bulk solution (feed), therefore, thermal convection is expected to happen on the membrane surface, working as microvortice to reduce concentration polarization. Reducing concentration polarization by introducing unstable flow motion as microvortice on ion-selective surface has been reported very recently by Karatay et al.[217].

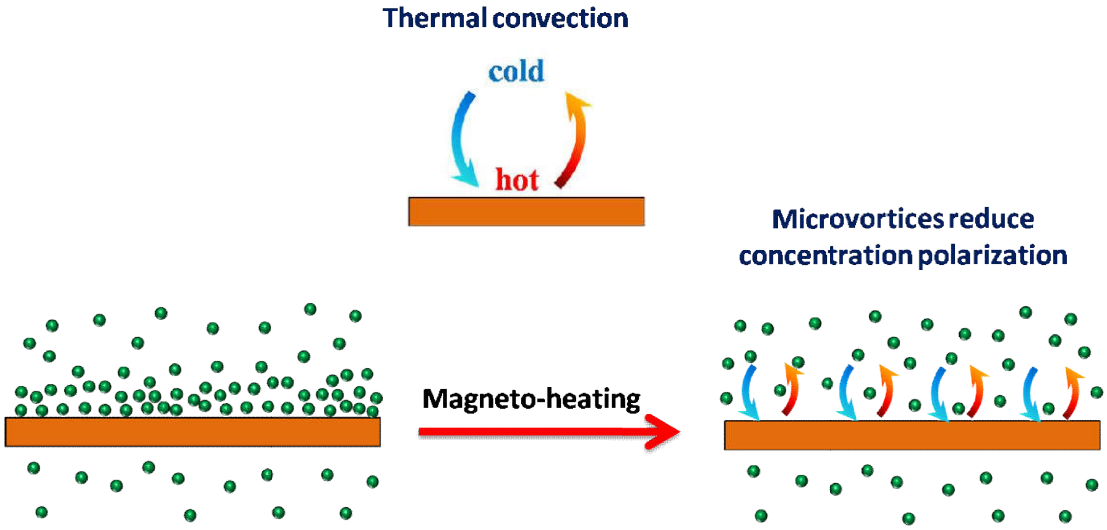

Figure 6.2. Schematic illustration for the mechanism of reducing concentration polarization on surface of MNP blended membrane, via membrane-induced thermal convection, triggered via remote control with AMF.

7. References

(1) Baker, R. W. Overview of Membrane Science and Technology. *Membrane Technology and Applications, Third Edition* **2012,** 1-14.

(2) Werber, J. R.; Osuji, C. O.; Elimelech, M. Materials for Next-Generation Desalination and Water Purification Membranes. *Nat Rev Mater.* **2016,** *1,* 16018-16032.

(3) Shannon, M. A.; Bohn, P. W.; Elimelech, M.; Georgiadis, J. G.; Marinas, B. J.; Mayes, A. M. Science and Technology for Water Purification in the Coming Decades. *Nature* **2008,** *452,* 301-310.

(4) Logan, B. E.; Elimelech, M. Membrane-Based Processes for Sustainable Power Generation Using Water. *Nature* **2012,** *488,* 313-319.

(5) Ulbricht, M. Advanced Functional Polymer Membranes. *Polymer* **2006,** *47,* 2217-2262.

(6) Ulbricht, M. Membrane Separations Using Molecularly Imprinted Polymers. *J. Chromatogr. B* **2004,** *804,* 113-125.

(7) Bernardo, P.; Drioli, E.; Golemme, G. Membrane Gas Separation: A Review/State of the Art. *Ind. Eng. Chem. Res.* **2009,** *48,* 4638-4663.

(8) Li, J.; Chase, H. A. Applications of Membrane Techniques for Purification of Natural Products. *Biotechnol. Lett.* **2010,** *32,* 601-608.

(9) Gultepe, E.; Nagesha, D.; Sridhar, S.; Amiji, M. Nanoporous Inorganic Membranes or Coatings for Sustained Drug Delivery in Implantable Devices. *Adv. Drug Del. Rev.* **2010,** *62,* 305-315.

(10) Jeon, G.; Yang, S. Y.; Kim, J. K. Functional Nanoporous Membranes for Drug Delivery. *J. Mater. Chem.* **2012,** *22,* 14814-14834.

(11) de Jong, J.; Lammertink, R. G. H.; Wessling, M. Membranes and Microfluidics: A Review. *Lab Chip* **2006,** *6,* 1125-1139.

(12) Huh, D.; Matthews, B. D.; Mammoto, A.; Montoya-Zavala, M.; Hsin, H. Y.; Ingber, D. E. Reconstituting Organ-Level Lung Functions on a Chip. *Science* **2010,** *328,* 1662-1668.

(13) Ismagilov, R. F.; Ng, J. M. K.; Kenis, P. J. A.; Whitesides, G. M. Microfluidic Arrays of Fluid-Fluid Diffusional Contacts as Detection Elements and Combinatorial Tools. *Anal. Chem.* **2001,** *73,* 5207-5213.

(14) Kawada, J.; Kimura, H.; Akutsu, H.; Sakai, Y.; Fujii, T. Spatiotemporally Controlled Delivery of Soluble Factors for Stem Cell Differentiation. *Lab Chip* **2012,** *12,* 4508-4515.

(15) Zou, X. Y.; Luo, F.; Xie, R.; Zhang, L. P.; Ju, X. J.; Wang, W.; Liu, Z.; Chu, L. Y. Online Monitoring of Ethanol Concentration Using a Responsive Microfluidic Membrane Device. *Anal. Methods* **2016,** *8,* 4028-4036.

(16) Wandera, D.; Wickramasinghe, S. R.; Husson, S. M. Stimuli-Responsive Membranes. *J. Membr. Sci.* **2010,** *357,* 6-35.

(17) Tokarev, I.; Gopishetty, V.; Zhou, J.; Pita, M.; Motornov, M.; Katz, E.; Minko, S. Stimuli-Responsive Hydrogel Membranes Coupled with Biocatalytic Processes. *ACS Appl. Mater. Interfaces* **2009,** *1,* 532-536.

(18) Liu, Z.; Wang, W.; Xie, R.; Ju, X. J.; Chu, L. Y. Stimuli-Responsive Smart Gating Membranes. *Chem. Soc. Rev.* **2016,** *45,* 460-474.

(19) Tokarev, I.; Minko, S. Stimuli-Responsive Porous Hydrogels at Interfaces for Molecular Filtration, Separation, Controlled Release, and Gating in Capsules and Membranes. *Adv. Mater.* **2010,** *22,*3446-3462.

(20) Yang, Q.; Adrus, N.; Tomicki, F.; Ulbricht, M. Composites of Functional Polymeric Hydrogels and Porous Membranes. *J. Mater. Chem.* **2011,** *21,* 2783-2811.

(21) Zhai, L. Stimuli-Responsive Polymer Films. *Chem. Soc. Rev.* **2013,** *42,* 7148-7160.

(22) Stuart, M. A. C.; Huck, W. T. S.; Genzer, J.; Muller, M.; Ober, C.; Stamm, M.; Sukhorukov, G. B.; Szleifer, I.; Tsukruk, V. V.; Urban, M.; Winnik, F.; Zauscher, S.; Luzinov, I.; Minko, S. Emerging Applications of Stimuli-Responsive Polymer Materials. *Nat. Mater.* **2010,** *9,* 101-113.

(23) Sugawara, Y.; Tamaki, T.; Yamaghchi, T. Development of an Aptamer-Functionalized Molecular Recognition Gating Membrane Targeting a Specific Protein on the Basis of the Aggregation Phenomena of DNA-Pnipam. *Polymer* **2015,** *62,* 86-93.

(24) Chu, L. Y.; Li, Y.; Zhu, J. H.; Wang, H. D.; Liang, Y. J. Control of Pore Size and Permeability of a Glucose-Responsive Gating Membrane for Insulin Delivery. *J. Control. Release* **2004,** *97,* 43-53.

(25) Ohashi, H.; Ebina, S.; Yamaguchi, T. Logistic Gate-Like Permeable Property of Gating Membrane with Ion-Recognition Polyampholyte. *Polymer* **2014,** *55,* 1412-1419.

(26) Ito, T.; Hioki, T.; Yamaguchi, T.; Shinbo, T.; Nakao, S.; Kimura, S. Development of a Molecular Recognition Ion Gating Membrane and Estimation of Its Pore Size Control. *J. Am. Chem. Soc.* **2002,** *124,* 7840-7846.

(27) Luo, T.; Lin, S. O.; Xie, R.; Ju, X. J.; Liu, Z.; Wang, W.; Mou, C. L.; Zhao, C. S.; Chen, Q. M.; Chu, L. Y. Ph-Responsive Poly(Ether Sulfone) Composite Membranes Blended with Amphiphilic Polystyrene-Block-Poly(Acrylic Acid) Copolymers. *J. Membr. Sci.* **2014,** *450,* 162-173.

(28) Lue, S. J.; Chen, C. H.; Shih, C. M.; Tsai, M. C.; Kuo, C. Y.; Lai, J. Y. Grafting of Poly(N-Isopropylacrylamide-Co-Acrylic Acid) on Micro-Porous Polycarbonate Films: Regulating Lower Critical Solution Temperatures for Drug Controlled Release. *J. Membr. Sci.* **2011,** *379,* 330-340.

(29) Frost, S.; Ulbricht, M. Thermoresponsive Ultrafiltration Membranes for the Switchable Permeation and Fractionation of Nanoparticles. *J. Membr. Sci.* **2013,** *448,* 1-11.

(30) Himstedt, H. H.; Yang, Q.; Qian, X. H.; Wickramasinghe, S. R.; Ulbricht, M. Toward Remote-Controlled Valve Functions Via Magnetically Responsive Capillary Pore Membranes. *J. Membr. Sci.* **2012,** *423,* 257-266.

(31) Luo, F.; Xie, R.; Liu, Z.; Ju, X. J.; Wang, W.; Lin, S.; Chu, L. Y. Smart Gating Membranes with in Situ Self-Assembled Responsive Nanogels as Functional Gates. *Sci. Rep.* **2015,** *5,* 14708-14720.

(32) Wu, C. J.; Xie, R.; Wei, H. B.; Xu, T. T.; Liu, Z.; Wang, W.; Ju, X. J.; Chu, L. Y. Fabrication of a Thermo-Responsive Membrane with Cross-Linked Smart Gates Via a 'Grafting-to' Method. *RSC Adv.* **2016,** *6,* 45428-45433.

(33) Wang, G.; Xie, R.; Ju, X. J.; Chu, L. Y. Thermo-Responsive Polyethersulfone Composite Membranes Blended with Poly(N-Isopropylacrylamide) Nanogels. *Chem. Eng. Technol.* **2012,** *35,* 2015-2022.

(34) Hoare, T.; Santamaria, J.; Goya, G. F.; Irusta, S.; Lin, D.; Lau, S.; Padera, R.; Langer, R.; Kohane, D. S. A Magnetically Triggered Composite Membrane for on-Demand Drug Delivery. *Nano Lett.* **2009,** *9,* 3651-3657.

(35) Hoare, T.; Timko, B. P.; Santamaria, J.; Goya, G. F.; Irusta, S.; Lau, S.; Stefanescu, C. F.; Lin, D. B.; Langer, R.; Kohane, D. S. Magnetically Triggered Nanocomposite Membranes: A Versatile Platform for Triggered Drug Release. *Nano Lett.* **2011,** *11,* 1395-1400.

(36) Csetneki, I.; Filipcsei, G.; Zrinyi, M. Smart Nanocomposite Polymer Membranes with on/Off Switching Control. *Macromolecules* **2006,** *39,* 1939-1942.

(37) Menne, D.; Pitsch, F.; Wong, J. E.; Pich, A.; Wessling, M. Temperature-Modulated Water Filtration Using Microgel-Functionalized Hollow-Fiber Membranes. *Angew. Chem. Int. Ed.* **2014,** *53,* 5706-5710.

(38) Kuroki, H.; Islam, C.; Tokarev, I.; Hu, H.; Liu, G. J.; Minkot, S. Tunable Ultrathin Membranes with Nonvolatile Pore Shape Memory. *ACS Appl. Mater. Interfaces* **2015,** *7,* 10401-10406.

(39) Adrus, N.; Ulbricht, M. Novel Hydrogel Pore-Filled Composite Membranes with Tunable and Temperature-Responsive Size-Selectivity. *J. Mater. Chem.* **2012,** *22,* 3088-3098.

(40) Shi, W. B.; Deng, J.; Qin, H.; Wang, D. S.; Zhao, C. S. Poly(Ether Sulfone) Membranes with Photo-Responsive Permeability. *J. Membr. Sci.* **2014,** *455,* 357-367.

(41) Vlassiouk, I.; Park, C. D.; Vail, S. A.; Gust, D.; Smirnov, S. Control of Nanopore Wetting by a Photochromic Spiropyran: A Light-Controlled Valve and Electrical Switch. *Nano Lett.* **2006,** *6,* 1013-1017.

(42) Nayak, A.; Liu, H. W.; Belfort, G. An Optically Reversible Switching Membrane Surface. *Angew. Chem. Int. Ed.* **2006,** *45,* 4094-4098.

(43) Chen, H.; Palmese, G. R.; Elabd, Y. A. Electrosensitive Permeability of Membranes with Oriented Polyelectrolyte Nanodomains. *Macromolecules* **2007,** *40,* 781-782.

(44) Himstedt, H. H.; Yang, Q.; Dasi, L. P.; Qian, X. H.; Wickramasinghe, S. R.; Ulbricht, M. Magnetically Activated Micromixers for Separation Membranes. *Langmuir* **2011,** *27,* 5574-5581.

(45) Hsu, C. C.; Wu, C. S.; Liu, Y. L. Multiple Stimuli-Responsive Poly(Vinylidene Fluoride) (Pvdf) Membrane Exhibiting High Efficiency of Membrane Clean in Protein Separation. *J. Membr. Sci.* **2014,** *450,* 257-264.

(46) Thevenot, J.; Oliveira, H.; Sandre, O.; Lecommandoux, S. Magnetic Responsive Polymer Composite Materials. *Chem. Soc. Rev.* **2013,** *42,* 7099-7116.

(47) Satarkar, N. S.; Biswal, D.; Hilt, J. Z. Hydrogel Nanocomposites: A Review of Applications as Remote Controlled Biomaterials. *Soft Matter* **2010,** *6,* 2364-2371.

(48) Timko, B. P.; Dvir, T.; Kohane, D. S. Remotely Triggerable Drug Delivery Systems. *Adv. Mater.* **2010,** *22,* 4925-4943.

(49) Lu, Y.; Shi, W. W.; Qin, J. H.; Lin, B. C. Fabrication and Characterization of Paper-Based Microfluidics Prepared in Nitrocellulose Membrane by Wax Printing. *Anal. Chem.* **2010,** *82,* 329-335.

(50) Fleische. R. L.; Alter, H. W.; Walker, R. M.; Furman, S. C.; Price, P. B. Particle Track Etching. *Science* **1972,** *178,* 255-263.

(51) Guillen, G. R.; Pan, Y. J.; Li, M. H.; Hoek, E. M. V. Preparation and Characterization of Membranes Formed by Nonsolvent Induced Phase Separation: A Review. *Ind. Eng. Chem. Res.* **2011,** *50,* 3798-3817.

(52) Strathmann, H.; Kock, K. Formation Mechanism of Phase Inversion Membranes. *Desalination* **1977,** *21,* 241-255.

(53) Amirilargani, M.; Sadrzadeh, M.; Mohammadi, T. Synthesis and Characterization of Polyethersulfone Membranes. *J Polym. Res.* **2010,** *17,* 363-377.

(54) Venault, A.; Chang, Y.; Wang, D. M.; Bouyer, D. A Review on Polymeric Membranes and Hydrogels Prepared by Vapor-Induced Phase Separation Process. *Polym. Rev.* **2013,** *53,* 568-626.

(55) Park, H. C.; Kim, Y. P.; Kim, H. Y.; Kang, Y. S. Membrane Formation by Water Vapor Induced Phase Inversion. *J. Membr. Sci.* **1999,** *156,* 169-178.

(56) Nunes, S. P.; Behzad, A. R.; Hooghan, B.; Sougrat, R.; Karunakaran, M.; Pradeep, N.; Vainio, U.; Peinemann, K. V. Switchable PH-Responsive Polymeric Membranes Prepared Via Block Copolymer Micelle Assembly. *ACS Nano* **2011,** *5,* 3516-3522.

(57) Qiu, X. Y.; Yu, H. Z.; Karunakaran, M.; Pradeep, N.; Nunes, S. P.; Peinemann, K. V. Selective Separation of Similarly Sized Proteins with Tunable Nanoporous Block Copolymer Membranes. *ACS Nano* **2013,** *7,* 768-776.

(58) Guo, H. F.; Ulbricht, M. Preparation of Thermo-Responsive Polypropylene Membranes Via Surface Entrapment of Poly(N-Isopropylacrylamide)-Containing Macromolecules. *J. Membr. Sci.* **2011,** *372,* 331-339.

(59) Clodt, J. I.; Filiz, V.; Rangou, S.; Buhr, K.; Abetz, C.; Hoche, D.; Hahn, J.; Jung, A.; Abetz, V. Double Stimuli-Responsive Isoporous Membranes Via Post-Modification of PH-Sensitive Self-Assembled Diblock Copolymer Membranes. *Adv. Funct. Mater.* **2013,** *23,* 731-738.

(60) Berndt, E.; Ulbricht, M. Synthesis of Block Copolymers for Surface Functionalization with Stimuli-Responsive Macromolecules. *Polymer* **2009,** *50,* 5181-5191.

(61) Ito, Y.; Ochiai, Y.; Park, Y. S.; Imanishi, Y. PH-Sensitive Gating by Conformational Change of a Polypeptide Brush Grafted onto a Porous Polymer Membrane. *J. Am. Chem. Soc.* **1997,** *119,* 1619-1623.

(62) Deng, J. P.; Wang, L. F.; Liu, L. Y.; Yang, W. T. Developments and New Applications of uv-Induced Surface Graft Polymerizations. *Prog. Polym. Sci.* **2009,** *34,* 156-193.

(63) Ran, J.; Wu, L.; Zhang, Z. H.; Xu, T. W. Atom Transfer Radical Polymerization (ATRP): A Versatile and Forceful Tool for Functional Membranes. *Prog. Polym. Sci.* **2014,** *39,* 124-144.

(64) Xie, R.; Chu, L. Y.; Chen, W. M.; Xiao, W.; Wang, H. D.; Qu, J. B. Characterization of Microstructure of Poly (N-Isopropylacrylamide)-Grafted Polycarbonate Track-Etched Membranes Prepared by Plasma-Graft Pore-Filling Polymerization. *J. Membr. Sci.* **2005,** *258,* 157-166.

(65) Gajda, M.; Ulbricht, M. Capillary Pore Membranes with Grafted Diblock Copolymers Showing Reversibly Changing Ultrafiltration Properties with Independent Response to Ions and Temperature. *J. Membr. Sci.* **2016,** *514,* 510-517.

(66) He, D. M.; Susanto, H.; Ulbricht, M. Photo-Irradiation for Preparation, Modification and Stimulation of Polymeric Membranes. *Prog. Polym. Sci.* **2009,** *34,* 62-98.

(67) Geismann, C.; Yaroshchuk, A.; Ulbricht, M. Permeability and Electrokinetic Characterization of Poly(Ethylene Terephthalate) Capillary Pore Membranes with Grafted Temperature-Responsive Polymers. *Langmuir* **2007,** *23,* 76-83.

(68) Geismann, C.; Ulbricht, M. Photoreactive Functionalization of Poly(Ethylene Terephthalate) Track-Etched Pore Surfaces with "Smart" Polymer System's. *Macromol. Chem. Phys.* **2005,** *206,* 268-281.

(69) Yamaguchi, T.; Nakao, S.; Kimura, S. Plasma-Graft Filling Polymerization - Preparation of a New Type of Pervaporation Membrane for Organic Liquid-Mixtures. *Macromolecules* **1991,** *24,* 5522-5527.

(70) Yamaguchi, T.; Miyata, F.; Nakao, S. Pore-Filling Type Polymer Electrolyte Membranes for a Direct Methanol Fuel Cell. *J. Membr. Sci.* **2003,** *214,* 283-292.

(71) Mika, A. M.; Childs, R. F. Salt Separation by Charged Gel-Filled Microporous Membranes. *Ind. Eng. Chem. Res.* **2003,** *42,* 3111-3117.

(72) Kapur, V.; Charkoudian, J.; Anderson, J. L. Transport of Proteins through Gel-Filled Porous Membranes. *J. Membr. Sci.* **1997,** *131,* 143-153.

(73) Kapur, V.; Charkoudian, J. C.; Kessler, S. B.; Anderson, J. L. Hydrodynamic Permeability of Hydrogels Stabilized within Porous Membranes. *Ind. Eng. Chem. Res.* **1996,** *35,* 3179-3185.

(74) Salam, A.; Ulbricht, M. Effect of Surface Modification on the Synthesis of Pore-Filling Polymeric Monoliths in Microfiltration Membranes Made from Poly(Propylene) and Poly(Ethylene Terephthalate). *Macromolecular Materials and Engineering* **2007,** *292,* 310-318.

(75) Xue, J.; Chen, L.; Wang, H. L.; Zhang, Z. B.; Zhu, X. L.; Kang, E. T.; Neoh, K. G. Stimuli-Responsive Multifunctional Membranes of Controllable Morphology from Poly(Vinylidene Fluoride)-Graft-Poly[2-(N,N-Dimethylamino)Ethyl Methacrylate] Prepared Via Atom Transfer Radical Polymerization. *Langmuir* **2008,** *24,* 14151-14158.

(76) Fei, Z. D.; Wan, L. S.; Wang, W. M.; Zhong, M. Q.; Xu, Z. K. Thermo-Responsive Polyacrylonitrile Membranes Prepared with Poly(Acrylonitrile-G-Isopropylacrylamide) as an Additive. *J. Membr. Sci.* **2013,** *432,* 42-49.

(77) Xu, F. J.; Li, J.; Yuan, S. J.; Zhang, Z. X.; Kang, E. T.; Neoh, K. G. Thermo-Responsive Porous Membranes of Controllable Porous Morphology from Triblock Copolymers of Polycaprolactone and Poly(N-Isopropylacrylamide) Prepared by Atom Transfer Radical Polymerization. *Biomacromolecules* **2008,** *9,* 331-339.

(78) Oak, M. S.; Kobayashi, T.; Wang, H. Y.; Fukaya, T.; Fujii, N. Ph Effect on Molecular Size Exclusion of Polyacrylonitrile Ultrafiltration Membranes Having Carboxylic Acid Groups. *J. Membr. Sci.* **1997,** *123,* 185-195.

(79) Song, X. L.; Xie, R.; Luo, T.; Ju, X. J.; Wang, W.; Chu, L. Y. Ethanol-Responsive Characteristics of Polyethersulfone Composite Membranes Blended with Poly(N-Isopropylacrylamide) Nanogels. *J. Appl. Polym. Sci.* **2014,** *131*.

(80) Iwata, H.; Oodate, M.; Uyama, Y.; Amemiya, H.; Ikada, Y. Preparation of Temperature-Sensitive Membranes by Graft-Polymerization onto a Porous Membrane. *J. Membr. Sci.* **1991,** *55,* 119-130.

(81) Yu, J. Z.; Zhu, L. P.; Zhu, B. K.; Xu, Y. Y. Poly(N-Isopropylacrylamide) Grafted Poly(Vinylidene Fluoride) Copolymers for Temperature-Sensitive Membranes. *J. Membr. Sci.* **2011,** *366,* 176-183.

(82) Yang, Q.; Himstedt, H. H.; Ulbricht, M.; Qian, X. H.; Wickramasinghe, S. R. Designing Magnetic Field Responsive Nanofiltration Membranes. *J. Membr. Sci.* **2013,** *430,* 70-78.

(83) Ng, Q. H.; Lim, J. K.; Ahmad, A. L.; Ooi, B. S.; Low, S. C. Magnetic Nanoparticles Augmented Composite Membranes in Removal of Organic Foulant through Magnetic Actuation. *J. Membr. Sci.* **2015,** *493,* 134-146.

(84) Gebreyohannes, A. Y.; Bilad, M. R.; Verbiest, T.; Courtin, C. M.; Dornez, E.; Giorno, L.; Curcio, E.; Vankelecom, I. F. J. Nanoscale Tuning of Enzyme Localization for Enhanced Reactor Performance in a Novel Magnetic-Responsive Biocatalytic Membrane Reactor. *J. Membr. Sci.* **2015,** *487,* 209-220.

(85) Gajda, A. M.; Ulbricht, M. Magnetic Fe_3O_4 Nanoparticle Heaters in Smart Porous Membrane Valves. *J. Mater. Chem. B* **2014,** *2,* 1317-1326.

(86) Satarkar, N. S.; Hilt, J. Z. Magnetic Hydrogel Nanocomposites for Remote Controlled Pulsatile Drug Release. *J. Control. Release* **2008,** *130,* 246-251.

(87) Satarkar, N. S.; Hilt, J. Z. Hydrogel Nanocomposites as Remote-Controlled Biomaterials. *Acta Biomater.* **2008,** *4,* 11-16.

(88) Geckil, H.; Xu, F.; Zhang, X. H.; Moon, S.; Demirci, U. Engineering Hydrogels as Extracellular Matrix Mimics. *Nanomedicine* **2010,** *5,* 469-484.

(89) Slaughter, B. V.; Khurshid, S. S.; Fisher, O. Z.; Khademhosseini, A.; Peppas, N. A. Hydrogels in Regenerative Medicine. *Adv. Mater.* **2009,** *21,* 3307-3329.

(90) Lin, C. C.; Metters, A. T. Hydrogels in Controlled Release Formulations: Network Design and Mathematical Modeling. *Adv. Drug Del. Rev.* **2006,** *58,* 1379-1408.

(91) Hoare, T. R.; Kohane, D. S. Hydrogels in Drug Delivery: Progress and Challenges. *Polymer* **2008,** *49,* 1993-2007.

(92) Buenger, D.; Topuz, F.; Groll, J. Hydrogels in Sensing Applications. *Prog. Polym. Sci.* **2012,** *37,* 1678-1719.

(93) Byrne, M. E.; Park, K.; Peppas, N. A. Molecular Imprinting within Hydrogels. *Adv. Drug Del. Rev.* **2002,** *54,* 149-161.

(94) Chen, L. X.; Xu, S. F.; Li, J. H. Recent Advances in Molecular Imprinting Technology: Current Status, Challenges and Highlighted Applications. *Chem. Soc. Rev.* **2011,** *40,* 2922-2942.

(95) Kasgoz, H.; Ozgumus, S.; Orbay, M. Modified Polyacrylamide Hydrogels and Their Application in Removal of Heavy Metal Ions. *Polymer* **2003,** *44,* 1785-1793.

(96) Ozay, O.; Ekici, S.; Baran, Y.; Aktas, N.; Sahiner, N. Removal of Toxic Metal Ions with Magnetic Hydrogels. *Water Res.* **2009,** *43,* 4403-4411.

(97) Ali, W.; Gebert, B.; Hennecke, T.; Graf, K.; Ulbrich, M.; Gutmann, J. S. Design of Thermally Responsive Polymeric Hydrogels for Brackish Water Desalination: Effect of Architecture on Swelling, Deswelling, and Salt Rejection. *ACS Appl. Mater. Interfaces* **2015,** *7,* 15696-15706.

(98) Li, D.; Zhang, X. Y.; Yao, J. F.; Simon, G. P.; Wang, H. T. Stimuli-Responsive Polymer Hydrogels as a New Class of Draw Agent for Forward Osmosis Desalination. *Chem. Commun.* **2011,** *47,* 1710-1712.

(99) Ekblad, T.; Bergstroem, G.; Ederth, T.; Conlan, S. L.; Mutton, R.; Clare, A. S.; Wang, S.; Liu, Y. L.; Zhao, Q.; D'Souza, F.; Donnelly, G. T.; Willemsen, P. R.; Pettitt, M. E.; Callow, M. E.; Callow, J. A.; Liedberg, B. Poly(Ethylene Glycol)-Containing Hydrogel Surfaces for Antifouling Applications in Marine and Freshwater Environments. *Biomacromolecules* **2008,** *9,* 2775-2783.

(100) Zhao, Y. F.; Zhu, L. P.; Yi, Z.; Zhu, B. K.; Xu, Y. Y. Zwitterionic Hydrogel Thin Films as Antifouling Surface Layers of Polyethersulfone Ultrafiltration Membranes Anchored Via Reactive Copolymer Additive. *J. Membr. Sci.* **2014,** *470,* 148-158.

(101) Lei, J.; Ulbricht, M. Macroinitiator-Mediated Photoreactive Coating of Membrane Surfaces with Antifouling Hydrogel Layers. *J. Membr. Sci.* **2014,** *455,* 207-218.

(102) Faxalv, L.; Ekblad, T.; Liedberg, B.; Lindahl, T. L. Blood Compatibility of Photografted Hydrogel Coatings. *Acta Biomater.* **2010,** *6,* 2599-2608.

(103) Dong, L. C.; Hoffman, A. S.; Yan, Q. Dextran Permeation through Poly(N-Isopropylacrylamide) Hydrogels. *J Biomater Sci Polym Ed* **1994,** *5,* 473-484.

(104) White, M. L. The Permeability of an Acrylamide Polymer Gel. *J. Phys. Chem.* **1960,** *64,* 1563-1565.

(105) Righetti, P. G.; Gelfi, C. Electrophoresis Gel Media: The State of the Art. *J. Chromatogr. B* **1997,** *699,* 63-75.

(106) Amsden, B. Solute Diffusion within Hydrogels. Mechanisms and Models. *Macromolecules* **1998,** *31,* 8382-8395.

(107) Kosto, K. B.; Deen, W. M. Hindered Convection of Macromolecules in Hydrogels. *Biophys. J.* **2005,** *88,* 277-286.

(108) Kim, J. T.; Anderson, J. L. Diffusion and Flow through Polymer-Lined Micropores. *Ind. Eng. Chem. Res.* **1991,** *30,* 1008-1016.

(109) Boschetti, E.; Guerrier, L.; Girot, P.; Horvath, J. Preparative High-Performance Liquid-Chromatographic Separation of Proteins with Hyperd Ion-Exchange Supports. *J. Chromatogr. B* **1995,** *664,* 225-231.

(110) Schild, H. G. Poly (N-Isopropylacrylamide) - Experiment, Theory and Application. *Prog. Polym. Sci.* **1992,** *17,* 163-249.

(111) Pelton, R. Temperature-Sensitive Aqueous Microgels. *Adv. Colloid Interface Sci.* **2000,** *85,* 1-33.

(112) Bromberg, L. E.; Ron, E. S. Temperature-Responsive Gels and Thermogelling Polymer Matrices for Protein and Peptide Delivery. *Adv. Drug Del. Rev.* **1998,** *31,* 197-221.

(113) Schmaljohann, D. Thermo- and PH-Responsive Polymers in Drug Delivery. *Adv. Drug Del. Rev.* **2006,** *58,* 1655-1670.

(114) De, S. K.; Aluru, N. R.; Johnson, B.; Crone, W. C.; Beebe, D. J.; Moore, J. Equilibrium Swelling and Kinetics of PH-Responsive Hydrogels: Models, Experiments, and Simulations. *J. Microelectromech. Syst.* **2002,** *11,* 544-555.

(115) Mi, P.; Ju, X. J.; Xie, R.; Wu, H. G.; Ma, J.; Chu, L. Y. A Novel Stimuli-Responsive Hydrogel for K^+-Induced Controlled-Release. *Polymer* **2010,** *51,* 1648-1653.

(116) Liu, X. W.; Zhu, S.; Wu, S. R.; Wang, P.; Han, G. Z. Response Behavior of Ion-Sensitive Hydrogel Based on Crown Ether. *Colloids Surf., A* **2013,** *417,* 140-145.

(117) Miyata, T.; Uragami, T.; Nakamae, K. Biomolecule-Sensitive Hydrogels. *Adv. Drug Del. Rev.* **2002,** *54,* 79-98.

(118) Ulijn, R. V.; Bibi, N.; Jayawarna, V.; Thornton, P. D.; Todd, S. J.; Mart, R. J.; Smith, A. M.; Gough, J. E. Bioresponsive Hydrogels. *Mater. Today* **2007,** *10,* 40-48.

(119) Jochum, F. D.; Theato, P. Temperature- and Light-Responsive Smart Polymer Materials. *Chem. Soc. Rev.* **2013,** *42,* 7468-7483.

(120) Tomatsu, I.; Peng, K.; Kros, A. Photoresponsive Hydrogels for Biomedical Applications. *Adv. Drug Del. Rev.* **2011,** *63,* 1257-1266.

(121) Kuksenok, O.; Yashin, V. V.; Balazs, A. C. Mechanically Induced Chemical Oscillations and Motion in Responsive Gels. *Soft Matter* **2007,** *3,* 1138-1144.

(122) Kouwer, P. H. J.; Koepf, M.; Le Sage, V. A. A.; Jaspers, M.; van Buul, A. M.; Eksteen-Akeroyd, Z. H.; Woltinge, T.; Schwartz, E.; Kitto, H. J.; Hoogenboom, R.; Picken, S. J.; Nolte, R. J. M.; Mendes, E.; Rowan, A. E. Responsive Biomimetic Networks from Polyisocyanopeptide Hydrogels. *Nature* **2013,** *493,* 651-655.

(123) Jaspers, M.; Dennison, M.; Mabesoone, M. F. J.; MacKintosh, F. C.; Rowan, A. E.; Kouwer, P. H. J. Ultra-Responsive Soft Matter from Strain-Stiffening Hydrogels. *Nat. Commun.* **2014,** *5,* 5808-5815.

(124) Osada, Y.; Gong, J. P. Soft and Wet Materials: Polymer Gels. *Adv. Mater.* **1998,** *10,* 827-837.

(125) Zrinyi, M. Intelligent Polymer Gels Controlled by Magnetic Fields. *Colloid. Polym. Sci.* **2000,** *278,* 98-103.

(126) Murdan, S. Electro-Responsive Drug Delivery from Hydrogels. *J. Control. Release* **2003,** *92,* 1-17.

(127) Scarpa, J. S.; Mueller, D. D.; Klotz, I. M. Slow Hydrogen-Deuterium Exchange in a Non-Alpha-Helical Polyamide. *J. Am. Chem. Soc.* **1967,** *89,* 6024-6030.

(128) Jeong, B.; Kim, S. W.; Bae, Y. H. Thermosensitive Sol-Gel Reversible Hydrogels. *Adv. Drug Del. Rev.* **2002,** *54,* 37-51.

(129) Roy, D.; Brooks, W. L. A.; Sumerlin, B. S. New Directions in Thermoresponsive Polymers. *Chem. Soc. Rev.* **2013,** *42,* 7214-7243.

(130) Chu, L. Y., *Smart Membrane Materials and System*. Springer-Verlag, Berlin Heidelberg and Zhejiang University, 2011.

(131) Pelton, R. Poly(N-Isopropylacrylamide) (Pnipam) Is Never Hydrophobic. *J. Colloid Interface Sci.* **2010,** *348,* 673-674.

(132) Singh, D.; Kuckling, D.; Choudhary, V.; Adler, H. J.; Koul, V. Synthesis and Characterization of Poly(N-Isopropylacrylamide) Films by Photopolymerization. *Polym. Adv. Technol.* **2006,** *17,* 186-192.

(133) Adrus, N.; Ulbricht, M. Rheological Studies on Pnipaam Hydrogel Synthesis Via in Situ Polymerization and on Resulting Viscoelastic Properties. *React. Funct. Polym.* **2013,** *73,* 141-148.

(134) Fanger, C.; Wack, H.; Ulbricht, M. Macroporous Poly (N-Isopropylacrylamide) Hydrogels with Adjustable Size "Cut-Off" for the Efficient and Reversible Immobilization of Biomacromolecules. *Macromol. Biosci.* **2006,** *6,* 393-402.

(135) Zhang, X. Z.; Wu, D. Q.; Chu, C. C. Effect of the Crosslinking Level on the Properties of Temperature-Sensitive Poly(N-Isopropylacrylamide) Hydrogels. *J. Polym. Sci. Pol. Phys.* **2003,** *41,* 582-593.

(136) Nagaoka, N.; Safranj, A.; Yoshida, M.; Omichi, H.; Kubota, H.; Katakai, R. Synthesis of Poly(N-Isopropylacrylamide) Hydrogels by Radiation Polymerization and Cross-Linking. *Macromolecules* **1993,** *26,* 7386-7388.

(137) Zhang, S.; Shi, Z. X.; Xu, H. J.; Ma, X. D.; Yin, J.; Tian, M. Revisiting the Mechanism of Redox-Polymerization to Build the Hydrogel with Excellent Properties Using a Novel Initiator. *Soft Matter* **2016,** *12,* 2575-2582.

(138) Chacko, R. T.; Ventura, J.; Zhuang, J. M.; Thayumanavan, S. Polymer Nanogels: A Versatile Nanoscopic Drug Delivery Platform. *Adv. Drug Del. Rev.* **2012,** *64,* 836-851.

(139) Oh, J. K.; Drumright, R.; Siegwart, D. J.; Matyjaszewski, K. The Development of Microgels/Nanogels for Drug Delivery Applications. *Prog. Polym. Sci.* **2008,** *33,* 448-477.

(140) Motornov, M.; Roiter, Y.; Tokarev, I.; Minko, S. Stimuli-Responsive Nanoparticles, Nanogels and Capsules for Integrated Multifunctional Intelligent Systems. *Prog. Polym. Sci.* **2010,** *35,* 174-211.

(141) Pich, A.; Richtering, W., *Chemical Design of Responsive Microgels*. Springer, 2010.

(142) Klinger, D.; Landfester, K. Stimuli-Responsive Microgels for the Loading and Release of Functional Compounds: Fundamental Concepts and Applications. *Polymer* **2012,** *53,* 5209-5231.

(143) Tan, B. H.; Pelton, R. H.; Tam, K. C. Microstructure and Rheological Properties of Thermo-Responsive Poly (N-Isopropylacrylamide) Microgels. *Polymer* **2010,** *51,* 3238-3243.

(144) Blackburn, W. H.; Lyon, L. A. Size-Controlled Synthesis of Monodisperse Core/Shell Nanogels. *Colloid. Polym. Sci.* **2008,** *286,* 563-569.

(145) Andersson, M.; Maunu, S. L. Structural Studies of Poly(N-Isopropylacrylamide) Microgels: Effect of SDS Surfactant Concentration in the Microgel Synthesis. *J. Polym. Sci. Pol. Phys.* **2006,** *44,* 3305-3314.

(146) Senff, H.; Richtering, W. Influence of Cross-Link Density on Rheological Properties of Temperature-Sensitive Microgel Suspensions. *Colloid. Polym. Sci.* **2000,** *278,* 830-840.

(147) Varga, I.; Gilanyi, T.; Meszaros, R.; Filipcsei, G.; Zrinyi, M. Effect of Cross-Link Density on the Internal Structure of Poly(N-Isopropylacrylamide) Microgels. *J. Phys. Chem. B* **2001,** *105,* 9071-9076.

(148) Ito, S.; Ogawa, K.; Suzuki, H.; Wang, B. L.; Yoshida, R.; Kokufuta, E. Preparation of Thermosensitive Submicrometer Gel Particles with Anionic and Cationic Charges. *Langmuir* **1999,** *15,* 4289-4294.

(149) Saxena, S.; Hansen, C. E.; Lyon, L. A. Microgel Mechanics in Biomaterial Design. *Acc. Chem. Res.* **2014,** *47,* 2426-2434.

(150) Issa, B.; Obaidat, I. M.; Albiss, B. A.; Haik, Y. Magnetic Nanoparticles: Surface Effects and Properties Related to Biomedicine Applications. *International Journal of Molecular Sciences* **2013,** *14,* 21266-21305.

(151) Jeong, U.; Teng, X. W.; Wang, Y.; Yang, H.; Xia, Y. N. Superparamagnetic Colloids: Controlled Synthesis and Niche Applications. *Adv. Mater.* **2007,** *19,* 33-60.

(152) Gubin, S. P., *Magnetic Nanoparticles*. Wiley-VCH Verlag, 2009.

(153) Gubin, S. P.; Koksharov, Y. A.; Khomutov, G. B.; Yurkov, G. Y. Magnetic Nanoparticles: Preparation Methods, Structure and Properties. *Usp. Khim.* **2005,** *74,* 539-574.

(154) Lee, N.; Hyeon, T. Designed Synthesis of Uniformly Sized Iron Oxide Nanoparticles for Efficient Magnetic Resonance Imaging Contrast Agents. *Chem. Soc. Rev.* **2012,** *41,* 2575-2589.

(155) Lu, A. H.; Salabas, E. L.; Schuth, F. Magnetic Nanoparticles: Synthesis, Protection, Functionalization, and Application. *Angew. Chem. Int. Ed.* **2007,** *46,* 1222-1244.

(156) Gupta, A. K.; Gupta, M. Synthesis and Surface Engineering of Iron Oxide Nanoparticles for Biomedical Applications. *Biomaterials* **2005,** *26,* 3995-4021.

(157) Laurent, S.; Forge, D.; Port, M.; Roch, A.; Robic, C.; Elst, L. V.; Muller, R. N. Magnetic Iron Oxide Nanoparticles: Synthesis, Stabilization, Vectorization, Physicochemical Characterizations, and Biological Applications. *Chem. Rev.* **2008,** *108,* 2064-2110.

(158) Wu, W.; He, Q. G.; Jiang, C. Z. Magnetic Iron Oxide Nanoparticles: Synthesis and Surface Functionalization Strategies. *Nanoscale Research Letters* **2008,** *3,* 397-415.

(159) Boistelle, R.; Astier, J. P. Crystallization Mechanisms in Solution. *J. Cryst. Growth* **1988,** *90,* 14-30.

(160) Schwarzer, H. C.; Peukert, W. Tailoring Particle Size through Nanoparticle Precipitation. *Chem. Eng. Commun.* **2004,** *191,* 580-606.

(161) Gupta, A. K.; Wells, S. Surface-Modified Superparamagnetic Nanoparticles for Drug Delivery: Preparation, Characterization, and Cytotoxicity Studies. *IEEE Trans. NanoBiosci.* **2004,** *3,* 66-73.

(162) Pillai, V.; Kumar, P.; Hou, M. J.; Ayyub, P.; Shah, D. O. Preparation of Nanoparticles of Silver-Halides, Superconductors and Magnetic-Materials Using Water-in-Oil Microemulsions as Nano-Reactors. *Adv. Colloid Interface Sci.* **1995,** *55,* 241-269.

(163) Langevin, D. Micelles and Microemulsions. *Annu. Rev. Phys. Chem.* **1992,** *43,* 341-369.

(164) Tartaj, P.; Morales, M. P.; Veintemillas-Verdaguer, S.; Gonzalez-Carreño, T.; Serna, C. J. Synthesis, Properties and Biomedical Applications of Magnetic Nanoparticles. *Handbook of magnetic materials* **2006,** *16,* 403-482.

(165) Rabenau, A. The Role of Hydrothermal Synthesis in Preparative Chemistry. *Angew. Chem. Int. Ed.* **1985,** *24,* 1026-1040.

(166) Byrappa, K.; Adschiri, T. Hydrothermal Technology for Nanotechnology. *Prog. Cryst. Growth Charact. Mater.* **2007,** *53,* 117-166.

(167) Demazeau, G. Solvothermal Reactions: An Original Route for the Synthesis of Novel Materials. *J. Mater. Sci.* **2008,** *43,* 2104-2114.

(168) Walton, R. I. Subcritical Solvothermal Synthesis of Condensed Inorganic Materials. *Chem. Soc. Rev.* **2002,** *31,* 230-238.

(169) Dong, H.; Chen, Y. C.; Feldmann, C. Polyol Synthesis of Nanoparticles: Status and Options Regarding Metals, Oxides, Chalcogenides, and Non-Metal Elements. *Green Chem.* **2015,** *17,* 4107-4132.

(170) Fievet, F.; Lagier, J.; Figlarz, M. Preparing Monodisperse Metal Powders in Micrometer and Submicrometer Sizes by the Polyol Process. *MRS Bull.* **1989,** *14,* 29-34.

(171) Wang, L. Y.; Bao, J.; Wang, L.; Zhang, F.; Li, Y. D. One-Pot Synthesis and Bioapplication of Amine-Functionalized Magnetite Nanoparticles and Hollow Nanospheres. *Chem. Eur. J* **2006,** *12,* 6341-6347.

(172) Wang, X.; Zhuang, J.; Peng, Q.; Li, Y. D. A General Strategy for Nanocrystal Synthesis. *Nature* **2005,** *437,* 121-124.

(173) Deng, H.; Li, X. L.; Peng, Q.; Wang, X.; Chen, J. P.; Li, Y. D. Monodisperse Magnetic Single-Crystal Ferrite Microspheres. *Angew. Chem. Int. Ed.* **2005,** *44,* 2782-2785.

(174) Hervault, A.; Thanh, N. T. K. Magnetic Nanoparticle-Based Therapeutic Agents for Thermo-Chemotherapy Treatment of Cancer. *Nanoscale* **2014,** *6,* 11553-11573.

(175) Hergt, R.; Dutz, S.; Muller, R.; Zeisberger, M. Magnetic Particle Hyperthermia: Nanoparticle Magnetism and Materials Development for Cancer Therapy. *J. Phys. Condens. Matter* **2006,** *18,* S2919-S2934.

(176) Ma, M.; Wu, Y.; Zhou, H.; Sun, Y. K.; Zhang, Y.; Gu, N. Size Dependence of Specific Power Absorption of Fe_3O_4 Particles in Ac Magnetic Field. *J. Magn. Magn. Mater.* **2004,** *268,* 33-39.

(177) Hergt, R.; Dutz, S.; Roder, M. Effects of Size Distribution on Hysteresis Losses of Magnetic Nanoparticles for Hyperthermia. *J. Phys. Condens. Matter* **2008,** *20,* 385214-385226.

(178) Pankhurst, Q. A.; Connolly, J.; Jones, S. K.; Dobson, J. Applications of Magnetic Nanoparticles in Biomedicine. *J. Phys. D: Appl. Phys.* **2003,** *36,* R167-R181.

(179) Rosensweig, R. E. Heating Magnetic Fluid with Alternating Magnetic Field. *J. Magn. Magn. Mater.* **2002,** *252,* 370-374.

(180) Gonzales-Weimuller, M.; Zeisberger, M.; Krishnan, K. M. Size-Dependant Heating Rates of Iron Oxide Nanoparticles for Magnetic Fluid Hyperthermia. *J. Magn. Magn. Mater.* **2009,** *321,* 1947-1950.

(181) Beković, M.; Hamler, A. Experimental System for Determining the Magnetic Losses of Super Paramagnetic Materials; Planning, Realization and Testing. *Applied Measurement Systems, InTech* **2012,** 63-76.

(182) Minkowycz, W.; Sparrow, E. M.; Abraham, J. P., *Nanoparticle Heat Transfer and Fluid Flow*. CRC press: 2012.

(183) Martinez-Boubeta, C.; Simeonidis, K.; Makridis, A.; Angelakeris, M.; Iglesias, O.; Guardia, P.; Cabot, A.; Yedra, L.; Estrade, S.; Peiro, F.; Saghi, Z.; Midgley, P. A.; Conde-Leboran, I.; Serantes, D.; Baldomir, D. Learning from Nature to Improve the Heat Generation of Iron-Oxide Nanoparticles for Magnetic Hyperthermia Applications. *Sci. Rep.* **2013,** *3,* 1652-1659.

(184) Hergt, R.; Hiergeist, R.; Zeisberger, M.; Schuler, D.; Heyen, U.; Hilger, I.; Kaiser, W. A. Magnetic Properties of Bacterial Magnetosomes as Potential Diagnostic and Therapeutic Tools. *J. Magn. Magn. Mater.* **2005,** *293,* 80-86.

(185) Schmidt, A. M. Thermoresponsive Magnetic Colloids. *Colloid. Polym. Sci.* **2007,** *285,* 953-966.

(186) Campbell, S. B.; Patenaude, M.; Hoare, T. Injectable Superparamagnets: Highly Elastic and Degradable Poly(N-Isopropylacrylamide)-Superparamagnetic Iron Oxide Nanoparticle (Spion) Composite Hydrogels. *Biomacromolecules* **2013,** *14,* 644-653.

(187) http://www.dextran.net/about-dextran/dextran-chemistry/physical-properties.aspx (accessed 25.10.2016).

(188) Geismann, C.; Tomicki, F.; Ulbricht, M. Block Copolymer Photo-Grafted Poly(Ethylene Terephthalate) Capillary Pore Membranes Distinctly Switchable by Two Different Stimuli. *Sep. Sci. Technol.* **2009,** *44,* 3312-3329.

(189) Ghosh, S.; Cai, T. Controlled Actuation of Alternating Magnetic Field-Sensitive Tunable Hydrogels. *J. Phys. D: Appl. Phys.* **2010,** *43,* 415504-415513.

(190) Galicia, J. A.; Cousin, F.; Dubois, E.; Sandre, O.; Cabuil, V.; Perzynski, R. Static and Dynamic Structural Probing of Swollen Polyacrylamide Ferrogels. *Soft Matter* **2009,** *5,* 2614-2624.

(191) Anderson, W.; Kozak, D.; Coleman, V. A.; Jamting, A. K.; Trau, M. A Comparative Study of Submicron Particle Sizing Platforms: Accuracy, Precision and Resolution Analysis of Polydisperse Particle Size Distributions. *J. Colloid Interface Sci.* **2013,** *405,* 322-330.

(192) Fissan, H.; Ristig, S.; Kaminski, H.; Asbach, C.; Epple, M. Comparison of Different Characterization Methods for Nanoparticle Dispersions before and after Aerosolization. *Anal. Methods* **2014,** *6,* 7324-7334.

(193) Fan, J. C.; Shi, Z. X.; Lian, M.; Li, H.; Yin, J. Mechanically Strong Graphene Oxide/Sodium Alginate/Polyacrylamide Nanocomposite Hydrogel with Improved Dye Adsorption Capacity. *J. Mater. Chem. A.* **2013,** *1,* 7433-7443.

(194) Ma, D.; Zhang, L. M. Fabrication and Modulation of Magnetically Supramolecular Hydrogels. *J. Phys. Chem. B* **2008,** *112,* 6315-6321.

(195) Wang, J.; Ugaz, V. M. Using in Situ Rheology to Characterize the Microstructure in Photopolymerized Polyacrylarnide Gels for DNA Electrophoresis. *Electrophoresis* **2006,** *27,* 3349-3358.

(196) Adrus, N. B. Stimuli-Responsivehydrogels and Hydrogel Pore-Filled Composite Membranes. Universität Duisburg-Essen, 2012.

(197) https://www.hielscher.com/de/disperse.htm (accessed 31.10.2016).

(198) Wittmar, A.; Vorat, D.; Ulbricht, M. Two Step and One Step Preparation of Porous Nanocomposite Cellulose Membranes Doped with Tio2. *RSC Adv.* **2015,** *5,* 88070-88078.

(199) Chen, D. T. N.; Wen, Q.; Janmey, P. A.; Crocker, J. C.; Yodh, A. G. Rheology of Soft Materials. *Annu. Rev. Condens. Matter Phys.* **2010,** *1,* 301-322.

(200) Shewan, H. M.; Stokes, J. R. Viscosity of Soft Spherical Micro-Hydrogel Suspensions. *J. Colloid Interface Sci.* **2015,** *442,* 75-81.

(201) Shewan, H. M.; Stokes, J. R. Analytically Predicting the Viscosity of Hard Sphere Suspensions from the Particle Size Distribution. *J. Non-Newtonian Fluid Mech.* **2015,** *222,* 72-81.

(202) Pal, R. Rheology of Simple and Multiple Emulsions. *Curr. Opin. Colloid Interface Sci.* **2011,** *16,* 41-60.

(203) Otsubo, Y.; Umeya, K. Rheological Properties of Silica Suspensions in Polyacrylamide Solutions. *J. Rheol.* **1984,** *28,* 95-108.

(204) Kamibayashi, M.; Ogura, H.; Otsubo, Y. Shear-Thickening Flow of Nanoparticle Suspensions Flocculated by Polymer Bridging. *J. Colloid Interface Sci.* **2008,** *321,* 294-301.

(205) Wagner, N. J.; Brady, J. F. Shear Thickening in Colloidal Dispersions. *Physics Today* **2009,** *62,* 27-32.

(206) Zhou, Z.; Hollingsworth, J. V.; Hong, S.; Wei, G. M.; Shi, Y.; Lu, X.; Cheng, H.; Han, C. C. Effects of Particle Softness on Shear Thickening of Microgel Suspensions. *Soft Matter* **2014,** *10,* 6286-6293.

(207) Burdukova, E.; Li, H. H.; Ishida, N.; O'Shea, J. P.; Franks, G. V. Temperature Controlled Surface Hydrophobicity and Interaction Forces Induced by Poly (N-Isopropylacrylamide). *J. Colloid Interface Sci.* **2010,** *342,* 586-592.

(208) Oh, S. J.; Kim, N.; Lee, Y. T. Preparation and Characterization of PVDF/TiO_2 Organic-Inorganic Composite Membranes for Fouling Resistance Improvement. *J. Membr. Sci.* **2009,** *345,* 13-20.

(209) Susanto, H.; Ulbricht, M. Influence of Ultrafiltration Membrane Characteristics on Adsorptive Fouling with Dextrans. *J. Membr. Sci.* **2005,** *266,* 132-142.

(210) Mehta, A.; Zydney, A. L. Permeability and Selectivity Analysis for Ultrafiltration Membranes. *J. Membr. Sci.* **2005,** *249,* 245-249.

(211) Miyano, T.; Matsuura, T.; Sourirajan, S. Effect of Polyvinylpyrrolidone Additive on the Pore-Size and the Pore-Size Distribution of Polyethersulfone (Victrex) Membranes. *Chem. Eng. Commun.* **1993,** *119,* 23-39.

(212) Lafreniere, L. Y.; Talbot, F. D.; Matsuura, T.; Sourirajan, S. Effect of Poly (Vinylpyrrolidone) Additive on the Performance of Poly (Ether Sulfone) Ultrafiltration Membranes. *Ind. Eng. Chem. Res.* **1987,** *26,* 2385-2389.

(213) Sun, W. N.; Chen, C. X.; Li, J. D.; Lin, Y. Z. Ultrafiltration Membrane Formation of PES-C, PES and PPESK Polymers with Different Solvents. *Chin. J. Polym. Sci.* **2009,** *27,* 165-172.

(214) Kurzhals, S.; Zirbs, R.; Reimhult, E. Synthesis and Magneto-Thermal Actuation of Iron Oxide Core-Pnipam Shell Nanoparticles. *ACS Appl. Mater. Interfaces* **2015,** *7,* 19342-19352.

(215) Purushotham, S.; Chang, P. E. J.; Rumpel, H.; Kee, I. H. C.; Ng, R. T. H.; Chow, P. K. H.; Tan, C. K.; Ramanujan, R. V. Thermoresponsive Core-Shell Magnetic Nanoparticles for Combined Modalities of Cancer Therapy. *Nanotechnology* **2009,** *20,* 305101-305111.

(216) Frimpong, R. A.; Hilt, J. Z. Poly(N-Isopropylacrylamide)-Based Hydrogel Coatings on Magnetite Nanoparticles Via Atom Transfer Radical Polymerization. *Nanotechnology* **2008,** *19,* 175101-175107.

(217) Karatay, E.; Andersen, M. B.; Wessling, M.; Mani, A. Coupling between Buoyancy Forces and Electroconvective Instability near Ion-Selective Surfaces. *Phys. Rev. Lett.* **2016,** *116,* 194501-194505.

Appendix A

Mixed matrix membranes prepared at room temperature via NIPS process

1. Preparation

Based on a base dope solution with 14.5 wt% of PES in NMP, membranes with different compositions have been prepared by blending with different mass ratios of NG or MNP to PES: pure PES membrane, NG-PES membrane with 10 % of PNIPAAm NG, MNP-PES membrane with 10 % of MNP, and MNP-NG-PES membrane with 7.5 % MNP and 10 % of PNIPAAm NG. The preparation procedure is analogous to procedure described in section 3.5.3, but with dope solution, the casting knife, the casting plate and the water bath kept at room temperature.

2. Characterization

2.1 Morphology of the membranes

SEM imaging with the ESEM Quanta 400 FEG was used to observe the morphology and the distribution of nanomaterials (MNP and NG) in the porous membranes. The procedure was analogous to the protocol described in section 3.4.6.1.

The result is shown in **Figure A1**. Overall, the membranes prepared at room temperature have analogous macroscopic structures as the membranes prepared under 45 ^{o}C (cf. **Figure 4.35**). For all membranes, the cross-section images show typical anisotropic morphology with a µm-thin dense layer on top and a macroporous support layer (**a1, b1, c1** and **d1**). When looking more carefully, it seems that, in comparison with membrane prepared under 45 ^{o}C, membranes prepared at room temperature have more macrovoids and less microvoids in cross-section. The second column (**a2**, **b2**, **c2**, and **d2**) are detailed images for cross-sections and nanomaterials can be occasionally visualized. However, in comparison with the membranes prepared under 45 ^{o}C (cf. **Figure 4.35)**, it is more difficult to identify them, perhaps more homogeneous structure was obtained due to higher viscosity of dope solutions at room temperature (cf. section 4.3.3). Especially for the NG-PES membrane, less NG accumulation on the pore walls can be visualized. The third column (**a3**, **b3**, **c3** and **d3**) shows images of the top surface of different membranes. MNP could be seen beneath the surface of MNP-PES membrane (**b3**); for MNP-NG-PES

membrane (**d3**), both NG and MNP can be identified in the top surface. For NG-PES membrane (**c3**), occasionally, voids created by NG could been found, but NG themselves were missing. Perhaps they were leached out during sample preparation. But still, it can be seen they buried relatively deep in the membrane.

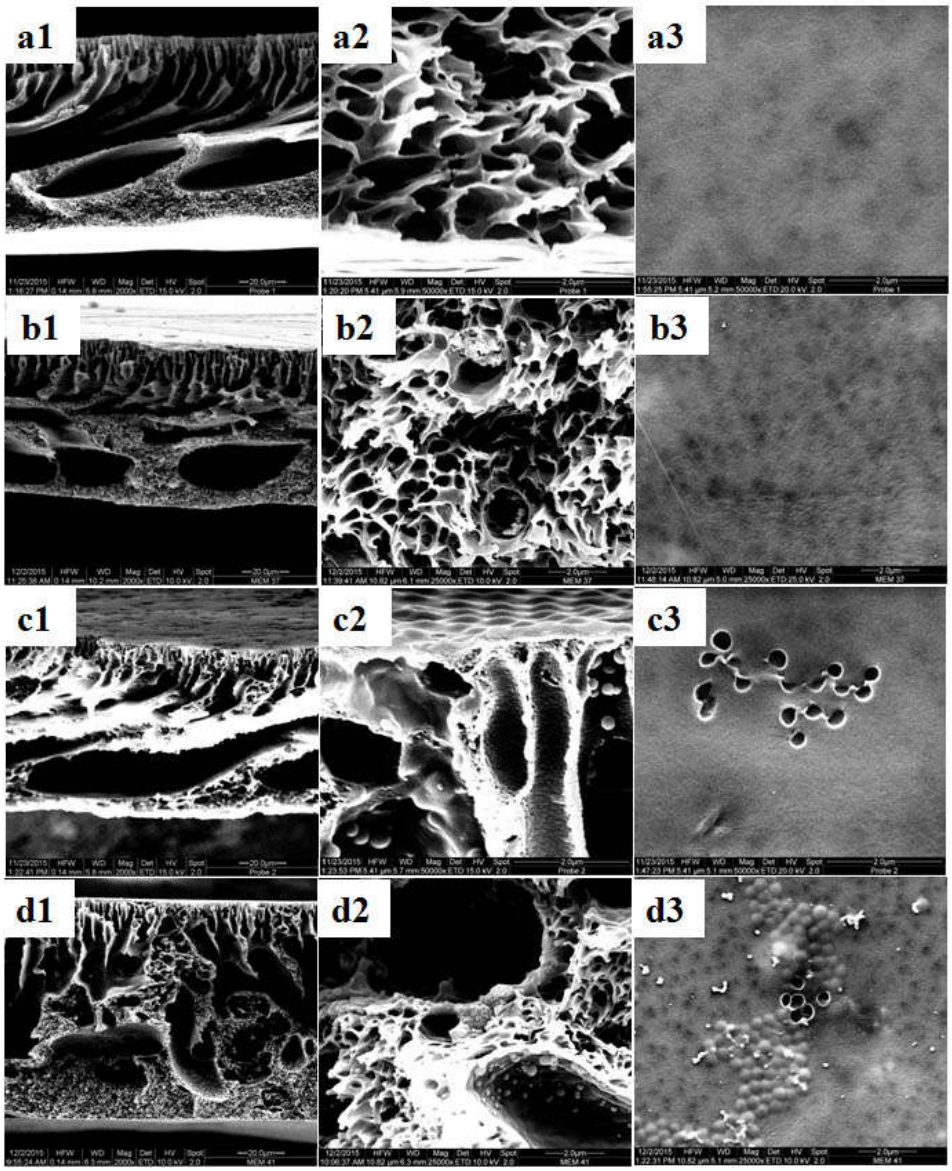

Figure A1. SEM images of the different membranes prepared at room temperature via NIPS: a1-a3 PES membrane (14.5% PES) ; b1-b3MNP-PES membrane (14.5% PES, 1.45% MNP); c1-c3 NG-PES membrane(14.5% PES, 1.45% PNIPAAm NG), and d1-d3 MNP-NG-PES membrane(14.5% PES, 1.45% PNIPAAm NG, 1.09% MNP); column 1: cross-section overview; column 2: details in cross-section; column 3: overview on top layer surface.

2.2 Water permeability and thermo-responsivity

Pure water filtration for membranes, at 25 ^{o}C and 40 ^{o}C was carried out analogous to the protocol described in section 3.4.6.1, to evaluate their water permeability and thermo-responsivity(for membraneS containing NG). Self-constructed dead-end filtration cell with 3.14 cm^2 effective membrane area was used. The trans-membrane pressure was adjusted by gas pressure, and the temperature of feed was controlled by thermostat (Julabo, Germany). Mass of permeate was measured gravimetrically and flux through of the membrane, J, and membrane permeability, P, were calculated according to **Equation (3.5)** (cf. section 3.4.6.1). Here, for the characterization of permeability of different types membranes at room temperature, 3 membrane samples were used and the average permeability was calculated. And for the thermo-responsivity of NG-PES and MNP-NG-PES membrane, one specific sample from each type of membrane was chosen and characterized. The results are shown in **Figure A2** and **Figure A3**.

As shown in **Figure A2**, generally corresponding membranes prepared at room temperature have higher permeability than membrane prepared under 45 ^{o}C (cf. **Figure 4.36**), perhaps due to more presence of macrovoids their cross-sections (cf. **Figure A1**).

Thermo-responsivity of NG-PES and MNP-NG-PES membranes is shown in **Figure A3**. The responsivity of membranes prepared at room temperature was not as high as the responsivity of corresponding membranes prepared under 45 ^{o}C. While for membranes prepared under 45 ^{o}C, the water permeability change was 4 times for NG-PES membrane and 9 times for MNP-NG-PES membrane upon temperature change of feed; for membrane prepared at room temperature, it dropped to only 2 times for NG-PES membrane and 3 times for MNP-NG-PES membrane.

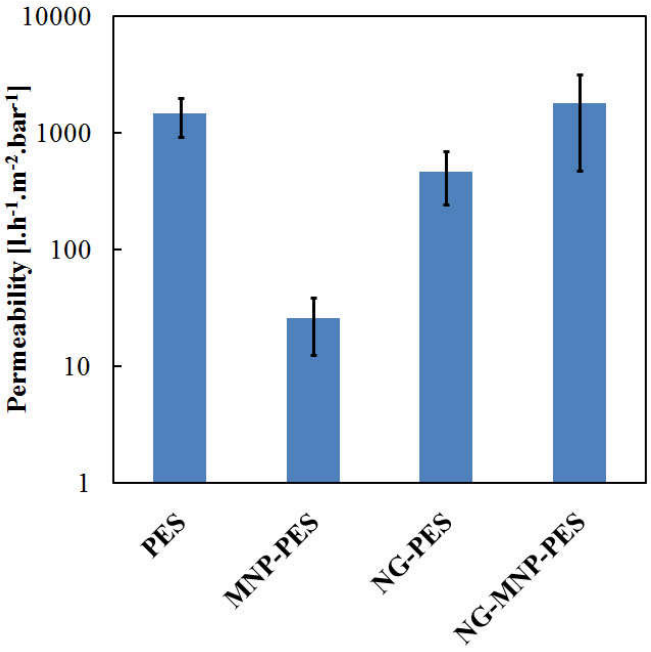

Figure A2. Pure water permeability of different membranes (prepared at room temperature) at 25 °C; for each type of membrane, data from at least 3 independent samples were taken and averaged.

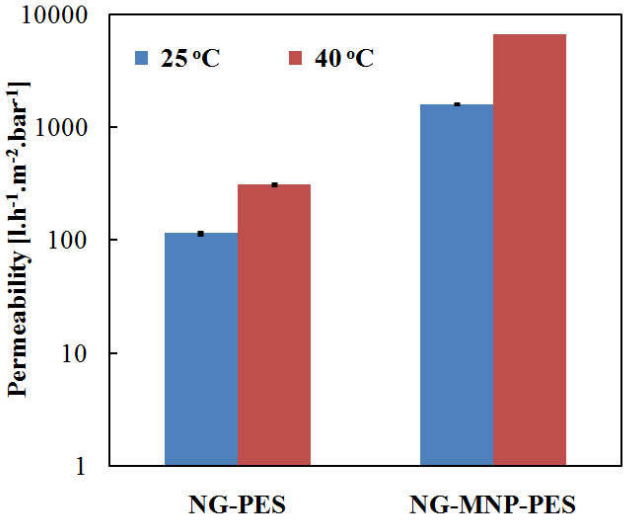

Figure A3. Thermo-responsive water permeability of NG-PES and MNP-NG-PES membranes prepared at room temperature.

Appendix B

Self-made filtration cell for filtration experiment under AMF

(a)

(b)

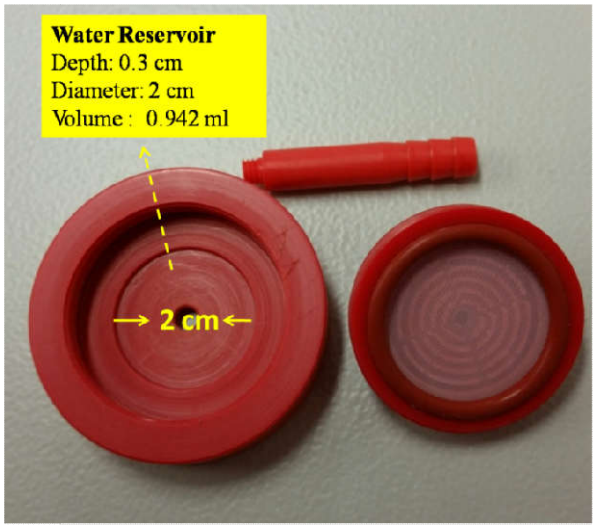

Figure B1. Self-made filtration cell: (a) assembled and (b) inner structure.

Appendix C

List of Tables

List of Figures

Abbreviations

AMF	alternating magnetic field
ADC	analytical disc centrifugation
APS	ammonium persulfate
ATRP	atom transfer radical polymerization
ATR-IR	attenuated total reflection infrared spectroscopy
BP	benzophenone
DLS	dynamic light scattering
DMAc	*N,N′*-dimethylacetamide
EDX	energy dispersive X-ray spectroscopy
HP-GPC	performance gel permeation chromatography
HPC	hydroxypropylcellulose
IEP	isoelectric point
KPS	potassium persulfate
LCST	lower critical solution temperature
MNP	magnetic nanoparticles
MC	methylcellulose
MF	microfiltration
MBA	*N,N′*-Methylenebisacrylamide
NF	nanofiltration
NG	nanogel

NIPS	non-solvent induced phase separation
NMP	*N*-methyl-2-pyrrolidone
PAN	polyacrylonitrile
PAA	poly(acrylic acid)
PHEMA	poly(2-hydroxyethyl methacrylate)
PNIPAAm	poly(*N*-isopropylacrylamide)
PEG	poly(ethylene glycol)
PET	polyethylene terephthalate
PES	polyethersulfone
PPG	poly(propylene glycol)
PSf	polysulfone
PVA	poly(vinyl alcohol)
PVDF	polyvinylidenefluoride
PVME	poly(vinyl methyl ether)
PVMO	poly(vinyl methyl oxazolidone)
PVP	poly(vinyl pyrrolidone)
RAFT	addition-fragmentation chain transfer polymerization
RO	reverse osmosis
SEM	scanning electron microscopy
SLP	specific loss power
SQUID	superconducting quantum interference device
TOC	total organic carbon analyses

TEMED	tetramethylethylenediamine
UF	ultrafiltration
VIPS	vapor induced phase separation
VSM	vibrating sample magnetometer

Appendix D

List of Publications and Conferences

Publications

1. X. Lin, R. Huang, M. Ulbricht, **Novel magneto-responsive membrane for remote control switchable molecular sieving.** *J. Mater. Chem. B.* **2016**, 4, 867-879.

2. X. Lin, B. Nguyen Quoc, M. Ulbricht, **Magneto-responsive polyethersulfone-based iron oxide cum hydrogel mixed matrix composite membranes for switchable molecular sieving**. *ACS Appl. Mater. Interfaces.* **2016**, 8, 29001−29014.

Conferences

2016 PERMEA 2016 - Membrane Science and Technology Conference of Visegrád Countries, Prague, Czech Republic, 16th - 19th, May.

Magneto-responsive polymer hydrogel-based composite membranes for switchable molecular sieving (oral presentation)

2015 Euromembrane 2015, Aachen, Germany, 6th - 10th, September.

Designing magneto-responsive separation membranes (oral presentation.)

2015 15th Network Young Membrains, Aachen, Germany, 4th - 5th, September.

Designing magneto-responsive separation membranes (oral presentation.)

2015 3rd IWaTec Winter School on Sustainable Use of Resources, EI Gouna, Egypt, 21st - 28th, February.

Magneto-responsive membranes for molecular separation (oral presentation.)

2014 1st Leibniz Young Polymer Scientist Forum, Aachen, Germany, 27th -28th, August

Designing magneto-responsive separation membranes (oral and poster presentation)

2014 Gordon Research Conference "Membranes: Materials and Processes", New London, USA, 5th - 11th, July

Designing magnetically responsive separation membranes (oral and poster presentation)

2014 DECHEMA Membrane Day: New development in Cross Flow Filtration: Membrane, Module and Process, Frankfurt, Germany, 9th, April.

Designing magnetically responsive separation membranes (poster presentation)

Awards

2016 Student lecture award, PERMEA 2016

2015 Award for best group presentation, 15th Network Young Membrains

2014 Award for best group presentation, 1st Leibniz Young Polymer Scientist Forum

2014 Prize for best poster, DECHEMA Membrane Day

Appendix E

Curriculum vitae

The curriculum vitae is not contained in online version